Mathematical Modelling and Simulations of the Hemodynamics in the eye

Matteo Carlo Maria Aletti



Mathematical Modelling and Simulations of the Hemodynamics in the eye

THÈSE DE DOCTORAT

Présentée par

Matteo Carlo Maria Aletti

pour obtenir le grade de

DOCTEUR DE
L' UNIVERSITÉ PIERRE ET MARIE CURIE - Paris VI

Spécialité : Mathématiques Appliquées

Soutenue publiquement le 30 mai 2017 devant le jury composé de :

Jean-Frédéric Gerbeau	Directeur de thèse
Damiano Lombardi	Co-Directeur de thèse
Stéphanie Salmon	Rapporteur
Christian Vergara	Rapporteur
Olivier Pironneau	Président du jury
Giovanna Guidoboni	Examinatrice

Après avis favorables des rapporteurs: Stéphanie Salmon et Christian Vergara

Thèse préparée au sein de l'équipe-projet REO
Laboratoire Jacques-Louis Lions
Université Pierre et Marie Curie - Paris 6
et **Centre de Recherche Inria de Paris**
2 rue Simone Iff
75589 Paris Cedex 12

This research was made possible by a Marie Curie grant from the European Commission in the framework of the REVAMMAD ITN (Initial Training Research network), Project number 316990.

Acknowledgements

I would like to thank the reviewers Christian Vergara and Stéphanie Salmon who accepted to read this manuscript and provided interesting remarks, questions and insights and also Olivier Pironneau and Giovanna Guidoboni that participated to the final examination.

Je souhaite remercier Jean-Frédéric Gerbeau, mon directeur de thèse, qui m'a donné l'opportunité de travailler sur un sujet très interessant. Les discussions scientifiques et ses conseils ont été essentiels pour ce travail.

Vorrei ringraziare anche Damiano Lombardi. Ha collaborato moltissimo a questo progetto con numerosissime discussioni su ogni dettaglio di questo lavoro: dalle linee generali, ai possibili sviluppi e perfino al debugging. Una presenza costante piena di entusiasmo e ottimismo che mi ha consentito di lavorare con tranquillità e fiducia per questi tre anni.

I would also like to thank all the members of the REVAMMAD project. Via interesting discussions and instructive presentations they all have contributed to enrich my skills on subjects that were quite far from my original background. In particular, Francesco Calivà, Andrew Hunter and Bashir Al-Diri provided the geometries used for the simulations of the blood flow in the retina and the discussions with Giovanna Guidoboni were essential for the analysis of the clinical literature and for the mathematical modelling of the eye.

I'd like to thank all the members of the REO team: they have always been available for scientific discussions. I'd like to thank Benoit who shared the office with me back in Rocquencourt: you got me started with felisce and we made a great coding team! Thank you Sanjay for so many interesting discussions. Mikel and Alba, thank you for the great travel to California and for being my favourite Basque friends. Grazie Elisa per avermi aiutato con la burocrazia francese quando sono arrivato, ma anche per le tante serate e per la buona cucina. Thank you Chloé for your support throughout all these years with many good advices and a lot of energy, especially during the writing period. Not to mention all the Massy games nights! Merci Eliott de m'avoir appris le français, d'utiliser cvgraph :), pour les (vraiment!) très nombreuses discussions, pour les parties d'échecs, pour le lunch script.. Thank you Noemie for all the "troisème navette" that we have taken togheter and for the micro-circulation discussions! Grazie Lèa per aver alzato il mio livello culturale con cinema, libri e mostre e anche per aver partecipato al progetto "Matteo se lève tôt" che, a dire le verità, è fallito, ma almeno ci abbiamo provato! Thank you Nicolas and Fabien for all the fun and for the running training. Grazie Lara e Alberto per aver portato il buon umore nell'ufficio italiano, per le cene, le lunghe chiaccherate e soprattutto le pause gelato! Many thanks to all the other people that passed by Inria in these years and with whom I had the chance to spend some time and share some thoughts.

Ringrazio i miei genitori, Laura, Pietro (e Davide!) per il sostegno, l'aiuto a distanza e per la sopportazione! Infine, grazie a Ilaria che con il suo entusiasmo e la sua energia ha accorciato la distanza geografica.

Abstract

The structure of the eye offers a unique opportunity to directly observe the microcirculation, by means, for instance, of fundus camera, which are cheap devices commonly used in the clinical practice. This can facilitate the screening of systemic diseases such as diabetes and hypertension, or eye diseases such as glaucoma. A key phenomenon in the microcirculation is the autoregulation, which is the ability of certain vessels to adapt their diameter to regulate the blood flow rate in response to changes in the systemic pressure or metabolic needs. Impairments in autoregulation are strongly correlated with pathological states.

The hemodynamics in the eye is influenced by the intraocular pressure (IOP), the pressure inside the eye globe, which is in turn influenced by the ocular blood flow. The interest in the IOP stems from the fact that it plays a role in several eye-diseases, such as glaucoma. Mathematical modelling can help in interpreting the interplay between these phenomena and better exploit the available data.

In the first part of the thesis we present a simplified fluid-structure interaction model that includes autoregulation. A layer of fibers in the vessel wall models the smooth muscle cells that regulate the diameter of the vessel. The model is applied to a 3D image-based network of retinal arterioles.

In the second part, we propose a multi-compartments model of the eye. We use the equations of poroelasticity to model the blood flow in the choroid. The model includes other compartments that transmit the pulsatility from the choroid to the anterior chamber, where the measurements of the IOP are actually performed. We present some preliminary results on the choroid, the aqueous humor and on the choroid coupled with the vitreous.

Finally, we present a reduced order modelling technique to speed up multi-physics simulations. We use high fidelity models for the compartments of particular interest from the modelling point of view. The other compartments are instead replaced by a reduced representation of the corresponding Steklov-Poincaré operator.

Résumé

La structure de l'œil permet d'observer la microcirculation, grâce aux caméras de fond d'oeil. Ces appareils sont bon marché et couramment utilisés dans la pratique clinique, permettant le dépistage de maladies oculaires. La capacité des vaisseaux à adapter leur diamètre (autorégulation) afin de réguler le débit sanguin est importante dans la microcirculation. L'hémodynamique de l'œil est impactée par la pression à l'intérieur du globe oculaire (IOP), qui est à son tour influencée par le flux sanguin oculaire. Les altérations de l'autorégulation et l'IOP jouent un rôle dans les maladies oculaires. La modélisation mathématique peut aider à interpréter l'interaction entre ces phénomènes et à mieux exploiter les données médicales disponibles.

Dans la première partie, nous présentons un modèle simplifié d'interaction fluide-structure qui inclut l'autorégulation, appliqué à un réseau 3D obtenu par imagerie médicale. Les cellules musculaires lisses régulant le diamètre du vaisseau sont modélisées dans la structure.

Ensuite, nous utilisons des équations de poroélasticité pour décrire le flux sanguin dans la choroïde, dans un modèle multi-compartiments de l'œil. Cette approche permet de rendre compte de la transmission de la pulsatilité de la choroïde à la chambre antérieure, où l'IOP est mesurée. Nous présentons des résultats préliminaires sur la choroïde, l'humeur aqueuse et sur la choroïde couplée avec la vitrée.

Enfin, nous présentons un modèle d'ordre réduit pour accélérer des simulations multi-physiques. Des modèles de haute précision sont utilisés pour les compartiments d'intérêt et une représentation réduite de l'opérateur de Steklov-Poincaré est utilisée pour les autres compartiments.

Contents

Chapter 1

Introduction

Contents

1.1 Motivation

Several ocular diseases, for example glaucoma, age related macula generation or diabetic retinopathy, are still a challenge for the ophthalmologists. Fluid and structure mechanics plays an important role in these and other pathologies of the eye. The understanding of the mechanical factors behind their development is important to find new treatments. Mathematical models provide access to hidden quantities, clarify the physical mechanisms underlying the diseases and give the possibility of studying the different risk factors independently. For these reasons, there is an increasing need for mathematical tools. For instance, in the case of glaucoma, one of the most common ocular diseases, the mathematical modelling of ocular mechanics and hemodynamics has been used to study the progression of the disease [HGA+13].

The interest in the study of the hemodynamics in the eye and, in particular, in the retina also stems from the fact that the eye is the only location of the human body where the micro-circulation can be observed non-invasively. In fact, because of the optical properties of the eyeball it is possible to acquire images or videos of the retina in vivo. Besides providing information about micro-circulation in general, retinal images are also used to perform measurements and to support diagnosis. The most common images are the retinal fundus images (Figure 1.1) that are simple to take and require relatively cheap devices. These images are of lower quality

Figure 1.1: An example of retinal fundus image. The dark area in the center is the macula that contains the fovea: the center of the vision. The light area in the nasal zone (the left in this image) is the optic disk, a blind spot of the retina where the central retinal artery enters the eye and the central retinal vein leaves it. Some lesions are visible in the lower region of the image. Image number three of the DRIVE dataset [SAN+04].

compared to other types of images, but they are used in everyday clinical prac-

tice. Lots of imaging techniques have therefore been developed for the automatic analysis of these images. State of the art algorithms perform, automatically or semi-automatically, vessel segmentation [SAN+04, ADHS09] and measurements of vessels widths and branching angles [LHS+04, PRMT+11]. Other techniques have been developed for specific diseases. For example, automatic algorithms localize and count retinal lesions in patients with diabetic retinopathy. This statistical information supports early diagnosis and the planning of screening invervals [SBW+02], [OEHB16].

Retinal fundus images are a source of geometrical information that can be used for modelling the hemodynamics. Imaging tools provide data about the vessels network such as lengths, widths, artery/vein classifications and connectivities at the bifurcations. In this thesis we focused on three-dimensional geometries, but 0D models are also an option [CLC+17]. Image-based modelling contains patient specific information. Therefore it brings more specific data with respect to hemodynamics models based on idealized networks of vessels.

When studying the blood flow in the retina, we have to take into account that the largest vessels have a diameter of less than $200\mu m$ [PRBR+08]. The hemodynamics is in the microcirculation regime and the Fahraeus effect, the Fahraeus-Lindquist effect and the plasma skimming may be relevant in determining the distribution of hematocrit and the velocity profile [PNG92, PLCG89]. However, we did not consider those effects. Instead, we addressed the modelling of autoregulation that is another typical aspect of the microcirculation. Blood autoregulation is a process common to several organs of the body [SM99] where arterioles adapt their diameter in response to a change in the feeding pressure or in the metabolic demand of the tissue. By changing their diameter, the arterioles adapt their hydraulic resistance and therefore control the blood flow rate. This is possible because arterioles wall contains a layer of smooth muscle cells that can contract or dilate in response to chemical signals. Moreover, impaired autoregulation has been associated to various diseases such as diabetic retinopathy and glaucoma [KPR95, RPK95, GRS+84].

Blood autoregulation in the retina has been recently modelled on 0D networks [AHS+13] and on 1D networks [CM15]. In [ACS08, AHS+13], the authors investigated the biological factors that induce smooth muscle cells contraction. We did not focus on this aspect and we considered the problem from the perspective of the fluid-structure interaction. We investigated the mechanical part of the process, how the smooth muscle cells contraction actually reduces the blood flow rate. In particular, we proposed a simplified shell model for the vessel wall that contains a layer of smooth cells. The smooth muscle cells in this layer contain a passive elastic response, but also an active component that allows them to contract and dilate. This model is applied to a large image-based 3D network of arterioles. For this reason, the fluid-structure interaction approach that we used is a simplified approach in which the model of the wall is embedded in the fluid problem considerably reducing the computational costs. Similar simplified approaches were already present in the literature [FVCJ+06, NV08, Pir14, CDQ14], but none of them was suitable for the modelling of autoregulation.

Another important factor that influences the hemodynamics of the retina is the intraocular pressure (IOP), which is the pressure inside the eye globe. The level of IOP has an impact on retinal blood flow (see for example [GHC+14a, CM16]) and it is an important risk factor in glaucoma. However, ocular blood flow has an impact on the IOP as well. In fact, measurements of IOP exhibits oscillations with the time scale of the heartbeat. These oscillations are clearly a fluid-structure interaction phenomenon due to the pulsatility of the blood flow inside the choroid, a tissue located behind the retina. In the second part of this thesis we described this phenomenon. Its modelling is not straightforward since numerous compartments of the eye are involved in this interaction. In the literature we find models for the different compartments, especially for what concerns the mechanics of the external shell. However, there is a lack of multiple compartments models where the different parts of the eye are all considered.

Multi-physics and multi-domain simulations are computationally intensive. In view of future clinical applications it is important to keep the computational costs reasonably low. For this reason, in the last part of the thesis we focused on a reduced order modelling technique to reduce the cost of these simulations. Our idea was that all the domains included in the model are necessary for a complete description of the phenomenon, but the solution on some of these domains may not be interesting from the clinical point of view. The proposed technique aims at replacing these domains with a reduced representation of the corresponding Steklov-Poincaré operator computed offline.

1.2 Contents and manuscript organization

This manuscript is organized as follows. Chapters 2 and 3 deal with the modelling of retinal hemodynamics. In particular, a new simplified fluid-structure interaction model is proposed in Chapter 2 and it is used to describe the interaction between the vessel wall of arterioles and the blood. A non-linear Koiter model describes the endothelium layer, while the smooth muscle cells, that are present on the vessel wall, are described via a layer of elastic fibers. By introducing some simplifying assumptions, the structure equation appears as a boundary condition for the fluid problem strongly reducing the computational costs. Chapter 3 deals with the modelling of autoregulation that has been added to the model introduced in Chapter 2 by including an active component in the force exerted by the smooth muscle cells. The approach is tested on a realistic geometry obtained from 2D fundus images of the retina and the results are compared to experimental data.

Chapters 4 and 5 deal with a global view of the eye. In Chapter 4 the anatomy of the eye is detailed with a focus on the state of the art of the modelling of the eye fluid dynamics and mechanics. The available models for the different compartments are briefly listed and summarized. In Chapter 5 we present a 3D model of the eye with multiple compartments. The model focuses on describing the pulsatility observed in the IOP that is generated from blood pulsatility in the choroid. In the

chapter we explain the modelling choices concerning both geometry and physics, we present a poro-elastic model for the circulation in the choroid and we show some preliminary results.

In Chapter 6 we present a reduced order model for speeding up multi-physics simulations. The method has been devised for modelling multi-physics systems where one, or more, compartments can be replaced by a reduced representation of the corresponding Steklov-Poincaré operator. High-fidelity models can be employed only on the other, more interesting, compartments. The approach is based on the low rank decomposition of the Steklov-Poincaré operator representing the action of one of the compartments. The method exploits an offline-online decomposition strategy. Several numerical testcases are presented on 3D examples of fluid-fluid and fluid-structure interactions.

In Appendix A we annexed a proceeding on a retinal imaging tool that we have developed for the reconstruction of the geometries used in the first two chapters.

1.3 My contributions

1.3.1 Publications

The study about retinal hemodynamics (Chapter 2) and autoregulation (Chapter 3) leaded to the following papers

- Matteo Aletti, Jean-Frédéric Gerbeau, and Damiano Lombardi
  A simplified fluid–structure model for arterial flow. Application to retinal hemodynamics.
  Computer Methods in Applied Mechanics and Engineering, 306:77–94, 2016;

- Matteo Aletti, Jean-Frédéric Gerbeau, and Damiano Lombardi
  Modeling autoregulation in three-dimensional simulations of retinal hemodynamics
  Journal for Modeling in Ophthalmology, 1(1):88–115, 2016.

The reduced order method presented in Chapter 6 is published in

- Matteo Aletti and Damiano Lombardi
  A reduced order representation of the Poincaré-Steklov operator: an application to coupled multi-physics problems
  International Journal for Numerical Methods in Engineering, 2017.

During my collaboration with the University of Lincoln on the extraction of geometries from retinal fundus images I contributed to this proceeding (attached in Appendix A)

- Francesco Caliva, Matteo Aletti, Bashir Al-Diri, and Andrew Hunter
  A new tool to connect blood vessels in fundus retinal images
  In Engineering in Medicine and Biology Society (EMBC), 2015 37th Annual International Conference of the IEEE, pages 4343–4346. IEEE, 2015.

1.3.2 Implementation

The simulations reported in this manuscript were done with FELiSCe (Finite Elements for Life SCience and Engineering) an in-house finite-element code developed at Inria in the REO team. FELiSCe is a parallel C++ code based on the linear algebra library PETSc. The models of Chapters 2 and 3 are based on the Navier-Stokes solver which was already available in FELiSCe. However, they required the development of a differential geometry module for the computation of surface integrals involving the variety of terms arising from the non-linear Koiter shell model and from the fibers model.

The global model of the eye introduced in Chapter 5 required the addition of new classes implementing solvers for the Navier-Stokes-Boussinesq equations, the linear elasticity equation and the Biot's equations. In order to exchange data between domains with non-conform interface meshes, it was also necessary to implement generic interpolation techniques for the evaluation of a finite-element function on a different surface mesh.

The coupling between two or more compartments is handled via CVGraph. CVGraph is a C++ library developed at Inria in the REO team. The goal of this library is to provide a flexible framework to run multi-physics simulations. The idea is that each domain has its own solver and its own executable. CVGraph handles the communications between the executables and also the coupling schemes, so that minimal changes are required to the single domain software to be included in a larger model with multiple domains. My contribution to this part was to further improve the CVGraph library and his interface with FELiSCe. In particular, we worked on the automatization of the interpolation between non-conform interfaces and on the generalization of the library to the case of more than two domains.

The reduced order technique presented in Chapter 6 was implemented in FELiSCe. We used SLEPc, an external library dedicated to sparse eigenvalue problems, for the computation of Laplace-Beltrami eigenfunctions. We implemented a general interface that enables the use of the reduction technique for different types of problems, such as the linear elasticity equation, the Stokes equations and the flow in porous media.

We also worked on the generation of the geometries used in the simulations. The meshes used in Chapters 2 and 3 have been obtained from the segmentation of retinal fundus image using a software based on [ADHS09]. We developed a tool for performing connectivity detection (see Appendix A) and in particular we also developed a code to generate a 3D surface mesh starting from the 2D connected segmentation based on Matlab and Gmsh [GR09].

Chapter 2

A simplified fluid-structure model for arterial flow. Application to retinal hemodynamics

---

This chapter is based on [AGL16b]

In this chapter a simplified fluid-structure interaction model for applications in hemodynamics is proposed. This work focuses on simulating the blood flow in arteries, but it could be useful in other situations where the wall displacement is small. As in other approaches presented in the literature, our simplified model mainly consists of a fluid problem on a fixed domain, with Robin-like boundary conditions and a first order transpiration. Its main novelty is the presence of fibers in the solid. As an interesting numerical side effect, the presence of fibers makes the model less sensitive than others to strong variations or inaccuracies in the curvatures of the wall. An application to retinal hemodynamics is investigated.

Contents

2.1 Introduction

Fluid-structure interaction plays an important role in the cardiovascular system. In many situations, complex nonlinear models that include large displacements and deformations have to be considered. This is, for example, the case for valve simulation [LS13, vAdB04, vAv06, AGPT09] or in the aorta [BCZH06, CRD+11, MXA+12]. It is well-known that these simulations are very demanding, and in spite of the progress achieved in recent years ([FLV15, BČG+14, BF14] to name but a few), they remain challenging and the subject of active research.

In this chapter, we consider those situations where it is assumed that the problem under study can be addressed using simplified approaches. The idea is to radically simplify the solid model in order to replace the full fluid-structure problem by a fluid problem with non-standard boundary conditions at the fluid-structure interface. Various approaches have been recently proposed in this direction [FVCJ+06, NV08, CDQ14, Pir14].

In [NV08], F. Nobile and C. Vergara started from a Koiter linear shell model and neglected the flexural terms. After discretization, the resulting fluid-structure equations are reduced to a fluid problem with Robin boundary conditions. In this approach, the fluid domain was moving. In [Pir14], O. Pironneau further simplified this approach by fixing the fluid domain, introducing a zero order transpiration boundary condition, and by assuming that the curvature of the artery was constant. More precisely, whatever the geometry of the vessel is, the stiffness term is always computed as if the vessel were a cylinder. With these simplifications, the authors were able to perform a comprehensive mathematical analysis of the problem [CRGMP14]. In [FVCJ+06], A. Figueroa et al. also assumed that the computational domain was fixed and used a zero order transpiration boundary condition. The structural model was derived assuming homogeneity throughout the thickness. Compared to the two previous approaches, this one requires adding new degrees of freedom to the fluid problem. This drawback is, however, counterbalanced by the fact that the resulting model is more stable on real geometries featuring variations of curvature, according to [CDQ14] where an extensive comparison was proposed.

The main focus of the present study is the simulation of the autoregulation of blood flow in the retinal arteries. This phenomenon is very important since defective autoregulation may play a role in many retinal diseases, including glaucoma which is the second leading cause of blindness worldwide [AHS+13]. Autoregulation consists of an active change of the artery diameter in response to a change in the mean perfusion pressure. This is clearly a fluid-structure interaction problem, but it is typically a case in which a full structural model does not seem necessary, at least to render the basic phenomenon, which is a slight contraction of the vessel wall. The application of the model proposed in this article to the autoregulation of blood flow is presented in more detail in Chapter 3.

In our approach, we choose to keep the computational domain fixed, as in [FVCJ+06], and we adopt transpiration boundary conditions. Nevertheless, the phenomenon of autoregulation cannot be addressed with the zero order transpira-

tion formula usually adopted in the literature. Our model will therefore be based on first order transpiration. For the structure, we will start from a Koiter shell model without flexural terms as in [NV08]. But, as noted in [CDQ14], this leads to a simplified model that may be unstable in real geometries due to inaccuracies in the curvature obtained from medical images. Even when the curvatures are computed accurately, this model, called inertial-algebraic, may be inaccurate in geometries with a locally flat fluid-structure interface. Note that the model proposed in [Pir14] does not suffer from this problem since it assumes everywhere a cylinder-like geometry in the terms involving the curvature. In our model, we will show that the introduction of fibers allows us to overcome this problem thanks to the presence of a surface Laplace operator.

In summary, the main features of our simplified fluid-structure model are the following: it mainly consists of a fluid problem on a fixed domain, with Robin-like boundary conditions, which makes it insensitive to the added-mass effect; it takes into account in a simplified manner the presence of fibers in the solid; it is less sensitive than others to strong variations or inaccuracies in the curvatures and, as a consequence, it remains robust in the presence of flat regions in the surface.

The structure of the article is as follows: in Section 2 the structure model is proposed; in Section 3 the fluid model and the coupling are presented; Section 4 deals with numerical discretization issues and Section 5 contains numerical illustrations, including an initial simulation in a retinal arteries network.

2.2 Structure model

In this section, a simplified structure model is introduced to describe the dynamics of the wall. Similarly to other studies presented in the literature, the starting point is the Koiter thin shell model (see [NV08, Pir14]). The resulting model aims to render the motion of a thin shell with one or several fiber layers. When the kinematics of the fibers is considered, it is relevant to keep second order terms in their deformation because they have an important role in the stability of the model (the gradient terms in equation (2.5) below). As a consequence, to be consistent with the approximation made for the fibers, second order terms will also be kept in the shell model. This leads to the inclusion of non-linear terms in the shell model.

2.2.1 Notation

Let Γ be the reference position of the structure and a smooth mapping $\boldsymbol{\phi}$ defining its position: $\boldsymbol{\phi} : \omega \subset \mathbb{R}^2 \to \Gamma \subset \mathbb{R}^3$, $\boldsymbol{\phi} = \boldsymbol{\phi}(\xi_1, \xi_2)$, $\forall (\xi_1, \xi_2) \in \omega$. Let $(\boldsymbol{a}_1, \boldsymbol{a}_2)$ be the local covariant basis given by $\boldsymbol{a}_\alpha = \partial_\alpha \boldsymbol{\phi} = \frac{\partial \boldsymbol{\phi}}{\partial \xi_\alpha}$, $\alpha = 1, 2$. In what follows, Greek letters for the indices take values in $\{1, 2\}$ and latin letters in $\{1, 2, 3\}$. Einstein notation is used to denote summation over repeated indices. The normal unit vector is defined as $\boldsymbol{a}_3 = \frac{\boldsymbol{a}_1 \times \boldsymbol{a}_2}{|\boldsymbol{a}_1 \times \boldsymbol{a}_2|}$. Let $\boldsymbol{A}$ and $\boldsymbol{B}$ be the matrix representations of the first and second fundamental forms associated with the reference configuration Γ and let $\boldsymbol{S} = \boldsymbol{A}^{-1}\boldsymbol{B}$ be the representation of the shape operator. The entries of $\boldsymbol{A}$ and $\boldsymbol{B}$ are

respectively given by $a_{\alpha\beta} = a_{\beta\alpha} = \boldsymbol{a}_\alpha \cdot \boldsymbol{a}_\beta$ and $b_{\alpha\beta} = b_{\beta\alpha} = \boldsymbol{a}_3 \cdot \partial_\alpha \boldsymbol{a}_\beta$. The entries of $\boldsymbol{A}^{-1}$ are denoted by $a^{\alpha\beta}$, thus $a^{\alpha\sigma}a_{\sigma\beta} = \delta_{\alpha\beta}$. Given a tensor $\boldsymbol{M} = (m_{\sigma\beta})$, the entries of $\boldsymbol{A}^{-1}\boldsymbol{M}$ are denoted by $m^\alpha_\beta = a^{\alpha\sigma}m_{\sigma\beta}$. The surface covariant derivative of a vector field $\boldsymbol{q} : \omega \to \mathbb{R}^3$ is denoted by

$$q_{\alpha||\beta} = \partial_\beta q_\alpha - \Gamma^\sigma_{\alpha\beta} q_\sigma - b_{\alpha\beta} q_3 \quad \text{and} \quad q_{3||\beta} = \partial_\beta q_3 + b^\sigma_\beta q_\sigma, \tag{2.1}$$

where $\Gamma^\sigma_{\alpha\beta}$ are the Christoffel symbols. The covariant gradient of a scalar field $q : \omega \to \mathbb{R}$ is denoted by $\nabla_c q = (\partial_\alpha q)_{\alpha=1,2}$. In what follows, we denote by $\langle u, v\rangle$ the standard $L^2(\Omega)$ inner product and by $\langle u, v\rangle_\omega$ the $L^2(\Gamma)$-scalar product $\int_w uv\sqrt{a}\, d\boldsymbol{\xi}$ where $a = det(\boldsymbol{A})$.

2.2.2 Nonlinear Koiter shell model

The equations for the Koiter shell model are introduced following [Cia00]. The hypotheses are the following:

- the displacement of the structure is parallel to the normal of the reference configuration;
- the bending terms are negligible;
- the material is linear, isotropic and homogeneous.

As a consequence of these assumptions, only the membrane part of the Koiter model is considered, the shell deformation is described by the change of metric tensor $\boldsymbol{G}$ and the stress is linear in the deformation. The tensor $\boldsymbol{G}$ is a function of the displacement field $\boldsymbol{\eta}$ and reads:

$$g_{\alpha\beta} = \frac{1}{2}(\boldsymbol{\eta}_{\alpha||\beta} + \boldsymbol{\eta}_{\beta||\alpha}) + a^{ij}\boldsymbol{\eta}_{i||\alpha}\boldsymbol{\eta}_{j||\beta},$$

with $a^{3\beta} = a^{\alpha 3} = 0, a^{33} = 1$. The constitutive law for the stress-strain relationships is expressed by means of the elastic tensor $\mathcal{E}$, whose contravariant components read:

$$\mathcal{E}^{\alpha\beta\sigma\tau} = \frac{4\lambda^s\mu^s}{\lambda^s + 2\mu^s} a^{\alpha\beta}a^{\sigma\tau} + 2\mu^s a^{\alpha\sigma}a^{\beta\tau} + 2\mu^s a^{\alpha\tau}a^{\beta\sigma},$$

where λ^s, μ^s are the Lamé coefficients of the structure.

The equilibrium configuration for the shell (see [Cia00] for an extensive discussion) is the stationary point of the energy functional:

$$\psi^\kappa(\boldsymbol{\eta}) = \frac{1}{2}\int_\omega \mathcal{E}^{\alpha\beta\sigma\tau} g_{\sigma\tau}(\boldsymbol{\eta}) g_{\alpha\beta}(\boldsymbol{\eta})\ h_\kappa\sqrt{a}\, d\boldsymbol{\xi} - \int_\omega \boldsymbol{f}\cdot\boldsymbol{\eta}\ h_\kappa\sqrt{a}\, d\boldsymbol{\xi},$$

where h_κ is the Koiter shell thickness and $\boldsymbol{f}$ are the external forces.

Given a test field $\boldsymbol{\chi}$, defined in a suitable functional space (according to the boundary conditions of the structure), the equilibrium equations in weak form are

obtained by:

$$\Psi^\kappa(\boldsymbol{\eta}, \boldsymbol{\chi}) := \langle \delta_\eta \psi^\kappa(\boldsymbol{\eta}), \boldsymbol{\chi} \rangle_\omega = 0, \tag{2.2}$$

where δ_η denotes the Fréchet derivative with respect to $\boldsymbol{\eta}$.

The form Ψ^κ is specialised for the present case according to the assumptions. By using the hypothesis of a pure normal displacement, *i.e.* $\boldsymbol{\eta} = \eta \boldsymbol{n}$, and Eq.(2.1), the covariant components of the change of metric tensor $\boldsymbol{G}$ reduce to:

$$g_{\alpha\beta} = -b_{\alpha\beta}\eta + \frac{1}{2} a^{\sigma\tau} b_{\sigma\alpha} b_{\tau\beta} \eta^2 + \frac{1}{2} \partial_\alpha \eta \partial_\beta \eta.$$

After some algebra (see the details of the computation in 2.7), the form reads:

$$\begin{aligned} \Psi^\kappa(\eta, \chi) := \frac{2E}{1-\nu^2} \int_\omega \left(c_1\eta - 3c_2\eta^2 + 2c_3\eta^3\right) \chi - 2\nabla\chi^T (C_1\eta + C_2\eta^2)\nabla\eta + \\ -\nabla^T\eta \left[(C_1 + 2C_2\eta)\,\chi\right] \nabla\eta + \frac{1}{2} \left(\nabla\eta^T A^{-1} \nabla\eta\right) \nabla^T \chi A^{-1} \nabla\eta \; h_\kappa \sqrt{a}\, d\boldsymbol{\xi} - \\ \int_\omega \boldsymbol{f}_n \cdot \chi \; h_\kappa \sqrt{a}\, d\boldsymbol{\xi}, \end{aligned} \tag{2.3}$$

where E is the Young modulus of the material, ν the Poisson coefficient, the constant tensors (C_j) and the coefficients (c_k) are expressed as a function of the mean and Gauss curvatures (respectively ρ_1 and ρ_2) and the Poisson ratio as follows:

$$\begin{aligned} c_1 &= 4\rho_1^2 - 2(1-\nu)\rho_2, \\ c_2 &= 4\rho_1^3 + (\nu - 3)\rho_1\rho_2, \\ c_3 &= 4\rho_1^4 - 4\rho_1^2\rho_2 + \frac{1}{2}(1+\nu)\rho_2^2, \\ C_1 &= \left[\nu\rho_1 I + \frac{1}{2}(1-\nu)S\right] A^{-1}, \\ C_2 &= \left[\nu\rho_1^2 I + \frac{1}{2}(1-\nu)S^2\right] A^{-1}. \end{aligned} \tag{2.4}$$

Several remarks are in order. First in the work presented in [NV08, Pir14] only the linear term in (2.3) is kept (the one multiplied by c_1). In this case, the shell behaves like a linear spring, whose stiffness constant depends upon the local curvatures. The non-linearities introduce two contributions: a non-linear spring and a non-linear membrane part.

2.2.3 Fiber layer

In this section, the equations for a generic fiber layer are detailed. The main hypotheses are the following:

- the energy of the shell and of the fiber layer sum up;
- from a kinematical point of view, the fibers are perfectly attached to the shell;

- the fiber is characterized by an affine stress-strain constitutive law.

The second hypothesis implies that the deformation of the fibers equals the deformation of the underlying shell structure in the direction of the fibers.

Let $\mathbf{w} \in \mathbb{T}_{\boldsymbol{x}}(\Gamma)$ be a unitary vector belonging to the tangent space of Γ defined in the point $\boldsymbol{x} \in \Gamma$. The deformation of the fiber in the $\mathbf{w}$ direction can thus be written as:

$$\varepsilon_{1D} = \mathbf{w}^T \boldsymbol{G} \mathbf{w} = -d_1 \eta + \frac{d_2}{2}\eta^2 + \frac{1}{2}\nabla\eta^T P_{\mathbf{w}} \nabla\eta, \tag{2.5}$$

where the scalar coefficients d_j and the projector $P_{\mathbf{w}}$ are defined as $d_1 = \mathbf{w}^T \boldsymbol{B} \mathbf{w}$, $d_2 = \mathbf{w}^T \boldsymbol{B}\boldsymbol{S} \mathbf{w}$, $P_{\mathbf{w}} = \mathbf{w} \otimes \mathbf{w}$. Note that the d_j may be negative , for instance on a cylinder with outward normal. A constitutive stress-strain relationship for the fibers is assumed of the form:

$$\sigma_{1D} = k_0 + k_1 \varepsilon_{1D},$$

so that k_0 represents the pre-stress of the fiber and k_1 is the linear elastic coefficient.

Let $\varrho_{\mathbf{w}}$ be the fraction of the total number of fibers aligned with the direction $\mathbf{w}$ and h_f the thickness of the fibers layer. The elastic energy of the fibers aligned in the direction $\mathbf{w}$ is expressed in the form:

$$\psi^{\mathbf{w}}(\eta) = \frac{1}{2}\int_\omega \varrho_{\mathbf{w}} \left[k_0 + k_1 \varepsilon_{1D}(\eta)\right] \varepsilon_{1D}(\eta)\ h_f \sqrt{a}\, d\boldsymbol{\xi} + \int_\omega r_{\mathbf{w}}\ h_f \sqrt{a}\, d\boldsymbol{\xi},$$

where $r_{\mathbf{w}}$ represents the potential energy of a force acting on the fibers aligned with the direction $\mathbf{w}$.

The equilibrium equations are introduced in weak form, as the scalar product of the Fréchet derivative of the energy with a test function:

$$\begin{aligned}\Psi^{\mathbf{w}}(\eta, \chi) = \int_\omega & \varrho_{\mathbf{w}} \nabla\chi^T \left[k_0 + k_1\left(-d_1 + \frac{d_2}{2}\eta^2\right) + \frac{k_1}{4} W\right] P_{\mathbf{w}} \nabla\eta + \\ & \varrho_{\mathbf{w}} \left[k_0\left(-d_1 + d_2\eta\right) + k_1\left(-d_1^2\eta - \frac{3d_1 d_2}{2}\eta^2 + \frac{d_2^2}{2}\eta^3\right) + \frac{k_1}{2}(-d_1 + d_2\eta) W\right]\chi + \\ & (\delta_\eta r_{\mathbf{w}})\chi\ h_f\sqrt{a}\, d\boldsymbol{\xi},\end{aligned} \tag{2.6}$$

where $W = \left(\nabla\eta^T P_{\mathbf{w}} \nabla\eta\right)$. Remark that the contribution of the first line is of the membrane type, whereas the second line contains algebraic terms in the test function and hence it renders a non-linear spring-like behavior.

When $\eta = 0$, the reference configuration is the equilibrium configuration only if the stress exerted by the fibers due to their pre-stress is balanced by the underlying shell. This, in weak form, can be written as:

$$\int_\omega (-\varrho_{\mathbf{w}} k_0 d_1 + \delta_\eta r_{\mathbf{w}})\chi\ h_f \sqrt{a}\, d\boldsymbol{\xi} = 0,$$

that holds for arbitrary test functions χ, hence

$$r_{\mathbf{w}} = \varrho_{\mathbf{w}} k_0 d_1 \eta.$$

To conclude this section, let us remark that, in general, the fibers are not parallel to only one direction. Consider two linearly independent unitary vectors $\mathbf{w}, \mathbf{v} \in \mathbb{T}_{\boldsymbol{x}}(\Gamma)$ and the associated fiber densities $\varrho_{\mathbf{w}}, \varrho_{\mathbf{v}}$ defined in each point of Γ. In such a case we can simply sum the two associated energies $\psi^{\mathbf{w}}$ and $\psi^{\mathbf{v}}$.

2.2.4 Equations for the structure dynamics

The equations for the structure dynamics are obtained by adding the inertia terms to the elastic contributions highlighted in the previous sections. In particular the dynamics equations in weak form can be written as:

$$\int_{\omega} \rho^s h^s (\partial_{tt}^2 \eta) \chi \sqrt{a}\, d\boldsymbol{\xi} + \Psi^{\kappa}(\eta, \chi) + \Psi^{\mathbf{w}}(\eta, \chi) + \Psi^{\mathbf{v}}(\eta, \chi) = 0,$$

where Ψ^{κ}, defined in Eq.(2.3), represents the contribution of the shell and $\Psi^{\mathbf{w}}, \Psi^{\mathbf{v}}$, defined in Eq.(2.6), represent the contribution of the fibers aligned in the directions $\mathbf{w}$ and $\mathbf{v}$ respectively. The total thickness of the structure is denoted by h^s and its density is denoted by ρ^s.

In the following, for the sake of simplicity, the overall contribution of the structure will be denoted as:

$$\Psi^s = \Psi^{\kappa} + \Psi^{\mathbf{w}} + \Psi^{\mathbf{v}}. \tag{2.7}$$

2.3 Fluid-structure coupling

The fluid is governed by the incompressible Navier-Stokes equations:

$$\begin{aligned} &\rho^f (\partial_t \boldsymbol{u} + \boldsymbol{u} \cdot \nabla \boldsymbol{u}) = \nabla \cdot \boldsymbol{\sigma}^f && \text{in } \Omega_t \\ &\nabla \cdot \boldsymbol{u} = 0 && \text{in } \Omega_t \end{aligned}$$

where $\boldsymbol{u}$ is the velocity, ρ^f is the fluid density and $\boldsymbol{\sigma}^f = \mu^f(\nabla \boldsymbol{u} + (\nabla \boldsymbol{u})^T) - p\boldsymbol{I}$ is the fluid stress tensor, where μ^f is the dynamic viscosity and p is the pressure. The domain Ω_t is, in general, time-dependent, since the wall is an elastic structure which is moving because of the interactions with the fluid. We denote by Ω a fixed reference domain. We normalize both the equations for the structure and the fluid by ρ^f and we introduce the kinematic viscosity $\nu^f = \frac{\mu^f}{\rho^f}$. The quantities E, k_0, k_1, f^s, ρ^s and p are also divided by ρ^f, but for the sake of simplicity their notation is not changed.

The boundary $\partial\Omega_t$ is subdivided into two subsets Γ_t, the interface between the fluid and the structure, and Σ_t, representing the artificial boundaries of the domain where inlet and outlet boundary conditions are enforced on the normal component of the stress tensor.

Two conditions have to be satisfied on the fluid-structure interface Γ_t: the continuity of the velocity and the stress. Since the structure displacement is assumed to be parallel to the normal direction, it holds, for $\boldsymbol{x} \in \Gamma$, $\boldsymbol{u}(\boldsymbol{I} - \boldsymbol{n} \otimes \boldsymbol{n})|_{\boldsymbol{x}+\eta(\boldsymbol{x})\boldsymbol{n}(\boldsymbol{x})} = \boldsymbol{0}$ and $\boldsymbol{u} \cdot \boldsymbol{n}|_{\boldsymbol{x}+\eta(\boldsymbol{x})\boldsymbol{n}(\boldsymbol{x})} = \partial_t \eta$. The continuity of the normal component of the normal

stress gives $\boldsymbol{\sigma}^f_{\boldsymbol{nn}}|_{\boldsymbol{x}+\eta(\boldsymbol{x})\boldsymbol{n}(\boldsymbol{x})} = -f^s - p^{ref}$, where p^{ref} denotes a given external pressure and f^s denotes the contribution to the normal stress coming from the elastic energy of the structure.

As stated in the introduction, in this chapter we set up a simplified fluid-structure interaction model, that can provide solutions at a moderate computational cost. To this end, the structure equations are treated as a boundary condition for the fluid problem and the problem is discretized on a fixed mesh. In order to render the motion of the wall, a transpiration approach is adopted. A zero-th order transpiration was investigated in [Pir14, GP13, CRGMP14], and proves to be satisfactory to study the propagation of pressure waves. However, in view of the application that motivated this work (hemodynamics autoregulation, see Chapter 3), it is important to compute the flow variation induced by the wall dynamics. Thus, a first order transpiration condition is considered.

We denote by $\boldsymbol{y} \in \Gamma_t$ a point on the actual boundary and by $\boldsymbol{x} \in \Gamma$ the corresponding point on the reference configuration. The mapping $\boldsymbol{y} = \Phi(\boldsymbol{x})$ is written as $\boldsymbol{y} = \boldsymbol{y}(\boldsymbol{x}) = \boldsymbol{\eta}(\boldsymbol{x}) + \boldsymbol{x}$. The displacement is assumed to be given by $\boldsymbol{\eta}(\boldsymbol{x}) = \eta(\boldsymbol{x})\boldsymbol{n}(\boldsymbol{x})$, where $\boldsymbol{n}(\boldsymbol{x})$ is the outward normal to the reference domain at the point $\boldsymbol{x}$. An additional assumption is made: the normal is supposed to remain the same during the evolution, that is $\boldsymbol{n}(\boldsymbol{x}) = \boldsymbol{n}(\boldsymbol{y})$. This assumption, which was also used in [NV08, Pir14], can be obtained by assuming small deformations since the difference $|\boldsymbol{n}(\boldsymbol{x}) - \boldsymbol{n}(\boldsymbol{y})|$ is of order one in $\nabla\eta$. The first order transpiration conditions are obtained through a first order Taylor expansion around the reference configuration $\eta = 0$:

$$\begin{aligned} \boldsymbol{u}(\boldsymbol{y}) &= \boldsymbol{u}(\boldsymbol{x}) + \nabla\boldsymbol{u}(\boldsymbol{x})(\boldsymbol{y} - \boldsymbol{x}) + O(||\boldsymbol{y} - \boldsymbol{x}||^2), \\ \boldsymbol{u}(\boldsymbol{y}) &= \boldsymbol{u}(\boldsymbol{x}) + (\eta\nabla\boldsymbol{u}\boldsymbol{n})(\boldsymbol{x}) + O(\eta^2), \end{aligned} \tag{2.8}$$

where the gradient is taken with respect to the $\boldsymbol{x}$ coordinate. The tangential component of the velocity is computed by multiplying Eq.(2.8) by $(\boldsymbol{I} - \boldsymbol{n} \otimes \boldsymbol{n})$:

$$(\boldsymbol{I} - \boldsymbol{n} \otimes \boldsymbol{n})\boldsymbol{u}(\boldsymbol{y}) = (\boldsymbol{I} - \boldsymbol{n} \otimes \boldsymbol{n})(\boldsymbol{u}(\boldsymbol{x}) + \eta\nabla\boldsymbol{u}(\boldsymbol{x})\boldsymbol{n}(\boldsymbol{x})) + O(\eta^2).$$

Using the no-slip boundary conditions and neglecting the high-order terms:

$$(\boldsymbol{I} - \boldsymbol{n} \otimes \boldsymbol{n})\boldsymbol{u}(\boldsymbol{x}) = -\eta(\boldsymbol{I} - \boldsymbol{n} \otimes \boldsymbol{n})(\nabla\boldsymbol{u}(\boldsymbol{x})\boldsymbol{n}(\boldsymbol{x})) \quad \text{on } \Gamma.$$

From Eq.(2.8), the normal component of the velocity can be written as

$$\boldsymbol{n} \otimes \boldsymbol{n}\boldsymbol{u}(\boldsymbol{y}) = \boldsymbol{n} \otimes \boldsymbol{n}(\boldsymbol{u}(\boldsymbol{x}) + \eta\nabla\boldsymbol{u}(\boldsymbol{x})\boldsymbol{n}(\boldsymbol{x})) + O(\eta^2).$$

Neglecting high order terms, the continuity of the normal velocity gives:

$$\partial_t\eta = \boldsymbol{u} \cdot \boldsymbol{n} + \eta\nabla\boldsymbol{u}\boldsymbol{n} \cdot \boldsymbol{n}.$$

We make the additional simplifying assumption that the viscous part of $\boldsymbol{\sigma}^f_{\boldsymbol{nn}}|_{\boldsymbol{x}+\eta(\boldsymbol{x})\boldsymbol{n}(\boldsymbol{x})}$ is negligible compared to the pressure, i.e, $\boldsymbol{\sigma}^f_{\boldsymbol{nn}}|_{\boldsymbol{x}+\eta(\boldsymbol{x})\boldsymbol{n}(\boldsymbol{x})} =$

$-p|_{\boldsymbol{x}+\eta(\boldsymbol{x})\boldsymbol{n}(\boldsymbol{x})}$. Then, the value of $\boldsymbol{\sigma}^f_{\boldsymbol{nn}}|_{\boldsymbol{x}+\eta(\boldsymbol{x})\boldsymbol{n}(\boldsymbol{x})}$ is approximated by using a first order Taylor expansion on p

$$\boldsymbol{\sigma}^f_{\boldsymbol{nn}}|_{\boldsymbol{x}+\eta(\boldsymbol{x})\boldsymbol{n}(\boldsymbol{x})} = -p - \eta\nabla p \cdot \boldsymbol{n}$$

The equations for the coupled system are written in weak form, on a fixed reference frame. Let $\boldsymbol{v}, q, \chi, \boldsymbol{w}$ be test functions defined in suitable functional spaces according to the boundary conditions of the problem. In particular let $(\boldsymbol{u}, \boldsymbol{v}) \in V \subset H^2(\Omega)$, let $(p, q) \in M \subset H^1(\Omega)$ and $(\eta, \chi) \in H^1(\Gamma)$, $\boldsymbol{w} \in H^1(\mathbb{T}(\Gamma))$. Then:

$$\begin{cases} \langle \partial_t \boldsymbol{u}, \boldsymbol{v}\rangle + c(\boldsymbol{u}; \boldsymbol{u}, \boldsymbol{v}) + a(\boldsymbol{u}, \boldsymbol{v}) + b(p, \boldsymbol{v}) = 0 & \text{in } \Omega, t > 0 \\ \langle \nabla \cdot \boldsymbol{u}, q\rangle = 0 & \text{in } \Omega, t > 0 \\ \rho_s h_s \langle \partial^2_{tt}\eta, \chi\rangle_\omega + \Psi^s(\eta, \chi) + \langle p^{ref}, \chi\rangle_\omega = \langle p + \eta\nabla p \cdot \boldsymbol{n}, \chi\rangle_\omega & \text{on } \Gamma \\ \langle \partial_t \eta, \chi\rangle_\omega = \langle \boldsymbol{u} \cdot \boldsymbol{n} + \eta\nabla \boldsymbol{u}\boldsymbol{n} \cdot \boldsymbol{n}, \chi\rangle_\omega & \text{on } \Gamma \\ \langle (\boldsymbol{I} - \boldsymbol{n} \otimes \boldsymbol{n})(\boldsymbol{u} + \eta\nabla \boldsymbol{u}\boldsymbol{n}), \boldsymbol{w}\rangle_\omega = 0 & \text{on } \Gamma. \\ \text{Plus suitable boundary conditions on } \partial\Omega \setminus \Gamma \end{cases} \tag{2.9}$$

The forms a, b, c read:

$$\begin{aligned} &a : \boldsymbol{V} \times \boldsymbol{V} \to \mathbb{R}, \quad a(\boldsymbol{u}, \boldsymbol{v}) = \nu^f(\nabla \boldsymbol{u} + \nabla \boldsymbol{u}^T, \nabla \boldsymbol{v})_\Omega && \forall (\boldsymbol{u}, \boldsymbol{v}) \in \boldsymbol{V} \times \boldsymbol{V} \\ &b : M \times \boldsymbol{V} \to \mathbb{R}, \quad b(p, \boldsymbol{v}) = -(p, \nabla \cdot \boldsymbol{v})_\Omega && \forall (p, \boldsymbol{v}) \in M \times \boldsymbol{V} \\ &c(\boldsymbol{w}) : \boldsymbol{V} \times \boldsymbol{V} \to \mathbb{R}, \quad c(\boldsymbol{w}; \boldsymbol{u}, \boldsymbol{v}) = (\boldsymbol{w} \cdot \nabla \boldsymbol{u}, \boldsymbol{v})_\Omega && \forall (\boldsymbol{u}, \boldsymbol{v}) \in \boldsymbol{V} \times \boldsymbol{V} \end{aligned}$$

2.4 Numerical discretization

2.4.1 Time discretization

The approximation of the generic quantity f at time $t_k = k\Delta t$ is denoted by f^k. The following notation is introduced: $\nabla_{\boldsymbol{n}} f = \nabla f \cdot \boldsymbol{n}$, $\nabla_{\boldsymbol{nn}} \boldsymbol{f} = \nabla \boldsymbol{f}\boldsymbol{n} \cdot \boldsymbol{n}$, $f_{\boldsymbol{n}} = \boldsymbol{f} \cdot \boldsymbol{n}$.

An implicit-explicit time discretization is adopted in order to avoid the resolution of non-linear problems. As regards the tangential velocity boundary condition, the Taylor contribution accounting for the motion of the wall is taken at the current time step:

$$\langle (\boldsymbol{I} - \boldsymbol{n} \otimes \boldsymbol{n})\boldsymbol{u}^{k+1}, \boldsymbol{w}\rangle_\omega = -\langle \eta^k (\boldsymbol{I} - \boldsymbol{n} \otimes \boldsymbol{n})\nabla \boldsymbol{u}^k \boldsymbol{n}, \boldsymbol{w}\rangle_\omega \text{ on } \Gamma. \tag{2.10}$$

The normal component of the velocity, which is directly related to the wall displacement η is discretized by adopting a similar strategy:

$$\langle \eta^{k+1}, \chi\rangle_\omega = \langle (1 + \Delta t \nabla_{\boldsymbol{nn}} \boldsymbol{u}^k)\eta^k, \chi\rangle_\omega + \Delta t \langle u^{k+1}_{\boldsymbol{n}}, \chi\rangle_\omega. \tag{2.11}$$

The structure equation is discretized as follows:

$$\rho_s h_s \langle \frac{\eta^{k+1} - 2\eta^k + \eta^{k-1}}{\Delta t^2}, \chi \rangle_\omega + \Psi^s(\eta^{k+1,k}, \chi) + \langle p^{ref}, \chi \rangle_\omega = \langle p^{k+1} + \eta^k \nabla_{\boldsymbol{n}} p^k, \chi \rangle_\omega, \tag{2.12}$$

where Ψ^s is the energy of the structure defined in Eq. (2.7). The non-linear terms in Ψ^s are treated in a semi-implicit way detailed in Appendix 2.8 (from equations (2.19) to (2.21)). After linearization Ψ^s is replaced by the sum of a bilinear form of η^{k+1} and χ and a linear functional of χ. In order to eliminate the current displacement from the bilinear form, every istance of η^{k+1} is replaced by Eq.(2.11) to obtain:

$$\Psi^s(\eta^{k+1,k}, \chi) = \Phi^{k+1}(u_{\boldsymbol{n}}^{k+1}, \chi) + \phi^k(\chi). \tag{2.13}$$

The bilinear form $\Psi^s(\eta^{k+1,k}, \chi)$ is now divided into two contributions: the first one $\Phi^{k+1}(u_{\boldsymbol{n}}^{k+1}, \chi)$ is a bilinear form that depends on the current velocity and the second one $\phi^k(\chi)$ is a linear functional of χ where old quantities appear as parameters (see Eq. (2.22) for detailed expressions). By injecting Eq.(2.13) into Eq.(2.12) and by collecting all the force terms in one functional, the following is obtained:

$$\frac{\rho^s h^s}{\Delta t} \langle u_{\boldsymbol{n}}^{k+1}, \chi \rangle_\omega + \Phi^{k+1}(u_{\boldsymbol{n}}^{k+1}, \chi) - \langle p^{k+1}, \chi \rangle_\omega = \mathcal{F}(\chi; \eta^k, p^k, u_{\boldsymbol{n}}^k). \tag{2.14}$$

The details of the expression for $\mathcal{F}$ are reported in Eq. (2.23). Remark that the left-hand side is now made up of the unknowns of the fluid problem, and the right-hand side is computed by using the values of the variables at the previous time step. In this way, the motion of the structure has been implicitly embedded as a boundary condition for the fluid problem. In addition, as the acceleration of the structure is treated implicitly, possible numerical instabilities due to the added-mass effect [CGN05] are avoided.

The linear part of the Navier-Stokes equations is discretized by an implicit Euler scheme, and the convective term in a semi-implicit way: $c(\boldsymbol{u}^k; \boldsymbol{u}^{k+1}, \boldsymbol{v}) = \langle \boldsymbol{u}^k \cdot \nabla \boldsymbol{u}^{k+1}, \boldsymbol{v} \rangle$.

Some comments on the stability of the scheme are in order. In the work by Nobile and Vergara [NV08], stability was proven for a similar model where the fluid problem was solved on a moving domain and a linear Koiter model was embedded into the fluid boundary conditions. In the work by Pironneau [Pir14] a complete mathematical analysis of a similar method was done on a fixed domain where the coupling was defined by a zero order transpiration. The proof of stability of the formulation proposed in the present work seems to be more complicated because of the first order transpiration that results in a non-linear mixed boundary condition on the surface Γ for the continuous problem.

2.4.2 Application of the boundary conditions

Eq.(2.9) is discretized using P1-P1 finite elements with an SUPG stabilization. In this section, several remarks on the imposition of the boundary conditions for

the system are presented.

The boundary conditions are separated into a tangential boundary condition of Dirichlet type for the velocity and a generalised Robin boundary condition in the normal direction. In order to impose the conditions via penalization and to avoid cancellation errors, a unique vector-type boundary condition is written. Let $\boldsymbol{z} = \boldsymbol{w} + \chi \boldsymbol{n}$ be a test function , with $\boldsymbol{w} \cdot \boldsymbol{n} = 0$. It holds:

$$-\langle p^{k+1}\boldsymbol{n}, \boldsymbol{z}\rangle_\omega + \ell(\boldsymbol{u}^{k+1}, \boldsymbol{z}) = \mathcal{R}(\boldsymbol{z}),$$

where ℓ is a bilinear form and $\mathcal{R}$ is a linear functional, deduced from Eq.(2.14) and Eq.(2.10) (see 2.8).

The implementation of this boundary condition has to be done carefully when working with real geometries. In particular, we observed that with normals constant per element, spurious contributions could appear on the tangential velocity (see Remark below). It is therefore desirable to reinterpolate the normals on the P1 finite elements nodes.

Remark 1

Let us explain the trouble that may come from a piecewise-P0 approximation of the normal when a penalization method on the weak form is adopted. Consider, for instance, the case of a Dirichlet boundary condition $\boldsymbol{u} = (\boldsymbol{I} - \boldsymbol{n} \otimes \boldsymbol{n})\boldsymbol{g}$*, where* $\boldsymbol{g}$ *is a generic vector defined on* Γ*. When this condition is imposed via penalization the weak formulation reads:*

$$\int_\Gamma (\boldsymbol{u} - \boldsymbol{T}\boldsymbol{g}) \cdot \boldsymbol{w} \approx 0$$

where $\boldsymbol{T} = (\boldsymbol{I} - \boldsymbol{n} \otimes \boldsymbol{n})$ *is the projector in the tangent space, and "*≈ 0*" means "of the order of the inverse of the penalization parameter". If a piecewise-P0 approximation to the normal field is used, the projector operator* $\boldsymbol{T}^{el}$ *is defined element-wise and is discontinuous. The k-th component of this equation is written by introducing the basis functions used to discretize the problem, namely* φ*, providing:*

$$\int_\Gamma (u_{k,i}\varphi_i - (T^{el}_{kr} g_r)_i \varphi_i) w_{k,j} \varphi_j \approx 0,$$

where $(T^{el}_{k,j} g_j)_i = \int_\Gamma T^{el}_{k,r} g_r \phi_i$*. This equation leads to* $u_{k,i} \approx (T^{el}_{k,r} g_r)_i$*, and hence it does not guarantee that* $n^{el}_s n^{el}_k u_{k,i} \approx 0$*, for* $s = 1, 2, 3$*. On the other hand, if the piecewise-P1 normal and the corresponding operator* $\boldsymbol{T}$ *are used, the quantity* $\boldsymbol{T}\boldsymbol{g}$ *is computed for each node and the following identity holds:*

$$\int_\Gamma (u_{k,i}\varphi_i - T_{kr,i} g_{r,i} \varphi_i)\varphi_j \approx 0, \quad l = 1...3$$

which leads to $u_{k,i} \approx T_{kr,i} g_{r,i}$*. The velocity satisfies the condition* $n_s n_k u_{k,i} = 0$*, for* $s = 1, 2, 3$*. This is particularly relevant for the accuracy in the computation of the normal component of the velocity and thus of the displacement field.* $\diamondsuit$

	Koiter layer		Fibers Layer	
	E[dyn/cm^2]	$h_\kappa[cm]$	k_0[dyn/cm^2]	h_f [cm]
Without fibers	$7.5 \cdot 10^5$	0.1	0	0
With fibers	$3.75 \cdot 10^5$	0.1	$2.78 \cdot 10^5$	0.1

Table 2.1: Structure parameters for the two simulations.

2.5 Numerical testcases

In this section, three numerical experiments are presented where the different features of the proposed method are tested.

In the first test case, a pressure wave in a circular cylinder is simulated, in a similar setting to that in [NV08]. In the second numerical experiment, a similar problem is solved in a different geometry, characterized by the presence of a flat region. Finally, the proposed method is applied to an image-based geometry describing a part of the retinal arteriolar network.

2.5.1 Pressure wave in a cylinder

In this test case, the Stokes equations are solved in a cylindrical domain ($L =$ 6cm, $R = 0.5$cm). Two different configurations are compared, one with fibers and one without. The parameters are reported in Tab.2.1. The values for the Young modulus and for the fibers pre-stress are chosen such that, after linearization, the spring coefficient ($\frac{h^k E}{(1-\nu^{s2})R^2} + \frac{h_f k_0 \varrho_{\mathbf{w}}}{R^2}$) coincides for the two configurations. The remaining structure parameters are: $\rho^s = 1$ g/cm^3, $h_s = h_\kappa + h_f$ and $\nu^s = 0.5$. For the sake of simplicity, we set $k_1 = 0$. Fibers are assumed to be aligned with the principal directions of curvature: $\mathbf{w}$ is the circumferential direction and $\mathbf{v}$ the longitudinal direction. The fibers' fraction is chosen such that fibers are mostly aligned with the circumferential direction ($\varrho_{\mathbf{w}} = 0.9$,$\varrho_{\mathbf{v}} = 0.1$).

For such a simple geometry, the fibers' directions and curvatures are known analytically. However, in view of applying the method to realistic geometries, where this information is in general not available, we assume that the directions and the curvatures are unknown, and we estimate them numerically from the computational mesh.

Fig.2.1 presents curvature estimations. On the left, the Gaussian curvature (analytically equal to zero) and the mean curvature (analytically equal to one) are plotted against the longitudinal coordinate of the cylinder. Notice the presence of numerical oscillations in the computation of the curvature. This problem may have negative effects on other simplified FSI models, as observed in [CDQ14]. In the proposed model, it is partially overcome by the addition of the fiber layer as shown below. In the right panel of Fig.2.1, the estimated principal curvature directions are shown.

The fluid parameters are: $\rho^f = 1$ g/cm^3 and $\mu^f = 0.035$ cm $^2/s$. The boundary conditions at the inlet and at the outlet are $\boldsymbol{\sigma}(\boldsymbol{u}, p)\boldsymbol{n} = -\bar{p}\boldsymbol{n}$. A pressure equal to

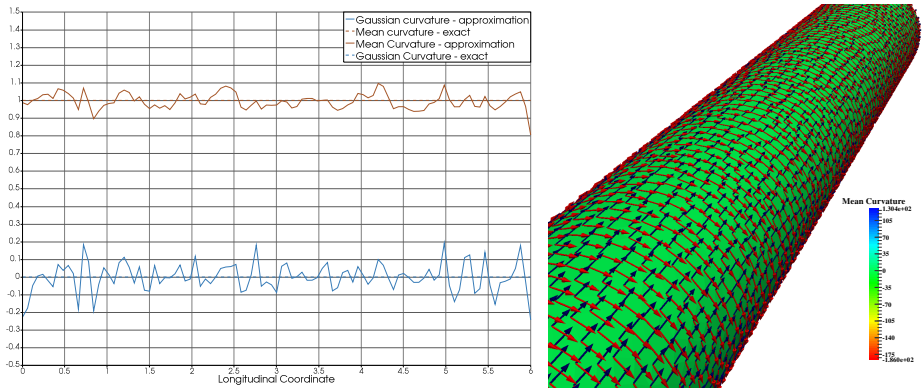

Figure 2.1: On the left panel the mean (brown) and the Gaussian (blue) curvature estimated from the computational mesh are compared to the exact values: one and zero, respectively. On the right panel the principal directions of curvature are depicted: red arrows represent the local direction of maximum curvature, the blue ones refer to the minimum. On the surface the mean curvature is displayed.

zero is assigned at the outlet ($\bar{p} = 0$) and at the inlet

$$\bar{p} = \begin{cases} 5000 \text{ dyn/cm}^2 & t \leq 0.005s \\ 0 & t > 0.005s. \end{cases}$$

In Figures 2.2 and 2.3 the displacement is shown against the longitudinal coordinate, for two different time instants: $t = 0.004$ and $t = 0.012$, respectively. First, there is a difference between the non-linear model and its linear version, both with and without the fiber layer. The pressure wave amplitude is lower for the non-linear model, and the wave velocity is higher. This results from the fact that the non-linear model is characterized by a greater stiffness (due to the non-linear spring contribution).

By comparing the models with and without fibers, it is interesting to notice the regularizing effect of the fibers. The difference in the peak amplitude and in the wave velocity is due to the difference in inertia and stiffness.

2.5.2 Pressure wave in a flat cylinder

The effect of adding a fiber layer to the structure model is even more visible in presence of flat regions in the surface. In realistic geometries, a locally flat region may occur for several reasons including a lack of precision in the segmentation process. This is why the fluid-structure interaction in a flattened cylinder (see Figure 2.4) is investigated.

For this geometrical setting the inertial-algebraic model proposed in [NV08] cannot be used. The main reason is that this model reduces to a structure that behaves pointwise like a spring, whose stiffness constant depends on the curvatures. When both the curvatures vanish, the spring coefficient is zero. Therefore, the displace-

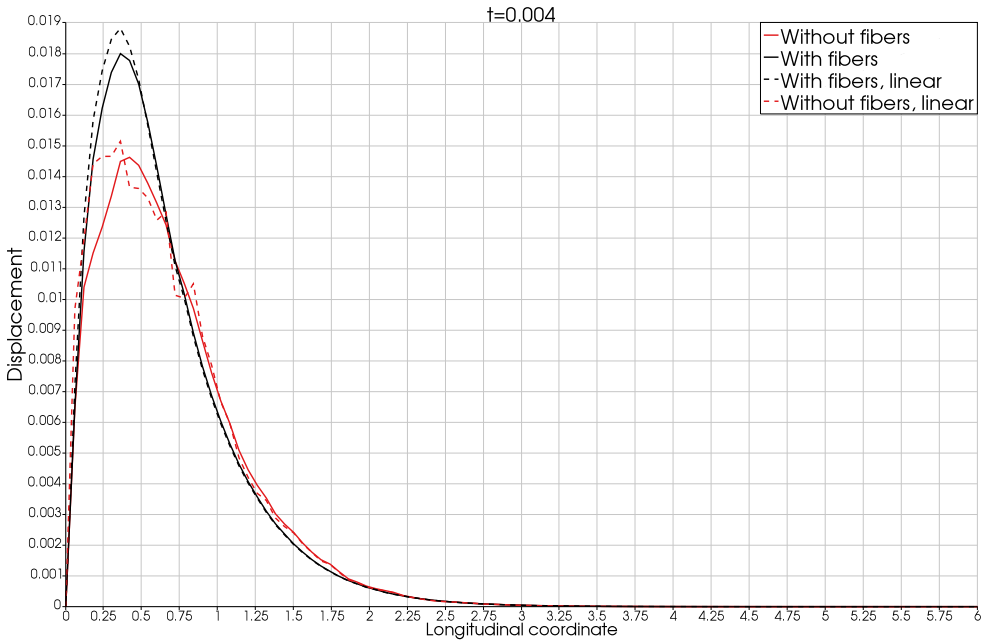

Figure 2.2: Displacement in the longitudinal direction for different structure parameters (see Table 2.1) for $t = 0.004$. Red lines refer to the case without fibers, while black ones to the case with fibers. Solid lines refer to the full model and dashed lines to the corresponding linear version.

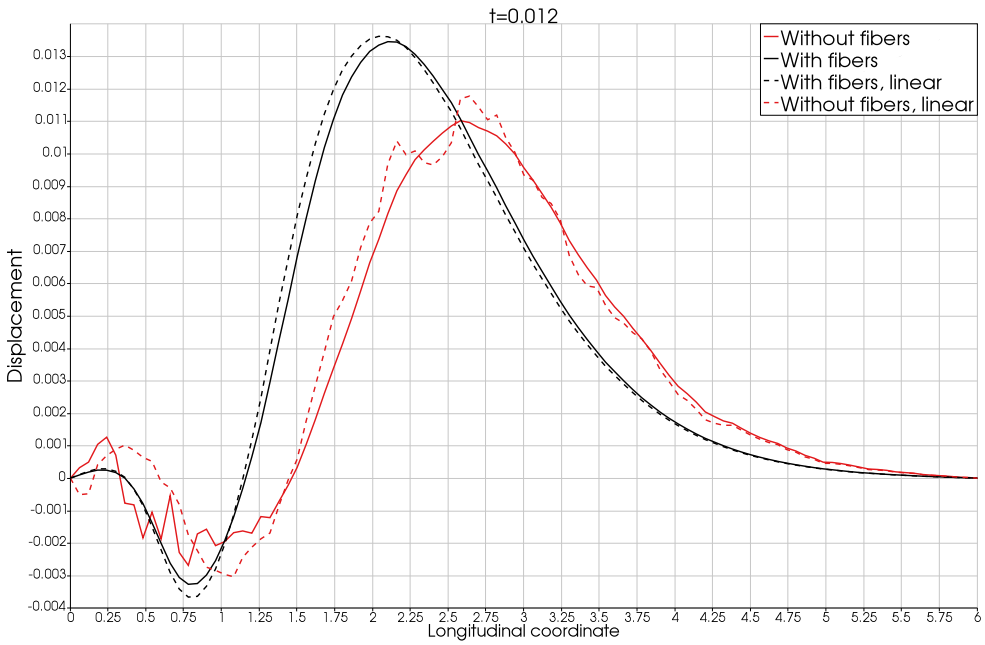

Figure 2.3: Displacement in the longitudinal direction for different structure parameters (see Table 2.1) for $t = 0.012$. Red lines refer to the case without fibers, while black ones to the case with fibers. Solid lines refer to the full model and dashed lines to the corresponding linear version.

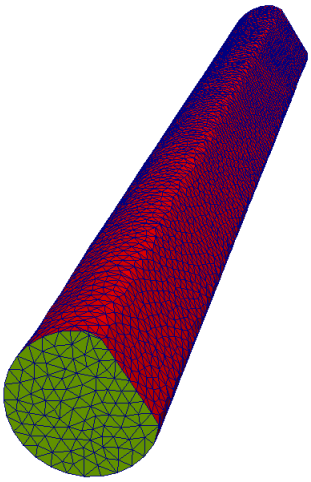

Figure 2.4: The domain of the second test case. One side of the cylinder is flat, *i.e.* all the curvatures vanish.

ment becomes very large, leading to unphysical solutions. Adding the non-linear part of the Koiter shell model mitigates this behavior.

In Fig.2.5 the displacement is shown in the longitudinal direction in the center of the flat region for $t = 0.012$. Notice that, in the flat region, the structure without fibers is characterized by a significantly large displacement. This is due to the fact that, in this region, the structure behaves like a membrane, whose stiffness is low. In Fig.2.6 the same curves are reported for the displacement in the non-flat region. In this portion, the behavior of the structure is similar to that found in the first test case.

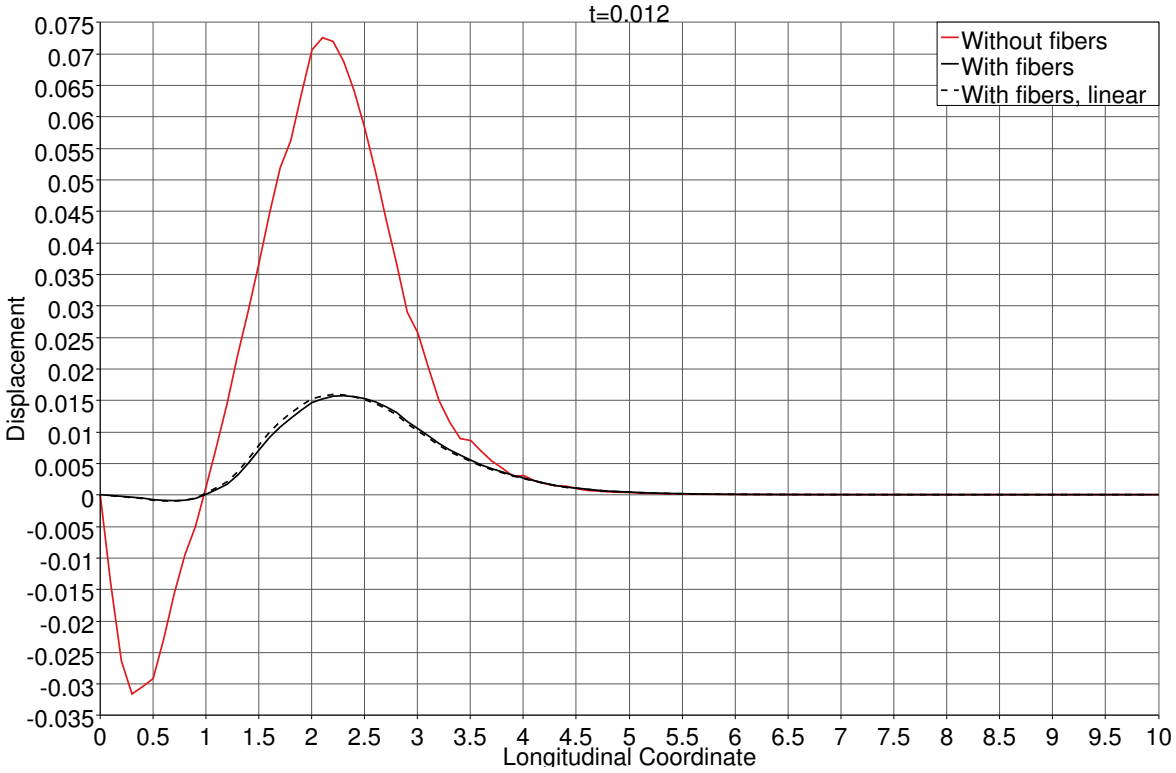

Figure 2.5: Displacement in the flat region. Comparison between the model with fibers (black dashed line linear, black solid line full-model) and the model without (red solid line).

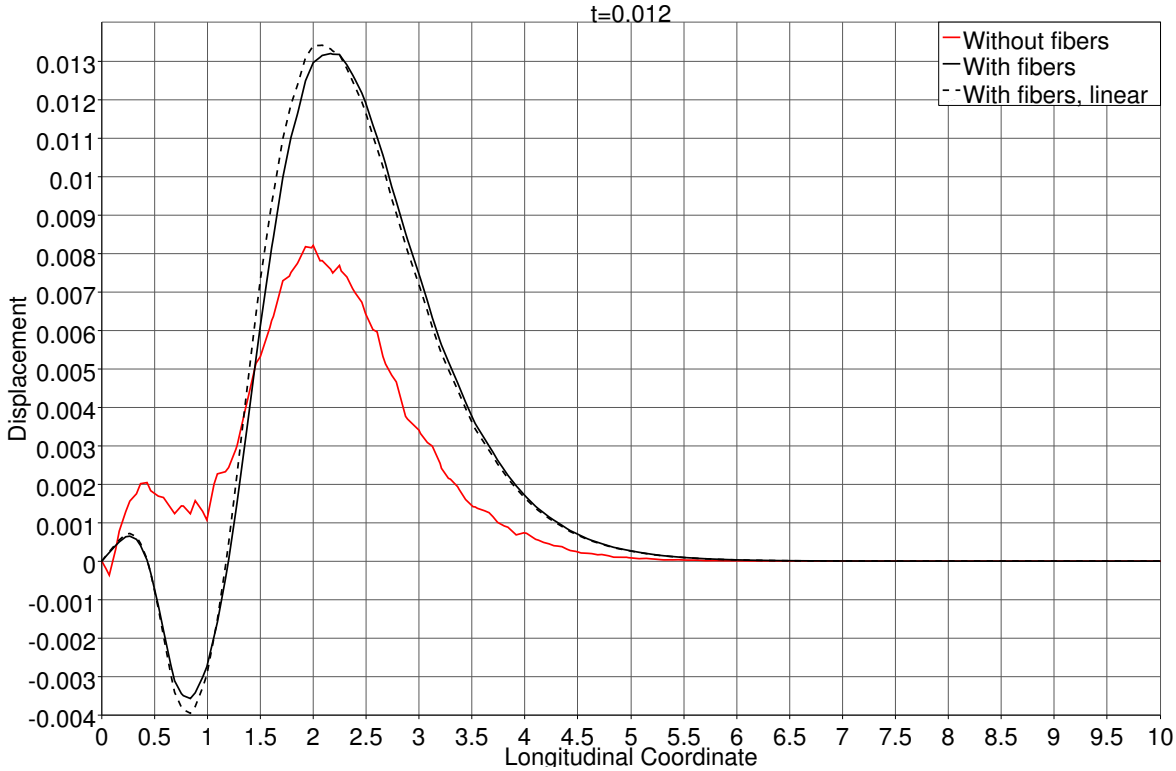

Figure 2.6: Displacement in the rounded region. Comparison between the model with fibers (black dashed line linear, black solid line full-model) and the model without (red solid line).

2.6 Application

In the last test case the model is applied to a realistic geometry. The network represents the inferior temporal arteriole network in the human retina. The original image was taken in the Drive dataset [SAN+04]. The vasculature has been segmented by applying the imaging methods presented in [ADHS09, CAADH15]. The 2D data have then been expanded into a 3D-network by assuming a circular section and projecting the results onto a sphere representing the eye. The typical diameter of this network varies between $70\mu m$ and $160\mu m$.

Several physical parameters appear in the equations of the structure and in that of the fluid. The parameters are chosen to be comparable to those found in [AHS+13, GHC+14b, PRBR+08] and they are a realistic and representative set of parameters for retinal arterioles. The parameters used for the arteriole wall are $\rho_s = 1\text{g/cm}^3$, $E = 0.05MPa$, $\nu = 0.5$, $h_\kappa = 5\mu m$, $h_f = 20\mu m$, $k_0 = 0.4MPa$, $k_1 = 0$,$\varrho_{\mathbf{w}} = \varrho_{\mathbf{v}} = 0.5$. For the sake of simplicity, the blood is assumed to be Newtonian, even if for this kind of vessels a non-Newtonian model would be more appropriate. We used $\rho^f = 1\text{g/cm}^3$, $\mu^f = 0.03\text{cPa}$. Autoregulation is not included in this test since it will be addressed in Chapter 3.

Pressure conditions are applied at the inlet:

$$P_{in}(t)[\text{mmHg}] = \begin{cases} 25.12\sin(\pi t/0.25) + 45 & t \in [0, 0.25] \\ 45 & t \in [0.25, 0.8]. \end{cases}$$

The mean value over time of the incoming pressure is 50mmHg. At the outlets of the domain, the downstream circulation is connected to a venous pressure of 20mmHg via Windkessel compartments. More precisely, we use an RCR model where the parameters are $R_{prox} = 6.\,10^8\text{Pa s cm}^{-3}$, $R_{dist} = 6.10^9$ Pa s cm^{-3} and the capacitance is $1.67\,10^{-8}$ cm^{3}s^{-1} Pa^{-1}. On the lateral surface an external pressure, modelling the intra-ocular pressure, of 15mmHg is also imposed.

The displacement of the arterial wall is shown in Fig.2.7 at the systolic peak and in Fig.2.8 at the end of the diastolic phase. The fact that the displacement is smaller towards the end of the network is mainly due to two reasons: the pressure at the end of the network is significantly lower (the pressure drop is between 5 and 10 mmHg) and the diameter of the vessels is smaller. Indeed, the spring contribution to the structure is characterized by a coefficient that, at the first order approximation in η, depends on the inverse of the vessel radius squared (as in the Laplace law). This can be quantitavely observed in Fig. 2.9 by comparing Point 2 and Point 6 (orange and black curves) or by comparing Point 3 and Point 4. In these two cases, we observe similar pressure curves (dashed lines) and different displacement (solid lines).

In the same figure we also observe the propagation of the pressure wave through the vessel network: by comparing Point 1 with Point 5 (red and green curves) we see that the position of the pressure (and displacement) peak is delayed in Point 5 with respect to Point 1. On the other hand the amplitude of the wave is reduced, which

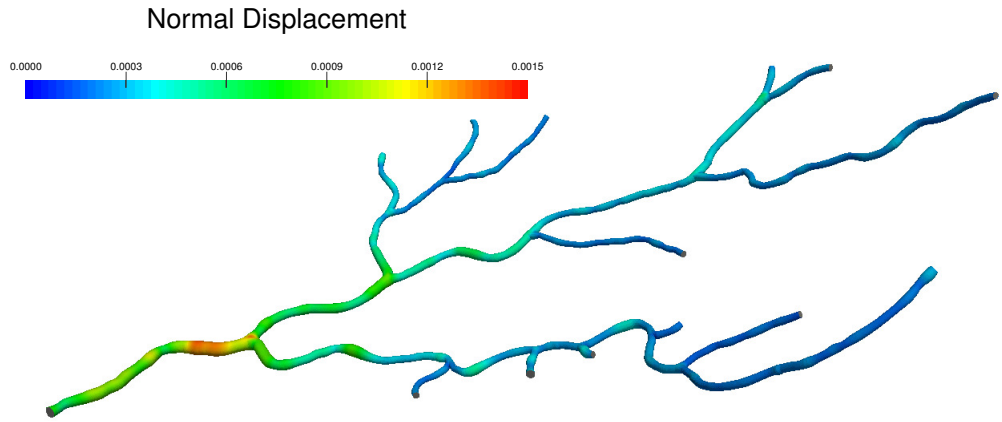

Figure 2.7: Displacement field on the retinal vasculature during the systolic peak.

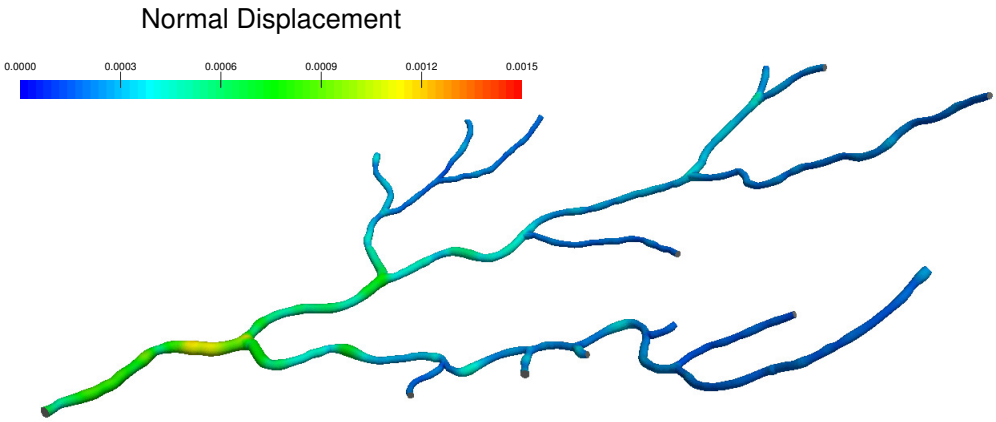

Figure 2.8: Displacement field on the retinal vasculature at the end of diastolic phase.

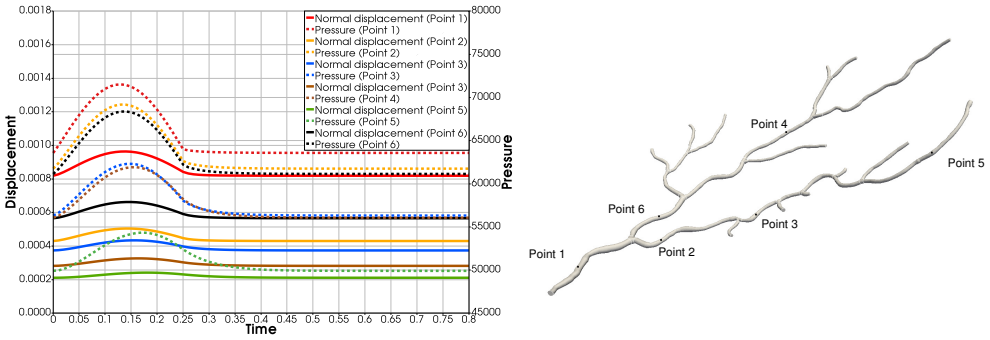

Figure 2.9: Left-hand side: the values of the displacement (solid lines, [cm], left axis) and pressure (dashed lines, [Pa], right axis) over time for six different points on the network. Right-hand side: the network of arterioles.

is compatible with the fact that no pulsation is observed at the capillary level.

From a practical viewpoint, it is interesting to note that these fluid-structure results have been obtained at a computational cost similar to a fluid problem. It would be interesting to compare the results with those provided by more complex approaches, as was done in [CDQ14] for other simplified models. This will be the object of future work.

2.7 Appendix: derivation of the nonlinear elastic energy

In this Appendix, the expression of the elastic energy for the non-linear Koiter model is derived, when the simplifying hypotheses for the problem (see Section 2.2.2) are taken into account.

We refer to Section 2.2.1 for the differential geometry notation.

The expression of the energy functional, when $\boldsymbol{f} = \boldsymbol{0}$,

$$\psi^{\kappa}(\boldsymbol{\eta}) = \frac{1}{2}\int_{\omega} \mathcal{E}^{\alpha\beta\sigma\tau} g_{\sigma\tau}(\boldsymbol{\eta}) g_{\alpha\beta}(\boldsymbol{\eta}) \;\; h_{\kappa}\sqrt{a}\, d\boldsymbol{\xi},$$

is written in terms of the elasticity tensor defined on the surface and of the change of metric tensor. The elasticity tensor, $\mathcal{E}^{\alpha\beta\sigma\tau}$, depends on the Lamé coefficients λ^s and μ^s and on inverse of the first fundamental form, $\boldsymbol{A}^{-1}$, of the surface. In order to simplify the calculations the term $\mathcal{E}^{\alpha\beta\sigma\tau} g_{\sigma\tau}(\boldsymbol{\eta}) g_{\alpha\beta}(\boldsymbol{\eta}) \;\; h_{\kappa}$ is split into two different contributions:

$$\begin{aligned}\mathcal{E}^{\alpha\beta\sigma\tau} g_{\sigma\tau}(\boldsymbol{\eta}) g_{\alpha\beta}(\boldsymbol{\eta}) = &\underbrace{\frac{4\lambda^s\mu^s}{\lambda^s+2\mu^s} a^{\alpha\beta}a^{\sigma\tau} g_{\sigma\tau}(\boldsymbol{\eta}) g_{\alpha\beta}(\boldsymbol{\eta})}_{I} \\ &+ \underbrace{2\mu^s a^{\alpha\sigma}a^{\beta\tau} g_{\sigma\tau}(\boldsymbol{\eta}) g_{\alpha\beta}(\boldsymbol{\eta}) + 2\mu^s a^{\alpha\tau}a^{\beta\sigma} g_{\sigma\tau}(\boldsymbol{\eta}) g_{\alpha\beta}(\boldsymbol{\eta})}_{II}.\end{aligned}$$

In the following the dependence of $\boldsymbol{G}$ on $\boldsymbol{\eta}$ is dropped for sake of compactness in

the notation. Since $\boldsymbol{A}$,$\boldsymbol{B}$,$\boldsymbol{G}$ are symmetric, the two contributions can be further simplified and written in a more compact form as functions of the tensor $\boldsymbol{A}^{-1}\boldsymbol{G}$:

$$I = \frac{4\lambda^s\mu^s}{\lambda^s+2\mu^s}(a^{\alpha\beta}g_{\alpha\beta})^2 = \frac{4\lambda^s\mu^s}{\lambda^s+2\mu^s}(\,\mathrm{tr}(\boldsymbol{A}^{-1}\boldsymbol{G}))^2 \tag{2.15}$$

$$II = 4\mu^s a^{\alpha\sigma}g_{\sigma\tau}a^{\tau\beta}g_{\beta\alpha} = 4\mu^s\,\mathrm{tr}((\boldsymbol{A}^{-1}\boldsymbol{G})^2). \tag{2.16}$$

By injecting Eq.(2.15) and (2.16) into the expression of the energy functional, the following is obtained:

$$\begin{aligned}
\psi^\kappa(\eta) &= \frac{1}{4}\int_\Gamma h^\kappa \mathcal{E}^{\alpha\beta\sigma\tau}g_{\sigma\tau}g_{\alpha\beta}\sqrt{a}\,d\boldsymbol{\xi} \\
&= \frac{1}{4}\int_\Gamma h^\kappa\left[\frac{4\lambda^s\mu^s}{\lambda^s+2\mu^s}\,\mathrm{tr}(\boldsymbol{A}^{-1}\boldsymbol{G})^2 + 4\mu^s\,\mathrm{tr}((\boldsymbol{A}^{-1}\boldsymbol{G})^2)\right]\sqrt{a}\,d\boldsymbol{\xi} \\
&= \frac{1}{4}\int_\Gamma h^\kappa\left[\frac{2E\nu}{1-\nu^2}\,\mathrm{tr}(\boldsymbol{A}^{-1}\boldsymbol{G})^2 + \frac{2E}{1+\nu}\,\mathrm{tr}((\boldsymbol{A}^{-1}\boldsymbol{G})^2)\right]\sqrt{a}\,d\boldsymbol{\xi} \\
&= \frac{1}{2}\int_\Gamma \frac{h^\kappa E}{1-\nu^2}\left[\nu\,\mathrm{tr}(\boldsymbol{A}^{-1}\boldsymbol{G})^2 + (1-\nu)\,\mathrm{tr}((\boldsymbol{A}^{-1}\boldsymbol{G})^2)\right]\sqrt{a}\,d\boldsymbol{\xi},
\end{aligned} \tag{2.17}$$

where the relationships between the Lamé coefficients μ^s, λ^s and the Young modulus and the Poisson ratio are used, namely:

$$\lambda^s = \frac{E\nu}{(1+\nu)(1-2\nu)},\ \mu^s = \frac{E}{2(1+\nu)}.$$

The expression of the change of metric tensor is rewritten, by considering that the displacement field is, by hypothesis, aligned with the outward normal:

$$g_{\alpha\beta} = -b_{\alpha\beta}\eta + \frac{1}{2}s_{\tau\alpha}b_{\tau\beta}\eta^2 + \frac{1}{2}\partial_\alpha\eta\partial_\beta\eta,$$

where $s_{\tau\alpha}$ denotes the components of the matrix representation of $\boldsymbol{S}$.

In order to expand the terms in Eq.(2.17) in terms of η, we write the components of the tensor $\boldsymbol{A}^{-1}\boldsymbol{G}$

$$g^\delta_\beta = (\boldsymbol{A}^{-1}\boldsymbol{G})_{\delta\beta} = a^{\delta\alpha}g_{\alpha\beta} = -a^{\delta\alpha}b_{\alpha\beta}\eta + \frac{1}{2}a^{\delta\alpha}a^{\sigma\tau}b_{\sigma\alpha}b_{\tau\beta}\eta^2 + \frac{1}{2}a^{\delta\alpha}\partial_\alpha\eta\partial_\beta\eta.$$

By introducing the notation $\partial^\alpha = a^{\alpha\sigma}\partial_\sigma$, g^δ_β it simplifies to

$$g^\delta_\beta = -s_{\delta\beta}\eta + \frac{1}{2}s_{\delta\sigma}s_{\sigma\beta}\eta^2 + \frac{1}{2}\partial^\delta\eta\partial_\beta\eta.$$

After some algebraic calculations the quantities $\mathrm{tr}(\boldsymbol{A}^{-1}\boldsymbol{G})$ and $\mathrm{tr}((\boldsymbol{A}^{-1}\boldsymbol{G})^2)$ can be written in terms of traces of powers of $\boldsymbol{S}$, which are, in turn, directly related to the curvatures of the surfaces.

It holds:

$$\begin{aligned}\operatorname{tr}(\boldsymbol{A}^{-1}\boldsymbol{G}) =& -\operatorname{tr}(\boldsymbol{S})\eta + \frac{1}{2}\operatorname{tr}(\boldsymbol{S}^2)\eta^2 + \frac{1}{2}\nabla\eta^T\boldsymbol{A}^{-1}\nabla\eta \\ \operatorname{tr}((\boldsymbol{A}^{-1}\boldsymbol{G})^2) =& \operatorname{tr}(\boldsymbol{S}^2)\eta^2 - \operatorname{tr}(\boldsymbol{S}^3)\eta^3 - \eta\nabla\eta^T\boldsymbol{S}\boldsymbol{A}^{-1}\nabla\eta \\ &+\frac{1}{4}\eta^4\operatorname{tr}(\boldsymbol{S}^4) + \frac{1}{2}\eta^2\nabla\eta\boldsymbol{S}^2\boldsymbol{A}^{-1}\nabla\eta + \frac{1}{4}(\nabla\eta^T\boldsymbol{A}^{-1}\nabla\eta)^2.\end{aligned} \tag{2.18}$$

The traces of powers of $\boldsymbol{S}$ can be written in terms of the curvatures as:

$$\begin{aligned}\operatorname{tr}(\boldsymbol{S}) &= \lambda_1 + \lambda_2 = 2\rho_1 \\ \operatorname{tr}(\boldsymbol{S}^2) &= \lambda_1^2 + \lambda_2^2 = 4\rho_1^2 - 2\rho_2 \\ \operatorname{tr}(\boldsymbol{S}^3) &= \lambda_1^3 + \lambda_2^3 = 8\rho_1^3 - 6\rho_1\rho_2 \\ \operatorname{tr}(\boldsymbol{S}^4) &= \lambda_1^4 + \lambda_2^4 = 16\rho_1^4 + 2\rho_2^2 - 16\rho_1^2\rho_2,\end{aligned}$$

where ρ_1 is the mean curvature $1/2(\lambda_1+\lambda_2)$ and ρ_2 is the Gaussian curvature $\lambda_1\lambda_2$.

By using Eq.(2.18) we derive the final expression for the elastic energy functional

$$\begin{aligned}\psi^\kappa(\eta) =& \frac{1}{4}\int_\omega h^\kappa \mathcal{E}^{\alpha\beta\sigma\tau} g_{\sigma\tau} g_{\alpha\beta}\sqrt{a}\, d\boldsymbol{\xi} \\ =& \frac{1}{2}\int_\omega \frac{h^\kappa E}{(1-\nu^2)}\left[\nu\operatorname{tr}(\boldsymbol{A}^{-1}\boldsymbol{G})^2 + (1-\nu)\operatorname{tr}((\boldsymbol{A}^{-1}\boldsymbol{G})^2)\right]\sqrt{a}\, d\boldsymbol{\xi} \\ =& \frac{1}{2}\int_\omega \frac{h^\kappa E}{(1-\nu^2)}\Big[c_1\eta^2 - 2c_2\eta^3 + c_3\eta^4 + \frac{1}{4}((\nabla\eta)^T\boldsymbol{A}^{-1}\nabla\eta)^2 + \\ &- 2\nu\rho_1\eta(\nabla\eta)^T\boldsymbol{A}^{-1}\nabla\eta + \nu(2\rho_1^2-\rho_2)\eta^2(\nabla\eta)^T\boldsymbol{A}^{-1}\nabla\eta + \\ &- (1-\nu)\eta(\nabla\eta)^T\boldsymbol{S}\boldsymbol{A}^{-1}\nabla\eta + \frac{1}{2}(1-\nu)\eta^2(\nabla\eta)^T\boldsymbol{S}^2\boldsymbol{A}^{-1}\nabla\eta\Big]\sqrt{a}\, d\boldsymbol{\xi},\end{aligned}$$

where the coefficients c_j depend on the Poisson ratio and on the curvatures (they are reported in Eq.(2.4)).

In order to compute the form Ψ^κ in Eq.(2.2), the first variation with respect to η of the energy functional has to be computed and tested, to get the weak form, against a function χ belonging to a suitable functional space. The procedure to derive the first variation (Fréchet derivative) involves several integrations by parts on the surface that produce extra terms involving the curvatures. These terms, however, disappear when the first variation is tested against the function χ. The final result is reported in Eq.(2.3).

2.8 Appendix: Details on the time discretization of the boundary condition

The nonlinear form $\Psi^s(\eta,\chi)$ depends on the forms associated to the non-linear Koiter shell and the fibers (see Eq.(2.7)). For the sake of simplicity, we consider

only fibers in the $\boldsymbol{w}$ direction.

$$\Psi^s(\eta,\chi) = \frac{2E}{1-\nu^2}\int_\omega \left(c_1\eta - 3c_2\eta^2 + 2c_3\eta^3\right)\chi - 2\nabla\chi^T(C_1\eta + C_2\eta^2)\nabla\eta + \quad (2.19)$$
$$-\nabla^T\eta\left[(C_1+2C_2\eta)\,\chi\right]\nabla\eta + \frac{1}{2}\left(\nabla\eta^T A^{-1}\nabla\eta\right)\nabla^T\chi A^{-1}\nabla\eta\; h_\kappa\sqrt{a}\,d\boldsymbol{\xi} -$$
$$\int_\omega \boldsymbol{f}_n\cdot\chi\; h_\kappa\sqrt{a}\,d\boldsymbol{\xi} + \int_\omega \varrho_{\mathbf{w}}\nabla\chi^T\left[k_0 + k_1\left(-d_1 + \frac{d_2}{2}\eta^2\right) + \frac{k_1}{4}W\right]P_{\mathbf{w}}\nabla\eta +$$
$$\varrho_{\mathbf{w}}\left[k_0 d_2\eta + k_1\left(-d_1^2\eta - \frac{3d_1d_2}{2}\eta^2 + \frac{d_2^2}{2}\eta^3\right) + \frac{k_1}{2}(-d_1+d_2\eta)W\right]\chi\; h_f\sqrt{a}\,d\boldsymbol{\xi}.$$

We use a semi-implicit approach to discretize this form in time. The scheme is the following

$$\Psi^s(\eta^{k+1},\chi;\eta^k) = \frac{2E}{1-\nu^2}\int_\omega \left(c_1 - 3c_2\eta^k + 2c_3{\eta^k}^2\right)\eta^{k+1}\chi - 2\nabla\chi^T(C_1\eta^k + C_2{\eta^k}^2)\nabla\eta^{k+1} +$$

$$-\nabla^T\eta^k\left[\left(C_1+2C_2\eta^{k+1}\right)\chi\right]\nabla\eta^k + \frac{1}{2}\left(\nabla{\eta^k}^T A^{-1}\nabla\eta^k\right)\nabla^T\chi A^{-1}\nabla\eta^{k+1}\; h_\kappa\sqrt{a}\,d\boldsymbol{\xi} -$$

$$\int_\omega \boldsymbol{f}_n^{k+1}\cdot\chi\; h_\kappa\sqrt{a}\,d\boldsymbol{\xi} + \int_\omega \varrho_{\mathbf{w}}\nabla\chi^T\left[k_0 + k_1\left(-d_1 + \frac{d_2}{2}{\eta^k}^2\right) + \frac{k_1}{4}W^k\right]P_{\mathbf{w}}\nabla\eta^{k+1} +$$

$$\varrho_{\mathbf{w}}\left[k_0 d_2\eta^{k+1} + k_1\left(-d_1^2 - \frac{3d_1d_2}{2}\eta^k + \frac{d_2^2}{2}{\eta^k}^2\right)\eta^{k+1} + \frac{k_1}{2}(-d_1 + d_2\eta^{k+1})W^k\right]\chi\; h_f\sqrt{a}\,d\boldsymbol{\xi}.$$

This form is linear with respect to χ and affine with respect to η^{k+1}. The coefficients of the form depend on the current displacement η^k. It is useful to split the form into two sub-contributions in order to highlight the bilinear part

$$\Psi^s(\eta^{k+1},\chi;\eta^k) = \mathcal{B}(\eta^{k+1},\chi;\eta^k) + \mathcal{G}(\chi;\eta^k). \quad (2.20)$$

The bilinear form $\mathcal{B}(\eta^{k+1}, \chi; \eta^k)$ has the following expression:

$$\mathcal{B}(\eta^{k+1}, \chi; \eta^k) = \frac{2E}{1-\nu^2} \int_\omega \left(c_1 - 3c_2\eta^k + 2c_3{\eta^k}^2 - 2(\nabla^T\eta^k C_2 \nabla\eta^k)\right) \eta^{k+1}\chi$$
$$- 2\nabla\chi^T(C_1\eta^k + C_2{\eta^k}^2)\nabla\eta^{k+1} + \frac{1}{2}\left(\nabla{\eta^k}^T A^{-1}\nabla\eta^k\right)\nabla^T\chi A^{-1}\nabla\eta^{k+1}\ h_\kappa\sqrt{a}\,d\boldsymbol{\xi} +$$
$$+ \int_\omega \varrho_{\mathbf{w}}\nabla\chi^T\left[k_0 + k_1\left(-d_1 + \frac{d_2}{2}{\eta^k}^2\right) + \frac{k_1}{4}W^k\right] P_{\mathbf{w}}\nabla\eta^{k+1} +$$
$$\varrho_{\mathbf{w}}\left[k_0 d_2 + k_1\left(-d_1^2 - \frac{3d_1d_2}{2}\eta^k + \frac{d_2^2}{2}{\eta^k}^2\right) + \frac{k_1}{2}d_2W^k\right]\eta^{k+1}\chi\ h_f\sqrt{a}\,d\boldsymbol{\xi}.$$

On the other hand, the functional $\mathcal{G}(\chi; \eta^k)$ has the form

$$\mathcal{G}(\chi; \eta^k) = -\frac{2E}{1-\nu^2}\int_\omega (\nabla^T\eta^k C_1\nabla\eta^k)\chi\ h_\kappa\sqrt{a}\,d\boldsymbol{\xi} - \tag{2.21}$$
$$\int_\omega \boldsymbol{f}_n^{k+1}\cdot\chi\ h_\kappa\sqrt{a}\,d\boldsymbol{\xi} - \int_\omega \varrho_{\mathbf{w}}\frac{k_1}{2}d_1W^k\chi\ h_f\sqrt{a}\,d\boldsymbol{\xi}.$$

We use the strong formulation of Eq.(2.11),

$$\eta^{k+1} = (1 + \Delta t\nabla_{\mathbf{nn}}\boldsymbol{u}^k)\eta^k + \Delta t u_{\mathbf{n}}^{k+1},$$

to replace η^{k+1} in Eq.(2.20) obtaining:

$$\Psi^s(\eta^{k+1}, \chi; \eta^k) = \Delta t\mathcal{B}(u_{\mathbf{n}}^{k+1}, \chi; \eta^k) + \mathcal{B}((1 + \Delta t\nabla_{\mathbf{nn}}\boldsymbol{u}^k)\eta^k, \chi; \eta^k) + \mathcal{G}(\chi; \eta^k),$$

which is in the same form as Eq.(2.13). We, finally, define:

$$\begin{aligned}\Phi^{k+1}(u_{\mathbf{n}}^{k+1}, \chi) &= \Delta t\mathcal{B}(u_{\mathbf{n}}^{k+1}, \chi; \eta^k)\\ \phi^k(\chi) &= \mathcal{B}((1 + \Delta t\nabla_{\mathbf{nn}}\boldsymbol{u}^k)\eta^k, \chi; \eta^k) + \mathcal{G}(\chi; \eta^k).\end{aligned} \tag{2.22}$$

The expression for $\mathcal{F}$ in equation (2.14) is obtained by combining Eq.(2.22) and Eq.(2.12).

$$\mathcal{F} = \langle\eta^k\nabla_{\mathbf{n}}p^k - p^{ref} - \frac{\rho_s h_s}{\Delta t^2}((\Delta t\nabla_{\mathbf{nn}}\boldsymbol{u}^k - 1)\eta^k + \eta^{k-1}), \chi\rangle_\omega - \phi^k(\chi). \tag{2.23}$$

On the interface surface Γ those two boundary conditions (Eq.(2.10), Eq.(2.14)) hold:

$$\begin{cases}\langle(\boldsymbol{I} - \boldsymbol{n}\otimes\boldsymbol{n})\boldsymbol{u}^{k+1}, \boldsymbol{w}\rangle_\omega = -\langle\eta^k(\boldsymbol{I} - \boldsymbol{n}\otimes\boldsymbol{n})\nabla\boldsymbol{u}^k\boldsymbol{n}, \boldsymbol{w}\rangle_\omega\\ \frac{\rho^s h^s}{\Delta t}\langle u_{\boldsymbol{n}}^{k+1}, \chi\rangle_\omega + \Phi^{k+1}(u_{\boldsymbol{n}}^{k+1}, \chi) - \langle p^{k+1}, \chi\rangle_\omega = \mathcal{F}(\chi; \eta^k, p^k, u_{\boldsymbol{n}}^k).\end{cases}$$

Let $\mathbf{z} : \Gamma \mapsto \mathbb{R}^3$ be a vector-valued function of $\mathbf{H}^1(\Gamma)$, such that $\boldsymbol{z} \cdot \boldsymbol{n} = \chi$ and $(\boldsymbol{I} - \boldsymbol{n} \otimes \boldsymbol{n})\boldsymbol{z} = \boldsymbol{w}$. We also recall that $\boldsymbol{w} \cdot \boldsymbol{n} = 0$. By introducing the notation $\boldsymbol{T} = (\boldsymbol{I} - \boldsymbol{n} \otimes \boldsymbol{n})$ and by reorganizing the terms $\frac{\rho^s h^s}{\Delta t}\langle u_{\boldsymbol{n}}^{k+1}, \chi\rangle_\omega + \Phi^{k+1}(u_{\boldsymbol{n}}^{k+1}, \chi)$ we get

$$\begin{cases} \langle \boldsymbol{T}\boldsymbol{u}^{k+1}, \boldsymbol{w}\rangle_\omega = -\langle \eta^k \boldsymbol{T}\nabla \boldsymbol{u}^k \boldsymbol{n}, \boldsymbol{w}\rangle_\omega \\ \langle \alpha^k u_{\boldsymbol{n}}^{k+1}, \chi\rangle_\omega + \widetilde{\Phi}^{k+1}(u_{\boldsymbol{n}}^{k+1}, \chi) - \langle p^{k+1}, \chi\rangle_\omega = \mathcal{F}(\chi; \eta^k, p^k, u_{\boldsymbol{n}}^k), \end{cases}$$

where

$$\begin{aligned} \alpha^k = \frac{\rho^s h^s}{\Delta t} + \frac{2E\Delta t h_\kappa}{1-\nu^2}(c_1 - 3c_2\eta^k + 2c_3{\eta^k}^2 - 2(\nabla^T \eta^k C_2 \nabla \eta^k) \\ + \varrho_{\mathbf{w}} h_f \left[k_0 d_2 + k_1 \left(-d_1^2 - \frac{3d_1 d_2}{2}\eta^k + \frac{d_2^2}{2}{\eta^k}^2 \right) + \frac{k_1}{2} d_2 W^k \right] \end{aligned}$$

and

$$\widetilde{\Phi}^{k+1} = \frac{2E\Delta t}{1-\nu^2}\int_\omega -2\nabla\chi^T(C_1\eta^k + C_2{\eta^k}^2)\nabla u_{\boldsymbol{n}}^{k+1} + \frac{1}{2}\left(\nabla {\eta^k}^T A^{-1}\nabla\eta^k\right)\nabla^T\chi A^{-1}\nabla u_{\boldsymbol{n}}^{k+1}\ h_\kappa\sqrt{a}\, d\boldsymbol{\xi} +$$
$$+ \int_\omega \varrho_{\mathbf{w}}\Delta t \nabla\chi^T \left[k_0 + k_1\left(-d_1 + \frac{d_2}{2}{\eta^k}^2\right) + \frac{k_1}{4}W^k \right] P_{\mathbf{w}}\nabla u_{\boldsymbol{n}}^{k+1}\ h_f\sqrt{a}\, d\boldsymbol{\xi}.$$

Finally, we replace $\boldsymbol{w}$ by $\boldsymbol{T}\boldsymbol{z}$ and χ by $\boldsymbol{z}\cdot\boldsymbol{n}$, we multiply the equation for the tangential component by α^k and we sum the result

$$\underbrace{\langle \alpha^k \boldsymbol{u}^{k+1}, \boldsymbol{z}\rangle_\omega + \widetilde{\Phi}^{k+1}(u_{\boldsymbol{n}}^{k+1}, \boldsymbol{z}\cdot\boldsymbol{n})}_{\ell(\boldsymbol{u}^{k+1}, \boldsymbol{z})} - \langle p^{k+1}, \boldsymbol{z}\cdot\boldsymbol{n}\rangle_\omega = \underbrace{\mathcal{F}(\boldsymbol{z}\cdot\boldsymbol{n}; \eta^k, p^k, u_{\boldsymbol{n}}^k) - \langle \eta^k \boldsymbol{T}\nabla\boldsymbol{u}^k\boldsymbol{n}, \boldsymbol{T}\boldsymbol{z}\rangle_\omega}_{\mathcal{R}(\boldsymbol{z})}.$$

Chapter 3

Modelling autoregulation in three-dimensional simulations of retinal hemodynamics

---

This chapter is based on [AGL16a]

Autoregulation is a mechanism necessary to maintain an approximately constant blood flow rate in the microcirculation when acute changes in systemic pressure occur. Failure of autoregulation in the retina has been associated with various diseases, including glaucoma.

In this work, we propose an initial attempt to model autoregulation in a 3D network of retinal arteries. The blood flow is modeled with the time-dependent Stokes equations. The arterial wall model includes the endothelium and the smooth muscle fibers. Various simplifying assumptions lead to a fluid-structure model where the structural part appears as a boundary condition for the fluid.

The numerical simulations are performed on a patient-specific network of 25 segments of retinal arteries located in the inferior temporal quadrant. The results are first compared with experimental data for a given value of perfusion pressure. Then, to assess the autoregulation mechanism, flow rate-pressure curves are simulated with various perfusion pressures. The results obtained with the proposed 3D fluid-structure model are in good agreement with experimental data and 0D models.

Contents

3.1 Introduction

Retinal hemodynamics is strongly influenced by vascular autoregulation. This mechanism is necessary to maintain an approximately constant flow rate in the microcirculation when acute changes in the pressure occur, and it is present in various tissues and organs [SM99]. Failure or impairment of autoregulation in the retina has been associated with various diseases, for instance, diabetic retinopathy and glaucoma [KPR95, RPK95, GRS+84].

In the retina, this phenomenon has been studied both in animals [JAB03] and in humans [JSHB07, BBW+99, HAB+96, DEDK96, RRG+86, NMY02]. Retinal vessels contract or relax in response to a change in the perfusion pressure or to a specific metabolic need. However, the mechanisms underlying the metabolic pathways that trigger vessel contraction or relaxation are still under investigation.

Autoregulation has been modeled on 0D networks of arterioles [ACS08] and also specifically in the retina [AHS+13]. The present work is an initial attempt to address this phenomenon with 3D patient-specific networks, focusing on the mechanical aspects.

This work is not motivated by any specific clinical application. Its goal is to propose a first step toward a 3D model of the hemodynamics of the eye. Even if existing 0D models can provide valuable information, we believe that 3D models can be useful to better understand the complex mechanical interactions which occur within the eye. With modern segmentation tools, patient-specific vasculature can be automatically reconstructed from retinal fundus images. With 3D models, it will be possible to use these rich data to address new issues where geometry plays an important role. For instance, it could be interesting to investigate the blood flow when a dysfunction occurs in a very localized part of the retina. Venular-arteriolar communication [HH02] gives another example where a precise representation of the geometry would also be useful. Nowadays, it is even possible to acquire video of the retinal vasculature showing the pulsatility of the arterial wall. A data assimilation procedure in a 3D fluid-structure model could allow us to estimate the local mechanical properties of the vessel, as was done for the aorta [MBX+12, BBG+14].

The numerical simulation of autoregulation in 3D requires a system of equations that model the mechanical interaction between the blood and the arterial wall. Various approaches have been proposed in the literature to address this problem in large arteries. The most complete models are based on the nonlinear elastodynamics equation coupled with the Navier-Stokes equations set in a moving domain. We refer, for example, to the monograph [FG09] or to [BCZH06, CRD+11, MXA+12, FLV15], to name but a few. These models are very demanding from a computational viewpoint and are valid for large displacements, which is not always necessary, especially in small arteries. Less expensive approaches have been proposed, where the arterial wall equation is drastically simplified [FVCJ+06, NV08, Pir14]. The model used in the present work adopts this latter approach, but it introduces new features, such as active fibers, which are useful when addressing the autoregulation problem. In [CDQ14] the authors observed that using simplified models on image-based geom-

etry might cause numerical instabilities, due to inaccurate approximations of the normals and the principal curvatures of the surface. A side effect of including fibers in this model is the improvement of the numerical stability, owing to a Laplace operator added to the structure equation. This model has been introduced in Chapter 2, where a complete derivation and the numerical schemes can be found. In this chapter we focus on modelling the autoregulation mechanism and the numerical simulation of this phenomenon in patient-specific retinal arteries. The numerical tests are carried out on a portion of the retinal vasculature consisting of twenty-five arterial segments located in the inferior-temporal quadrant and reconstructed from a retinal fundus image.

The structure of the chapter is as follows: in Section 2, the fluid-structure framework is introduced; Section 3 addresses the structural model, with special emphasis on the fibers. Section 4 deals with the autoregulation mechanism and Section 5 presents the numerical results. Section 6 presents some limitations of the study and the conclusion.

3.2 Fluid-structure coupling: main modelling assumptions

The first modelling assumption is to neglect the convective terms in the fluid momentum equation. This approximation is justified since, by considering a maximum vessel diameter $D = 200\ \mu m$, a velocity $v = 5\ cm/s$ and a kinematic viscosity $\nu = 0.04\ cm^2/s$, we obtain a Reynolds number of 2.5. The second main assumption is to suppose that the blood behaves as an homogeneous Newtonian fluid, which is questionable since microvessels are considered [WKK+03, PRBR+08]. We make this hypothesis for the sake of simplicity because it is assumed not to affect too much the autoregulation, which is the mechanism this chapter focuses on.

The domain Ω_t in which the fluid flows, is in general, time-dependent, since the wall is an elastic structure in interaction with the fluid. The boundary $\partial\Omega_t$ is subdivided into two subsets: Γ_t, which is the interface between the fluid and the structure, and Σ_t, representing the artificial boundaries of the domain where inlet and outlet boundary conditions are enforced. Considering the small displacements of the retinal arteries wall, the domain Ω_t is considered to have a fixed reference configuration denoted by Ω. A schematic representation of this setting is given in Fig. 3.1. This approximation considerably reduces the computational cost. The fluid equations are therefore:

$$\begin{cases} \rho^f \partial_t \boldsymbol{u} = \nabla \cdot \boldsymbol{\sigma}^f & \text{in } \Omega, \\ \nabla \cdot \boldsymbol{u} = 0 \text{ in } \Omega, \end{cases}$$

where $\boldsymbol{u}$ is the velocity, ρ^f is the fluid density and $\boldsymbol{\sigma}^f = \mu^f(\nabla \boldsymbol{u} + (\nabla \boldsymbol{u})^T) - p\boldsymbol{I}$ is the fluid stress tensor, where μ^f is the dynamic viscosity and p is the pressure.

The velocity on the fixed fluid-structure interface Γ is obtained by a Taylor expansion. This approach is known as a "transpiration condition". In the literature,

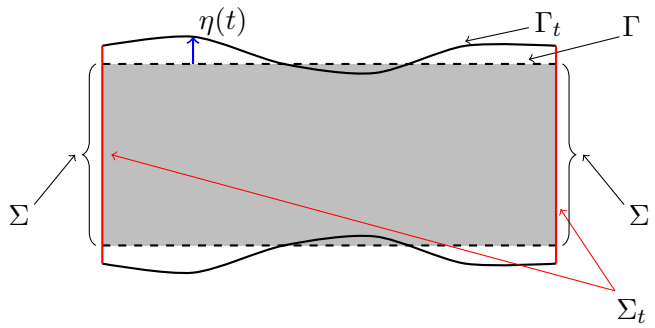

Figure 3.1: The fluid domain Ω_t is within the two curved lines, however the equations are solved on the fixed computational domain Ω depicted in gray. The displacement field η, which depends on time, maps Γ into Γ_t.

this is usually a zero-th order expansion. Here, a first order transpiration condition is adopted in order to compute the variation of the flow induced by the wall dynamics, which is important in order to model autoregulation. The main geometrical assumption is that the normal to the structure $\boldsymbol{n}$ is constant in time. Moreover, the kinematics of the vessel wall is assumed to be, at each time, parallel to the normal. With $\boldsymbol{\eta}$ denoting the displacement of the wall, the following holds:

$$\boldsymbol{\eta} = \eta \boldsymbol{n}, \quad \forall t. \tag{3.1}$$

Two conditions have to be satisfied on the fluid-structure interface Γ_t: the continuity of the velocity and the continuity of the stress. Since the structure displacement is assumed to be parallel to the normal direction, the equations for the continuity of the velocity are, for all $x \in \Gamma$, $\boldsymbol{u}(\boldsymbol{I} - \boldsymbol{n} \otimes \boldsymbol{n})|_{\boldsymbol{x}+\eta(\boldsymbol{x})\boldsymbol{n}(\boldsymbol{x})} = \boldsymbol{0}$ and $\boldsymbol{u} \cdot \boldsymbol{n}|_{\boldsymbol{x}+\eta(\boldsymbol{x})\boldsymbol{n}(\boldsymbol{x})} = \partial_t \eta$. The balance of the normal component of the normal stress gives $\boldsymbol{\sigma}^f_{\boldsymbol{nn}}|_{\boldsymbol{x}+\eta(\boldsymbol{x})\boldsymbol{n}(\boldsymbol{x})} = -f^s - p_{iop}$, where p_{iop} denotes the external pressure acting on the structure, in this case the intra ocular pressure, and f^s represents the stress coming from the structure.

The simplifying assumptions on the structure dynamics, which will be detailed in the following section, allow us to treat the structure equations as a boundary condition for the fluid problem.

The equations for the coupled system are written in weak form, on a fixed domain. Let $\boldsymbol{v}, q, \chi, \boldsymbol{w}$ be test functions defined in suitable functional spaces according to the boundary conditions of the problem. In particular let $\boldsymbol{u}(t)$ and $\boldsymbol{v} \in \mathbf{V}$, let $p(t)$ and $q \in M$, where $V = \mathbf{H}^2(\Omega)$ and $M = H^1(\Omega)$. Then:

$$\begin{cases} \langle \partial_t \boldsymbol{u}, \boldsymbol{v} \rangle_\Omega + a(\boldsymbol{u}, \boldsymbol{v}) + b(p, \boldsymbol{v}) = 0 & \text{in } \Omega, t > 0 \\ \langle \nabla \cdot \boldsymbol{u}, q \rangle_\Omega = 0 & \text{in } \Omega, t > 0 \\ \rho_s h_s \langle \partial_{tt}^2 \eta, \chi \rangle_\Gamma + \Psi^s(\eta, \chi) + \langle p_{iop}, \chi \rangle_\Gamma = \langle p + \eta \nabla p \cdot \boldsymbol{n}, \chi \rangle_\Gamma & \text{on } \Gamma \\ \langle \partial_t \eta, \chi \rangle_\Gamma = \langle \boldsymbol{u} \cdot \boldsymbol{n} + \eta \nabla \boldsymbol{u} \boldsymbol{n} \cdot \boldsymbol{n}, \chi \rangle_\Gamma & \text{on } \Gamma \\ \langle (\boldsymbol{I} - \boldsymbol{n} \otimes \boldsymbol{n})(\boldsymbol{u} + \eta \nabla \boldsymbol{u} \boldsymbol{n}), \boldsymbol{w} \rangle_\Gamma = 0 & \text{on } \Gamma. \end{cases} \tag{3.2}$$

The forms a, b read:

$$\begin{aligned} &a : \boldsymbol{V} \times \boldsymbol{V} \to \mathbb{R}, \quad a(\boldsymbol{u}, \boldsymbol{v}) = \nu^f \langle \nabla \boldsymbol{u} + \nabla \boldsymbol{u}^T, \nabla \boldsymbol{v} \rangle_\Omega \qquad \forall (\boldsymbol{u}, \boldsymbol{v}) \in \boldsymbol{V} \times \boldsymbol{V} \\ &b : M \times \boldsymbol{V} \to \mathbb{R}, \quad b(p, \boldsymbol{v}) = -\langle p, \nabla \cdot \boldsymbol{v} \rangle_\Omega \qquad \forall (p, \boldsymbol{v}) \in M \times \boldsymbol{V}. \end{aligned}$$

where $\langle \cdot, \cdot \rangle_\Omega$ and $\langle \cdot, \cdot \rangle_\Gamma$ denote the standard scalar product in $L^2(\Omega)$ and in $L^2(\Gamma)$, respectively and ν^f is the kinematic viscosity. It should be noted that in this framework the structure dynamics is embedded as a boundary condition of the fluid problem. The system in Eq.(3.2) is discretised by means of finite elements (P1-P1, with a SUPG stabilisation) and by a mixed semi-implicit scheme in time. All the details of the implementation of this approach are provided in the Chapter 2.

Remark 1
Numerically, the tangential velocity sometimes exhibits oscillations on the fluid-structure interface, especially on complex geometries. The reason for these oscillations is not completely understood. They might be due to the approximation of the normals and the curvatures, as already noted in [CDQ14], or to the first order transpiration terms adopted in our approach. We observed that this problem can be alleviated by the following consistent stabilization term:

$$\langle (\boldsymbol{I} - \boldsymbol{n} \otimes \boldsymbol{n})(\boldsymbol{u} + \eta \nabla \boldsymbol{u} \boldsymbol{n}), \boldsymbol{w} \rangle_\Gamma = -\beta \langle h \nabla (\boldsymbol{I} - \boldsymbol{n} \otimes \boldsymbol{n}) \boldsymbol{u}, \nabla \boldsymbol{w} \rangle_\Gamma \text{ on } \Gamma,$$

where $\beta \geq 0$ is the stabilization coefficient and h is the surface element size.

3.3 Modelling the vessel wall dynamics

Retinal arteriolar structure consists of a thin layer of endothelium layer and a layer of smooth muscle cells which is more developed with respect to vessels of the same size in other organs [PRBR+08]. From a modelling perspective, the wall is considered as an elastic shell, so as to render the behavior of the endothelium, and several fiber layers to model the smooth muscles.

This Section is organised as follows. After introducing the notation, the model of the structure is presented in its general form, as it appears in system (3.2). The model for the endothelium is described, followed by a presentation of the fiber layer. First a derivation of a constitutive law for the smooth muscle fibers is presented. This constitutive law is then used to close the kinematical and mechanical description of

the fiber layer surrounding the endothelium.

3.3.1 Notation

Let Γ be the reference position of the vessel wall, *i.e.* the position at which it is in a normal state of equilibrium, without external influences. The geometrical configuration of Γ is described by a regular map Φ such that $\boldsymbol{\xi} \in \omega \subseteq \mathbb{R}^2 \mapsto \boldsymbol{x} = \Phi(\boldsymbol{\xi}) \in \Gamma$. Let $\boldsymbol{A}$ be the first fundamental form and $\boldsymbol{B}$ the second fundamental form associated with the reference configuration Γ. Let $\boldsymbol{S} = \boldsymbol{A}^{-1}\boldsymbol{B}$ be the representation of the shape operator. The eigenvalues of the shape operator are the principal curvatures of the surface Γ, the mean curvature being the average of the principal curvatures and the Gaussian curvature being their product. The surface parametrization is denoted by Greek letters and the curvilinear coordinates domain is denoted by $\omega \subseteq \mathbb{R}^2$.

3.3.2 Equations for the structure dynamics

The equations for the structure dynamics, appearing as a boundary condition of the system (3.2), are obtained by adding the inertia terms to the elastic energy of the structure. In particular, the dynamics equations in weak form can be written as:

$$\int_\omega \rho^s h^s (\partial^2_{tt}\eta)\chi\sqrt{a}\, d\boldsymbol{\xi} + \Psi^s(\eta, \chi) = 0,$$

where the thickness of the structure is denoted by h^s and its density by ρ^s. The form Ψ^s describes the behavior of the structure. It is considered as the sum of several contributions:

$$\Psi^s = \Psi^\kappa + \Psi^{\mathbf{w}} + \Psi^{\mathbf{v}}, \tag{3.3}$$

where Ψ^κ, defined in Eq.(3.4), represents the contribution of the endothelium and $\Psi^{\mathbf{w}}, \Psi^{\mathbf{v}}$, defined in Eq.(3.14), represent the contribution of the fibers aligned in the directions $\mathbf{w}$ and $\mathbf{v}$ respectively.

Each of these terms is analyzed in detail in the following part of this section. In general, all the weak forms are derived as follows: given an elastic model and the corresponding energy, the equilibrium configuration for the structure can be seen as the stationary point of the energy functional:

$$\Psi(\eta, \chi) := \langle \delta_\eta \psi(\eta), \chi \rangle_\Gamma = 0,$$

where δ_η denotes the Frechet derivative with respect to η and ψ is the elastic energy.

3.3.3 The endothelium layer

A nonlinear Koiter shell model is adopted to describe the endothelium dynamics. The equations and a detailed mathematical derivation are presented in [Cia00]. The choice of this nonlinear model, rather than the simpler linear version, is motivated by the consistency with the fiber layer description. In particular, when the fiber kinematics (see Eq.(3.13)) is described, some nonlinear contributions arise. The

terms appearing in the Koiter model that have the same order with respect to the displacement field η have thus to be kept. The displacement field, as pointed out in Eq.(3.1), is parallel to the normal to the reference configuration.

The simplifying hypotheses from a mechanical point of view are the following:

- the bending terms are negligible;
- the material is linear, isotropic and homogeneous.

The equilibrium configuration is the stationary point of the energy functional [Cia00]:

$$\psi^\kappa(\eta) = \frac{1}{2}\int_\omega \mathcal{E}^{\alpha\beta\sigma\tau} g_{\sigma\tau}(\eta) g_{\alpha\beta}(\eta)\ \ h_\kappa\sqrt{a}\, d\boldsymbol{\xi} - \int_\omega \boldsymbol{f}\cdot\eta\ h^\kappa\sqrt{a}\, d\boldsymbol{\xi},$$

where $\sqrt{a} = \sqrt{det(A)}$, h^κ is the shell thickness and $\boldsymbol{f}$ are the external forces, $g(\eta)$ is the change of metric tensor. The properties of the material are contained in the elastic tensor $\mathcal{E}$, whose contravariant components read:

$$\mathcal{E}^{\alpha\beta\sigma\tau} = \frac{4\lambda^s\mu^s}{\lambda^s+2\mu^s}A^{\alpha\beta}A^{\sigma\tau} + 2\mu^s A^{\alpha\sigma}A^{\beta\tau} + 2\mu^s A^{\alpha\tau}A^{\beta\sigma},$$

where λ^s, μ^s are the Lamé coefficients of the structure.

By exploiting the hypothesis of normal displacement (see Eq.(3.1)), the expression for the change of metric tensor becomes:

$$g_{\alpha\beta} = -B_{\alpha\beta}\eta + \frac{1}{2}A^{\sigma\tau}B_{\sigma\alpha}B_{\tau\beta}\eta^2 + \frac{1}{2}\partial_\alpha\eta\partial_\beta\eta,$$

where the derivative with respect to the Greek letters denotes the derivation with respect to the surface parametrization.

The form Ψ^κ describing the equilibrium of the nonlinear Koiter shell model under the assumptions made reads:

$$\begin{aligned}\Psi^\kappa(\eta,\chi) := \frac{2E}{1-\nu^2}\int_\omega \left(c_1\eta - 3c_2\eta^2 + 2c_3\eta^3\right)\chi - 2\nabla\chi^T(C_1\eta + C_2\eta^2)\nabla\eta + \\ -\nabla^T\eta\left[(C_1+2C_2\eta)\,\chi\right]\nabla\eta + \frac{1}{2}\left(\nabla\eta^T A^{-1}\nabla\eta\right)\nabla^T\chi A^{-1}\nabla\eta\ h^\kappa\sqrt{a}\, d\boldsymbol{\xi} - \\ \int_\omega \boldsymbol{f}_n\cdot\chi\ h^\kappa\sqrt{a}\, d\boldsymbol{\xi}, \qquad (3.4)\end{aligned}$$

where E is the Young modulus of the material, ν the Poisson coefficient, the constant tensors (C_j) and the coefficients (c_k) are expressed as functions of the mean and

Gaussian curvatures (respectively ρ_1 and ρ_2) and the Poisson ratio as follows:

$$
\begin{aligned}
c_1 &= 4\rho_1^2 - 2(1-\nu)\rho_2, \\
c_2 &= 4\rho_1^3 + (\nu-3)\rho_1\rho_2, \\
c_3 &= 4\rho_1^4 - 4\rho_1^2\rho_2 + \frac{1}{2}(1+\nu)\rho_2^2, \\
C_1 &= \left[\nu\rho_1 I + \frac{1}{2}(1-\nu)S\right] A^{-1}, \\
C_2 &= \left[\nu\rho_1^2 I + \frac{1}{2}(1-\nu)S^2\right] A^{-1}.
\end{aligned}
$$

Notice that, at the first order, the endothelium behaves pointwise as a spring with constant c_1. However the overall behavior can be roughly considered as the sum of two contributions: a nonlinear spring and a nonlinear membrane. More details about this derivation can be found in Chapter 2.

3.3.4 The smooth muscle cells model

In this section, a model describing the behavior of the smooth muscle cells (SMC) is investigated. The resulting model is a 1D idealisation of the SMC muscle fibers. The equations derived in the present section are used as a constitutive law to close the model for the fiber layers.

The layer of SMCs, which in large vessels is also responsible for adaptive changes in the stiffness, has the ability to contract or relax following electrochemical stimuli in order to regulate the blood flow (see, e.g., [MKH10, Mil90]).

There is no autonomic innervation in the retinal vasculature [Lat67]. This implies that the regulation is carried out by mechanisms that take place locally in the eye [Bek13]. The contraction of the smooth muscle cells is controlled by the concentration of calcium ions, which trigger the phosphorylation of myosin light chains [SM99]. The different chemical pathways are not investigated in the present work and we make the simplifying assumption that the concentration of calcium ions depends only on changes of the pressure. However, if more sophisticated models are available they can be included to relate the concentration of calcium ions to the other mechanisms.

A chemical state model of the smooth muscle cells has been proposed by Hai and Murphy [HM88]. This model takes four chemical species into account: myosin (M), phosphorilated myosin (M_p), phosphorilated actin myosin cross-bridge (AM_p) and unphosphorilated actin myosin cross-bridge (AM). It describes the evolution of the concentrations $(\alpha_M, \alpha_{M_p}, \alpha_{AM}, \alpha_{AM_p})$ of those species with a linear system of differential equations $\dot{\boldsymbol{\alpha}} = \boldsymbol{K}\boldsymbol{\alpha}$ under the constraint $\alpha_M + \alpha_{M_p} + \alpha_{AM} + \alpha_{AM_p} = 1$, where $\boldsymbol{K}$ depends on the concentration of calcium ions.

The chemical model by Hai and Murphy [HM88] was used by Yang *et al.* [YCJBR03a, YCJBR03b] to describe the myogenic response. More recently, the approach by Yang *et al.* has been extended to a continuum mechanics frame-

work [SKH08, MKH10]. Such models have also been coupled with a membrane model to compute the concentration of calcium ions as a response to external stimuli [SS14]. The overall mechanism is reproduced in the following way: an external stimulus causes a change in calcium concentration which alters the chemical state of the SMC. Once the chemical state is known, it is possible to compute the active component of the forces in the cell and thus its mechanical behavior.

In what follows, we refer to the model of Yang *et al.* [YCJBR03a, YCJBR03b] and propose a further simplification in order to derive a constitutive equation for a 1D fiber. In the model presented in [YCJBR03a], the mechanics of a single SMC is described by two elements in parallel: a spring characterized by an exponential force-length relationship (to describe the passive structural behavior of the overall cell) and an active element for the cross-bridges. The total force is given by

$$F = F_{cell} + F_{cb}, \tag{3.5}$$

where cb stands for cross-bridges. The active element is itself made of three elements in series which model the active force of the actin-myosin cross-bridges, their passive elasticity properties and the viscous effects, respectively. The total length of the active element L_{cb} can be expressed as the sum of the length of these three components:

$$L_{cb} = L_{cb,a} + L_{cb,el} + L_{cb,visc}, \tag{3.6}$$

where $a, el, visc$ stand for active, elastic and viscous, respectively. The length of the cell and of the active element representing the cross-bridges are the same and they are equal to the total length L.

$$L = L_{cell} = L_{cb}. \tag{3.7}$$

The system of equations is closed by observing that the elements in series have the the same force:

$$F_{cb,a} = F_{cb,el} = F_{cb,visc}. \tag{3.8}$$

Finally, considering the constitutive laws of the three components of the active element, it is possible to solve the system and obtain the total force. Such force depends on the total length of the cell, on its time derivative and also on the cell chemical state described by the proportion of phosphorilated and dephosphorilated actin-myosin:

$$F = F(L, \frac{dL}{dt}, \alpha_{AM}, \alpha_{AM_p}).$$

This expression can be simplified if the visco-elastic effects are neglible compared to the elastic effects. In such a case the total force is a function of only the total length and the concentration of phosphorilated actin-myosin:

$$F = F(L, \alpha_{AM_p}). \tag{3.9}$$

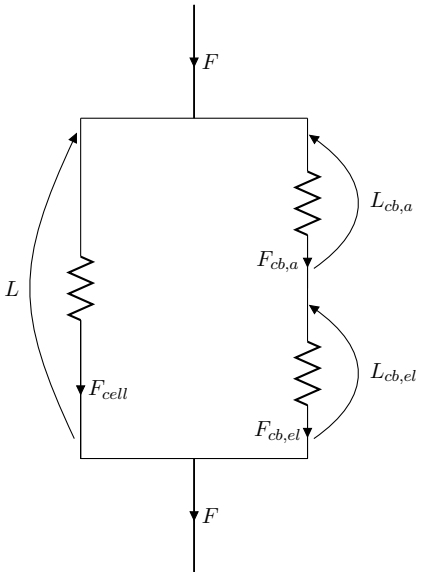

Figure 3.2: Scheme of the equivalent circuit describing the model by Yang et al. (2003) when viscous effects are neglected.

Its expression can be obtained by solving the following system whose equivalent circuit is depicted in Fig.3.2:

$$\begin{cases} F_{cell} &= k_{cell}(e^{\alpha_{cell}\left(\frac{L}{L_0}-1\right)}-1) \\ F_{cb,a} &= f_{AM_p}\alpha_{AM_p}e^{-b\left(\frac{L_{cb,a}}{L_{opt}}-1\right)^2} \\ F_{cb,el} &= k_{el}\left(e^{\alpha_{el}\left(\frac{L_{cb,el}}{L_{cb,el,0}}-1\right)}-1\right) \\ F_{cb,a} &= F_{cb,el} \\ F &= F_{cell}+F_{cb,a} \\ L &= L_{cb,a}+L_{cb,el}, \end{cases} \tag{3.10}$$

where the first three equations represent the constitutive law of the cell, the active part of the cross-bridges and their elastic part. Therefore, the parameters $k_{cell}, \alpha_{cell}, L_0, f_{AM_p}, b, L_{opt}, k_{el}, \alpha_{el}$ and $L_{cb,el,0}$ describe the structural properties of the SMC. The last three equations are obtained by combining equations (3.5),(3.6),(3.7) and (3.8).

Since it is not possible to obtain a closed-form solution for system (3.10), we make an approximation to obtain an affine stress-strain relationship. Eq.(3.9) is linearized with respect to the reference configuration L_{ref}:

$$F \sim F_0(\alpha_{AM_p}) + F_1(\alpha_{AM_p})(L - L_{ref}), \tag{3.11}$$

where the analytical expressions for F_0 and F_1 are known and are derived through

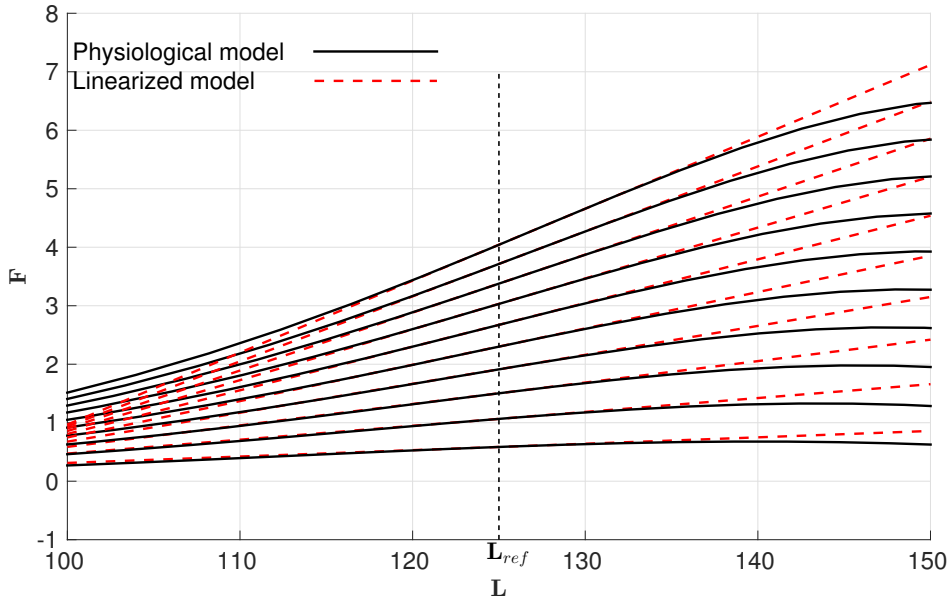

Figure 3.3: Force-length relationship from system (3.10), coefficients taken from Yang et al. (2003). Numerical approximation (black) compared with its approximation (dashed red) linearized with respect to the L_{ref}.

a Taylor expansion. In order to corroborate the final result, the physiological model in system (3.10) is compared with its linearized version for different values of α_{AM_p}. The result is presented in Fig.3.3, which shows that a simple affine constitutive law is indeed valid for an approximated description of the SMC fibers for the retina in physiological regimes.

The constitutive law adopted, which is the simplest law that approximately describes the behaviour of the SMCs is:

$$\sigma_{1D} = k_0 + k_1 \varepsilon_{1D},$$

where σ_{1D} is the elastic stress, k_0 is the pre-stress of the fiber, k_1 is the elastic modulus, ε_{1D} is the fiber deformation.

Equation (3.11) can finally be used to identify the parameters k_0, k_1, after a rescaling. The SMCs are assumed to have a cylindrical shape with a radius r_{smc}. The force is divided by πr_{smc}^2 in order to obtain the stress. The result reads:

$$k_0(\alpha_{AM_p}) = \frac{1}{\pi r_{smc}^2} F_0(\alpha_{AM_p}),$$
$$k_1(\alpha_{AM_p}) = \frac{1}{\pi r_{smc}^2} F_1(\alpha_{AM_p}),$$

In practice, it is difficult to have access to the value of α_{AM_p}, which depends on

many factors. This is why in the following section, the functions k_0 and k_1 will be simply assumed to depend on an "activation parameter" ζ:

$$\sigma_{1D} = k_0(\zeta) + k_1(\zeta)\varepsilon_{1D}, \tag{3.12}$$

3.3.5 The fiber layer

In this section, the equations describing the dynamics of an SMC fiber layer are detailed. The main hypotheses are the following:

- the fibers are perfectly attached to the shell;
- the fibers are characterized by an affine stress-strain constitutive law.

The kinematic hypothesis implies that the deformation of the fibers equals the deformation of the underlying shell structure in the direction of the fibers.

Let $\mathbf{w} \in \mathbb{T}_{\boldsymbol{x}}(\Gamma)$ be a unitary vector belonging to the tangent space of Γ defined at the point $\boldsymbol{x} \in \Gamma$. The deformation of the fiber in the $\mathbf{w}$ direction can thus be written as:

$$\varepsilon_{1D} = \mathbf{w}^T \boldsymbol{G}\mathbf{w} = -d_1\eta + \frac{d_2}{2}\eta^2 + \frac{1}{2}\nabla\eta^T P_{\mathbf{w}}\nabla\eta, \tag{3.13}$$

where the scalar coefficients d_j and the projector $P_{\mathbf{w}}$ are defined as $d_1 = \mathbf{w}^T\boldsymbol{B}\mathbf{w}$, $d_2 = \mathbf{w}^T\boldsymbol{B}\boldsymbol{S}\mathbf{w}$, $P_{\mathbf{w}} = \mathbf{w}\otimes\mathbf{w}$. The constitutive stress-strain relationship is given by Eq.(3.12).

Let $\varrho_{\mathbf{w}}$ be the fraction of the total number of fibers aligned in the direction $\mathbf{w}$. The elastic energy of the fibers aligned in the direction $\mathbf{w}$ is of the form:

$$\psi^{\mathbf{w}}(\eta) = \frac{1}{2}\int_\omega \varrho_{\mathbf{w}}\left[k_0 + k_1\varepsilon_{1D}(\eta)\right]\varepsilon_{1D}(\eta)\; h^f\sqrt{a}\,d\boldsymbol{\xi} + \int_\omega r_{\mathbf{w}}\; h^f\sqrt{a}\,d\boldsymbol{\xi},$$

where h^f is the thickness of the smooth muscle cell layer, $r_{\mathbf{w}}$ represents the potential energy of a force acting on the fibers aligned with the direction $\mathbf{w}$.

The equilibrium equations are introduced in weak form as the scalar product with a test function of the Frechet derivative of the energy with respect to the displacement:

$$\begin{aligned}\Psi^{\mathbf{w}}(\eta,\chi) = \int_\omega \varrho_{\mathbf{w}}\nabla\chi^T\left[k_0 + k_1\left(-d_1 + \frac{d_2}{2}\eta^2\right) + \frac{k_1}{4}W\right]P_{\mathbf{w}}\nabla\eta + \\ \varrho_{\mathbf{w}}\left[k_0\left(-d_1 + d_2\eta\right) + k_1\left(-d_1^2\eta - \frac{3d_1d_2}{2}\eta^2 + \frac{d_2^2}{2}\eta^3\right) + \frac{k_1}{2}(-d_1 + d_2\eta)W\right]\chi + \\ (\delta_\eta r_{\mathbf{w}})\chi\; h^f\sqrt{a}\,d\boldsymbol{\xi},\end{aligned} \tag{3.14}$$

where $W = \left(\nabla\eta^T P_{\mathbf{w}}\nabla\eta\right)$. We remark that the contribution of the first line is of membrane type, whereas the second line contains algebraic terms in the test function and hence it renders a nonlinear spring-like behavior.

When $\eta = 0$ and the SMCs are not activated, i.e. $\zeta = \bar{\zeta}$, the reference configuration is the equilibrium configuration only if the stress exerted by the fibers due to

their pre-stress is balanced by the underlying shell. By injecting $\eta = 0, \zeta = \bar{\zeta}$ into Eq.(3.14), we obtain:

$$\int_\omega (-\varrho_{\mathbf{w}} \bar{k}_0 d_1 + \delta_\eta r_{\mathbf{w}}) \chi h^f \sqrt{a}\, d\boldsymbol{\xi} = 0,$$

hence, for any arbitrary test function χ, the following holds

$$r_{\mathbf{w}} = \varrho_{\mathbf{w}} \bar{k}_0 d_1 \eta, \tag{3.15}$$

where $\bar{k}_0 = k_0(\bar{\zeta})$.

Remark 2

The consequence of Eq.(3.15) is the appearance, in the balance of the normal forces on Γ, of a force term. This is the main result of the SMCs contraction. Indeed, by combining Eq.(3.14) and Eq.(3.15) and, by setting $k_1 = 0$ for the sake of simplicity, we get:

$$\Psi^{\mathbf{w}}(\eta, \chi) = \int_\omega \varrho_{\mathbf{w}} k_0(\zeta) d_2 \eta \chi + \varrho_{\mathbf{w}} k_0(\zeta) \nabla \chi^T P_{\mathbf{w}} \nabla \eta \; h^f \sqrt{a}\, d\boldsymbol{\xi} + \int_\omega \varrho_{\mathbf{w}} (\bar{k}_0 - k_0(\zeta)) d_1 \chi \; h^f \sqrt{a}\, d\boldsymbol{\xi}.$$

This weak formulation represents the contribution to the structure equation due to the fibers in direction $\mathbf{w}$. The effect of the activation on the wall mechanics is twofold: first, there is a change in the constants that characterize the passive behavior of the structure (namely in the spring- and membrane-like contributions), and second, a force term of the following form appears:

$$\int_\omega \varrho_{\mathbf{w}} (\bar{k}_0 - k_0(\zeta)) d_1 \chi \; h^f \sqrt{a}\, d\boldsymbol{\xi}.$$

When ζ reaches its maximum value, this term is negative, representing a force in the normal direction that induces a negative displacement. Remark that the sign of d_1 depends on the curvature along the fiber direction and it is, in general, negative when the normal is pointing outward.

Remark 3

In order to get an intuitive insight in the normal equilibrium for the structure, an example in an idealized setting is proposed. The structure is a cylinder of radius R, a linear Koiter shell is considered, that is in equilibrium under a pressure load. The displacement with respect to the reference configuration is constant and, hence, space and time derivatives of the displacement field vanish. Under these conditions the equilibrium displacement is the solution of an algebraic equation:

$$\left(\frac{E h^\kappa}{1 - \nu^2} c_1 + \varrho_{\mathbf{w}} h^f (k_0(\zeta) d_2 - k_1 d_1^2) \right) \bar{\eta} = p - p_{iop} - \varrho_{\mathbf{w}} h^f d_1 (\bar{k}_0 - k_0(\zeta)),$$

the coefficient of $\bar{\eta}$ depends on both the mechanical properties of the structure $(E, \nu, \varrho_{\mathbf{w}}, k_0(\zeta), k_1)$ and on its geometrical properties (c_1, d_1, d_2 which depend on the curvature). The force term depends on both the mechanical properties $(\varrho_{\mathbf{w}}, k_0(\zeta))$ and the geometry d_1. Let us separate the shell contribution, the fiber contribution and the transmural presssure:

$$\left(\frac{Eh^{\kappa}}{1-\nu^2}c_1\right)\bar{\eta} = \Delta p - \sigma_{fiber},$$

where σ_{fiber} denotes the active and passive contributions of the fibers. When the tangential stress in a cylinder is computed by using the Koiter shell model, the following is obtained:

$$\sigma_\theta = \frac{E}{1-\nu^2}\frac{\bar{\eta}}{R}.$$

Injecting this relationship into the equilibrium equation yields:

$$\sigma_\theta \frac{h^{\kappa}}{R} = \Delta p - \sigma_{fiber}.$$

The shell (arteriolar endothelium) is in equilibrium under the load exerted by the fibers and the transmural pressure. The tangential wall tension is simply the integral of the stress across the thickness (by making the assumption of constant stress in the section, the tension is given by $\sigma_\theta h^{\kappa}$), so that the equilibrium equation reduces to the Laplace law.

REMARK 4

In general, the fibers are not parallel to only one direction. In what follows, two linearly independent unitary vectors $\mathbf{v}, \mathbf{w} \in \mathbb{T}_{\boldsymbol{x}}(\Gamma)$ and the associated fiber fractions $\varrho_{\mathbf{v}}$ and $\varrho_{\mathbf{w}}$ defined in each point of Γ are considered. In such a case the two associated energy fields $\psi^{\mathbf{w}}$ and $\psi^{\mathbf{v}}$ sum up. If medical imaging or histological examination provide the fiber orientations, this information can be used to set $\mathbf{v}$, $\varrho_{\mathbf{v}}$, $\mathbf{w}$ and $\varrho_{\mathbf{w}}$. When this information is missing, these values can be based on a qualitative knowledge of the fibers orientation. For example, it is indicated in [PRBR+08, p. 287] that the smooth muscle cells are oriented both circularly and longitudinally. One possible choice is therefore to take the principal direction of curvature, and $\varrho_{\mathbf{v}} = \varrho_{\mathbf{w}} = \frac{1}{2}$.

With this choice, the fiber layer behaves as an isotropic homogeneous membrane.

3.3.6 Summary

For the sake of clarity, we now summarize the model derived in the previous sections. The whole system is made of the Stokes equations

$$\begin{cases} \langle \partial_t \boldsymbol{u}, \boldsymbol{v} \rangle_\Omega + a(\boldsymbol{u}, \boldsymbol{v}) + b(p, \boldsymbol{v}) = 0 & \text{in } \Omega, t > 0, \\ \langle \nabla \cdot \boldsymbol{u}, q \rangle_\Omega = 0 & \text{in } \Omega, t > 0, \\ \langle (\boldsymbol{I} - \boldsymbol{n} \otimes \boldsymbol{n})(\boldsymbol{u} + \eta \nabla \boldsymbol{u} \boldsymbol{n}), \boldsymbol{w} \rangle_\Gamma = 0 & \text{on } \Gamma, t > 0, \\ \sigma(\boldsymbol{u}, p)\boldsymbol{n} = -p_{in}(t)\boldsymbol{n} & \text{on } \Gamma_{in}, t > 0, \end{cases}$$

and by the continuity of the normal velocity and of the normal stresses at the vessel wall:

$$\begin{cases} \rho_s h_s \langle \partial_{tt}^2 \eta, \chi \rangle_\Gamma + \Psi^s(\eta, \chi) + \langle p_{iop}, \chi \rangle_\Gamma = \langle p + \eta \nabla p \cdot \boldsymbol{n}, \chi \rangle_\Gamma & \text{on } \Gamma, t > 0, \\ \langle \partial_t \eta, \chi \rangle_\Gamma = \langle \boldsymbol{u} \cdot \boldsymbol{n} + \eta \nabla \boldsymbol{u} \boldsymbol{n} \cdot \boldsymbol{n}, \chi \rangle_\Gamma & \text{on } \Gamma, t > 0. \end{cases}$$

The behavior of the two-layer structure is modeled by $\Psi^s(\eta, \chi)$, defined in (3.3).

3.4 Autoregulation and pressure feedback

As indicated in Eq.(3.12), the pre-stress and the elastic modulus of the SMCs are assumed to be a function of a parameter ζ describing the activation of the SMCs. Inspired by [AHS+13], we use the following expression for k_0:

$$k_0(\zeta) = k_{0,ref} + k_{0,a}^{max} S(\zeta), \quad S(\zeta) = \frac{1 - e^{-s(\zeta - p_{ref})}}{1 + \frac{1}{\omega} e^{-s(\zeta - p_{ref})}}, \tag{3.16}$$

where p_{ref} is a given reference pressure, $k_{0,ref}$ is the pre-stress in the absence of activation, $\omega = -k_{0,a}^{min}/k_{0,a}^{max}$, where $k_{0,a}^{max}$ and $k_{0,a}^{min}$ are given parameters. The parameter s affects the slope of the curve and can be estimated by using $s = \frac{1}{p_{max} - p_{ref}} \ln(\frac{1+q/\omega}{1-q})$, where ln is the natural logarithm, and p_{max} is the value for which the active component of the pre-stress is equal to $q k_{0,a}^{max}$. A similar behavior could be assumed for the elastic modulus of the fibers k_1, but in what follows, we simply suppose that $k_1 = 0$. A plot of the sigmoid function is presented in Fig.3.4 for typical values of the parameters.

We now present our strategy to compute the activation parameter ζ. As mentioned in Section 3.3.4, SMCs react to changes in the concentration of calcium ions. The calcium ion concentration is in turn varied by several regulatory mechanisms [JAB03, PRBR+08, Bek13]. Since the focus of this work is the mechanical aspect of autoregulation, we make the simplifying assumption that the activation variable ζ directly depends on the feeding pressure. The rationale behind this choice is that an increase in the feeding pressure triggers the mechanims that will eventually affect the activation state of the smooth muscle cells. If models describing regulatory mechanisms and the concentration of calcium ions along the network were available,

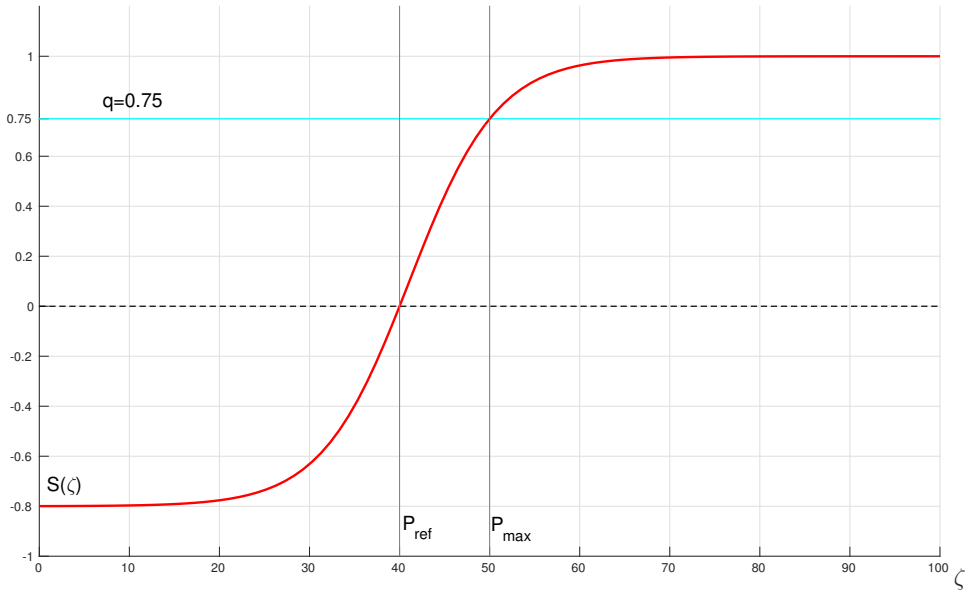

Figure 3.4: Sigmoid function for the parameters $\omega = 0.8$,$P_{max} = 50$,$q = 0.75$. $S(\zeta)$ on the y-axis and ζ on the x-axis.

they could be used to provide a more physiological expression of ζ.

We estimate ζ by using the mean values of the incoming pressure over the different cardiac cycles. These values are used to reconstruct ζ as a piecewise linear function in time, in the following way:

$$\begin{cases} \zeta(t) = \frac{1}{T_{i+1}-T_i}((T_{i+1}-t)\zeta_i + (t-T_i)\zeta_{i+1}) \quad \forall t \in (T_i, T_{i+1}) \text{ for } i = 1, 2, \dots \\ \zeta_{i+1} = \frac{1}{(T_{i+1}-T_i)|\Sigma_{in}|}\int_{T_i}^{T^{i+1}}\int_{\Sigma_{in}} p\, d\Gamma\, dt, \quad \text{for } i = 1, 2, \dots \\ \zeta_0 = p_{ref} \end{cases}$$

where Σ_{in} denotes the inlet of the computational domain and T_i the starting time of the i-th heart cycle.

As usual in computational hemodynamics, the 3D domain is truncated and the downstream vessels is taken into account by using 0D Windkessel models. More precisely, each terminal vessel in our 3D network is connected to the venous pressure via an RCR compartment. For simplicity, all these compartments are assumed to share the same values for the resistances (R_{prox} and R_{distal}) and the capacitance (C). The autoregulation in the Windkessel element is governed by the following hypotheses: the proximal resistance R_{prox} remains constant over time; the distal resistance is given by:

$$R_{distal}(\zeta) = R_{distal,ref} + \alpha S(\zeta) R_{distal,ref}, \tag{3.17}$$

with $\alpha = 1 - R_{distal,max}/R_{distal,ref}$; the capacitance varies so that the characteristic time $\tau = R_{distal}(\zeta)C(\zeta)$ remains constant.

3.5 Numerical simulations

This section is structured as follows. First, we present a validation of the model on a test case where the mean incoming pressure coincides with the reference pressure. The values obtained for the velocity are compared with the experimental data presented in the work by Riva *et al.* [RGSP85]. Second, we present a numerical experiment where the mean incoming pressure is varied. Different flow rate-incoming pressure curves are obtained for different values of the maximum pre-stress of the fibers.

3.5.1 Reference case and validation

3.5.1.1 Data

The geometry was obtained using a retinal fundus image in the Drive dataset [SAN+04]. The image was segmented and the vessels tree reconstructed by using the algorithms presented in [ADHS09, CAADH15]. We considered only the inferior temporal arteriole and its branches. Twenty-five segments were obtained via the segmentation algorithm. The 3D tree was reconstructed from the 2D image by first assuming a circular section for the vessels and then by projecting the results over a sphere. The detailed bifurcations were not available from the segmentation and they were reconstructed using B-splines. The mesh generation was carried out using `gmsh` [GR09] and then refined using `Feflo.a`, an anisotropic local remeshing sotware developed at Inria. Fig.3.5 shows two snapshots of the geometry used for the computations. The computational mesh has 822,071 tetrahedra and 105,604 triangles on the surface, for a total number of vertices of 165,238.

In [GHC+14b], the authors suggest taking a pressure at the inlet of the central retinal artery that is equal to two thirds of the mean brachial arterial pressure. With typical values of systolic and diastolic brachial pressure (120/80mmHg), this gives 62 mmHg. In addition, a pressure drop of about 20 mmHg is assumed to take place from the upstream of the central retinal artery to the downstream of the lamina cribrosa. Thus, we choose $p_{ref} = 40$mmHg, which is a reference value for the pressure at the beginning of our 3D network. Regarding the outlet boundary condition we set the venous pressure at 20 mmHg, which is compatible with the value used as a reference in [GHC+14b] after the venules compartment. The reference values for the Windkessel parameters are $R_{distal} = 6 \cdot 10^8$ P cm^{-3}, $R_{prox} = 6 \cdot 10^7$ P cm^{-3}, $C = 1.67 \cdot 10^{-10}$ s cm^3 P^{-1}. The blood viscosity is given by $\nu^f = 0.03$ cm^2 s^{-1}, and its density by $\rho^f = 1$ g/cm^3. The structure parameters are the Young modulus of the endothelium $E = 0.05$ MPa and its Poisson ratio $\nu = 0.5$, the thickness of the endothelium $h^\kappa = 5\mu m$ and the total thickness of the vessel $h^s = 25\mu$m. The density of the structure is set equal to 1g/cm^3. The fiber layer

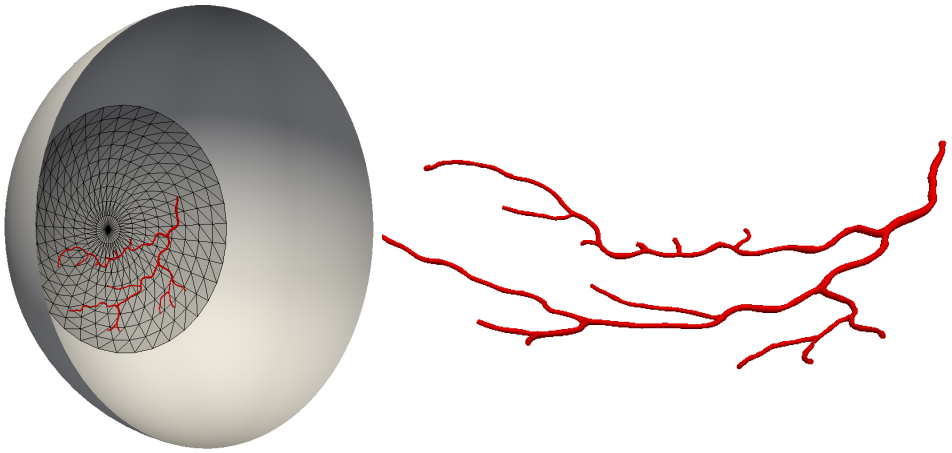

Figure 3.5: Computational mesh (left) and a broader view with the sphere used for the reconstruction (right).

thickness is $h^f = 20\mu$m The mechanical properties of the fibers are the pre-stress $k_0 = 0.4$MPa and the elastic modulus $k_1 = 0$. The intra-ocular pressure p_{iop} is kept constant at 15mmHg.

The duration of the cardiac cycle is $0.8s$, and the duration of diastole is $0.25s$. The time-profile of the incoming pressure is the following:

$$P_{in}(t) = \begin{cases} (p_{sys} - p_{dia})\sin(\pi t/0.25) + p_{dia} & t \in [0, 0.25] \\ p_{dia} & t \in [0.25, 0.8], \end{cases}$$

where $p_{dia} = 0.9\bar{P}$ and $p_{sys} = p_{dia} + 0.16\pi\bar{P}$ are the diastolic and systolic pressure for a given value of mean pressure $\bar{P}$. A summary of these choices is presented in Table 3.5.1.1.

3.5.1.2 Results

In order to have a reference solution where autoregulation does not play a role and that can be used to assess the model, we set $\bar{P} = 40$mmHg. We use $\boldsymbol{u} = 0, \eta = 0$ as initial conditions, and observe a quasi periodic behavior after two cardiac cycles. In Fig.3.6 we report a snapshot from the simulation taken at the time instant $t = 3s$, *i.e.* during the diastole. The figure also displays the surface of the computational mesh. To compare the results of our simulation with the experimental data presented in [RGSP85], we compute the mean value (in time, over a cardiac cycle) of the blood velocity at the center of different sections of the artery along the network. The value of the diameter is taken as the mean value of the diameters over the segment (between two bifurcations) which contains the section. The chosen points of the network are depicted in Fig.3.7, and a comparison of the data is given in Fig.3.8. In order to have a fair comparison, the mean velocity over time has been computed

Fluid parameters	
ν^f	0.03 cm^2 s^{-1}
ρ^f	1 g cm^{-3}
Boundary conditions and Windkessel parameters	
P_{venous}	20 mmHg
P_{iop}	15 mmHg
R_{distal}	$6 \cdot 10^8$ P cm^{-3}
$R_{proximal}$	$6 \cdot 10^7$ P cm^{-3}
C	$1.67 \cdot 10^{-10}$ s cm^3 P^{-1}
Structure parameter	
ρ^s	1 g cm^{-3}
E	0.05 MPa
ν	0.5
k_0	0.4 MPa
k_1	0
h^k	5 μm
h^f	20 μm
h^s	25 μm

Table 3.1: Summary of the model parameters. In the table P stands for Poise.

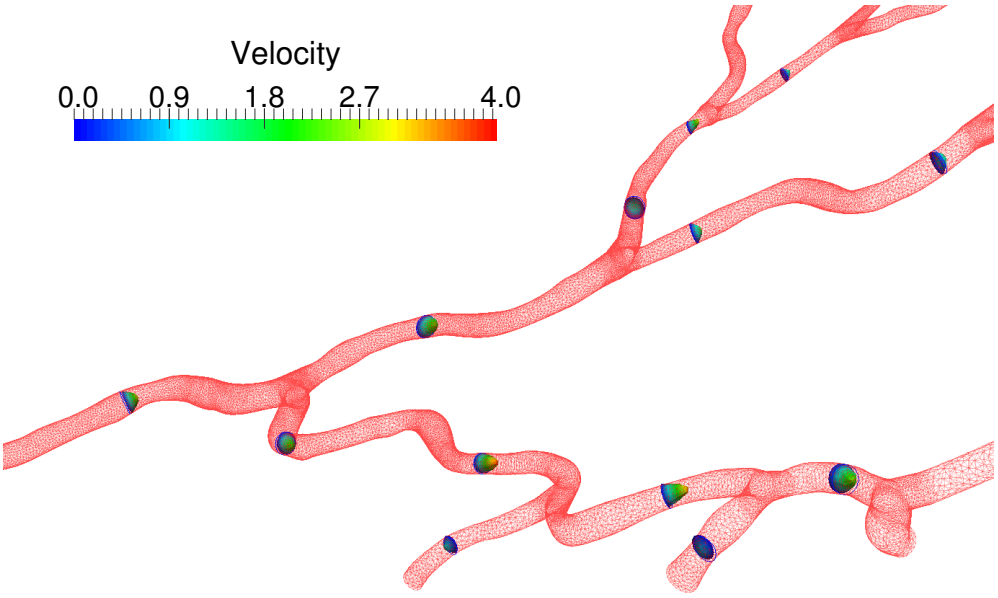

Figure 3.6: Velocity profiles [cm/s] on some slices of the domain. Values are taken during the diastolic phase of the fourth cardiac cycle ($t = 3s$).

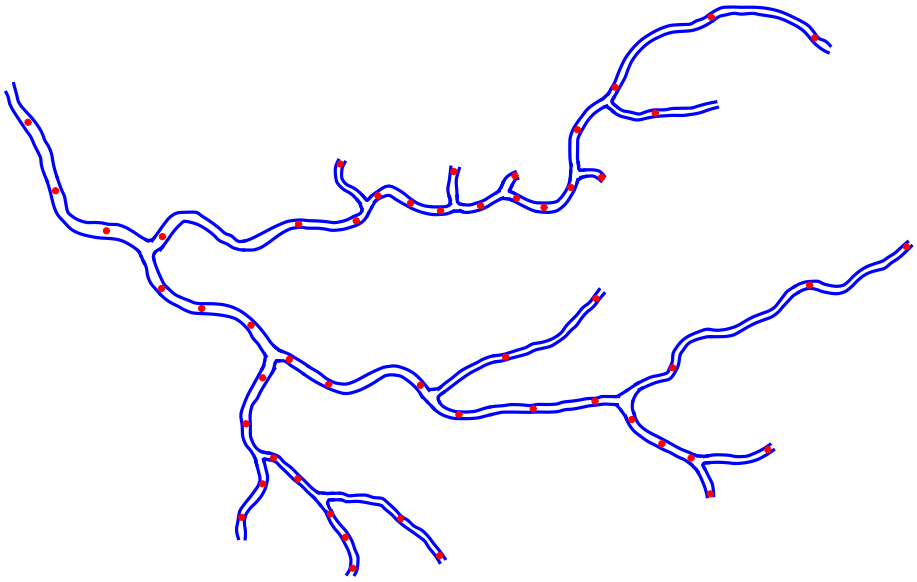

Figure 3.7: Points where the mean velocity has been measured for comparison with experimental data presented in [RGSP85]

using the same formula as was used in [RGSP85] (one third of the systolic velocity plus two thirds of the diastolic velocity). The results of the model are within the same range of values as the experimental data. The two sets of points also show a similar variability. However, there is a region for which either the velocity has been underestimated or the diameter has been overestimated (around 100 μm, 1 cm/s). We can provide two explanations for this discrepancy. First, the errors might come from the segmentation: the points with the lowest velocity are in the terminal vessels, which are the smallest and therefore the most difficult to capture with the segmentation algorithms. Second, it is possible that the assumption that all terminal vessels experience the same downstream equivalent resistance is too rough an approximation of reality.

3.5.2 Autoregulation

3.5.2.1 Data

For this test case we used the geometry and the data reported in Section 3.5.1.1. The control mechanism has been detailed in Section 3.4. For the present simulation, the parameters defining the sigmoid activation function (see Eq.(3.16)) are the following: $\omega = 0.8$ and $P_{max} = 50\text{mmHg}, q = 75\%$.

3.5.2.2 Results

In Fig. 3.9 the relationship between the flow rate and the pressure at the inlet is depicted for a representative cardiac cyle in two distinct scenarios: without

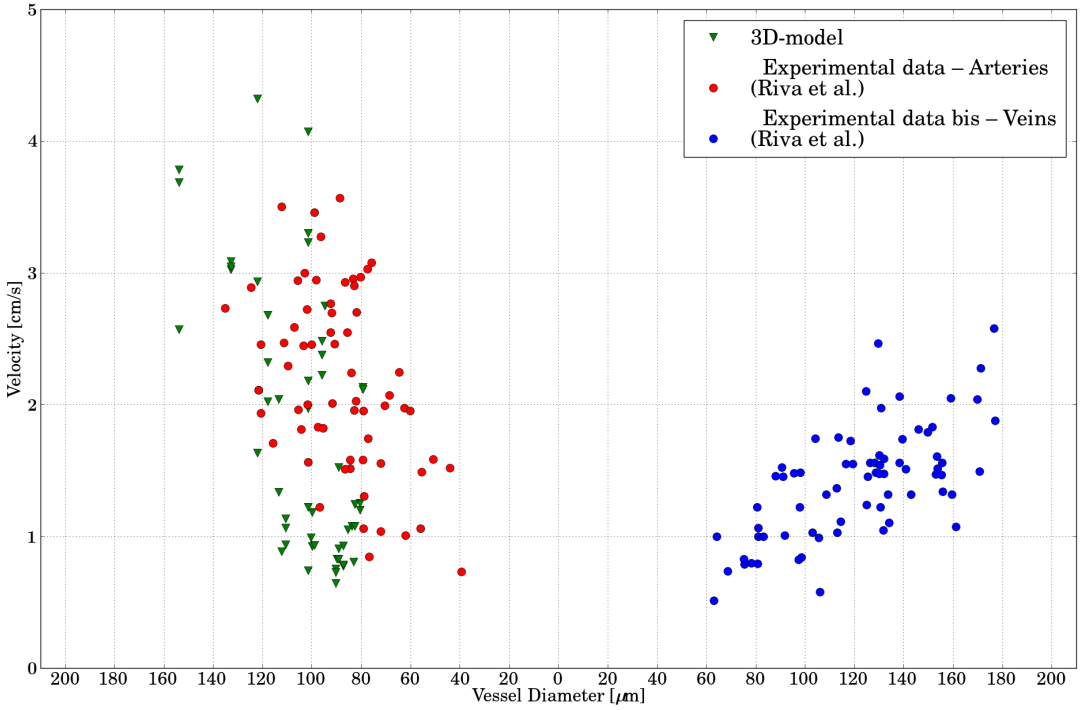

Figure 3.8: Comparison between the experimental data taken from [RGSP85]. Mean velocity in time (y-axis) and diameter (x-axis, arteries on the left side and veins on the right side). Experimental data are depicted by circles: red refers to arteries and blue refers to veins. Data computed by the proposed model are depicted by green triangles.

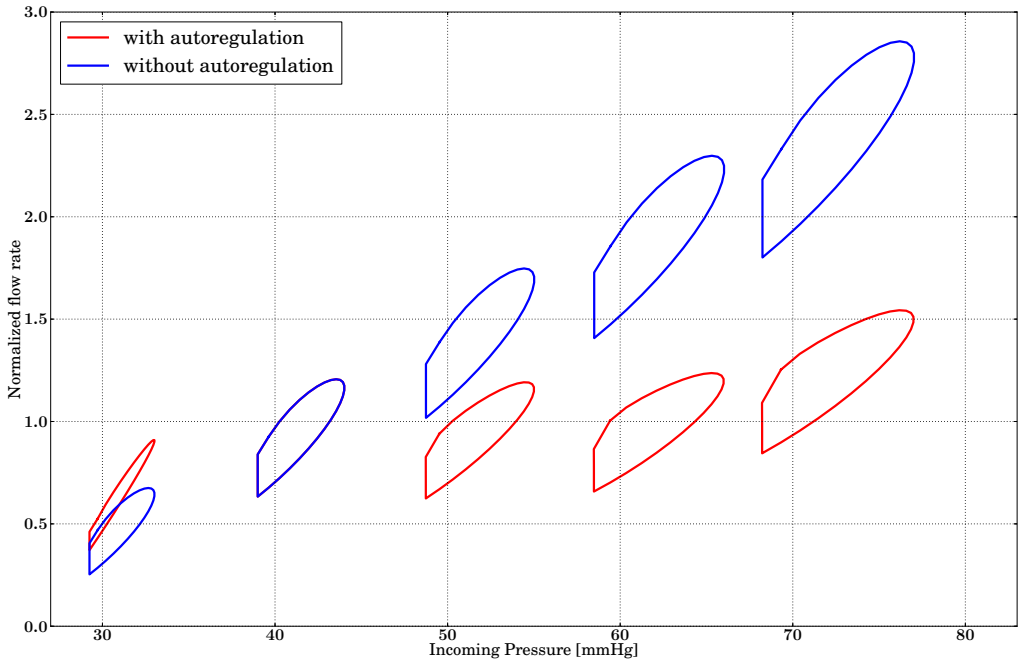

Figure 3.9: Normalized flow rate (y-axis) with respect to incoming pressure (x-axis). Each circle represents one cardiac cycle from a different simulation. The blue circles correspond to the simulations without autoregulation: $K_{0,a}^{max} = 0$ and $\alpha = 0$, for different values of $\bar{P}$. The red circles refer to the autoregulation parameters $K_{0,a}^{max} = 0.1$MPa and $\alpha = 0.15$.

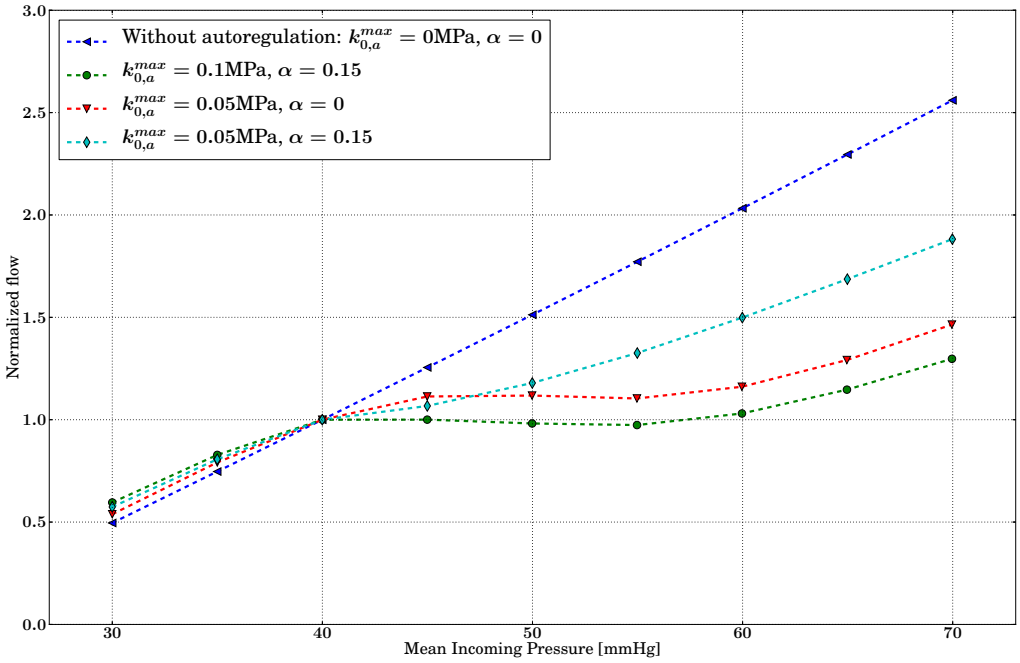

Figure 3.10: Autoregulation curves. Mean incoming pressure on the fourth cardiac cycles (x-axis) and normalized flow rate over the fourth cardiac cycle (y-axis). Different lines correspond to different values for the autoregulation parameters. Each point on a curve refers to a different simulation with a given mean incoming pressure.

autoregulation (in blue) and with autoregulation (in red). Each loop is a cardiac cycle for a simulation performed by imposing a different mean incoming pressure. The chosen values are $\bar{P} = [30, 40, 50, 60, 70]$mmHg. In the autoregulated case, the parameters determining the control intensity are: $k_{0,a}^{max} = 0.1$MPa and $\alpha = 0.15$. It should be noted that for a mean pressure of $\bar{P} = 40$mmHg there is only one loop since it is the reference pressure, *i.e.* the pressure for which the smooth muscle cells maintain their reference length. By observing these curves it can be inferred that the control mechanism acts directly on the vessels resistance. In particular, when the mean pressure is higher than the reference pressure, the flow rate is diminished, whereas when the mean pressure is lower, the SMCs action tends to increase the flow rate.

Each point of the curves represented in Fig. 3.10 is the value of the flow entering the network for a given value of inlet pressure. The mean inlet pressure $\bar{P}$ is varied from 30mmHg to 70mmHg. The parameters governing autoregulation are chosen as follows: $k_{0,a}^{max}$ takes three values: 0 (no autoregulation), 0.05MPa and 0.1Mpa. The autoregulation parameter α, defined in equation (3.17), indicates how much the downstream circulation is able to vary its overall resistance. Two different cases were considered: $\alpha = 0$ (no autoregulation) and $\alpha = 0.15$ (for which the maximum value of distal resistance is equal $1.15R_{distal,ref}$). For each numerical experiment four cardiac cycles are simulated. The values of the flow are taken in the last cycle and the flow is normalized with respect to the value obtained for $\bar{P} = p_{ref} = 40$mmHg. Fig.3.10 shows that using $k_{0,a}^{max} = 0.1$MPa and using autoregulation in the Windkessel model (circles, green), it is possible to replicate a plateau in the flow rate-pressure relationship. This result is similar to that obtained in [AHS+13] with a 0D approach. The impact of autoregulation in the Windkessel for this choice of parameters can be observed by comparing the green curve (circles) with the red one (down triangles), which was obtained with the same $k_{a,0}^{max}$ and by turning the Windkessel autoregulation off ($\alpha = 0$).

3.6 Limitations and conclusions

In this chapter, we have proposed a first attempt at modelling autoregulation in a 3D network of retinal arteries. Our approach is based on a simplified fluid-structure model whose computational cost is of the same order as the cost of a pure fluid problem. The model used for the wall includes smooth muscle fibers, whose active constitutive law has been derived by approximating physiological models proposed in the literature. The simulations performed in a real network of 25 segments of retinal arteries have provided velocities which are in good agreement with published experimental data. By varying the parameters of the active component of the constitutive law, we have been able to reproduce flow rate-pressure curves which are comparable with experimental data or results obtained with 0D models. In particular, a characteristic plateau of the flow rate has been found for pressures ranging from 40 to 60 mmHg.

To the best of our knowledge, this study is the first to propose 3D simulations of blood flow in a real network of retinal arteries, including an autoregulation mechanism. It can be viewed as a first step toward a more complete 3D model of the hemodynamics of the eye. In spite of encouraging results, many limitations remain and the model could be improved in various ways.

First, the diameter of the vessels considered in this work is below $200\mu m$, which means that the hemodynamics is in a microcirculation regime [WKK+03, PRBR+08]. In such vessels, the Fahraeus effect, the Fahraeus-Lindqvist effect and plasma skimming may be relevant in determining the distribution of hematocrit and the velocity profile [PNG92, PLCG89].

Second, our autoregulation model describes how smooth muscle fibers control the blood flow, but not the physiological mechanisms that trigger the contraction or the relaxation. The feedback mechanism could be improved to include other aspects than only the inlet pressure.

Besides these limitations, future works could also improve the models used for the downstream vasculature, and should address other important phenomena like the interaction with other compartments, such as the lamina cribrosa or the intraocular pressure.

Chapter 4

Modelling the eye: state of the art

The eye is a complex organ where each compartment has a specific function and structure. In this chapter we focus on fluid and structure mechanics. We briefly introduce the anatomy of the eye and then we review the state of the art in the modelling of the human eye. This analysis of the literature was done in preparation of the work of Chapter 5.

Contents

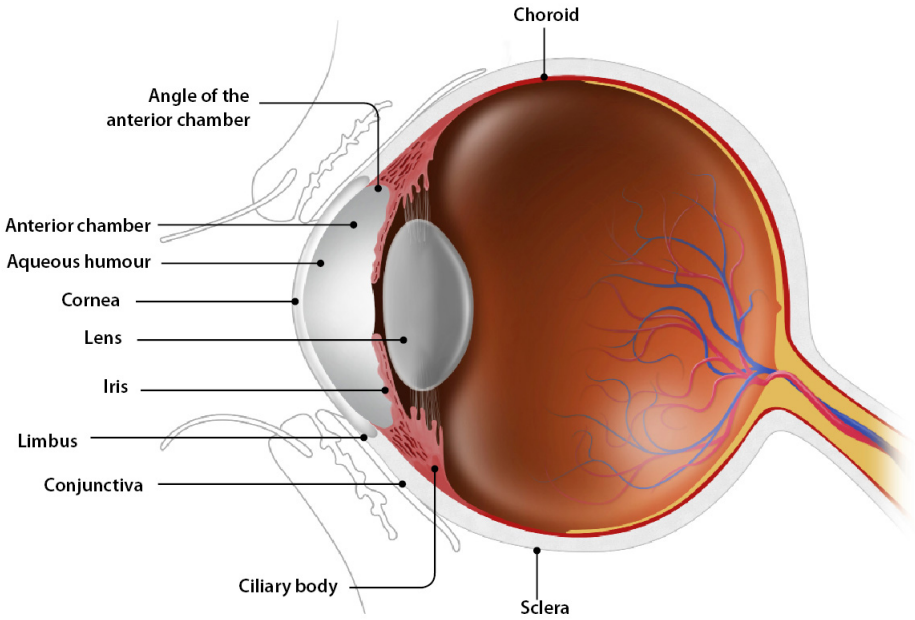

Figure 4.1: Scheme of the eyeball from above. Image taken from http://www.bpac.org.nz/BPJ/2013/August/redeye.aspx

4.1 Introduction

In the eye there are several compartments (see Fig. 4.1). There are two separated cavities: the *vitreous* and the *anterior cavity*. The anterior cavity is divided into two chambers: the *anterior* and the *posterior chambers*. The two cavities are the fluid compartments of the eye, but they are quite different: the anterior cavity is filled with a fluid similar to water called *aqueous humor*, while the vitreous is filled with a gel characterized by more complex mechanical properties. The *sclera*, the white part of the eye, and the *cornea*, the transparent part in the front, form the external shell of the eyeball. The *uvea* denotes the area of the eye that includes the *choroid*, the *iris* and the *ciliary body*. The choroid is located between the *retina* and the sclera and it is a vascular tissue responsible for delivering nutrients to the back of the retina. The ciliary body is located at the end of the choroid and plays two important roles: it contains the *ciliary muscle* that controls the shape of *lens* and the *ciliary processes* that secrete the aqueous humor. The lens is attached to the ciliary body through the *suspensory legaments* or *zonules*. The iris, the coloured part of the eye, is the last component of the uvea and starts from the ciliary body and enters into the anterior cavity. The iris separates the two chambers of the anterior cavity and the aqueous humor can flow from the posterior to the anterior chamber passing through the *pupil* which is the hole in the center of iris. The iris also contains a muscle that is able to regulate the diameter of the pupil for optic purposes. In this chapter we discuss the state of the art of the modelling of fluid and structure mechanics, with a specific focus on the mechanisms that impact the

Intraocular Pressure (IOP) and trying, when possible, to limit ourselves to studies on the human eye.

4.2 Fluid dynamics modelling in the eye

Blood, aqueous humor and vitreous humor are the three different fluids present in the eye. Eye circulation is divided mainly in two systems: the retinal circulation, whose literature and further developments are discussed in Chapters 2 and 3, and the choroidal circulation. The vitreous humor exhibits visco-elastic properties [LLB91], but it is often referred to and modelled as a fluid even if it is mostly composed by a mixture of a fluid and a gel [Bis00] and it would be natural to model it as a solid. The aqueous humor is a fluid with a viscosity similar to water [BM56] and several models for its production, drainage and flow have already been developed and are the object of the next subsection. A detailed summary of fluid modelling in the eye can be found in the review paper by Siggers and Ethier [SE12].

4.2.1 Modelling of the aqueous humor

The aqueous humor is the fluid inside the anterior cavity. Its role is to deliver nutrients and remove wastes from the cornea and the lens, but also to keep the eye inflated. It is produced at an approximately constant rate by the ciliary processes

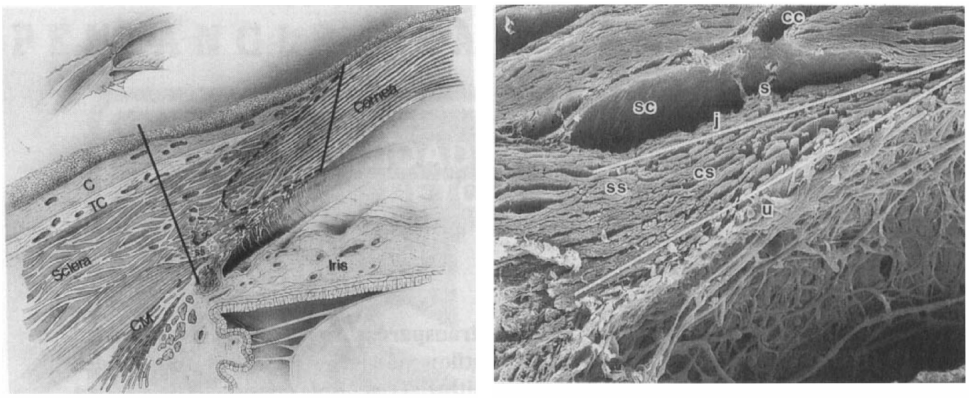

The Limbus. Solid lines demarcate the pathologist's limbus; the dotted line, the histologist's limbus. Conj = conjunctiva; TC, Tenon's Capsule; CM, ciliary muscle; TM, Trabecular Meshwork; SC, Schlemm's Canal; SS, Scleral Spur showing circumferential collagen fibres.

Scanning Electron Micrograph of cross section of aqueous outflow pathways in a human eye. U, Uveal Meshwork; CS, Corneo-Scleral Meshwork; JCT, Juxtacanalicular Meshwork; SS, Scleral Spur; SC, Schlemm's Canal; S, Septum; CC, Collector Channel.

Figure 4.2: An image of the limbus (left panel) and a zoom of the region of the trabecular meshwork (right panel). Adapted from *The anatomy of the limbus* by Van Buskirk [VB89].

that are folds of the ciliary body located in the posterior chamber. It passes through the pupil, enters the anterior chamber and exits through a small region located in the angle between the iris and the cornea. Before mixing with the blood of

the *episcleral vein*, the aqueous humor passes through a porous region called the *trabecular meshwork* and is collected into the *Schlemm's canal* which works as a rain gutter. The fluid leaves the canal passing through several extremely small *collector channels* and finally reaches the episcleral vein (see Figure 4.2).

Several authors have pointed out how the temperature gradients inside the anterior cavity have a strong impact on the flow of the aqueous humor. In fact, the temperature in the anterior cavity varies significantly from the cornea, which is directly exposed to the external temperature, to the inside of the eye. This gradient induces a flow which is considered to be of a larger order of magnitude with respect to the flow caused by the production/drainage mechanism [CGDF02].

Since the pressure inside the anterior chamber, the *intraocular pressure* (IOP), is an important risk factor for several diseases such as the glaucoma, this flow has been heavily studied and modelled. The main aspects that have been investigated are: the production, the drainage, the fluid-structure interaction with the iris and the thermal coupling.

Production and Drainage

The production of the aqueous humor (AH) happens in the ciliary processes. Two mechanisms of production have been observed: *ultrafiltration* and *active secretion* [Mos87, Kie98, GPLB10]. The flow rate due to the ultrafiltration process depends on both the pressure gradient between the capillary pressure and the IOP and on the *osmotic* pressure gradient. The active secretion instead provides an approximately constant flow rate. In [MSA+16] a 3D model, at the cellular scale, for the active secretion of AH is proposed.

An accurate modelling of the production rate of the aqueous humor is crucial when studying the stationary value of the IOP. However, if the flow generated by the thermal convection is the focus of the study, the flow induced by the production and drainage mechanisms can be neglected. This is the reason why in most of the models for AH flow the flow rate production is either considered constant or neglected.

Three outflow pathways have been observed in the literature. The main one, through the trabecular meshwork, and two minor ones: the *uveoscleral pathway* and the *posterior pathway* [Mos87, Kie98, GPLB10]. In the former one, the aqueous humor diffuses through the iris towards the ciliary muscle and finally is drained in the choroid or in the sclera. The posterior pathway is considered to be negligible with respect to the other two and therefore rarely mentioned in the medical literature. When the AH follows this pathway it does not enter the anterior chamber and, right after the production, it goes into the vitreous (see Figure 4.3).

An important question debated in the literature is whether the flow rate through the different pathways is dependent on the IOP or not. The importance of the question arises from the fact that an accurate description of the mechanisms that regulate the IOP is crucial for the understanding of the diseases. The outflow rate of the trabecular pathway depends on the pressure drop between the IOP and the pressure in the episcleral vein. The hydraulic resistance associated with the trabecular

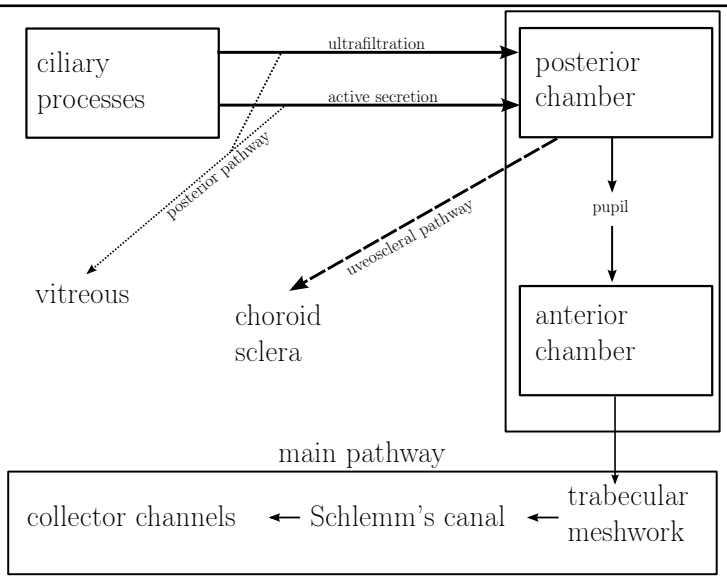

Figure 4.3: Simplified scheme of the production/drainage mechanisms of the aqueous humor.

meshwork, the Schlemm's canal and the collector channels is sometimes considered as dependent on the pressure of the anterior chamber through the so-called Brubaker correction [Mos87, Kie98] and it is probably due to a compression of the trabecular meshwork. According to [AN09] the uveoscleral flow rate is only slightly dependent on changes in the IOP and only for the small values [Kie98]. Measurements of the drainage are difficult to perform and for the secondary pathways they are mainly based on indirect measurements of the flow through the trabecular meshwork. The impact of the uveoscleral pathway is however unclear and its percentage ranges from 4% to 40% depending on the study, however those measurements are reported without the corresponding value for the IOP which could explain such a large difference. A review of the different studies aimed at quantitatively estimating the flow can be found in [McL09]. Some of the conclusions of the review indicate that AH flow shows strong daily variations: during the sleep it is reduced by a factor two. It has also been found that the flow decreases by 25% when aging from 20 to 80 years old. Finally the study suggests that AH flow is independent of IOP. The mechanisms of AH production and drainage are still not completely clear and this is reflected by inconsistency and disagreement between different studies.

Flow

There is a consensus in the literature to model AH with incompressible Navier-Stokes equations with water-like properties. When the thermal coupling is investigated the Boussinesq approximation is used to take this effect into account and different positions of the patients are investigated by changing the orientation of the gravity force. Buoyancy forces are the most important driving mechanism of the flow (see for instance [CGDF02, FG06]). For this reason, in several models for AH

flow the production mechanisms are treated in a simplified manner. Some authors assume a constant flow rate and others neglect its presence. These assumptions are consistent with the idea that thermal flow is the main phenomenon, however for studying IOP variations an accurate production model should be used. For describing AH drainage a variety of models have been used and the trabecular meshwork is usually described as porous medium (see for instance [KABP06, FdOdSM14, CE13]). Few studies consider the flow in the trabecular meshwork and in the Schlemm's canal (see [VRH+12], where also collector channels are considered). Most of the simulations are carried out on simplified two-dimensional geometries, but recently some work has been done on realistic 3D domains [VRH+12]. According to these studies the assumption that the intra-ocular pressure (IOP) is constant inside the anterior chamber is confirmed. Although sometimes fluid-structure interaction with the other compartments is considered (see [HBT01], where fluid-structure interaction with the iris is analyzed) this aspect and the investigation of time evolution and pulsatility are mostly neglected. In the following part of this section the different studies are briefly presented and the main modelling point as well as the results are summarised.

In the work by Canning et al. [CGDF02] incompressible unsteady Navier-Stokes equations with thermal coupling are considered on a simplified three-dimensional geometry of the anterior chamber. Several simplifications, including the Boussinesq approximation, are done based on dimensional arguments and on the lubrification assumption, *i.e.* that the distance between the cornea and the iris is much smaller that the radius of the iris itself. The final system of equations is steady, linear, axis-symmetric and can be solved analytically. The objective of the study is to investigate the behavior of particulate matter such as red and white blood cells and pigment particles in AH flow. They conclude that the thermal forces are the most-important driving force and that even a small temperature difference can drive this flow.

The work by Fitt and Gonzalez [FG06] follows the model presented above. In addition it investigates the limitations of the lubrification assumption by making a comparison with a numerical simulation which gives a good agreement. In this work five different situations are investigated: the thermally driven flow, the flow driven by the production and drainage of AH, the differences in the thermally driven flow induced by patient position, the flow generated by the *phacodenesis* that is the tremor of the lens (for which an unsteady model is needed) and flow caused by the Rapid Eye Movements occurring during the sleep. According to the authors everything is negligible compared to the thermally induced flow. However the analytical argument used to prove that there is no flow occurring because of eye movement seems questionable.

In a more recent study by Ferreira et Al. [FdOdSM14] the flow in the anterior chamber is numerically investigated. For their simulations a two-dimensional geometry of the anterior chamber is used which is more realistic than the one used for the two studies summarized above, however the posterior cavity is still absent. Unsteady Navier-Stokes equations are considered for the flow in the anterior cavity

and Darcy's law is used to describe the trabecular meshwork. Since the goal of this study is to investigate the delivery of a drug released at by a therapeutic lens, also the cornea is included in the study, but it is considered as rigid. The boundary conditions for the flow are the following: cornea, iris and lens are assumed rigid hence no-slip conditions are enforced at those interfaces, the inlet flow is prescribed at the boundary representing the space between the iris and lens and the pressure is given at the outlet, after the trabecular meshwork, representing the pressure of the Schlemm's canal. Thermal forces are not considered in the study and stationary simulations shows a constant pressure inside the anterior chamber, the IOP, and all the pressure drop occurs at the level of the trabecular meshwork. They have also studied the dependence of the IOP on different values of the inlet flow rate and of the porosity parameter of the trabecular meshwork.

In the study by Crowder and Ervin [CE13] the dependence of the IOP on different parameters (flow rate, AH viscosity and permeability of the trabecular meshwork) is also investigated. Stokes equations for the AH are coupled with Darcy's flow for describing the trabecular meshwork and thermal effect are neglected. After assuming the domain to be axisymmetric, the equations are solved in 2D on a simplified, but realistic geometry that takes into account both the anterior and the posterior chambers of the anterior cavity.

Other extensions of the model proposed by Canning [CGDF02] includes the works by Avtar and Srivastava [AS06] and by El-Shahed et al. [ES+05] where different boundary conditions at the level of cornea are investigated to model the fact the the cornea could be considered as a porous interface. It is also worth to mention the work by Ooi and Ng [ON08] where the AH flow is studied via the Navier-Stokes equations with Boussinesq approximation on a two-dimensional geometry and temperature distribution is computed in the whole eye-ball.

The literature on the modelling of aqueous humor flow is not limited to 2D models and we found some studies also in 3D. One of the first papers to address this problem is the work by Heys and Barocas [HB02], where they have studied the formation of *Krukenberg's spindle*, a pigment, by solving stationary Navier-Stokes equations with the Boussinesq approximation on a simplified three-dimensional geometry that includes both posterior and anterior chambers.

Another interesting work was done by Kumar et Al. [KABP06] where the authors have studied the thermally driven flow inside a simplified three-dimensional geometry of a rabbit's eye. Iris and cornea are described as fixed interfaces and the inlet is imposed as a constant term at the level of the pupil (the model does not include the posterior chamber). The drainage of the fluid is rendered by the presence of the trabecular meshwork described by a two-layers porous medium. Different orientations of the eye were considered as well as different pupil opening size. Some of the findings of this work include the fact that the temperature difference across the anterior chamber is a parameter of great impact on the flow while the pupil opening size did not affect much the flow. They have also observed that the pressure drop occurs only in the trabecular meshwork compartment.

In a more recent study by Villamarin et Al. [VRH+12], as it is now the standard

approach, the flow of the aqueous humor is modelled by stationary Navier-Stokes equations with the Boussinesq approximation. The peculiarity of this work is the use of an image-based geometry extremely detailed which includes both chambers of the anterior cavity, the trabecular meshwork, the Schlemm's canal and the collector's channels. The three-dimensional geometry is obtained from an image-based two-dimensional slice and by the addition of the collector channels. The boundary conditions are imposed consistently with the other works in the literature: iris, lens and cornea are fixed and the production rate of the AH is imposed at the inlet, which is now located at the level of the ciliary body.

Interaction with the Iris

In none of the models considered above the iris was allowed to move. It was indeed considered as a fix body located inside the anterior cavity where no-slip boundary conditions were assumed for the fluid problem. However, the iris is kind of floating inside the anterior cavity and it can also contract and dilate to vary the size of the pupil opening according to the optical needs. An interesting study addressing the interaction between the aqueous humor and the iris is the one by Heys and Barocas [HBT01]. The work is done on an idealised two-dimensional geometry including both chambers, the iris and the cornea. The fluid is modelled via unsteady Navier-Stokes equations, without thermal coupling, while the iris is described as an incompressible linear elastic material. The cornea is described via a spherical elastic shell with only normal displacement. The reason why they decided to use unsteady Navier-Stokes equations instead of steady Stokes equations is that they are interested in modelling the blinking and their claim is that in such a transient phenomenon the convective term is significant. This also motivated the inclusion of an elastic cornea, even if they found displacements of the order of ten micro-meters, because they have included the blinking as an external force term acting on the cornea. The AH production is included by a constant inlet value of 2.5 micro-liters per minute. The three drainage pathways, although in a simplified manner, are all included in the model. In particular the trabecular meshwork is modelled as 0D resistive element (main pathway) in parallel with a given constant flow going out from the same portion of the boundary, which is supposed to mimic the presence of the uveoscleral pathway. Although this looks anatomically inaccurate this is one of the few models that somehow takes the uveoscleral pathway into account. The posterior pathway is described again by a resistive element located at the interface between the posterior chamber and the vitreous which is also supposed to include the zonules resistance. The reason why they have decided to include it is that they are interested in a disease called *iris bombé* where the distance between the iris and the lens is almost reduced to zero causing an increase in the pressure of the posterior chamber and making the presence of the posterior pathway extremely relevant.

In a recent work by Jouzdani et al. [JAB13] the authors started from the model by Heys and Barocas presented above and they have added an active component in the radial direction to the stress tensor of the iris with the idea of describing

the contraction/dilation of the pupil. The other works on this topic done in the group of Barocas are summarized in Table 2 of [JAB13] and the different modelling choices are compared, e.g. whether the iris is nonlinear/linear or active and whether Stokes/Navier-Stokes transient/steady have been used for describing the aqueous humor.

4.2.2 Choroid, pulsation and ocular volume changes

The intraocular pressure (IOP) has a reference value for an healthy human eye of 15 mmHg and it exhibits oscillations synchronized with blood pulsatility. This phenomenon, well-known in the medical literature (see [SFL+89] for further references), is clearly an effect of the fluid-structure interactions occurring in the eye. The aqueous humor is obtained from the plasma flowing in the ciliary capillaries and it is later drained in the venous blood. There are only two possible reasons that could cause total volume variations of the eyeball. The first one is that the blood enter the eye through the ophthalmic artery with a pulsation and leaves it at a constant flow rate. The second one is the possible compressibility of the tissues, but we know that most of them are nearly incompressible. The ophthalmologist have found an exponential pressure-volume relationship where by pressure they mean the IOP: $IOP = p_0 e^{k\Delta V}$, where p_0 is a reference value for the IOP, usually 15 mmHg, K is the so-called ocular rigidity and ΔV denotes the ocular volume changes [DGDB+09]. This approach has been widely used in the literature as a tool to perform indirect measurement of the Ocular Blood Flow (OBF) [SFL+89, LFO+89]. The idea being that the only cause of variation for the ocular volume is the difference between the flow rate coming in and out of the eye. Therefore, by taking the time derivative of the IOP curve (see for instance [DGDB+09]) and by knowing the ocular rigidity coefficient they are able to compute the OBF. The ocular blood flow is mainly composed of choroidal blood flow (approximately 85% see [DGDB+09]) and retinal blood flow. The choroid is a highly vascularized tissue and its structure permits significant changes in the volume. The main drawback of this description, by means of the pressure-volume relationship, is that this relationship varies and it is in general impossible to determine it in vivo. The different assumptions on which this reasoning is based are discussed in [Kra92]. In the book chapter written by Kiel [Kie98] the approach based on the pressure-volume relationship is extensively discussed and summarized. Then another approach, called *hydraulic model*, is presented. The model consists of a 0D description of AH production and drainage mechanisms to compute the IOP. This model is of course very helpful in understanding the behavior of the stationary value of the IOP, but it cannot show its pulsatility since it does not take into account the pulsatility of choroidal blood. What is missing is a bridge between the two approaches, which can be done by investigating the choroidal circulation and the fluid-structure interaction occurring at the eye-scale.

4.2.3 Models for the Vitreous Humor

The vitreous humor, also simply referred to as the vitreous or the vitreous body, is the largest chamber of the eye. Water occupies approximately 99% of the volume. From the mechanical viewpoint it is worth mentioning the presence of a network of collagen type II fibrils and of hyaluronic acid that give the vitreous humor a gel-like consistency [Bis00]. Located between the lens and the retina, one of its functions is to keep the eye inflated and to force the retina to stay attached to the choroid. Despite being composed almost exclusively by water, its rheological properties are not those of a Newtonian fluid. Although the subject is still under debate, the vitreous is commonly referred to as a visco-elastic fluid. Several clinical studies, see for instance [Zim80, LLB91, SKHSK11], measured the visco-elastic properties of the vitreous using Maxwell-Voigt models.

The modelling of the vitreous has been also tackled from the mathematical viewpoint mostly with a focus on the *saccadic movements*. These movements are rotations of the eye of about 15-20 degrees necessary to use the *fovea*, the part of the retina where there is the highest resolution, to see a part of the scene. In the study by David et al. [DSDJ98] a visco-elastic model based on a series of the Maxwell and Voigt model on a simplified spherical geometry is used to study the saccadic motions. The visco-elastic model is solved analytically after some simplifying assumptions and compared to a Newtonian model solved numerically after having supposed an axisymmetric situation. The authors have found a good agreement between the two models for the particular situation of the saccadic motion, suggesting that a Newtonian model would be enough.

In the work by Repetto et al. [RSS10] the vitreous is described by a spherical geometry where the lens appears as a small geometrical perturbation of magnitude δ. They are also interested in the study of saccadic eye movement, which is included in the model by a torsion imposed on the vertical axis of amplitude ε. Navier-Stokes equations are used to describe the flow and, by means of a series expansion in both δ and ε they are able to find a semi-analytical solution. The authors comment on the Womersley number of the system that has to be small enough to perform the mathematical analysis and to avoid boundary layers. They also consider the Peclet number which is found be large suggesting that, when studying for instance drug delivery, convection needs to be taken into account. Other papers have followed this one, where a similar approach is used to investigate saccadic eye movements, the main motivation being the study of retinal detachment. In [RSC05] the authors have combined experiments and models after having assumed the vitreous to be Newtonian. In [SRC07] we find an experimental study where, again under the Newtonian assumption, the authors study the effect of the shape of the chambers and the resulting wall shear stress. In [Rep06] they introduce the analytical tools they we have briefly summarized above and they motivate the use of a Newtonian model by two arguments: the first one is that vitreous naturally liquefies with aging and the second one is that it is sometimes replaced by aqueous humor with surgery. A deeper review of the work done by this group can be found in [SE12, Section 4].

We conclude this section by mentioning the study carried out by Modarreszadeh and Abouali [MA14], where a 3D numerical simulation of the vitreous is performed by using a visco-elastic fluid, based on Giesekus model, on an idealized geometry.

4.3 Models of eye mechanics

As extensively discussed in the previous sections, the eye consists of two fluids cavities, that keep the eye inflated, surrounded by an external shell. This shell is divided in mainly two regions: the cornea and the sclera.

The cornea is the front part of the eye and it is completely transparent to allow the light to reach the retina. It is composed of five different layers: (from the outside to the inside) the *corneal epithelium*, the *Bowman's layer*, the *corneal stroma*, the *Descemet's membrane* and the *corneal endothelium*. From the mechanical viewpoint, the stroma is the most important layer that occupies approximately 90% of the corneal thickness.

The point where the cornea touches the sclera is a complex region anatomically and also mathematically because of the difficulties in prescribing realistic boundary conditions. This region, called the *limbus*, is an annular region where we find other important anatomical components. Two thin shell layers external to the sclera called the *Tenon's capsule* and the *conjuntiva* starts in this region as well as the compartments of the main drainage pathway of the aqueous humor (see Section 4.2.1) the trabecular meshwork and the Schlemm's canal. The uvea, the ensemble of iris, choroid and ciliary body, also starts here. The reader interested in the details of limbus' anatomy can read the paper by Van Buskirk [VB89] where there is a complete description of the limbus.

The sclera similarly to the cornea is divided into four different layers: the *episclera*, the *stroma*, the *lamina fusca* and the *endothelium*. The sclera can be divided in two different regions: the posterior sclera, which is the largest, and the peripapillary sclera an annular region surrounding the *optic nerve*. The *optic nerve*, located temporally with respect to the *posterior pole* of the eye is the only way to access the retina both for the blood, in fact it contains the central retinal artery and the central retinal vein and for the axons carrying the optical information.

Inside the optic nerve there is a mesh-like structure called *lamina cribrosa*. This vascularized structure holds the pressure difference between inside and outside the eye.

The mechanical modelling of these compartments is an older field of research and an extensive review is beyond the scope of this work. However, we summarize some interesting recent works on the subject.

In a recent work Simonini and Pandolfi [SP15] have modelled the mechanical behavior of the cornea by means of a finite elements model both on idealized and patient-specific geometries (geometrical raw data are also available for download). Only the corneal stroma is taken into account in the modelling because first, it is the stiffer layer and second, the other layers mechanical properties are

unknown. A model based on the definition of an elastic energy is employed where the presence of fibrils is also taken into account (following previous studies such as [PH08, PV12, SMP14]). The authors have also considered the problem of retrieving a stress-free configuration which is computed by solving an inverse problem where the image-based geometry is considered as the result of a given intra-ocular pressure. We have chosen to present this paper because it addresses several interesting aspects of the mechanical modelling of the cornea (presence of fibrils, stress-free configuration, limbus boundary conditions, patient-specific geometries) and also because the references cited in the paper could be used as a starting point for a deeper review of the topic.

In the study by Grytz and Meschke [GM10] the sclera and the cornea are described by means of a shell model. Its energy function is composed of a Neo-Hookean isotropic part and of an anisotropic one that models the presence of fibrils and the material is assumed incompressible. The authors use the same elastic energy for the two compartments, but the mechanical properties do change as well as the shell-thickness. To obtain the anisotropic part of the energy, they start from a previous study [GM09] where fibrils were described as helical shaped rods characterized by two geometrical parameters: the crimp-angle and the ratio between the filament cross-section and the radius of the helix. The only material parameter is the fibril Young modulus. This micro-scale behavior is up-scaled to the macro-scale by using a structure tensor, which encodes the information about the plane that contains the fibers, and a dispersion parameter that regulates the distribution on two orthogonal in-plane directions. Two families of fibers are included in the model. The focus of this work is to describe the remodelling of such a complex fibrils network, since it appears that fibrils tend to accommodate for stress changing their orientation. Although the model is used on an idealised geometry the results are validated with experimental data from [WKSL72]. An improvement of this work [GMJ11] consists of a more detailed description of the region around the optic nerve where the peripapillary sclera and the lamina cribrosa are taken into account.

The mechanics of the lamina cribrosa has also been investigated. If interested in coupling between mechanics and hemodynamics this tissue is particularly interesting. It is a vascular tissue and it surrounds the central retinal artery and the central retinal vein. In [GHC+14a] the authors use a non-linear isotropic elastic circular plate as a model for the lamina cribrosa. The IOP acts on the inner surface of this plate and the retrolaminar tissue pressure acts on the outer surface. On the lateral surface, where the lamina is attached to the sclera, the tension is imposed assuming the Laplace law. The model is solved by exploiting the symmetries of the geometry and the stress in the center of the lamina is used as an external force acting on the vessel wall of the central retinal artery. The goal is to understand the effects of changes in the IOP on the hydraulic resistance of the central retinal artery. The effect of the presence of blood vessels in this compartment is investigated in [CGH+14] where the authors use a poro-elastic model where blood vessels are viewed as pore inside an elastic matrix.

4.4 Models of the eye as a global system

To the best of our knowledge a few works have been done to build a global model of the eye able to include both the fluid and the structure behavior. In the work by Uchio et al. [UOK+99] a 3D model of the eye is proposed, which is still very simple. Fluids are in practice neglected and the focus is on the mechanics of the sclera and of the cornea for which they use a shell model calibrated on their own experiments. Kiel and colleagues [KHR+11] proposed a complex compartmental model where the choroid, the aqueous humor and the ciliary body are considered. In particular, IOP is computed by means of an exponential pressure-volume relationship, while the volume of the eye is given as an effect of the choroidal circulation (see also [KS92]). In the study by Kotha and Murtomäki [KM14] a drug delivery model for which they need a global description of the eye is developed. The drug enters from a patch placed on the sclera. Diffusion equations are used in the Sclera, in the Retina and in the Vitreous, while Navier-Stokes equations are used to model flow in the Choroid to obtain the advection field for the advection-diffusion equation used in the Choroid.

Chapter 5

Modelling the eye as a multi-domain system

In order to reproduce the mechanisms behind the oscillations of the intraocular pressure we propose a model of the eye with multiple compartments. This is necessary because the oscillations registered at the level of the anterior chambers originate from blood pulsatility in the choroid.

The model includes mostly structure and fluid mechanics. The hemodynamics is included in the model of the choroid. This tissue is described as a poro-elastic medium able to inflate during an heart beat.

We explain the modelling choices in terms of geometries and equations. We show some preliminary results on the poro-elastic model of the choroid, on the flow in the anterior cavity and on a two-compartment model of the choroid and the vitreous.

Contents

5.1 Introduction

In this chapter we introduce a multi-domain and multi-physics model of the eye. The model reproduces the mechanics and the impact of the hemodynamics on the different structures. We are mainly interested in reproducing the mechanisms that build up the intraocular pressure, in particular we investigate the oscillation of the intraocular pressure caused by blood pulsatility in the choroid.

This layer, located between the sclera and the retina, inflates during the heart beat exerting a pressure on the vitreous that is finally transmitted to the anterior chamber. These compartments are surrounded by the corneoscleral shell, an external and more rigid structure.

For now, we work on a geometry of the eye that includes several compartments such as the choroid, the vitreous and the sclera. The geometrical description of the eye that we are using is idealized, but it allows us to test, on a reasonable and realistic framework, models and algorithms that will later be used on more detailed and accurate geometries of the eye.

As explained in Chapter 4, models for the corneoscleral shell and for the fluid in the anterior cavity are already available in the literature. A hyper-elastic shell seems a reasonable choice for the corneoscleral shell, while Navier-Stokes-Boussinesq equations, or just Stokes equations depending on the phenomenon under investigation, are widely accepted for aqueous humor modelling. The most accurate choice for modelling the vitreous seems to be based on a visco-elastic fluid. However, for the sake of simplicity, we are going to use a simpler Newtonian fluid described by the Stokes equations. Therefore, most of the modelling effort has been dedicated to an accurate description of the choroid via a poro-elastic model and to the coupling between all these compartments.

In Section 5.2 all the modelling choices in terms of geometry (Section 5.2.1) and of equations (Section 5.2.2) are detailed. The flow in the anterior cavity, modelled by the Navier-Stokes-Boussinesq equations, is presented in Section 5.3. In Section 5.4 a model of the choroidal tissue as a poroelastic medium is introduced (Section 5.4.1). A numerical experiment regarding the choroid is presented in Section 5.4.2. In Section 5.4.3, the linear poro-elasticity equations are derived from a more general setting. In Section 5.5 a system with two compartments, the vitreous and the choroid, is analyzed. The coupling strategy based on fixed point iterations is presented in Section 5.5.1, then the approach used to interpolate the data exchanged on non-conformal interfaces is detailed in Section 5.5.2 and a preliminary result is presented in Section 5.5.3. The conclusions and the perspectives are summarized in Section 5.6.

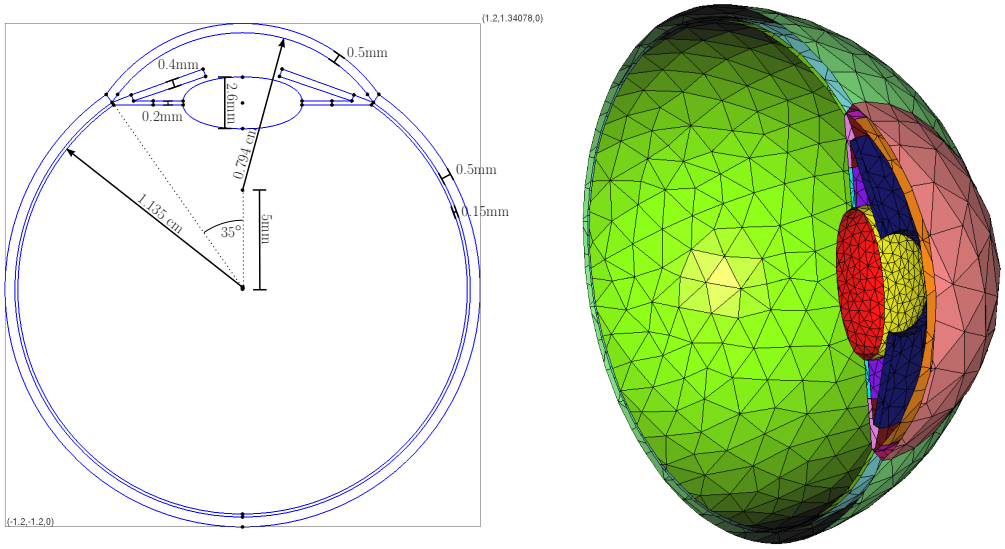

Figure 5.1: Two-dimensional cut of the geometry (left panel) and a portion of the surface of the corresponding three-dimensional mesh (right panel).

5.2 Multi-domain and multi-physics modelling of the eye

5.2.1 Geometry

The geometry used for the simulations of this chapter is an idealized representation of the eye. We have detailed the following compartments: the vitreous, the choroid, the sclera, the cornea, the lens, the ciliary body, the zonules and the iris. More details, such as the lamina cribrosa or the retinal layer should be added to the geometrical description of the eye, but are for now omitted for simplicity. In the left panel of Figure 5.1 we reported a two-dimensional slice of the eye. The actual geometry is obtain by revolution (see the right panel of Figure 5.1) around the central axis of the eye. As it can be observed from the figure, the geometry is idealized and it contains few domains. In the two-dimensional slice, the sclera is a portion of a ring with an inner radius of 1.15cm, an outer radius of 1.2cm for a thickness of 0.5mm. The portion that has been removed to leave the space for the cornea has a total angle of 70°. The 2D section of the cornea is a ring whose center is located $5mm$ closer to lens with respect to the center of the sclera and has an internal radius of approximately 0.794mm. The thickness of the cornea has been taken equal to that of the sclera. The uvea has been represented by its three compartments: the choroid, a portion of a ring with internal radius of 1.135cm and a thickness of 0.15mm, the ciliary body and the iris. A zoom of this region is in Figure 5.2. The portion of the interface between the anterior chamber and cornea of length 0.5mm represents the region where the aqueous humor exits the anterior chamber. The pupil has an aperture of 4mm and the lens is an ellipse with the major axis of 3mm and the minor one of 1.3mm. Here the zonules are represented

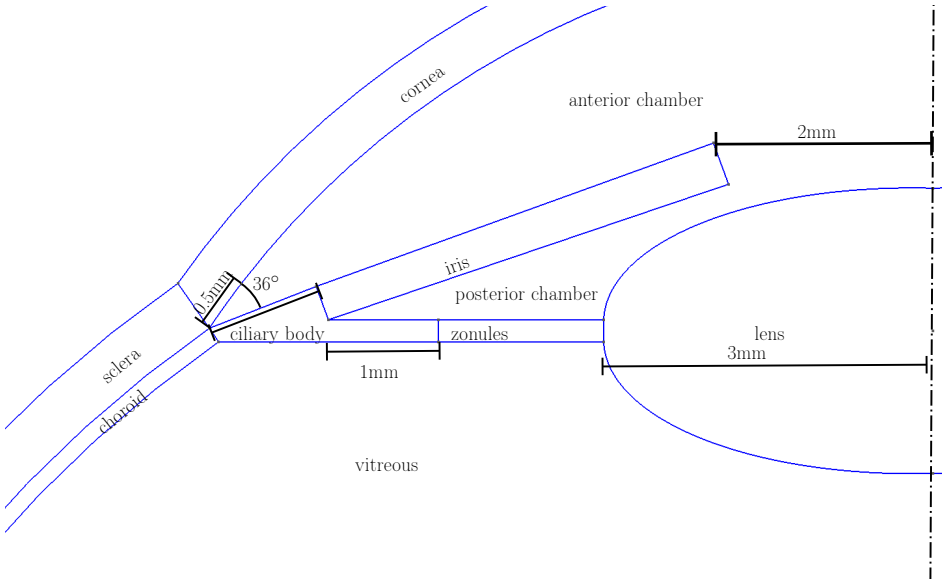

Figure 5.2: Details of the region close to limbus.

as an annular region around the lens for the sake of simplicity, while anatomically they are ligaments connecting the ciliary muscle with the lens. A few important compartments are missing. The retina has been omitted so far as well as the optic nerve and the lamina cribrosa. The trabecular meshwork as well as the Schlemm's canal and the collector's channel have not been included in the geometrical model. The reason for this choice is briefly explained in Section 5.2.2.

As far as the mesh generation is concerned, we originally planned to use tetrahedra for all the different compartments (see Figure 5.3). However it is impossible to use isotropic elements for the choroid and to have an acceptable number of degrees of freedom to render a transversal dynamic. A possibility that was considered was to use a kind of *poro-elastic shell*, i.e. reducing the 3D equations of poro-elasticity to 2D equations defined on the surface. However, when using a shell model coupled from both sides to different domains we need an adequate number of degrees of freedom per node. For this reason the construction of a poro-elastic shell is not straightforward for our application and it could be the object of a future work. We have decided to use a prismatic mesh with different layers (see Figure 5.4) for describing the choroid because it was the simplest way to obtain an anisotropic mesh. Another problem related to mesh generation is that when working with coupled problems that we want to solve separately we have to either use conform meshes, i.e. all the inner interface surfaces have to be discretized in the same way, or to be able to interpolate functions defined on the same surface which has been discretized in two different ways. We chose to work with non-conform meshes to have the pos-

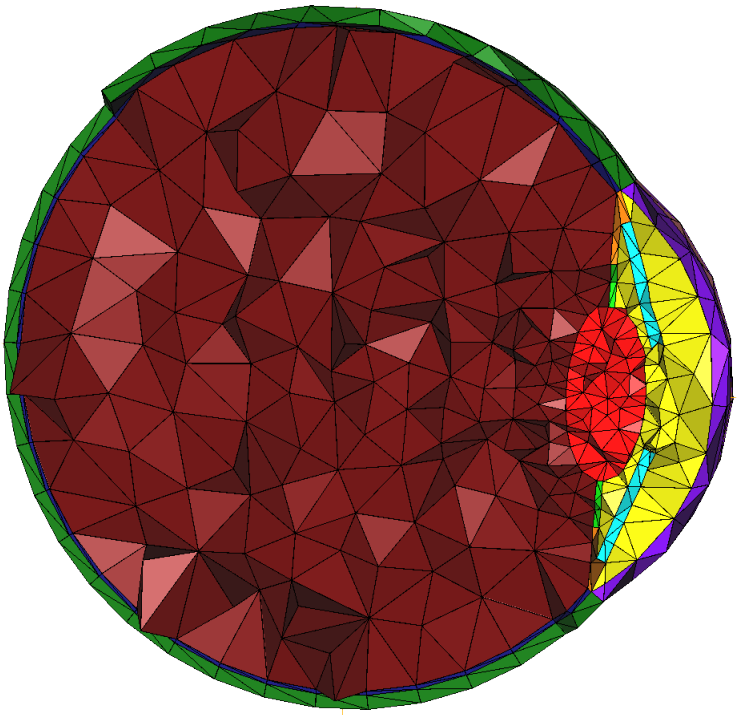

Figure 5.3: An example of a coarse tetrahedral 3D mesh of the eye.

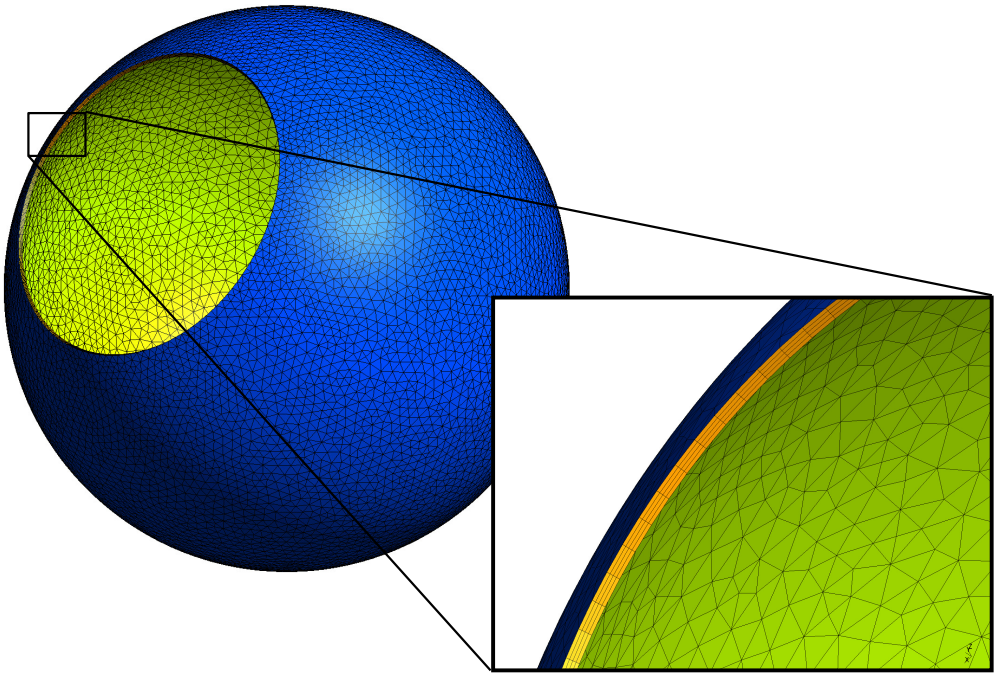

Figure 5.4: An example of choroidal mesh, in this case we use four layers of prisms across the thickness.

sibility of refining/derefining the single compartment without having to remesh all the eye.

5.2.2 Sub-domains and modelling choices

All the subdomains that could be included in the model are listed below. Despite being a rough simplification of the reality it is already an extremely complex model to handle. For this reason this decomposition is going to be further simplified to obtain a simpler system.

- Ω_C Cornea, thick elastic shell, nearly incompressible;
- Ω_S Sclera (including the Lamina Cribrosa), thick elastic shell, nearly incompressible;
- Ω_T Trabecular meshwork, poro-elasticity;
- Ω_A Aqueous Humor (anterior and posterior chambers), Navier-Stokes-Boussinesq equations;
- $\Omega_{C,I,Z}$ Ciliary Body and Iris and Zonules, 3D linear elasticity;
- Ω_L Lens, rigid body;
- Ω_V Vitreous Body, visco-elastic fluid;
- Ω_{Ch} Choroid, poro-elasticity.

The list includes several different subdomains and it is worth to notice that some compartments have already been neglected or condensed in larger sub-domains (see Figure 5.5). In some specific cases, think for instance of the lamina cribrosa included in the scleral domain Ω_S, the presence of different tissues in the same domain can be modelled by setting appropriate material properties in the corresponding subregions. The complexity of the system does not lie only in the number of subdomains, but also in the nature of the equations which includes hyper-elasticity equations, thick shells, poro-elasticity, Navier-Stokes-Boussinesq equations and visco-elastic fluids. For certain domains, such as $\Omega_C, \Omega_S, \Omega_A$, the modelling was strongly developed in the literature (see Chapter 4). For the other compartments we are going to use simple models mainly for two reasons. The first reason is a practical one: keeping an already complicated system as simple as possible. The second reason is that it is difficult to find experimental data and/or previous modelling studies to compare with and therefore it would be difficult to calibrate more complex models. The goal of this study it is to start tackling the problem of giving a comprehensive model of the eye. However, it is always possible to include more specific subdomains or to refine the models and the geometry in future works depending on the specific application at hand.

At this point we need to further simplify the system. It seems natural to neglect the geometrical presence of the trabecular meshwork because of its small size and

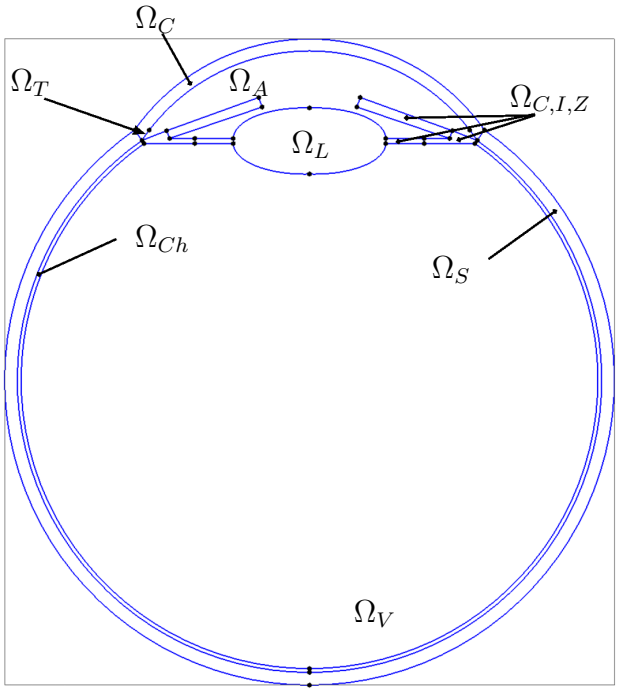

Figure 5.5: Decomposition in sub-domains.

to replace this complex poro-elastic region with a lumped 0D model at the outlet of the anterior chamber. When choosing the law of this resistive component we can include the Brubaker correction. This correction models the non-linear dependence of the outflow rate on the IOP probably due to the compression of the trabecular meshwork (see Section 4.2.1). Without resorting to a 3D poro-elastic model, we cannot expect to reproduce this phenomenon without adding it.

Once that the complexity of the limbus has been somehow neglected it is possible to use only one thick shell to describe the cornea and the sclera. The differences between the two regions will be rendered by using different material parameters.

After these simplifications we get the final list of subdomains that will be included in the model

- Ω_{CS} Corneoscleral shell, thick elastic shell, nearly incompressible, material properties changing in different portions of the domain;
- Ω_A Aqueous Humor in the anterior cavity, Navier-Stokes-Boussinesq equations;
- $\Omega_{C,I,Z,L}$ Ciliary Body, Iris, Zonules and Lens, 3D linear elasticity;
- Ω_V Vitreous Body, viscous fluid;
- Ω_{Ch} Choroid, poro-elasticity,

where more simplifications have been added. The lens is included in the same domain as the ciliary body, iris and zonules. As in the corneo-scleral shell, the differences between the sub-regions are rendered via discontinuous material properties. Moreover, we have for now neglected the visco-elasticity of the vitreous (and of the corneo-scleral shell). This important aspect will be the object of future works.

A few more comments on $\Omega_{C,I,Z,L}$. The components in this domain are quite different from each other. A linear-elastic model seems appropriate for the ciliary body and for the iris, but it neglects two aspects. First, these two tissues are vascularized. Therefore a poro-elastic model could be more appropriate following the ideas used in the choroid. Second, these two tissues contain two muscles responsible for pulling the lens and changing the diameter of the pupil aperture: this active component of the elastic energy is neglected for the sake of simplicity. We decided to include the zonules in the model, but the way they are included, geometrically and in terms of modelling, is questionable and it could be refined. Their role in the model is to connect the lens to the ciliary body and to separate and isolate the two cavities, still transmitting the pressure. As far as the lens is concerned, we plan to use a large Young modulus to have an almost rigid lens that can transmit pressures and displacement. However, we are neglecting the lens deformability that is important when investigating its optical properties.

Rigid movements of the eye have to be removed by applying appropriate boundary conditions at the external boundaries. In the reality the eye is attached to the socket via four muscles that can rotate the eye. A possible option is to prescribe the displacement of the Sclera in this four regions.

All the coupling conditions between the different subdomains are still to be specified. They have to guarantee the balance of forces and the continuity of the displacements.

A final simplification is that, for the fluid domains, we do not move the mesh and we adopt a zero order transpiration.

5.3 Modelling aqueous humor

As anticipated previously, Navier-Stokes-Boussinesq equations can be used to describe the flow of the aqueous humor in the anterior cavity. In view of the coupling with the other compartments we have also implemented this model. The equations read as follows:

$$\begin{cases} \partial_t \boldsymbol{u} - \nu \Delta \boldsymbol{u} + \boldsymbol{u} \cdot \nabla \boldsymbol{u} + \nabla p + \boldsymbol{g} \alpha T = \boldsymbol{g}(1 + \alpha T_0) & \text{in } \Omega \\ \nabla \cdot \boldsymbol{u} = 0 & \text{in } \Omega \\ \partial_t T - D \Delta T + \boldsymbol{u} \cdot \nabla T = 0 & \text{in } \Omega, \end{cases}$$

where $\boldsymbol{u}$ is the fluid velocity, p its pressure divided by the density $\rho = 1 g/cm^3$, $\nu = 0.009 \text{cm}^2/\text{s}$ the viscosity, $\boldsymbol{g}$ the gravity force, T the fluid temperature and $T_0 = 30^\circ$ the reference temperature and $D = 0.00135 \text{cm}^2/\text{s}$ the diffusivity coefficient

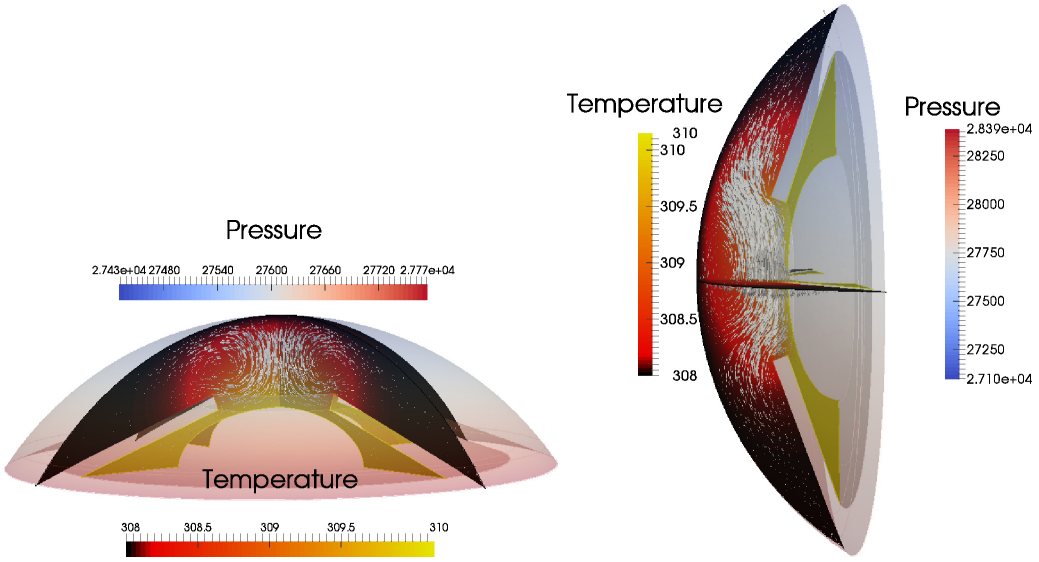

Figure 5.6: Flow of the aqueous humor in the anterior cavity. On the left the patient is laying while on the left is standing. The arrows represent fluid velocity and color the temperature (in Kelvin). The pressure, in dyne/cm^2, is represented on the transparent surface with a different color scale.

of the temperature and $\alpha = 3 \cdot 10^{-4} K^{-1}$ is the coefficient of thermal expansion.

As a first test, we imposed no-slip boundary conditions on all the boundaries, except for the inlet where a flow rate of $10^{-4} cm^3/s$ is imposed (by assuming constant normal velocity) and for the outlet, a small portion of the cornea-anterior chamber interface, where an RCR windkessel (parameters: $R_{prox} = 4 \cdot 10^7 dyne\ s/cm^5$, $R_{dist} = 1.6 \cdot 10^8 dyne\ s/cm^5$ and $C = 6.25 \cdot 10^9 cm^5/dyne$) models the presence of the trabecular meshwork, Schlemm's canal and collector channels and connects the aqueous humor with a venous pressure of 6mmHg. The temperature was assigned at the interface with cornea with $T = 35°$ and on the lowest interfaces with the lens, the zonules and the ciliary body: $T = 37°$. On the interface with the iris and the part of ciliary body close to the cornea, homogenous Neumann boundary conditions were imposed on the temperature.

The system was solved with a P1-P1 SUPG stabilized discretization for the fluid part and a P1 discretization for the temperature with a monolithic approach. The results are in Figure 5.6 where we observe two different configurations: the one where the patient is laying and one where he is standing. Consistently with the literature we retrieve two different configurations of aqueous humor recirculation depending on the direction of the gravity.

In order to avoid artificial recirculations close to the outlet region we slightly adapted the windkessel boundary condition. In the right hand of the weak formu-

lation we usually have a term of the form

$$p_w \int_{\Gamma_{out}} \boldsymbol{v} \cdot \boldsymbol{n}, \tag{5.1}$$

where p_w is the pressure computed via the windkessel model, $\boldsymbol{v}$ is a test function of the linear momentum equation, $\boldsymbol{n}$ is the normal unit vector and Γ_{out} is the outlet portion of the domain boundary. In this case, a solution with zero velocity, $\boldsymbol{u} = \boldsymbol{0}$, constant temperature, $T = \overline{T}$, and hydrostatic pressure, $p = p_w + (1 + \alpha(\overline{T} - T_0)\boldsymbol{g} \cdot \boldsymbol{x}$ is not compatible with the boundary term. We therefore replaced the term in Eq.(5.1) by

$$\int_{\Gamma_{out}} (p_w + h)\boldsymbol{v} \cdot \boldsymbol{n},$$

where h is given by

$$h = (1 - \alpha(T - T_0))(\boldsymbol{x} - \boldsymbol{x}_0) \cdot \boldsymbol{g},$$

and $\boldsymbol{x}_0$ is the barycenter of Γ_{out}. With this correction, the total force applied to the outlet remains $p_w|\Gamma_{out}|$ as expected, solutions with an hydrostatic pressure distribution are possible and the artificial recirculations disappear.

5.4 Poro-elastic model of the choroid

The choroid is the vascular tissue that delivers the nutrients to the outer layers of the retina. Such nutrients cannot be delivered from the retinal circulation itself because too many blood vessels on the inner retinal layers would block the light. This tissue is a thin structure with a thickness ranging from 0.1 to 0.2 mm. Inside, the blood vessels are organized in different layers: from the outermost to the innermost layer we find the largest vessels then the smallest and the capillaries.

The blood enters the choroid and, more generally, the uvea through the *posterior ciliary arteries* (PCAs) that originate from the *ophtalmic artery*. There are two types of PCAs: short PCAs (SPCAs) and long PCAs (LPCAs). The SPCAs pierce the sclera close to the optic nerve and supply approximately half of the choroid (up to the equator). The LPCAs supply the iris, the ciliary body and the choroid. They pierce the sclera close to the optic nerve, but they start branching next to the ciliary body. It is worth to mention the presence of the *anterior ciliary arteries* that supply the sclera, the conjunctiva and the extraocular muscle. The blood is drained through the vortex veins.

In this section, a poro-elastic model for the choroid is presented. The elastic solid matrix represents the tissue and the arterial circulation is modelled by the fluid flowing through the pores of the solid matrix. Blood enters the system in two regions representing the Short and Long PCAs and exits the system at the level of the capillaries.

For the description of the choroid we use the Biot's equations (see for instance [Cou04] or [CHE14]). In [CGSMVC10], the authors proposed a poro-elastic model in a more general framework that allows for large displacements. Their model was

used to describe blood circulation in the coronaries. In Section 5.4.3, we briefly present their derivation, that was helpful in the understanding of the role of the different terms and parameters of the equations. We also present a linearization of the equations presented therein. Under some specific assumptions, this leads to the Biot's system of equations which is used in the present work.

In the equations of linear poro-elasticity the balance of the linear momentum, where the inertial term is assumed to be negligible, is

$$\nabla \cdot \boldsymbol{\sigma} = \nabla \cdot \boldsymbol{\sigma}^{el}(\boldsymbol{u}) - b\nabla p = \boldsymbol{f},$$

where $\boldsymbol{u}$ is the displacement of the solid matrix, p is the pore-pressure, the pressure of the fluid inside the pores, b is the Biot coefficient and $\boldsymbol{f}$ are the external body forces. The expression of the elastic part of the stress tensor is that of the linear elasticity equations: $\boldsymbol{\sigma}^{el}(\boldsymbol{u}) = \frac{E^d}{2(1+\nu^d)}(\nabla \boldsymbol{u} + \nabla \boldsymbol{u}^T) + \frac{E^d \nu^d}{(1+\nu^d)(1-2\nu^d)}(\nabla \cdot \boldsymbol{u})\boldsymbol{I}$, where E^d and ν^d are the drained Young modulus and the drained Poisson ratio, respectively.

The second equation of the Biot's system is the balance of the fluid mass that reads as follows

$$\frac{1}{M}\partial_t p + b\nabla \partial_t \boldsymbol{u} + \nabla \cdot \boldsymbol{w} = s,$$

where M is the Biot's modulus, s is a volumetric source/sink term and $\boldsymbol{w}$ is the filtration velocity that can be related to the pressure by using Darcy's law

$$\boldsymbol{w} = -\boldsymbol{K}\nabla p,$$

where the tensor $\boldsymbol{K}$ is the permeability tensor.

The final system of the Biot's equations is

$$\begin{cases} \nabla \cdot \boldsymbol{\sigma}^{el}(\boldsymbol{u}) - b\nabla p = \boldsymbol{f} & \text{in } \Omega \\ \frac{1}{M}\partial_t p + b\nabla \partial_t \boldsymbol{u} - \nabla \cdot \boldsymbol{K}\nabla p = s & \text{in } \Omega. \end{cases}$$

The system could be solved in its mixed formulation by adding the filtration velocity $\boldsymbol{w}$ as an unknown and the Darcy's law as an equation, but for the sake of simplicity we use the Laplacian formulation.

The system is closed by boundary conditions of different forms: for the first equation we can assign the stress on a portion of the boundary or the displacement

$$\begin{cases} \boldsymbol{\sigma}^{el}\boldsymbol{n} - bp\boldsymbol{n} = \boldsymbol{h} & \text{on } \Gamma_{N,u} \\ \boldsymbol{u} = \boldsymbol{g} & \text{on } \Gamma_{D,u}, \end{cases}$$

and for the second equation we can either prescribe the normal component of the filtration velocity or the pressure:

$$\begin{cases} \boldsymbol{w} \cdot \boldsymbol{n} = -\boldsymbol{K}\nabla p \cdot \boldsymbol{n} = d & \text{on } \Gamma_{N,p} \\ p = z & \text{on } \Gamma_{D,p}. \end{cases}$$

REMARK 1 (BALANCE OF BLOOD MASS)
By integrating the second equation on the reference configuration Ω we have:

$$\rho^f b \frac{d}{dt}\int_\Omega \nabla\cdot\boldsymbol{u}\,d\Omega + \rho^f\frac{1}{M}\frac{d}{dt}\int_\Omega p\,d\Omega + \rho^f\int_{\partial\Omega}\boldsymbol{K}\nabla p\boldsymbol{n}\,d\Gamma = \rho^f\int_\Omega s\,d\Omega$$

that, assuming $\boldsymbol{w}\cdot\boldsymbol{n}=0$, reduces to:

$$\rho^f b\dot{V}(t) + \rho^f\frac{|\Omega|}{M}\dot{P}(t) = \rho^f S(t), \tag{5.2}$$

where $V(t)=\int_\Omega\nabla\cdot\boldsymbol{u}\,d\Omega$ is the current variation of the domain volume, $P(t)=\frac{1}{|\Omega|}\int_\Omega p\,d\Omega$ is the mean pressure over the domain and $\rho^f S(t)=\rho^f\int_\Omega s\,d\Omega$ is the current total flow rate of mass. If we work in the incompressible limit, $M\to+\infty$, we have

$$\rho^f b\dot{V}(t) = \rho^f S(t).$$

REMARK 2 (EFFECT OF THE SOURCE/SINK TERM ON THE LINEAR MOMENTUM EQUATION)
In the system under consideration, the inertial term in the linear momentum equation was neglected. If this term was included, it would depend on the total mass of the system and the presence of a distributed source/sink of fluid mass would also appear in the linear momentum equation and not only in the equation of fluid mass conservation.

5.4.1 Modelling of the Choroid

Lots of parameters appear in the equations of the poro-elasticity. In this section we explain how we plan to choose these parameters in order to mimic as accurately as possible the anatomical structure of the choroid. As discussed at the beginning of this section, the choroidal vessels are organized in layers with the largest vessels being in the outermost layers and the capillaries being in the innermost. Our idea for modelling this structure is to use a permeability tensor that varies across the different layers. In fact, large arterioles are supposed to offer less resistance in the longitudinal direction. On the other hand, in the capillaries there are no preferential directions and the resistance to blood flow is supposed to be higher. Of course many choices that follow this idea are possible, but since we lack of experimental data and also we will not have many degrees of freedom in the thickness direction we assumed to have only two layers: one with large arterioles, one with capillaries. The permeability of such poro-elastic medium has the following expression

$$\boldsymbol{K}(\boldsymbol{x}) = k_{cap}R^{cap}(\boldsymbol{x})\boldsymbol{I} + R^{arterioles}(\boldsymbol{x})(k_{arterioles,iso}\boldsymbol{I} + k_{arterioles}\boldsymbol{w}_{arterioles}\otimes\boldsymbol{w}_{arterioles}),$$

where $\boldsymbol{w}_{arterioles}$ is the preferred direction in the arterioles region, $R^{arterioles}$ and R^{cap} are the indicator functions of the arterioles and capillaries region respectively,

k_{cap}, $k_{arterioles,iso}$ and $k_{arterioles}$ are the permeability coefficients (with $k_{arterioles} \gg k_{arterioles,iso}$). In the arterioles region two coefficients are present, but in the preferred direction $k_{arterioles,iso}$ is negligible. For the sake of simplicity, we assume $k_{arterioles,iso} = k_{cap}$.

It is not straightforward to choose the coefficients k_{cap} and $k_{arterioles}$. In order to have an estimate of the difference in the orders of magnitude between the two coefficients we consider the aspect ratio of the domain $\alpha = \frac{L_{aniso}}{h}$ where L_{aniso} is a typical length in the anisotropic direction and h is the choroid thickness. By setting, approximately, $k_{arterioles} \sim \alpha^2 k_{cap}$ we obtain similar characteristic diffusion times for both regions. In our geometry, the thickness has a length scale of 10^{-2}cm and, in the longitudinal direction, the length scale is of the order of $1cm$, meaning that we have to keep approximately four orders of magnitude between the two parameters.

Now that the vessel structure has been described we have to include inlets and outlets of the system through the source/sink function $s = s(\boldsymbol{x}, t)$. The blood enters through two regions, R^{LPCAs} and R^{SPCAs}, whose indicator functions are $R^{LPCAs}(\boldsymbol{x})$ and $R^{SPCAs}(\boldsymbol{x})$, respectively. The first one refers to the long posterior ciliary arteries and it will be an annular region close to the ciliary body, the second one refers to the short posterior ciliary arteries and it will be a region close to the optic nerve. The flow rate of the blood entering the choroid is computed as follows

$$Q^{in}(t) = \rho^f \int_\Omega s^{SPCAs}(t) R^{SPCAs} + s^{LPCAs}(t) R^{LPCAs} d\Omega,$$

where s^{SPCAs} and s^{LPCAs} are two scalar functions of time. For the sake of simplicity we assume $s^{SPCAs} = s^{LPCAs} = s^{in} f(t)$. We denote by $R^{in}(\boldsymbol{x})$ the indicator function of the inlet region, $R^{in}(\boldsymbol{x}) = R^{SPCAs}(\boldsymbol{x}) + R^{LPCAs}(\boldsymbol{x})$, obtaining

$$Q^{in}(t) = \rho^f |R^{in}| s^{in} f(t),$$

where $|R^{in}|$ denotes the measure of the inlet region.

The blood leaves the choroid through the capillaries region R^{cap}. Another assumption is that the blood exits the choroid at a constant flow rate Q, i.e. blood has lost its pulsatility when it passes through the capillaries

$$Q^{out} = -\rho^f \int_\Omega s^{cap} R^{cap} d\Omega = -\rho^f |R^{cap}| s^{cap},$$

where s^{cap} is a scalar parameter to be computed from the given flow rate

$$s^{cap} = -\frac{Q^{out}}{\rho^f |R^{cap}|}.$$

We assume that the total amount of blood coming in and out of the choroid balances during an entire cardiac cycle

$$\tau Q^{out} + \int_0^\tau Q^{in} = 0$$

we obtain

$$\rho^f \underbrace{\frac{1}{\tau}\int_0^\tau f(t)dt}_{=1} |R^{in}|s^{in} = Q^{out} \rightarrow s^{in} = s^{cap}\frac{|R^{cap}|}{|R^{in}|},$$

where we have required that the function $f(t)$ that contains the information about the pulsatility is normalized over a cardiac cycle of duration τ.

The source/sink function reads as follows

$$s(\boldsymbol{x},t) = \frac{Q}{\rho^f}\left(f(t)\frac{R^{in}(\boldsymbol{x})}{|R^{in}|} - \frac{R^{cap}(\boldsymbol{x})}{|R^{cap}|}\right)$$

where Q is the choroidal flow rate, assumed to be known.

A slightly different option is to prescribe the pressure at ophthalmic artery instead of prescribing the flow rate: if we assume $P^{OA}(t)$ to be known we can compute the flow entering at the inlet region by

$$Q^{in}(t) = \frac{1}{R_{OA}}\frac{1}{|R^{in}|}\int_\Omega (P^{OA}(t) - p(\boldsymbol{x},t))R^{in}(\boldsymbol{x})d\Omega$$

and we choose s accordingly

$$s(\boldsymbol{x},t) = \frac{1}{\rho^f R_{OA}}(P^{OA}(t) - p(\boldsymbol{x},t))\frac{R^{in}(\boldsymbol{x})}{|R^{in}|} - \frac{Q}{\rho^f}\frac{R^{cap}(\boldsymbol{x})}{|R^{cap}|}.$$

This choice of s adds a reaction term on the mass equation and a force term and by integrating this equation on Ω we get:

$$\rho^f b\dot{V}(t) + \rho^f\frac{|\Omega|}{M}\dot{P}(t) + \rho^f\bar{p}_{in} = \rho^f P^{OA}(t) - \rho^f R_{OA}Q,$$

where $\bar{p}_{in}$ is the mean pressure on the inlet region. This second approach has the benefit to provide a value of reference for the pressure.

These two parameters, s and $\boldsymbol{K}$, are particularly important because their role is to take into account all the anatomical complexity that has been neglected. The other parameters of the system do not exhibit such a complex structure and they will be listed below in the numerical section.

5.4.2 A numerical experiment

Here we test the proposed model on a simple case where we study the pore-pressure distribution inside the choroid. The geometry is the one described in Section 5.2.1, but we simulate the choroid alone. For this reason the boundary conditions on the vitreous interface, on the sclera interface and on the ciliary body interface are prescribed arbitrarily and are therefore a rough approximation of the reality. In particular, we prescribed zero displacement on the sclera and ciliary body interfaces, while normal stress was applied at the vitreous interface: $\boldsymbol{\sigma n} = -p_{ext}\boldsymbol{n}$ and homogeneous Neumann boundary conditions for the pressure,

i.e. normal component of the filtration velocity equal to zero. The other coefficients are chosen to be realistic, but the goal of this test is just to check whether the model is able to reproduce certain expected behavior. The inlet region is defined by $R^{in} = R^{SPCAs} \cup R^{LPCAs}$, where both regions are located in outermost half of choroid: $\{\boldsymbol{x} \in \Omega_{Choroid} : 1.1425cm \leq |\boldsymbol{x}| \leq 1.15\text{cm}\}$ and, denoted by θ the angle between a point, the center of the eye and the posterior pole, R_{SPCAs} are the points with $\theta < 10°$ and R_{LPCAs} those with $142° \leq \theta \leq 145°$. The arterioles region, $R^{arterioles}$ is the outer half of the choroid, while the capillaries region, R^{cap}, is the inner one. The anisotropic direction is the longitudinal one. The ophthalmic pressure is given as a function of time where one cardiac cycle has duration of $0.8s$

$$P^{OA}(t) = p_{oa}(\mathbf{1}_{t<0.25s}\frac{0.8\pi}{5}\sin\left(\frac{\pi t}{0.25s}\right) + 0.9).$$

The remaining parameters are summarized in Table 5.1. As far as the discretization is concerned, $P1$ finite elements were used both for the pore-pressure and the displacement and an implicit Euler scheme with time step $dt = 0.015$ was used for time discretization. The mesh is the one depicted in Figure 5.4.

drained Young modulus	E^d	10^5	dyne/cm^2
drained Poisson ratio	ν^d	0.4	-
Biot's coefficient	b	1	-
Biot's modulus	M	10^6	dyne/cm^2
capillaries' permeability	k_{cap}	10^{-10}	cm^4/s/dyne
arterioles' permeability	$k_{arterioles}$	10^{-5}	cm^4/s/dyne
outlet flow	$\|Q\|$	600	μl/min
mean ophtalmic artery pressure	p_{oa}	45	mmHg
resistance	R_{OA}	$4 \cdot 10^4$	dyne s /cm^5
initial pressure	p_{init}	30	mmHg
external pressure	p_{ext}	10	mmHg

Table 5.1: Parameters used for the test of the isolated choroid.

In Figure 5.7 the pore pressure obtained a time $t = 4.785$, i.e. at the end of the diastolic phase of the sixth cardiac cycle. The maximum of the pressure is located in the inlet region because here is where the ophthalmic artery pressure is acting. The minimum of the pressure is located in the innermost layer, especially in the equatorial region, because it is the furthest area with respect to the feeding arteries. A gradient is always visible across the thickness meaning that blood pressure is higher in the arterioles than in the capillaries and that the fluid is going towards the innermost layer. It would be interesting to visualize the filtration velocity, however using a Laplacian formulation the filtration velocity has a really poor regularity and, if one is interested in this quantity, it would be more effective to use a mixed finite element formulation. In Figure 5.8 we observe the pore-pressure on the outer surface of the choroid. There is a clear pressure gradient in the longitudinal direction, which is the anisotropic direction, meaning that blood is moving towards the equator line

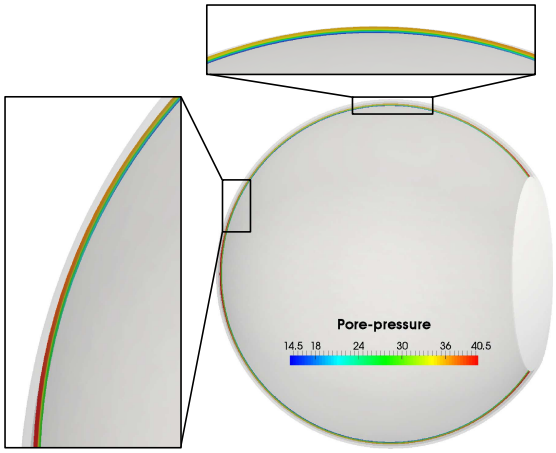

Figure 5.7: Pressure layers at the end of the diastolic phase of the sixth cardiac cycle. Cut with the plane $x = 0$.

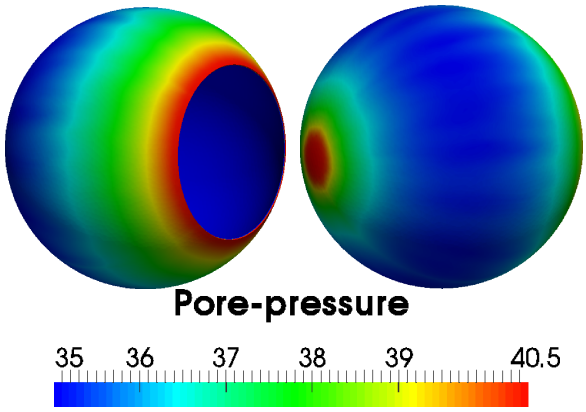

Figure 5.8: View of the pressure [mmHg] on the external surface of the Choroid at the end of the diastolic phase of the sixth cardiac cycle.

trying to reach all the regions of the choroid. The inlet region representing the short posterior ciliary arteries is bringing blood to the posterior part of the tissue while the long posterior ciliary arteries to the anterior part. This behavior is in agreement with what we expected.

5.4.3 Alternative derivation

In this section we derive the equations of the poro-elasticity, following the approach proposed in [CGSMVC10] and then linearizing the result to obtain the Biot's equations. This subsection is not necessary for reading the following sections, but it is useful for the reader not familiar with poro-elasticity to have a better understanding of the role of the different terms and parameters in the Biot's equations. A complete introduction to poro-elasticity can be found, for instance, in [Cou04] or in [CHE14].

5.4.3.1 Main assumptions and definitions

We consider two phases: the solid one representing the external matrix of the tissue and the fluid one representing arterial blood up to the capillaries. We assume that the fluid does not change its density:

$$\rho^f = \rho_0^f \quad \text{(fluid does not change its density)}.$$

The amount of fluid present in the system may change with time. Let m be the increase in fluid mass per unit of volume [$\mathrm{kg\,m^{-3}}$]. Its expression is derived by comparing the current and the reference state:

$$\begin{aligned} \text{current mass of fluid} &= \rho^f J\phi \\ \text{initial mass of fluid} &= \rho^f \phi_0 \\ m &= \rho^f (J\phi - \phi_0), \end{aligned}$$

where ϕ and ϕ_0 are the actual and the reference porosity (i.e. the local fraction of volume occupied by the fluid w.r.t to the total volume), $\boldsymbol{u}$ is the displacement field of the homogenized system and $J = \det \boldsymbol{F}$, $\boldsymbol{F} = \boldsymbol{I} + \hat{\nabla}\boldsymbol{u}$ represents the change of volume and the deformation gradient, respectively.

We recall here the expression for the time-derivative of the increase in fluid mass as it will be useful in the following

$$\dot{m} = \rho^f (\dot{J\phi}) = \rho^f (J\dot{\phi} + \dot{J}\phi),$$

by further manipulations and by using $\dot{J} = J\nabla \cdot \dot{\boldsymbol{u}}$ we get:

$$\frac{\dot{m}}{\rho^f J} = \dot{\phi} + \phi \nabla \cdot \dot{\boldsymbol{u}}. \tag{5.3}$$

It is also important to define the perfusion velocity

$$\boldsymbol{w} = \phi(\boldsymbol{v}^f - \dot{\boldsymbol{u}}), \tag{5.4}$$

where $\boldsymbol{v^f}$ is the fluid velocity. This quantity represents the relative velocity of the fluid with respect to the tissue, weighted by the porosity.

5.4.3.2 Mass conservation

We proceed in the derivation by writing the balance of mass for the two phases. First, we assume that no mass is added or removed from the skeleton:

$$\rho^s(1-\phi)J = \rho_0^s(1-\phi_0).$$

Second, we write the conservation of the fluid mass in the following way

$$\rho^f \frac{\partial}{\partial t}\phi + \rho^f \nabla \cdot (\phi \boldsymbol{v}^f) = \rho^f s,$$

where s is a volumetric source of mass.

Some manipulations are needed to obtain a more useful form. The fluid velocity is replaced by using the definition of perfusion velocity (5.4) obtaining:

$$\rho^f \frac{\partial}{\partial t}\phi + \rho^f \nabla \cdot (\phi \dot{\boldsymbol{u}}) + \rho^f \nabla \cdot \boldsymbol{w} = \rho^f s,$$

after expanding the gradient of a product between a scalar and a vector we get:

$$\rho^f \frac{\partial}{\partial t}\phi + \rho^f \nabla\phi \cdot \dot{\boldsymbol{u}} + \rho^f \phi \nabla \cdot \dot{\boldsymbol{u}} + \rho^f \nabla \cdot \boldsymbol{w} = \rho^f s.$$

The increase in fluid mass appears in the equation after using (5.3)

$$\rho^f \frac{\partial}{\partial t}\phi + \rho^f \nabla\phi \cdot \dot{\boldsymbol{u}} + \frac{\dot{m}}{J} - \rho^f \dot{\phi} + \rho^f \nabla \cdot \boldsymbol{w} = \rho^f s.$$

After the simplification of the first, second and fourth term, we obtain the final expression for the fluid mass conservation:

$$\frac{\dot{m}}{J} + \rho^f \nabla \cdot \boldsymbol{w} = \rho^f s. \tag{5.5}$$

REMARK 3 (ON THE BALANCE OF FLUID MASS)
It is interesting to integrate (5.5) over a certain reference domain V and to apply the divergence theorem

$$\int_V \frac{\dot{m}}{J} + \rho^f \int_{\partial V} \nabla \boldsymbol{w} \cdot \boldsymbol{n} = \rho^f \int_V s$$

The first term represents the increase in fluid mass, the second one represents the

flow coming in (or out) through the boundary of V while the right hand side is a source (or sink) of mass.

If, for example, there is a positive source ($s > 0$) and m is forced to be 0, there will be a flow coming out of V. On the other hand, if the fluid cannot exit the domain through its boundaries it has to accumulate inside and m will increase.

5.4.3.3 Second Piola-Kirchhoff tensor

In order to derive an equation for the balance of the linear momentum, we first define a free energy function. By means of its derivative, we are able to compute the second Piola-Kirchhoff.

For the definition of the free energy function ψ we again follow [CGSMVC10]

$$\psi = W^{el}(\boldsymbol{e}) - Mb\frac{m}{\rho^f}(J-1)f(J) + \frac{1}{2}M\left(\frac{m}{\rho^f}\right)^2 f(J),$$

where $\boldsymbol{e} = \frac{\boldsymbol{C}-\boldsymbol{I}}{2} = \frac{\boldsymbol{F}^T\boldsymbol{F}-\boldsymbol{I}}{2}$ is the strain tensor, b is the Biot's coefficient and $f(J)$ is a function of J still to be defined. The energy ψ is a sum of an elastic energy W^{el} and two other terms related to the increase in fluid mass m.

The second Piola-Kirchhoff tensor $\boldsymbol{\Sigma}$ is defined as the derivative of the free energy w.r.t. $\boldsymbol{e} = \frac{\boldsymbol{C}-\boldsymbol{I}}{2}$, keeping in mind that $\partial_{\boldsymbol{e}} J = J\boldsymbol{C}^{-1}$, we get

$$\boldsymbol{\Sigma} = \partial_e W^{el}(\boldsymbol{e}) - Mb\frac{m}{\rho^f}(f(J) + (J-1)f'(J))J\boldsymbol{C}^{-1} + \frac{1}{2}M\left(\frac{m}{\rho^f}\right)^2 f'(J)J\boldsymbol{C}^{-1}.$$

In order to remove the increase of fluid mass from the expression of $\boldsymbol{\Sigma}$ and to write it in terms of the pore-pressure, i.e. the pressure of the fluid inside the solid structure, we give a constitutive relationship for the enthalpy

$$g_m = 1/\rho^f(p - p_0),$$

where p is the pore-pressure and p_0 is a reference value. Since the free enthalpy is defined as the derivative of the free energy with respect to the increase in fluid mass we obtain the following result

$$\partial_m \psi = -Mb\frac{1}{\rho^f}(J-1)f(J) + mM\left(\frac{1}{\rho^f}\right)^2 f(J) = 1/\rho^f(p - p_0)$$

that, after a simple manipulation, simplifies to

$$p - p_0 = Mf(J)\left(b(1-J) + \frac{m}{\rho^f}\right). \tag{5.6}$$

The increase in fluid mass is then rewritten as a function of p

$$\frac{m}{\rho^f} = \frac{1}{Mf(J)}(p - p_0) - b(1-J). \tag{5.7}$$

By using equation (5.7) we get the following expression for the second Piola tensor

$$\boldsymbol{\Sigma} = \partial_e W^{el}(\boldsymbol{e}) - Mb^2(f(J) + \frac{1}{2}(J-1)f'(J))(J-1)J\boldsymbol{C}^{-1} - b(p-p_0)J\boldsymbol{C}^{-1} + \frac{1}{2}(p-p_0)^2\frac{f'}{Mf^2}J\boldsymbol{C}^{-1}$$

The only terms still to be specified in the second Piola-Kirchhoff tensor are the elastic potential and the function $f(J)$. Several choices of the elastic potential are possible. We keep following [CGSMVC10] and we choose the Ciarlet-Geymonat energy

$$W^{el} = k_1(J_1 - 3) + k_2(J_2 - 3) + K(J - 1 - \ln(J))$$

where $J_1 = \mathrm{tr}\boldsymbol{C}J^{-2/3}$ and $J_2 = \frac{1}{2}((\mathrm{tr}(\boldsymbol{C}))^2 - \mathrm{tr}(\boldsymbol{C}^2))J^{-4/3}$ are the first and the second strain invariants. The role of the material parameters k_1, k_2 and K will be clear after the linearization and, for the same reason, this choice of elastic potential is not crucial.

We compute the derivative of the elastic energy with respect to $\boldsymbol{e}$:

$$\partial_e W^{el} = k_1\partial_e J_1 + k_2\partial_e J_2 + K(J-1)\boldsymbol{C}^{-1}$$

Derivative of the first invariant:

$$\begin{aligned}
\partial_e J_1 &= \partial_e \mathrm{tr}\boldsymbol{C}J^{-2/3} \\
&= J^{-2/3}\partial_e \mathrm{tr}\boldsymbol{C} - \frac{2}{3}\mathrm{tr}\boldsymbol{C}J^{-2/3}\boldsymbol{C}^{-1} \\
&= J^{-2/3}\partial_e \mathrm{tr}(2\boldsymbol{e} - \boldsymbol{I}) - \frac{2}{3}\mathrm{tr}\boldsymbol{C}J^{-2/3}\boldsymbol{C}^{-1} \\
&= 2J^{-2/3}\boldsymbol{I} - \frac{2}{3}\mathrm{tr}\boldsymbol{C}J^{-2/3}\boldsymbol{C}^{-1}
\end{aligned}$$

Derivative of the second invariant:

$$\begin{aligned}
\partial_e J_2 &= \partial_e \frac{1}{2}((\mathrm{tr}(\boldsymbol{C}))^2 - \mathrm{tr}(\boldsymbol{C}^2))J^{-4/3} \\
&= \frac{1}{2}J^{-4/3}\partial_e((\mathrm{tr}(\boldsymbol{C}))^2 - \mathrm{tr}(\boldsymbol{C}^2)) - \frac{2}{3}((\mathrm{tr}(\boldsymbol{C}))^2 - \mathrm{tr}(\boldsymbol{C}^2))J^{-4/3}\boldsymbol{C}^{-1} \\
&= \frac{1}{2}J^{-4/3}(4\mathrm{tr}(\boldsymbol{C})\boldsymbol{I} - 4\boldsymbol{C}) - \frac{2}{3}((\mathrm{tr}(\boldsymbol{C}))^2 - \mathrm{tr}(\boldsymbol{C}^2))J^{-4/3}\boldsymbol{C}^{-1}.
\end{aligned}$$

We focus the attention on the function $f(J)$. After inserting the derivative of the elastic potential into the expression of $\boldsymbol{\Sigma}$ we get

$$\begin{aligned}
\boldsymbol{\Sigma} =& k_1\partial_e J_1 + k_2\partial_e J_2 + (K - Mb^2J(f(J) + \frac{1}{2}(J-1)f'(J)))(J-1)\boldsymbol{C}^{-1} \\
&+ (-b(p-p_0)J + \frac{1}{2}(p-p_0)^2\frac{f'}{Mf^2}J)\boldsymbol{C}^{-1}.
\end{aligned}$$

In the incompressible limit, the bulk modulus K tends to infinity and therefore we also need M to grow in order to balance K. For this reason we need that the term

multiplying M remains greater than a given positive constant for all J. Following [CGSMVC10], we assume that

$$J(f(J) + 1/2(J-1)f'(J)) = 1 \quad \forall J, \tag{5.8}$$

obtaining

$$\boldsymbol{\Sigma} = k_1\partial_e J_1 + k_2\partial_e J_2 + (K - Mb^2)(J-1)\boldsymbol{C}^{-1} - b(p-p_0)J\boldsymbol{C}^{-1} + \frac{1}{2}(p-p_0)^2\frac{f'}{Mf^2}J\boldsymbol{C}^{-1}.$$

We take this final expression as a starting point for the linearization.

5.4.3.4 Linearization

The goal of this subsection is to linearize $\boldsymbol{\Sigma}$ in the assumption of small strain. It is useful to recall some simple linearization:

$$\boldsymbol{C}^{-1} = (\boldsymbol{I} + 2\boldsymbol{e})^{-1} \sim \boldsymbol{I} - 2\boldsymbol{e}$$

$$J\boldsymbol{C}^{-1} \sim (1 + \operatorname{tr}(\boldsymbol{e}))(\boldsymbol{I} - 2\boldsymbol{e}) \sim \boldsymbol{I} + \operatorname{tr}(\boldsymbol{e})\boldsymbol{I} - 2\boldsymbol{e}.$$

The expression for f is obtained by integrating Eq.(5.8)

$$f = 2\frac{J - 1 - \ln J}{(J-1)^2} \quad f' = 2\frac{1 - J^2 + 2J\ln J}{J(J-1)^3}$$

and also f'/f^2

$$f'/f^2 = \frac{(1 - J^2 + 2J\ln J)(J-1)}{2J(J - 1 - \ln J)^2}$$

It is useful to do a Taylor development of f'/f^2

$$f'/f^2 \sim -\frac{7}{9} + \frac{J}{9} - \frac{4}{45}(J-1)^2$$

Linearizing the result with respect to $(J-1)$, we get

$$f'/f^2 \sim -\frac{2}{3} + \frac{(J-1)}{9}.$$

We replace all the terms in $\boldsymbol{\Sigma}$ except the first two:

$$\begin{aligned}\boldsymbol{\Sigma} \sim & k_1\partial_e J_1 + k_2\partial_e J_2 + (K - Mb^2)\operatorname{tr}(\boldsymbol{e})\boldsymbol{I} \\ & - b(p-p_0)((1 + \operatorname{tr}(\boldsymbol{e}))\boldsymbol{I} - 2\boldsymbol{e}) \\ & - \frac{1}{2M}(p-p_0)^2\left(\frac{2}{3}\boldsymbol{I} + \frac{5}{9}\operatorname{tr}(\boldsymbol{e})\boldsymbol{I} - \frac{4}{3}\boldsymbol{e}\right).\end{aligned}$$

Since $\mathrm{tr}(\boldsymbol{e}) \ll 1$, the expression simplifies to

$$\boldsymbol{\Sigma} \sim k_1 \partial_e J_1 + k_2 \partial_e J_2 + (K - Mb^2)\,\mathrm{tr}(\boldsymbol{e})\boldsymbol{I} - (b(p-p_0) + \frac{1}{3M}(p-p_0)^2)(\boldsymbol{I} - 2\boldsymbol{e})$$

By assuming that $\frac{p-p_0}{3M} \ll b$, meaning that we are close to the incompressible limit ($M \to +\infty$), we obtain:

$$\boldsymbol{\Sigma} \sim k_1 \partial_e J_1 + k_2 \partial_e J_2 + (K - Mb^2)\,\mathrm{tr}(\boldsymbol{e})\boldsymbol{I} - b(p-p_0)(\boldsymbol{I} - 2\boldsymbol{e}).$$

We conclude the linearization by considering the elastic terms:

$$\begin{aligned}
\partial_{\boldsymbol{e}} J_1 &= 2J^{-2/3}\boldsymbol{I} - \frac{2}{3}\mathrm{tr}\boldsymbol{C}J^{-2/3}\boldsymbol{C}^{-1} \\
&\sim (2 - \frac{4}{3}\,\mathrm{tr}(\boldsymbol{e}))\boldsymbol{I} - \frac{2}{3}(3 + 2\,\mathrm{tr}(\boldsymbol{e}))(1 - \frac{2}{3}\,\mathrm{tr}(\boldsymbol{e}))(\boldsymbol{I} - 2\boldsymbol{e}) \\
&\sim (2 - \frac{4}{3}\,\mathrm{tr}(\boldsymbol{e}))\boldsymbol{I} - 2(\boldsymbol{I} - 2\boldsymbol{e}) \\
&\sim -\frac{4}{3}\,\mathrm{tr}(\boldsymbol{e})\boldsymbol{I} + 4\boldsymbol{e},
\end{aligned}$$

$$\begin{aligned}
\partial_e J_2 &= J^{-4/3}(2\mathrm{tr}(\boldsymbol{C})\boldsymbol{I} - 2\boldsymbol{C}) - \frac{2}{3}((\mathrm{tr}(\boldsymbol{C}))^2 - \mathrm{tr}(\boldsymbol{C}^2))J^{-4/3}\boldsymbol{C}^{-1} \\
&\sim 2(1 - \frac{4}{3}\,\mathrm{tr}(\boldsymbol{e}))(2\boldsymbol{I} + 2\,\mathrm{tr}(\boldsymbol{e})\boldsymbol{I} - 2\boldsymbol{e}) - \frac{2}{3}((3 + 2\,\mathrm{tr}(\boldsymbol{e}))^2 - \mathrm{tr}(\boldsymbol{I} + 4\boldsymbol{e}))(1 - \frac{4}{3}\,\mathrm{tr}(\boldsymbol{e}))(\boldsymbol{I} - 2\boldsymbol{e}) \\
&\sim 4(\boldsymbol{I} + \mathrm{tr}(\boldsymbol{e})\boldsymbol{I} - \boldsymbol{e}) - \frac{16}{3}\,\mathrm{tr}(\boldsymbol{e})\boldsymbol{I} - \frac{2}{3}(6 + 8\,\mathrm{tr}(\boldsymbol{e}))(1 - \frac{4}{3}\,\mathrm{tr}(\boldsymbol{e}))(\boldsymbol{I} - 2\boldsymbol{e}) \\
&\sim 4\boldsymbol{I} + 4\,\mathrm{tr}(\boldsymbol{e})\boldsymbol{I} - 4\boldsymbol{e} - \frac{16}{3}\,\mathrm{tr}(\boldsymbol{e})\boldsymbol{I} + 8\boldsymbol{e} - 4\boldsymbol{I} \\
&\sim -\frac{4}{3}\,\mathrm{tr}(\boldsymbol{e})\boldsymbol{I} + 4\boldsymbol{e}.
\end{aligned}$$

We can finally sum up the Cauchy stress tensor

$$\boldsymbol{\Sigma} \sim \boldsymbol{\sigma} = (4(k_1+k_2) + 2b(p-p_0))\boldsymbol{e} + (K - Mb^2 - \frac{4}{3}(k_1+k_2))\,\mathrm{tr}(\boldsymbol{e})\boldsymbol{I} - b(p-p_0)\boldsymbol{I}.$$

We make the final assumption $b(p-p_0) \ll 2(k_1+k_2)$ and we conclude:

$$\boldsymbol{\Sigma} \sim \boldsymbol{\sigma} = 4(k_1+k_2)\boldsymbol{e} + (K - Mb^2 - \frac{4}{3}(k_1+k_2))\,\mathrm{tr}(\boldsymbol{e})\boldsymbol{I} - b(p-p_0)\boldsymbol{I}. \tag{5.9}$$

The first equation of linear poroelasticity can be obtained by considering the balance of linear momentum, after having neglected the inertia, $\nabla \cdot \sigma = \boldsymbol{f}$, where $\boldsymbol{f}$ are the external body forces and by setting the reference pressure p_0 equal to zero. The second one is obtained by linearizing and injecting Eq.(5.7) into Eq.(5.5) and by using Darcy's law to relate the filtration velocity to the pore-pressure.

5.4.3.5 Drained and Undrained parameters

The Cauchy stress tensor in Eq.(5.9) has the following structure:

$$\boldsymbol{\sigma} = \boldsymbol{\sigma}^{el}(\boldsymbol{e}) - b(p - p_0)\boldsymbol{I}.$$

In order to better understand the role of the different parameters we first consider the case of the system evolutions where there is no change of fluid mass, *i.e.* $m = 0$. This case is called the *undrained* test.

In such a case we have, from Eq.(5.6), that

$$p - p_0 = -Mb\,\mathrm{tr}(\boldsymbol{e}) \quad \text{(undrained case)}.$$

The expression of the Cauchy stress tensor changes accordingly:

$$\boldsymbol{\sigma}_{undrained} = 4(k_1 + k_2)\boldsymbol{e} + (K - \frac{4}{3}(k_1 + k_2))\,\mathrm{tr}(\boldsymbol{e})\boldsymbol{I}.$$

In the undrained processes the structure of the stress tensor is the same as in the case of the elastic materials. However, those coefficients (K, k_1, k_2) are not the coefficients of the solid matrix. They are the coefficients describing the system made of solid matrix and of the interstitial fluid in the particular situation where the fluid is blocked into the pores and cannot exit. Think, for instance, about a sponge wrapped with a film that blocks the water from coming in or out.

In some cases it is useful to work with Poisson ratio and Young modulus instead of working with (K, k_1, k_2). By comparing the previous expression with

$$\boldsymbol{\sigma}_{undrained} = \frac{E^u}{1 + \nu^u}\boldsymbol{e} + \frac{E^u\nu^u}{(1 + \nu^u)(1 - 2\nu^u)}\,\mathrm{tr}(\boldsymbol{e})\boldsymbol{I}$$

we obtain the following relationships $(G = 2(k_1 + k_2))$

$$\begin{cases} \nu^u &= \frac{3K-4(k_1+k_2)}{2(3K+2(k_1+k_2)} = \frac{3K-2G}{2(3K+G)} \\ E^u &= 2(k_1 + k_2)\frac{9K}{3K+2(k_1+k_2)} = \frac{9KG}{3K+G}. \end{cases}$$

The superscript ^{u} indicates that these parameters measure the elastic properties of the entire system in the undrained state. We mention the fact that, at this level, it is possible to consider the incompressible limit $(K \to \infty)$ obtaining

$$\begin{cases} \nu^u = \frac{1}{2} \quad \text{(incompressible limit)} \\ E^u = 6(k_1 + k_2) = 3G \quad \text{(incompressible limit)}. \end{cases}$$

We can also consider the *drained* case. Which is the case of the processes where the fluid is maintained at a given constant pressure $p = \bar{p} + p_0$. In such a case the fluid can enter/exit the domain freely from the boundaries to adjust for this pressure. If we make this experiment using constant pressure equal to the reference

pressure ($\bar{p} = p - p_0 = 0$) we have

$$\boldsymbol{\sigma}_{drained} = 4(k_1 + k_2)\boldsymbol{e} + (K - Mb^2 - \frac{4}{3}(k_1 + k_2))\,\mathrm{tr}(\boldsymbol{e})\boldsymbol{I}.$$

We denote by K^d the drained bulk modulus:

$$K^d = K - Mb^2.$$

At the incompressible limit both K and M increases and we assume that K^d remains finite.

As for the undrained case we define some coefficients (E^d, ν^d) based on K^d instead of K

$$\begin{cases} \nu^d & = \frac{3K^d - 4(k_1+k_2)}{2(3K^d + 2(k_1+k_2))} = \frac{3K^d - 2G}{2(3K^d + G)} \\ E^d & = 2(k_1 + k_2)\frac{9K^d}{3K^d + 2(k_1+k_2)} = \frac{9K^d G}{3K^d + G} \end{cases}$$

In conclusion of this section we can state that: if the fluid is completely isolated the solid incompressibility is inherited by the poro-elastic medium. The coefficients (E^u, ν^u) that describe this system are not those of the skeleton because they are the combination of the fluid and the solid responses. However, we can treat this particular material as an incompressible elastic solid. In the case in which the system is not isolated the material is no longer incompressible because the total volume is the sum of the fluid volume (which can change) and that of the solid matrix. This can be seen in the equations by considering the drained test where the fluid is completely free to move in and out of the domain. In such particular case we still obtain an elastic model (pore-pressure has again disappeared), but the bulk modulus of the solid has been greatly reduced and now it is equal to K^d. For all the other situations in which the fluid can change its pressure, but also vary its total mass, the result is in between.

5.5 Choroid coupled with the vitreous

In this section a test case with two compartments, the vitreous and the choroid, is presented. For the modelling of the choroid compartment we refer to the previous section, while for the dynamics of the vitreous we use the Stokes equations

$$\begin{cases} \partial_t \boldsymbol{v} - \nabla \cdot \boldsymbol{\sigma}^V = 0 & \text{in } \Omega_V \\ \nabla \cdot \boldsymbol{v} = 0 & \text{in } \Omega_V, \end{cases}$$

where $\boldsymbol{v}$ and p^V are the velocity and the pressure of the fluid inside the vitreous, $\sigma^V(\boldsymbol{v}, p^V) = \nu(\nabla \boldsymbol{v} + \nabla \boldsymbol{v}^T) - p^V \boldsymbol{I}$ is the stress tensor and ν is the viscosity of the fluid.

5.5.1 Coupling scheme

At the interface between the two domains, Γ_{V-Ch}, the continuity of the velocity and of the stresses is imposed

$$\begin{aligned}
&\dot{\boldsymbol{u}} = \boldsymbol{v} \quad \text{on } \Gamma_{V-Ch} \\
&\boldsymbol{\sigma}^{el}(\boldsymbol{u})\boldsymbol{n} - bp\boldsymbol{n} + \boldsymbol{\sigma}(\boldsymbol{v}, p^V)\boldsymbol{n} = 0 \quad \text{on } \Gamma_{V-Ch},
\end{aligned}$$

where $\boldsymbol{n}$ is the normal unit vector. The two problems are solved separately and the coupling is enforced by means of fixed point iterations with Aitken acceleration. In particular, at the $(k+1)$-th iteration we use the following Dirichlet-Neumann scheme. First, the Stokes problem in Ω_V is solved using the choroid velocity of the previous iteration as a Dirichlet datum

$$\begin{cases}
\partial_t \boldsymbol{v}_{k+1} - \nabla \cdot \boldsymbol{\sigma}^V(\boldsymbol{v}_{k+1}, p^V_{k+1}) = 0 & \text{in } \Omega_V \\
\nabla \cdot \boldsymbol{v}_{k+1} = 0 & \text{in } \Omega_V, \\
\boldsymbol{v}_{k+1} = \dot{\boldsymbol{u}}_k & \text{on } \Gamma_{V-Ch},
\end{cases}$$

then the stress $\boldsymbol{\sigma}^V(\boldsymbol{v}_{k+1}, p^V_{k+1})\boldsymbol{n}$ is used as a Neumann datum for the poro-elasticity problem

$$\begin{cases}
\nabla \cdot \boldsymbol{\sigma}^{el}(\boldsymbol{u}_{k+1}) - b\nabla p_{k+1} = 0 & \text{in } \Omega_{Ch} \\
\frac{1}{M}\partial_t p_{k+1} + b\nabla \partial_t \boldsymbol{u}_{k+1} - \nabla \cdot \boldsymbol{K}\nabla p_{k+1} = s & \text{in } \Omega_{Ch} \\
\boldsymbol{\sigma}^{el}(\boldsymbol{u}_{k+1})\boldsymbol{n} - bp_{k+1}\boldsymbol{n} = -\boldsymbol{\sigma}^V(\boldsymbol{v}_{k+1}, p^V_{k+1})\boldsymbol{n} & \text{on } \Gamma_{V-Ch}.
\end{cases}$$

With the Dirichlet-Neumann scheme we cannot impose a given Dirichlet datum on $\Gamma^V = \partial\Omega_V \setminus \Gamma_{V-Ch}$ without violating the incompressibility constraint. Assigning the velocity on Γ^V could be useful, especially in view of the coupling with the other compartments, we therefore considered also other coupling schemes. Neumann-Dirichlet scheme is not a feasible option because the fixed point scheme is not convergent and even by using the Aitken acceleration the number of iterations is greatly increased. For this reason, we are currently investigating the possibility of using a Robin-Robin scheme for the coupling with also the option of using an explicit coupling scheme as done in [FGS14].

5.5.2 Interpolation

As mentioned in the geometry section, we use non-conform meshes for different compartments (see Figure 5.9 where the two surface meshes of the interface Γ_{V-Ch} are depicted). One reason for this is to retain the possibility of remeshing independently the different compartments. A second reason is that, for example at the choroid-ciliary body interface, there is a triangular surface mesh on one side (the ciliary body side) and, since we use prisms, a quadrangular one on the other side (the choroid side). In order to handle this case we could introduce a layer of

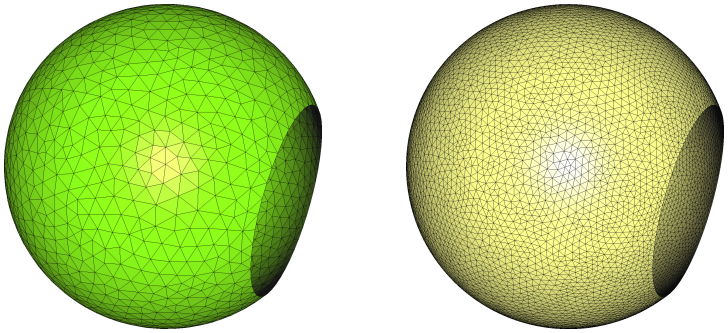

Figure 5.9: Interface Vitreous-Choroid, coarser discretization for the vitreous side (left panel) and a more refined mesh for the choroid side (right panel). An example of non-conform discretizations of the interface between two domains.

pyramids in the ciliary body to connect prisms and tetrahedra, but this raises many difficulties for the automatic mesh generator and the discretization. On the other hand, the drawback is that we have to exchange data defined on different meshes. We use an interpolator to evaluate finite-element functions on a different surface mesh. Let $V_{h_i}(\Gamma)$, with $i = 1, 2$, be the finite element space of size N_{h_i} associated with the surface mesh τ_{h_i}. Let $f_1 \in V_{h_1}(\Gamma)$ be an approximation of a certain function $f : \Gamma \to \mathbb{R}$. We construct a finite-element approximation in $V_{h_2}(\Gamma)$ of f starting from f_1 in the following way:

$$f_2 \in V_{h_2}(\Gamma) : f_2(\boldsymbol{x}) = \sum_{i=1}^{N_{h_2}} f_{2,i}\phi_i(\boldsymbol{x}) \quad \forall \boldsymbol{x} \in \tau_{h_2}, \quad f_{2,i} = f_2(\boldsymbol{x}_i) = f_1(\boldsymbol{p}_i),$$

where ϕ_j are the basis functions of $V_{h_2}(\Gamma)$, $\boldsymbol{x}_j$ are the points associated with the degrees of freedom of V_{h_2} and $\boldsymbol{p}_j$ are the projections of these points on the other mesh τ_{h_1}. By introducing the expression of f_1 we have

$$f_{2,i} = f_1(\boldsymbol{p}_i) = \sum_{j=1}^{N_{h_1}} f_{1,j}\psi_j(\boldsymbol{p}_i),$$

where ψ_j are the basis functions of $V_{h_1}(\Gamma)$. By defining an interpolation matrix $\mathbf{\Pi}$, we finally obtain

$$f_{2,i} = \Pi_{i,j} f_{1,j}, \quad \Pi_{i,j} = \psi_j(\boldsymbol{p}_i).$$

We remark that, even when using conformal meshes, the same interpolation matrix can be used to handle non-conform discretizations. With this approach it is now possible to assign the time-derivative of the choroid displacement as a Dirichlet datum for the vitreous compartment. But to assign the vitreous stress as a Neumann datum to the choroid we need a further step. The stress of the fluid is computed directly from the weak formulation and is obtained in the form $\boldsymbol{r}^V = \{r_i\} = \int_{\Gamma_{V-Ch}} \boldsymbol{\sigma}^V \boldsymbol{n} \cdot \phi_i^V \, d\Gamma$, where ϕ_i^V are the basis functions of the finite

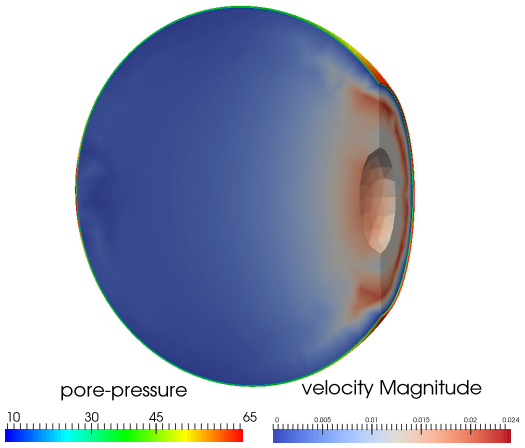

Figure 5.10: Velocity magnitude, cm/s of the fluid in the vitreous and pore-pressure, mmHg, during the systolic peak at the beginning of the fourth cardiac cycle.

element space of the vitreous domain. If the same mesh and the same discretization were used at the interface, this quantity could be directly added to the right hand side of the poro-elasticity linear system, but in our case we have to correctly perform the interpolation. We follow [DFGQ16] and we reconstruct the weak form of the stress on the choroid mesh as $\boldsymbol{r}^{Ch} = \boldsymbol{M}_{Ch}\boldsymbol{\Pi}_{V2Ch}\boldsymbol{M}_V^{-1}\boldsymbol{r}^V$, where $\boldsymbol{M}_{Ch}$ and $\boldsymbol{M}_V$ are the interface finite-element mass matrices of the choroid and of the vitreous, respectively and $\boldsymbol{\Pi}_{V2Ch}$ is the interpolation matrix from the finite-element space of the vitreous $V_V(\Gamma_{V-Ch})$ to the one of the choroid $V_{Ch}(\Gamma_{V-Ch})$. In this way the interpolation is done on the finite-element representation of the stress and not on its weak representation. Another option, following [FLLT98], would be to compute $\boldsymbol{r}^{Ch}$ as $\boldsymbol{r}^{Ch} = \boldsymbol{\Pi}_{Ch2V}^T\boldsymbol{r}^V$, where $\boldsymbol{\Pi}_{Ch2V}$ is the interpolation matrix from $V_{Ch}(\Gamma_{V-Ch})$ to $V_V(\Gamma_{V-Ch})$.

5.5.3 Numerical results

For the numerical experiment we assign Neumann boundary condition on Γ^V: $\boldsymbol{\sigma}^V(\boldsymbol{v}, \boldsymbol{p}^V)\boldsymbol{n} = -22000\text{dyne/cm}^2 \approx -16.5\text{mmHg}$ and we set the vitreous viscosity to $\nu = 0.004$ cm^2/s. The boundary conditions and the parameters of the choroid are the same as in the test case of Section 5.4.2. In Figure 5.10 a snapshot of the solution during the systolic peak is displayed. The choroid is not very visible because it is extremely thin, but we observe a maximum of the pressure in the regions where the posterior ciliary arteries enter the choroid and a minimum in the equatorial region and in the inner layer. In the vitreous we observe the maximum of the velocity close to the boundary Γ^V because the choroid is inflating (see Figure 5.11 where the volume of the choroid is displayed with respect to time) and the fluid in the vitreous is forced to exit from Γ^V. Of course this behavior is not realistic, but this is the

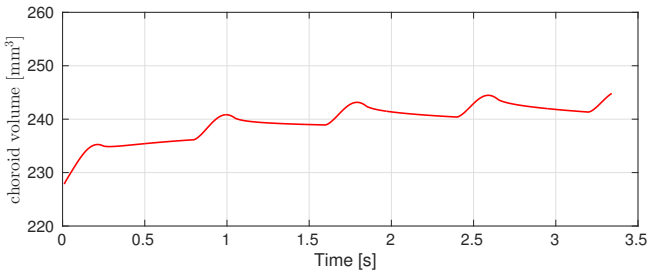

Figure 5.11: Volume of the choroid with respect to time. Blood gradually fills the choroid during the cardiac cycles. A peak corresponding to the systolic phase is present at the beginning of each cardiac cycle.

effect of the boundary conditions we have imposed. On one hand, the choroid cannot inflate in the direction of the sclera or in that of the ciliary body because we have imposed zero displacement. On the other hand, we cannot impose a velocity on Γ^V without violating the incompressibility constraint. If, as explained in the coupling section above, we change the coupling scheme and we enforce no-slip condition on Γ^V then the choroid could not inflate anymore. In such a case, we set to zero the derivative of the choroid volume in Eq.(5.2) obtaining

$$\rho^f \frac{|\Omega|}{M} \dot{P}(t) = S(t)$$

and we can see that this would cause a not realistic increase in the pore-pressure. This suggests that boundary conditions of this two-compartments model play a crucial role in the dynamics of the system and to obtain realistic results better boundary conditions should be imposed. However, the data to be assigned on Γ^V and on $\Gamma^{Ch} = \partial\Omega \setminus \Gamma_{V-Ch}$ are difficult to choose and it seems more natural to consider the system with all the compartments where the missing boundary conditions will be easier to assign.

5.6 Conclusions, on-going and future work

In this chapter we have introduced a global model for the description of fluid-dynamics and mechanics in the eye. We built a simplified, but realistic geometry for the simulations and we have introduced our modelling choices. Preliminary results concerning the modelling of the flow in the anterior cavity are compatible with state of the art models for this compartment and reproduce different recirculation cells depending on the direction of the gravity force. A poro-elastic model for the choroid flow able to take into account the layered structure and the presence of short and long posterior ciliary arteries feeding the tissue has been presented and numerical simulations show that the pore-pressure has a realistic structure exhibiting gradients both across the thickness, meaning that the pressure in the arterioles is higher than in the capillaries and that blood is reaching the innermost layer, and in the

longitudinal direction implying that blood in the arterioles is travelling towards the equator of the eye to reach every region of the choroid. Finally, we have coupled the choroid with a simple Newtonian model of the vitreous. Results show that the choroid is inflating following the pulsatility, however more accurate boundary condition are needed. The use of non-compatible meshes for the different compartments is handled via an interpolator and allows us for independent refinement of the different meshes and to use different elements as it is the case for the ciliary body-choroid interface where we are going to use a triangular mesh for the ciliary body side and a quadrilateral mesh for the choroid.

Following the plan discussed in Section 5.2.2 we are currently working on adding the lens, the ciliary body, the zonules and iris to the model as one linear elastic compartment with different material properties depending on the region. Enforcing the coupling between three different compartments is not trivial and an appropriate domain decomposition scheme is the current object of our study. In a later stage we will add the corneo-scleral shell and the anterior cavity and perform simulations of the eye mechanics with five different compartments. Other interesting developments would be to test visco-elastic models for the sclera and/or for the vitreous. Finally, we plan to apply the reduced order modelling technique that we have devised and that will be presented in the next chapter to the eye-simulations. The idea is that, depending on the goal of the numerical experiment, we might not be interested in a particular compartment, namely the vitreous when interested in simulating the pressure in the anterior chamber. However, it is clear that such compartment play a crucial role and cannot be completed excluded from the model. The idea developed in the next chapter is to replace such a compartment by a reduced representation of the corresponding Steklov-Poincaré operator.

Chapter 6

A Reduced Order representation of the Poincaré-Steklov operator: an application to coupled multi-physics problems

---

This chaper is based on [AL17]

In this chaper a model reduction method applied to coupled multi-physics systems is investigated. The case in which a system of interest interacts with an external system is considered. An approximation of the Poincaré-Steklov operator is computed by simulating, in an offline phase, the external problem when the inputs are the Laplace-Beltrami eigenfunctions defined at the interface. In the online phase, only the reduced representation of the operator is needed to account for the influence of the external problem on the main system. An online basis enrichment is proposed in order to guarantee a precise reduced-order computation. Several test-cases are proposed on different fluid-structure couplings.

Contents

6.1 Introduction

The present work deals with the study of a Reduced-Order Method to approximate the solution of coupled multi-physics systems. In particular, we investigate the case in which one system of interest, described by a possibly non-linear Partial Differential Equation (PDE) interacts with one (or more) other systems through its boundaries. Numerous applications in science and engineering are characterized by different compartments in interaction, think for instance to thermal-fluid-structural or electro-mechanical-fluid couplings. In several cases, one is not interested in the solution to all the systems, but only in the solution of a "main" system, that will be denoted by $\mathcal{P}_1$. The objective is thus to be able to compute precisely the solution of this system (by using a full-order classical method) but to reduce the computational costs associated to the solution of the systems in interaction with it (denoted as $\mathcal{P}_2$). This results in a significant speed up of the problem simulation, in the case in which the size of $\mathcal{P}_2$ is larger than that of $\mathcal{P}_1$. Indeed, classically, there are two ways to deal with coupled systems: a monolithic approach in which all the systems are simultaneously solved, or a Domain Decomposition method (see [QV99] for a complete review of the method). In the latter a fixed point iteration is adopted, in which all the systems are separately solved and share the interface data. In the case in which the secondary systems need a large number of degrees of freedom to be accurately solved, the computational cost associated to both the approaches may be large.

In this first work, for sake of simplicity, we made the assumption that there is only one system to be reduced and that it is described by linear PDEs. In this case the interaction of the linear system with $\mathcal{P}_1$ may be described by the Poincaré-Steklov operator. With a slight abuse of notation we call Poincaré-Steklov operator the one associated to a generic linear PDE, even if historically this name refers to the case in which the secondary system is described by a Laplace equation (see [AL85] for a first analysis of the problem).

The need to set up efficient solvers and to decouple the solution of the problems in interaction is related to the ability to solve the problem at the interface. The use of the Poincaré-Steklov operator as a preconditioner in fluid-structure interaction iterations was investigated in [DDFQ06]. An efficient non-linear coupling strategy was devised in [CPW14] to set up an uncertainty quantification method applied to networks of coupled systems. Unfortunately, the problem at the interface is in general not sparse and ill-conditioned (see [QV99]). To tackle this issue several strategies were proposed in the literature. They can be broadly divided into two classes: "local" and spectral approximations. A local approximation of the Poincaré-Steklov operator consists of solving one or more external problems ($\mathcal{P}_2$ in the present work) in a strip localised around the interface. Such a method was proposed for example in [PS05], for applications in hydrology. A similar procedure, based on a two-scale method, was presented in [GAG11]: a local problem in a strip localised around the interface is solved and then, thanks to the residual, a global correction is computed. A different strategy consists of approximating the leading part of the

action of the Poincaré-Steklov operator through a spectral decomposition. Such an approach was proposed in [Nat95, Nat97] in the case of elliptic problems and a multiscale version was proposed in [CZAL13] for applications in heterogeneous media. An approximation of the Poincaré-Steklov operator via a Padé expansion was detailed in [LP10] for the study of the vibrations in fluid-structure couplings. In [FN14] the Poincaré-Steklov operator is computed in the context of the wave propagation in elastodynamics by considering a family of smooth functions at the interface and by solving the problem $\mathcal{P}_2$ by taking these functions as inputs. In the recent work [BRD15] a compressed sensing approach is proposed to retrieve the discretised Poincaré-Steklov operator for coupled Helmholtz problems. The method consists of probing, randomly, the matrix associated to the Poincaré-Steklov operator, by selecting inputs from a kernel space and performing a direct full-order simulation for a small number of them.

In the present work, a low rank decomposition of the Poincaré-Steklov operator is computed by a Reduced-Order Modelling method. In the literature, similar works were recently proposed, based on a Reduced-Basis framework [HKP13, EP14, MRH15, IQR16]. In these, multi-domain systems are considered for coupled linear steady problems. The framework proposed in these works deals with parametrized systems whereas in the present work we focus on the acceleration of single-scenario simulations. In the present case, a parametrization can be considered for the problem $\mathcal{P}_1$; a remark on the possibility to extend the proposed approach to parametrized problems $\mathcal{P}_2$ is proposed at the end of Section 6.3.

The proposed approach is not applied to a specific set of problems but it is meant to be applied to a rather broad class of systems. As for most methods proposed in Reduced-Order Modeling ([QR14]), the strategy can be divided into two phases: an *offline* phase and an *online* one. In the offline phase, a deterministic sampling of the functional space of the input for the $\mathcal{P}_2$ at the interface is considered and the output is saved, at the interface. This is similar to what was proposed in [HKP13], in which harmonic functions at the interface are used and the offline phase is somewhat independent from the coupling. The output of $\mathcal{P}_2$ at the interface is used to get a Low Rank Decomposition of the Poincaré-Steklov operator. In order to make the method more robust in cases in which the inputs coming from $\mathcal{P}_1$ are outside the space spanned by the sampled functions used to construct the database, an *online* update of the reduced Steklov representation is performed, in the spirit of the methods proposed in [PW15, AZW15].

The advantages of the proposed framework are the following: it is a straightforward method, allowing to speed up coupled multi-physics time dependent systems in a domain decomposition approach. Moreover, the offline phase is completely independent of the nature of $\mathcal{P}_1$ and of the coupling. Its main limitations concern the assumptions made on $\mathcal{P}_2$: in the present work, $\mathcal{P}_2$, once discretized, has to be autonomous and linear. Although these assumptions are quite restrictive, they are fulfilled by a wide range of applications, for which a system of interest interacts with surrounding media or compartments whose dynamics is linear.

The structure of the chapter is as follows: in Section 6.2, the mathematical

formulation of the problem is detailed and few properties of the Poincaré-Steklov operator are recalled. In Section 6.3 the numerical method is described and then, in Section 6.4, its numerical properties are investigated from a theoretical point of view. In the last section, some numerical experiments are proposed to validate the method.

6.2 Problem formulation

In this section, the mathematical formulation of the problem is detailed. The aim is to deal with systems of partial differential equations defined on different domains, in interaction. To simplify, in this work, we investigate the case in which two problems are coupled, namely $\mathcal{P}_1$ and $\mathcal{P}_2$. Let the coupled systems be defined on a time interval $[0, T]$ and a space domain $\Omega \subseteq \mathbb{R}^d$, an open subset, such that $\Omega = \Omega_1 \cup \Omega_2$ where Ω_1 is the domain on which $\mathcal{P}_1$ is defined and Ω_2 is the domain on which $\mathcal{P}_2$ is defined. The interface between the two, where the coupling conditions are enforced, is denoted by $\Gamma := \overline{\Omega}_1 \cap \overline{\Omega}_2$. The problem of interest is $\mathcal{P}_1$, on which there are no hypotheses, it can be a generic non-linear PDE. The following working hypotheses on the problem $\mathcal{P}_2$ as well as on the coupling conditions are considered:

1. $\mathcal{P}_2$ is described by a linear PDE of the form $\mathcal{L}u_2 = 0$, where $\mathcal{L}$ is a linear operator.

2. it has no volume non-autonomous forcing terms.

The problem $\mathcal{P}_2$ is considered as time independent, when presenting the method hereafter. However, this restriction can be relaxed in several cases. Some examples and numerical experiments will be proposed in section 6.5.

The system can be written in strong form as follows:

$$\begin{aligned}
\mathcal{F}(u_1, \partial_t^{(\omega)} u_1, \nabla_x^{(\beta)} u_1) = 0, \quad & \text{on } \Omega_1 \\
h(u_1) = 0 \quad & \text{on } \partial\Omega_1/\Gamma, \\
\mathcal{L}u_2 = 0, \quad & \text{on } \Omega_2 \\
\ell_2 u_2 = 0, \quad & \text{on } \partial\Omega_2/\Gamma, \\
f_1(u_1, u_2) = 0, \ & \text{on } \Gamma, \\
f_2(u_1, u_2) = 0, \ & \text{on } \Gamma,
\end{aligned}$$

where $\mathcal{F}$ stands for a generic PDE describing the problem $\mathcal{P}_1$, depending upon time and space derivatives of maximal orders ω and β, respectively. The generic non-homogeneous boundary conditions for $\mathcal{P}_1$ are denoted by $h(u_1) = 0$. The homogeneous linear boundary conditions for the problem $\mathcal{P}_2$ on the boundary $\partial\Omega_2/\Gamma$ are expressed by the condition $\ell_2 u_2 = 0$. The boundary condition f_2 expressing the coupling conditions for $\mathcal{P}_2$ has to be affine in u_2, while the condition f_1 for the problem $\mathcal{P}_1$ can be generic. The goal is to decouple the problems and to be able to solve $\mathcal{P}_2$ efficiently. The main interest, though, is not to have the solution of $\mathcal{P}_2$ in

the whole domain Ω_2. Instead, only an accurate representation of the solution of $\mathcal{P}_2$ at the interface Γ is needed in order to have a good approximation of the solution of $\mathcal{P}_1$. The action of the linear problem $\mathcal{P}_2$ on the problem $\mathcal{P}_1$ through the coupling conditions can be described by means of the Poincaré-Steklov operator $\mathcal{S}$ defined as follows:

$$\mathcal{S}v = \mathcal{T}\ell(\mathcal{L}^{-1}v),$$

where the quite abstract notation $\mathcal{T}\ell(\mathcal{L}^{-1}v)$ stands for: solving the linear problem $\mathcal{P}_2$ on Ω_2 when the datum at the interface is v, compute the image of a linear operator of the solution ℓu_2 and take the trace $\mathcal{T}$ of it.

6.2.1 Classical domain decomposition iteration

The coupled problem described above can be solved by using the Domain Decomposition (DD) method. Since the proposed approach can be seen as a technique to speed up the DD iteration, we recall the basics of this method. A complete review and detailed treatment of the Domain Decomposition methods can be found in [QV99, TW05, SBG04, MQ89].

The method relies on the presence of two (or more) subdomains. These can be either physically related to two different physics, as it is the case in the present work, or they can be artificially generated. These subdomains can be chosen with or without overlapping. In the present work we consider non-overlapping subdomains. The idea is to couple the dynamics in the two subdomains by enforcing suitable transmission conditions at the interface. Then, the coupling is solved by fixed point iterations. A typical scheme is the Dirichlet to Neumann iteration in its multiplicative version, here applied, for instance, to the Laplace equation:

$$\begin{cases} -\Delta u_1^k = 0 & \Omega_1 \\ u_1^k = u_2^{k-1} & \Gamma \\ -\Delta u_2^k = 0 & \Omega_2 \\ \partial_n u_2^k = \partial_n u_1^k & \Gamma \end{cases}$$

where k denotes the current domain decomposition iteration and where the boundary conditions on $\partial\Omega$ have been omitted. Other coupling schemes can be considered, such as the Neumann-Neumann and Robin-Robin scheme. Since convergence is not always guaranteed, a relaxation of the Dirichlet condition can be introduced of the form:

$$u_1^k = \theta u_2^{k-1} + (1-\theta)u_1^{k-1}.$$

With the notation introduced, the problem $\mathcal{P}_1$ is defined by $\mathcal{F} = -\Delta u_1$, $\mathcal{P}_2$ is also, in this example, a Laplace equation, *i.e.* $\mathcal{L}u_2 = -\Delta u_2$. The condition for $\mathcal{P}_1$ at the interface are given by $f_1 = u_1 - u_2$ and the condition for the problem $\mathcal{P}_2$ are given by $f_2 = \partial_n u_2 - \partial_n u_1$. The Poincaré-Steklov operator associated to the problem $\mathcal{P}_2$ is

defined as:

$$\mathcal{S} : H^{-1/2}(\Gamma) \to H^{1/2}(\Gamma),$$
$$\mathcal{S}\partial_n u_1 = u_2 \quad \text{on } \Gamma,$$

so that ℓ is the identity operator on Γ and the operator is called the Neumann-to-Dirichlet map (N2D).

The discretisation of this example is shown when a finite element basis is used. This provides some insights into the algebraic nature of the discretised Poincaré-Steklov operator, and a motivation for the present work.

Let $b_i^{(h)} \in B(\Gamma)$ be a generic finite element function defined on Γ, then, the matrix S is the representation of the Poincaré-Steklov operator on the basis functions, namely:

$$S_{ij} := \langle \mathcal{S} b_j^{(h)}, b_i^{(h)} \rangle_\Gamma,$$

where h stands for the characteristic mesh length. In such a case, the whole coupled problem admits the following matrix representation:

$$\begin{bmatrix} A_{11} & 0 & A_{1\Gamma}, \\ 0 & A_{22} & A_{2\Gamma}, \\ A_{\Gamma 1} & A_{\Gamma 2} & A_{\Gamma\Gamma} \end{bmatrix} \begin{pmatrix} u_1, \\ u_2, \\ u_\Gamma \end{pmatrix} = \begin{pmatrix} f_1, \\ f_2, \\ f_\Gamma \end{pmatrix}$$

After some algebra (see [QV99] for a detailed derivation), a system for the solution at the interface can be obtained of the form:

$$\Sigma_h u_\Gamma = q_\Gamma,$$

where Σ_h is the Schur complement and it is the discrete representation of the Poincaré-Steklov operator. The Schur complement is in general dense and ill-conditioned for the problems of interest. As a consequence, computing directly the Poincaré-Steklov operator would be very expensive from a computational standpoint, even in the simple case in which both the problems are linear. Moreover, due to the ill-conditioned nature of the matrix, the solution of the system could be affected by large errors. This highlights an important reason to look for a reduced representation of the Poincaré-Steklov operator.

6.3 Outline of the method

The method can be divided, as for the majority of reduced-order modeling methods (see [QR14] for an overview in the recent advances in this subject), in two phases: an *offline* phase, and an *online* one.

6.3.1 Offline phase

In the offline phase, a number of simulations is performed in order to construct a database of meaningful solutions, to be exploited later on and speed up the online phase. Contrary to most of the classical methods of model reduction presented in the literature, we made the choice of simulating only $\mathcal{P}_2$ in the offline phase, and not the whole system. This strategy has two main advantages: it allows to perform the simulations in the offline phase without considering the coupling between the two subdomains. The problem $\mathcal{P}_2$ is linear and basis functions can be computed in a massive parallel way. Second, from the point of view of the memory usage, there is no need to save the whole solution of $\mathcal{P}_2$, but only a restriction of a linear operator applied to its solution on the interface Γ.

We need to choose a set of basis functions to represent the input datum. Such basis has to be defined on a generic Riemannian manifold, to be orthonormal and complete. In view of these desired properties, a reasonable choice is to a priori take the first N_ℓ eigenfunctions of the Laplace-Beltrami operator defined on the surface, with $N_\ell \ll N_\Gamma$, the number of degrees of freedom at the interface. The advantages of choosing the eigenfunctions of the Laplace-Beltrami operator are the following:

1. The basis is a complete basis of $V := L_2(\Gamma)$.

2. It is hierarchical.

3. It automatically accounts for symmetries in the geometry.

4. The extraction of the basis amounts to solve a sparse eigenvalue problem defined on Γ.

5. On particular (but meaningful) geometrical settings, the basis coincides with the eigenfunctions of the Poincaré-Steklov operator (see Appendix 6.7).

Let the eigenfunctions of the Laplace-Beltrami operator be denoted as follows: $v_i \in V,\ i = 1, \dots, N_\ell$ is such that $-\Delta_\Gamma v_i = \mu_i v_i$.

The problem in weak form reads:

$$\langle \nabla_\Gamma v_i, \nabla_\Gamma \omega \rangle_\Gamma = \mu_i \langle v_i, \omega \rangle_\Gamma,\ \forall\ \omega \in H^1(\Gamma),$$

where ∇_Γ denotes the surface gradient and $\langle u, v \rangle_\Gamma = \int_\Gamma uv\ d\Gamma$ is the inner product on the interface Γ. The problem is then discretised by using P_1 finite elements.

Once the basis has been extracted by solving a sparse eigenvalue problem, the problem $\mathcal{P}_2$ is solved, for every input function v_i. Only the image of a linear operator applied to the solution is stored on the boundary, *i.e.*: $y_i = \mathcal{S} v_i = \mathcal{T}\ell(u_2^{(i)})$, where $u_2^{(i)} = \mathcal{L}^{-1}(v_i)$.

In the case in which the boundary conditions on $\partial\Omega_2/\Gamma$ are not homogeneous, other problems can be solved in the offline phase to account for the contribution of the terms on $\partial\Omega_2/\Gamma$ at the interface.

6.3.2 Online phase

The action of the Poincaré-Steklov operator on a generic input datum d can be approximated as follows:

$$\mathcal{S}d \approx \mathcal{S}_0 + \sum_{j}^{N_\ell} \langle d, v_j \rangle_\Gamma \; y_j + \sum_{k}^{N_o^{(n)}} \langle d, w_k \rangle_\Gamma \; z_k,$$

where $\mathcal{S}_0$ accounts for eventual non-homogeneous boundary conditions for $\mathcal{P}_2$ on $\partial\Omega_2/\Gamma$, the second term corresponds to the contribution of the projection of the datum d in the space spanned by the Laplace-Beltrami eigenfunctions and the last term is an *online update* of the basis, such that $\langle w_k, y_j \rangle_\Gamma = 0$. The online update of the basis is similar, in the spirit, to what is proposed in [PW15, AZW15]. In particular, when an error criterion is not fulfilled, the basis is updated by adding elements to it, coming, in the present approach, from a full-order problem simulation. The main difference with respect to the cited works concerns the way the update is performed. In the present approach we decided not to use a thin SVD update, but simply to increase the basis size and perform an orthogonalisation through a Modified Gram Schmidt (MGS). This proved to be sufficient for the purposes of this work. The online update is performed as follows. Consider a generic time instant $t^{(n)}$. The approximation space in use is $V \cup W^{(n)}$, that is, the union of the set of the Laplace-Beltrami eigenfunctions and the set of the $N_o^{(n)}$ online basis functions possibly added in the previous time iterations. Once the datum $d^{(n)}$ is available, coming from $\mathcal{P}_1$, its reconstruction error on the space in use is:

$$\varepsilon_d^{(n)} := \left\| d^{(n)} - \sum_{i=1}^{N_\ell} \langle d^{(n)}, v_i \rangle_\Gamma v_i - \sum_{j=1}^{N_o^{(n)}} \langle d^{(n)}, w_j \rangle_\Gamma w_j \right\|_{\Gamma,2} .$$

Let $\overline{\varepsilon}_d$ be the tolerance chosen for the datum representation. If $\varepsilon_d^{(n)} > \overline{\varepsilon}_d$ then an online update is needed. Let the basis function to be added be:

$$w_{N_o^{(n)}+1=N_o^{(n+1)}} = C \left(d^{(n)} - \sum_{i=1}^{N_\ell} \langle d^{(n)}, v_i \rangle_\Gamma v_i - \sum_{j=1}^{N_o^{(n)}} \langle d^{(n)}, w_j \rangle_\Gamma w_j \right),$$

where C is the normalisation constant, chosen such that: $\|w_{N_o^{(n+1)}}\|_{\Gamma,2} = 1$. This step is performed through an MGS method. The corresponding output $z_{N_o^{(n+1)}}$ is computed by actually solving the problem $\mathcal{P}_2$. The main advantage of the online enrichment is that a higher precision is guaranteed. Theoretically, the online update could be required at all the evaluations of the secondary problem, but in practice, see also the numerical section, only a few online solution of $\mathcal{P}_2$ are required. In fact, the real drawback of using the online update is that the access to the high fidelity model for $\mathcal{P}_2$ is required both in the online and in the offline phase. For this reason, depending on the way in which the software is implemented and on the size of $\mathcal{P}_2$,

one may decide to skip the online phase and to rely only on the offline set of basis functions.

6.3.3 Retrieving the Poincaré-Steklov eigenfunctions

Once the output of $\mathcal{P}_2$ have been computed for all the basis functions on Γ, the eigenfunctions of the Poincaré-Steklov operator, if needed, can be retrieved. This allows to perform a Low Rank Decomposition of the operator that can be exploited in parametric Domain Decomposition methods. In particular, let the eigenfunctions of the Poincaré-Steklov operator be written as a linear combination of the Laplace-Beltrami eigenfunctions as:

$$\hat{\varphi}_i = \sum_{j=1}^{N_\ell} U_{ij} v_j,$$

where $\hat{\varphi}_i$ is the approximation of the Poincaré-Steklov operator eigenfunction, U is the representation of the Poincaré-Steklov eigenfunctions onto the Laplace-Beltrami eigenfunctions. The equation $\mathcal{S}\varphi_i = \lambda_i \varphi_i$, when discretized on the first N_ℓ eigenfunctions v_j, becomes:

$$\sum_{j=1}^{N_\ell} U_{ij} \mathcal{S} v_j = \hat{\lambda}_i \sum_{j=1}^{N_\ell} U_{ij} v_j.$$

This is projected onto the space spanned by the eigenfunctions of the Laplace-Beltrami operator leading to:

$$\sum_{j=1}^{N_\ell} U_{ij} \langle \mathcal{S} v_j, v_k \rangle_\Gamma = \hat{\lambda}_i \sum_{j=1}^{N_\ell} U_{ij} \delta_{jk}.$$

This is a reduced eigenvalue problem for the representation of the Poincaré-Steklov eigenfunctions on the Laplace-Beltrami ones (namely U_{ij}). The problem can be recasted as follows:

$$SU = U\Lambda,$$

where $S_{jk} := \langle \mathcal{S} v_j, v_k \rangle_\Gamma = \langle y_j, v_k \rangle_\Gamma$ is the representation of the Poincaré-Steklov operator onto the Laplace-Beltrami eigenfunction basis.

Having an eigenbasis for the operator $\mathcal{S}$ (think for instance to the N2D map) allows to easily recover the action of other maps on the data. Indeed, the eigenfunctions of all the maps coincide and only the spectrum changes and it can be recovered via a purely algebraic relation. This can be useful when dealing with DD iterations in which a Robin condition has a possibly varying parameter (see [DH97]) or if the scenario to be simulated changes on a given geometrical setting. In all these cases, it is not necessary to re-compute the *offline* phase, so that no extra computational cost is involved.

Remark 1

The proposed method can be applied straightforwardly to systems whose geometry

is fixed (corresponding to a single scenario for $\mathcal{P}_2$). An interesting perspective we briefly prospect on in this remark concerns the cases in which multiple scenarios are involved. This is for instance the case in which the interface depends upon a set of parameters $\boldsymbol{\mu}$. This leads to a parametric representation of the Poincaré-Steklov operator. To compute a low-rank decomposition of the operator, the M-DEIM method introduced in [NMA15] could be used. The authors introduced it to deal with problems that, after discretization, are featured by matrices that depend on parameters in a non-affine way. In the present context, given a sample of $\boldsymbol{\mu}$, the corresponding Laplace-Beltrami eigenfunction can be computed and the outputs of $\mathcal{P}_2(\boldsymbol{\mu})$ stored. These can be used to approximate, in the online phase, the action of $\mathcal{S}(\boldsymbol{\mu})$ on the input.

6.4 Numerical Analysis

In this section an analysis of the approximation properties of the method and its computational costs is detailed.

6.4.1 Properties of Poincaré-Steklov operator

Here we recall some properties of the Poincaré-Steklov operator in the case in which the problem $\mathcal{P}_2$ is linear elliptic and symmetric (see [KW12]). The numerical analysis of the method will be performed by assuming the same hypotheses. The numerical experiments, instead, will be presented in a more general setting.

In what follows, we denote the Neumann to Dirichlet map (N2D) by S. In this case, $f_2 = \partial_n u_2 - d(u_1)$, where $d(u_1)$ is the datum coming from $\mathcal{P}_1$. The operator S is defined from $H^{-1/2}(\Gamma)$ to $H^{1/2}(\Gamma)$ and it is the trace of the solution of $\mathcal{P}_2$. The corresponding inverse map S^{-1} is the Dirichlet to Neumann map (D2N), it takes elements from $H^{1/2}(\Gamma)$ and its result is in $H^{-1/2}(\Gamma)$. In this case $f_2 = u_2 - d(u_1)$ and the application of the map provides the normal derivative of u_2 on Γ.

The operator S is compact in $L^2(\Gamma)$, continuous and symmetric with respect to the $L^2(\Gamma)$ duality between $H^{-1/2}(\Gamma)$ to $H^{1/2}(\Gamma)$ (see [KW12] for the proof of these properties). Both S and S^{-1} are positive definite and they both induce a norm on $H^{-1/2}(\Gamma)$ and $H^{1/2}(\Gamma)$, respectively.

In this case, the eigenfunctions of S are a complete orthonormal basis of $L_2(\Gamma)$.

6.4.2 Convergence

In this section, the convergence of the proposed method is investigated in the case in which $\mathcal{P}_2$ is defined by a linear elliptic and symmetric operator, enjoying the properties introduced in section 6.4.1. In what follows, for sake of compactness in the notation, the standard $H^s(\Gamma)$ norm will be denoted by $\|\cdot\|_s$, where it is intended that $\|\cdot\|_0$ is the standard $L_2(\Gamma)$ norm. The result is summarised in the following proposition.

Proposition 1
Let $\partial\Omega_2$ be C^2 and let $S : H^{-1/2}(\Gamma) \to H^{1/2}(\Gamma)$ be the N2D map, S^{-1} the D2N map; let w be the datum and $\hat{w}$ its projection onto the subset of the first N_ℓ Laplace-Beltrami eigenfunctions. Then:

1. *if $w \in L_2(\Gamma)$, then $\lim_{N_\ell \to \infty} \|S(w - \hat{w})\|_0 = 0$.*
2. *if $w \in H^2(\Gamma)$, then: $\|S(w - \hat{w})\|_0 \leq C_1 N_\ell^{-2/d_\Gamma} |w|_2$.*
3. *if $w \in H^2(\Gamma)$, then: $\|S^{-1}(w - \hat{w})\|_0 \leq C_2 N_\ell^{-1/2d_\Gamma} |w|_2$.*

Proof. *In order to prove the first point, the following inequality is considered:*

$$\|S(w - \hat{w})\|_0 \leq \lambda_{max} \|w - \hat{w}\|_0,$$

where λ_{max} is the largest eigenvalue of the N2D map. Since the Laplace-Beltrami eigenfunctions are a complete basis of $L_2(\Gamma)$, the convergence follows. The second point can be proved by considering the approximation properties of the Laplace-Beltrami eigenfunctions (see for instance [CHQZ07, APV15]). Under the hypothesis that w satisfies the same boundary conditions as the eigenfunctions basis on $\partial\Gamma$, it holds:

$$\|w - \hat{w}\|_0 \leq c N_\ell^{-2/d_\Gamma} |w|_2,$$

Thus: $C_1 = \lambda_{max} c$, where c is a constant depending on the domain Γ .

The proof of the convergence for the inverse map is more delicate since the map causes a loss of regularity. Let us assume that the datum $w \in H^2(\Gamma)$. In this case, see [KW12]:

$$S^{-1}(w - \hat{w}) \in H^{1/2}(\Gamma).$$

Then, thanks to the trace inequality and the regularity of the Laplace problem (see [Sal15] for a detailed derivation), the following chain of inequalities holds:

$$\|S^{-1}(w-\hat{w})\|_0 \leq B_1 \|S^{-1}(w-\hat{w})\|_{1/2} \leq C_T B_1 \|u\|_{H^2(\Omega_2)} \leq C_T B_1 B_2 \|(w-\hat{w})\|_{3/2},$$

where u is the Dirichlet harmonic extension of $w - \hat{w}$, C_T, B_1, B_2 are constants that depend on Γ (B_1) and on Ω_2 (C_T, B_2). By the properties of interpolation of Sobolev spaces, see [BL12], the last term satisfies:

$$\|(w - \hat{w})\|_{3/2} \leq B_3 \|(w - \hat{w})\|_2^{3/4} \|(w - \hat{w})\|_0^{1/4},$$

where B_3 is a constant depending on Γ. This is sufficient at once to prove the convergence and to derive, thanks to the approximation properties of the Laplace eigenfunctions, the theoretical rate, as done for the map S. ∎

The result of the proposition shows that the method converges. When the N2D map is approximated, in a 3D problem, a linear (in the number of eigenfunctions)

convergence is expected. When the inverse map (D2N) is approximated, due to the loss of regularity induced by the map, a potentially slower convergence rate is obtained. In the very specific case of a solution w such that its higher order derivatives satisfy the same boundary conditions as the eigenfunctions basis on $\partial\Gamma$ we have exponential convergence (see for instance [CHQZ07, APV15]).

6.4.2.1 A semi-analytical example.

In this subsection a computation is shown in order to compute the rate of convergence of the method in a simple setting. Consider for instance the problem $\mathcal{P}_2$ defined as $-\Delta u = 0$ on a unit square $[0,1]^2$ with Dirichlet boundary conditions on three sides and a datum imposed on $y = 0$. Let the datum d be expanded in a Fourier series and let $\hat{d}_k$ be the $k-$th coefficient. Then, the N2D and the D2N maps can be computed analytically:

$$Sd = \sum_k^\infty \sqrt{2}\hat{d}_k \frac{\tanh(\pi k)}{\pi k}\sin(\pi k x),$$
$$S^{-1}d = \sum_k^\infty \sqrt{2}\hat{d}_k \frac{\pi k}{\tanh(\pi k)}\sin(\pi k x).$$

In the last two equations the regularising effect of S is evident: the Fourier coefficients of the image are going to zero faster with respect to those of the datum. On the other hand, for S^{-1}, the coefficients are multiplied by k and therefore they tend to zero more slowly. When computing the truncation error committed by retaining only $k = N_\ell$ space frequencies, the following expression is obtained:

$$\varepsilon_S = ||S(d-\hat{d})||_2 = \left(\sum_{k>N_\ell} \hat{d}_k^2 \tanh(k\pi)^2 \pi^{-2} k^{-2}\right)^{1/2},$$
$$\varepsilon_{S^{-1}} = ||S^{-1}(d-\hat{d})||_2 = \left(\sum_{k>N_\ell} \hat{d}_k^2 \pi^2 k^2 \tanh(k\pi)^{-2}\right)^{1/2},$$

where $\hat{d}$ is the projection of the datum on the first N_ℓ basis functions.

In Table 6.1 we reported the estimated rate of decay of the Fourier coefficients $\hat{d}_k$ and the L_2-norm of the errors for the two maps, for two different functions, characterized by a different regularity. The results show that the convergence, in this case, is faster than expected. In particular, the result of the proof is pessimistic since in this case the Poincaré-Steklov operator eigenfunctions coincide with the Laplace-Beltrami eigenfunctions at the interface.

d		Regularity	$\hat{d}_k$	$\|\|\varepsilon_S\|\|_0$	$\|\|\varepsilon_{S^{-1}}\|\|_0$
$\begin{cases} 0 \\ \frac{x^2}{2} - \frac{x}{5} + \frac{1}{50} \\ -\frac{x^2}{2} + \frac{3x}{5} - \frac{7}{50} \\ \frac{x^2}{2} - x + \frac{1}{2} \end{cases}$	$\begin{array}{ll} 0 & \leq x < 1/5 \\ 1/5 & \leq x < 2/5 \\ 2/5 & \leq x < 4/5 \\ 4/5 & \leq x \leq 1 \end{array}$	$H^2(0,1)$	k^{-3}	$k^{-3.5}$	$k^{-1.5}$
$\begin{cases} 3x+1 \\ 1 \\ 2-2x \end{cases}$	$\begin{array}{ll} 0 & \leq x < 1/3 \\ 1/3 & \leq x < 1/2 \\ 1/2 & \leq x \leq 1 \end{array}$	$H^1(0,1)$	k^{-2}	$k^{-2.5}$	$k^{-0.5}$

Table 6.1: Semi-analytical estimation of the rate of convergence of the method.

6.4.3 Theoretical analysis of the computational costs.

The computational cost of the procedure and the theoretical speed-up are presented. Let $\mathcal{N}_1, \mathcal{N}_2$ be the number of degrees of freedom of $\mathcal{P}_1$ and $\mathcal{P}_2$ respectively when they are discretised by means of a standard Finite Element method. Then, let I_{dd} be the average number of iterations of Domain Decomposition. We assume that the computational costs associated to the solution of an average iteration of Domain Decomposition amounts to:

$$\mathcal{C}_I \approx I_{dd} \left(C_1 \mathcal{N}_1^{\alpha_1} + C_2 \mathcal{N}_2^{\alpha_2} \right),$$

where the α_i depend on the solvers chosen for the two problems. When the GMRES method is used (without preconditioning) a quadratic behavior is expected ($\alpha_i \sim 2$). Other state of the art solvers, *e.g.* multigrid, shows approximately linear convergence ($\alpha_i \sim 1$, see for instance [GMSB16]). Let $\mathcal{N}_\Gamma$ be the number of degrees of freedom at the interface. Then, the method consists of approximating the result of $\mathcal{P}_2$ by projecting the datum at the interface onto the basis and to reconstruct the output of the Poincaré-Steklov operator, at the interface. Let N_ℓ be the number of modes. This operation has a computational cost, denoted by $\mathcal{C}_r$ of:

$$\mathcal{C}_r \approx 3 \mathcal{N}_\Gamma N_\ell + \mathcal{O}(1).$$

When applying the method, the average Domain Decomposition iteration has a reduced cost ($\mathcal{C}_R$) of:

$$\mathcal{C}_R \approx I_{rdd} \left(C_1 \mathcal{N}_1^{\alpha_1} + 3 \mathcal{N}_\Gamma N_\ell \right) + \mathcal{O}(1),$$

where the average number of Domain Decomposition iteration I_{rdd} may vary by virtue of a regularizing effect of the reduced-order model.

Few comments are in order. The speed up in the solution of the problem $\mathcal{P}_2$ is expected to be very large. Indeed, it is the ratio between a term that scales as the α_2-power of the number of degrees of freedom in the domain Ω_2 and a term which

is linear in the number of degrees of freedom of the interface. The overall speed-up of a single iteration is due to two contributions: the acceleration of the solution of $\mathcal{P}_2$ and a possible regularizing effect:

$$\frac{\mathcal{C}_I}{\mathcal{C}_R} \approx \frac{I_{dd}\left(C_1\mathcal{N}_1^{\alpha_1} + C_2\mathcal{N}_2^{\alpha_2}\right)}{I_{rdd}\left(C_1\mathcal{N}_1^{\alpha_1} + 3\mathcal{N}_\Gamma N_\ell\right)}, \tag{6.14}$$

so that the method is very efficient when the number of degrees of freedom of $\mathcal{P}_2$ is large. By observing Eq.(6.14) it is clear that the best conditions for expecting a significant speed up are: $\mathcal{N}_2 \gg \mathcal{N}_\Gamma$ and $\mathcal{N}_2 \gg \mathcal{N}_1$. In fact, the first condition guarantees a speed up in the solution of $\mathcal{P}_2$ and the second condition guarantees that $\mathcal{P}_2$ was the most costly part of the simulation. In other cases where the second condition is not satisfied, but we have, for instance, $\mathcal{N}_2 = \mathcal{N}_1$ the total solution cost will be reduced only by a factor two. Remark that in the case in which there are several systems in interaction, the speed up of the method is expected to be larger and larger.

The total cost of performing N_{sim} simulations each of which has N_T time steps can be roughly expressed, for the Full-order method ($\mathcal{C}_{DD}$) and for the Reduced-Order one ($\mathcal{C}_{ROM}$) as:

$$\begin{aligned} \mathcal{C}_{DD} &\approx N_{sim}N_T\mathcal{C}_I, \\ \mathcal{C}_{ROM} &\approx N_{sim}N_T\mathcal{C}_R + N_\ell C_2\mathcal{N}_2^{\alpha_2} + 6N_\ell^2\mathcal{N}_\Gamma, \end{aligned}$$

where the last term accounts for the overheads of the offline phase, consisting in solving N_ℓ problems $\mathcal{P}_2$ and by computing N_ℓ eigenfunctions of the Laplace-Beltrami operator defined at the interface.

When the online update of the basis is used to reduce the error in the computation, an extra cost has to be accounted for, consisting of solving one $\mathcal{P}_2$ problem, whose cost is $\propto \mathcal{C}_2\mathcal{N}_2^{\alpha_2}$ and a Modified Gram-Schmidt orthonormalisation for the input function at the interface.

6.5 Numerical Experiments

In this section three numerical experiments are shown, on systems characterised by different interactions and geometrical settings. The first two testcases were mainly motivated by the study of physiological flows, think for instance of blood vessels surrounded by soft tissues, and are models of fluid-fluid interaction. The last test is, instead, a paradigmatic example of fluid-structure interaction applications arising in an industrial context. Although the method is tested on fluid-fluid or fluid-structure interaction problems, we would like to emphasize that it finds application in a broad range of engineering problems.

In particular, the first test case is a simple example where the external problem is described by a Laplacian operator and where Proposition 2 holds. The second test case is used to quantitavely confirm the convergence properties derived in the

previous section and to test the online enrichment strategy. The third and last test case involves a more complex operator for the external problem, which is a stationary Stokes problem, and it is used to measure the speed up.

6.5.1 Incompressible flow interacting with a porous medium

In this testcase, the first system $\mathcal{P}_1$ is governed by the Navier-Stokes equations in interaction with a porous medium, $\mathcal{P}_2$, described by the Darcy equation. A full analysis of this coupling and of suitable domain-decomposition schemes can be found in [DQ03]. The geometrical setting is the following: the domain $\Omega = \Omega_1 \cup \Omega_2$ is a parallelepiped $(0,10) \times (0,5) \times (0,10)$ divided in two parallelepipeds $\Omega_1 = (0,10) \times (0,5) \times (9,10)$ and $\Omega_2 = (0,10) \times (0,5) \times (0,9)$ (see Fig.6.1). The two flows are separated by the planar interface $\Gamma = (0,10) \times (0,5) \times \{9\}$. In Ω_1, the fluid is described by the time-dependent Navier-Stokes equations: $\partial_t \boldsymbol{u} + \boldsymbol{u} \cdot \nabla \boldsymbol{u} = \nabla \cdot \boldsymbol{\sigma}(\boldsymbol{u}, p_1), \nabla \cdot \boldsymbol{u} = 0$, where $\boldsymbol{\sigma}(\boldsymbol{u}, p_1) = \nu(\nabla \boldsymbol{u} + \nabla \boldsymbol{u}^T) - p_1 \boldsymbol{I}$ is the Cauchy stress tensor, $\nu = 0.04$ the fluid viscosity and $\boldsymbol{u}$ and p_1 the fluid velocity and pressure. We denote by $\boldsymbol{n}_1$ the outward normal with respect to Ω_1 and by $\boldsymbol{n}_2$ the normal oriented outward with respect to Ω_2.

For the boundary conditions at $\partial\Omega_1 \setminus \Gamma$, we assigned a non-homogeneous natural condition, $\boldsymbol{\sigma}(\boldsymbol{u}, p)\boldsymbol{n}_1 = -10\sin(0.5(x+y)-100t)$, on $\Gamma_{in} = (0,10)\times(0,5)\times\{z = 10\}$, the top surface of Ω_1. On the lateral surface, $\Gamma_{lat,1} = \partial\Omega_1 \setminus (\Gamma \cup \Gamma_{in})$, mixed homogeneous boundary conditions were imposed on the normal velocity and on the tangential component of the normal stress. Moreover, the tangential velocity was set to zero at the interface Γ.

In the second compartment, Ω_2, the flow in the porous medium is described by the Darcy's equation: $-\mathrm{div}(K\nabla p_2) = 0$, where $K = 0.2$ is the permeability which was assumed to be a scalar.

On $\partial\Omega_2 \setminus \Gamma$ we imposed the following boundary conditions: zero pressure at $\Gamma_{out} = (0,10) \times (0,5) \times \{z = 0\}$ and homogenous Neumann conditions on $\Gamma_{lat,2} = \partial\Omega_2 \setminus (\Gamma \cup \Gamma_{lat,2})$.

The two systems are coupled by the following interface conditions on the normal direction:

$$\begin{cases} \boldsymbol{\sigma}(\boldsymbol{u}, p)\boldsymbol{n}_1 \cdot \boldsymbol{n}_1 = -p_2 & \Gamma \\ \nabla p_2 \cdot \boldsymbol{n}_2 = \frac{1}{K}\boldsymbol{u} \cdot \boldsymbol{n}_1 & \Gamma. \end{cases}$$

To solve the problem with an iterative scheme the following domain decomposition scheme is adopted:

$$\begin{cases} \boldsymbol{\sigma}(\boldsymbol{u}^k, p^k)\boldsymbol{n}_1 \cdot \boldsymbol{n}_1 + \alpha \boldsymbol{u}^k = -p_2^{k-1} + \alpha \boldsymbol{u}^{k-1} & \Gamma \\ \nabla p_2^k \cdot \boldsymbol{n}_2 = \frac{1}{K}\boldsymbol{u}^k \cdot \boldsymbol{n}_1 & \Gamma, \end{cases}$$

where k denotes the current domain decomposition iteration and $\alpha = 0.1$ is a relaxation parameter. A standard Aitken acceleration is used to reduce the number of fixed point iterations (see [DDFQ06]). The Steklov operator is therefore a Neumann to Dirichlet map in this case. We also remark that, in such a simple geometry, the

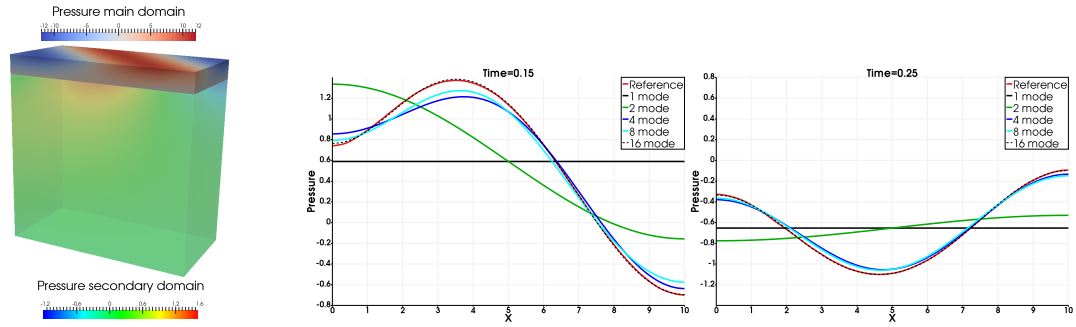

Figure 6.1: A snapshot of the reference solution for $t = 0.15$ (left panel). Pressure p at the interface Γ (first test case) along the line $y = 2.5$ for two different time instants (center and right panel). Finite elements results are compared with the reduced approach for different numbers of modal functions.

eigenfunctions of the Steklov and those of the Laplace-Beltrami operators coincide, see Appendix 6.7.

To discretise the system in space, P1-P1 stabilized finite elements are used. The computational mesh consists of 59268 tetrahedra for Ω_1 and 439458 for Ω_2, while on Γ there are 2776 degrees of freedom and the time step Δt is equal to 0.01.

The result of the reduction are shown in Figure 6.1, where the pressure p is displayed at the interface and the reduced solutions are compared to the reference one for two different time instants. We observe that, in this case, with one and two modes the behavior of the system substantially differs from the reference one. However, by adding few modes the convergence to the reference dynamics is quite fast.

6.5.2 A tube embedded in an inviscid fluid flow

The second testcase models a more complex system: $\mathcal{P}_1$ is a non-steady Stokes flow in a thin elastic tube, coupled with an external inviscid non-steady flow ($\mathcal{P}_2$). The geometry of the test is shown in Figure 6.2. The goal is twofold: to provide an example on how the hypothesis of time independence of $\mathcal{P}_2$ can be relaxed and to test the method robustness when dealing with ill-posed decoupled problems.

The whole domain is, as in the first test, a parallelepiped $\Omega = (0, 10) \times (0, 5) \times (0, 2)$. The first subdomain Ω_1 is the cylinder $(0, 10) \times \Gamma_{in}$ with Γ_{in} being the circle in the yz plane centered in $(x = 0, y = 2, z = 1)$ and with radius $r = 0.5$, Γ_{out} denotes the corresponding face in $x = 10$. The interface between the two domains is denoted by Γ and it is the lateral surface of Ω_1. The domain $\Omega_2 = \Omega \setminus \Omega_1$ is the remaining portion of Ω.

The problem $\mathcal{P}_1$ is the Stokes system and, at the interface Γ, we added an elastic shell to model the tube elasticity. For the sake of simplicity, we present the system

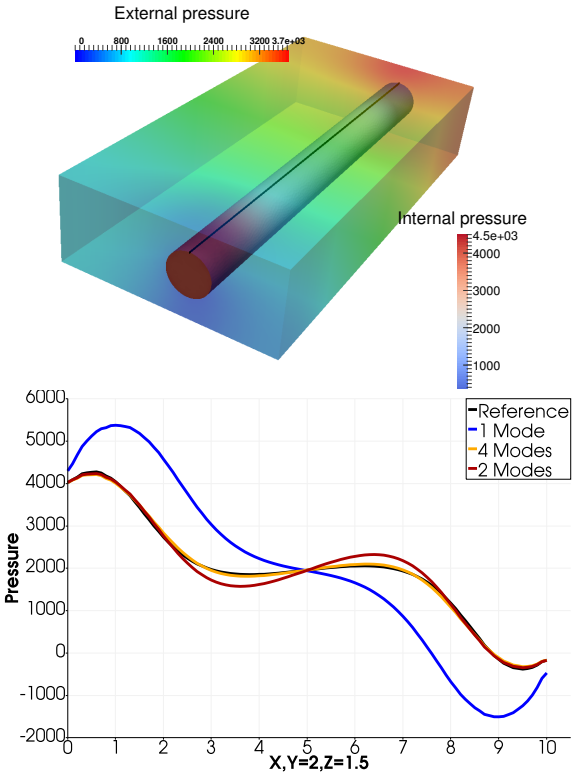

Figure 6.2: On the left panel, we have a snapshot of the reference solution for $t = 0.006$. The tube is the domain Ω_1 where we solve the Stokes equations. On the right panel pressure p_1 at the black line of the left panel has been displayed for different choices of the offline basis' dimension that are compared to the reference solution.

in its discretised form, at time $t_n = n\Delta t$:

$$\mathcal{P}_1 \begin{cases} \frac{1}{\Delta t}\boldsymbol{u}^n - \nu\Delta\boldsymbol{u}^n + \nabla p^n = \frac{1}{\Delta t}\boldsymbol{u}^{n-1} & \Omega_1 \\ \nabla\cdot\boldsymbol{u}^n = 0 & \Omega_1 \\ \boldsymbol{\sigma}(\boldsymbol{u}^n, p_1^n)\boldsymbol{n}_1 = -p_{in,(out)}(t_n) & \Gamma_{in,(out)} \\ \boldsymbol{\sigma}(\boldsymbol{u}^n, p_1^n)\boldsymbol{n}_1 + \boldsymbol{\mathcal{L}}(\boldsymbol{u}^n) = \boldsymbol{\mathcal{F}}^{n-1,n-2} - p_2^n\boldsymbol{n}_1 & \Gamma \\ \eta^n = \eta^{n-1} + \Delta t\boldsymbol{u}^n\cdot\boldsymbol{n}_1 & \Gamma, \end{cases}$$

where $p_{in}(t)$ is a given function of time and $p_{out} = 0$. The membrane is rendered by two terms $\boldsymbol{\mathcal{L}}(\boldsymbol{u}^n)$ and $\boldsymbol{\mathcal{F}}$ in the boundary condition, the first one being a symmetric operator on Γ and the second being a function of the values of the solution at the previous time steps. The structure equation is embedded in this two terms and the displacement is then computed through an algebraic equation. The resulting boundary condition is a generalized Robin condition. It is beyond the scope of this work to get into the details of this simplified fluid-structure interaction model; a detailed derivation can be found in [NV08].

The equation for $\mathcal{P}_2$ describes a time-dependent inviscid fluid flow of the form:

$$\begin{cases} \rho_2\partial_t\boldsymbol{u}_2 = -\nabla p_2 & \Omega_2 \\ \nabla\cdot\boldsymbol{u}_2 = 0 & \Omega_2 \\ \boldsymbol{u}_2 = 0 & \partial\Omega_2\setminus\Gamma \\ \boldsymbol{u}_2 = \boldsymbol{u} & \Gamma. \end{cases}$$

Remark that this is an example in which the working hypothesis on $\mathcal{P}_2$ are not fulfilled at continuous level. However, after time discretisation, this problem can be solved by the proposed approach. Indeed, we use an implicit Euler scheme by substituting $\partial_t\boldsymbol{u}_2 \sim \frac{\boldsymbol{u}_2^n - \boldsymbol{u}_2^{n-1}}{\Delta t}$, then we apply the divergence operator to the resulting momentum equation obtaining:

$$\mathcal{P}_2 \begin{cases} -\Delta p_2^n = 0 & \Omega_2 \\ \partial_{\boldsymbol{n}_2} p_2^n = 0 & \partial\Omega_2\setminus\Gamma \\ \partial_{\boldsymbol{n}_2} p_2^n = -\frac{\rho_2}{\Delta t}(\boldsymbol{u}^n\cdot\boldsymbol{n}_2 - \boldsymbol{u}^{n-1}\cdot\boldsymbol{n}_2) & \Gamma. \end{cases}$$

The problem $\mathcal{P}_2$, decoupled from $\mathcal{P}_1$, is an ill-posed problem. Hence, a relaxed interface condition is used:

$$\partial_{\boldsymbol{n}_2} p_2^{n,k} + \alpha p_2^{n,k} = -\frac{\rho_2}{\Delta t}(\boldsymbol{u}^{n,k}\cdot\boldsymbol{n}_2 - \boldsymbol{u}^{n-1,\infty}\cdot\boldsymbol{n}_2) + \alpha p_2^{n,k-1},$$

where the k refers to the current domain decomposition iteration.

The solution of this system is featured by counter-propagating elastic waves at the interface Γ. When the wave has a short wavelength it is expected that its approximation requires a large number of Laplace-Beltrami eigenfunctions. Therefore, this test is a good benchmark to investigate the performance of the method both in

its purely offline version and with the online update correction. The results of this comparison are reported in Figure 6.3. In the left and center panel, the error with respect to the reference solution at the interface and in the whole domain are shown in norm $L^2((0,T);L^2(\Gamma))$ and $L^2((0,T);L^2(\Omega_1))$, as a function of the number of modes, both without (purely offline) and with the online update of the basis. The trends are similar, and it can be seen that the rate of convergence of the method without online update is almost linear, as predicted by the theoretical analysis. The online update guarantees that the error on the datum is always below a given threshold and allows a significant improvement in terms of accuracy (almost one order of magnitude in certain cases). On the right panel the computational costs are shown: the number of Laplace-Beltrami basis functions (on the x axis) is plotted against the number of online added basis functions (on the y axis), for different tolerances, namely $\{0.01, 0.005, 0.001\}$ in $L_2(\Gamma)$ representation of the datum. The total cost in terms of number of problems $\mathcal{P}_2$ solved is the sum of the two.

6.5.3 Two elastic cylinders in a Stokes flow

In the last testcase, a linear elasticity problem ($\mathcal{P}_1$) on two cylinders is coupled with a steady Stokes flow ($\mathcal{P}_2$). This is an example of a system in which $\mathcal{P}_1$ is defined on a domain which is the union of non-connected sets. Moreover, both the main and the external problems have vector unknowns, and the external problem is a saddle point problem. This test is used to assess the speed-up performances of the method.

The geometry is depicted in Fig. 6.4. The domain Ω_1 is composed of two cylinders attached to a basement and their displacement $\boldsymbol{\eta}$ is given by the linear elasticity equations:

$$\mathcal{P}_1 \begin{cases} \rho^s \dfrac{\partial^2 \eta}{\partial t^2} - \operatorname{div}(\boldsymbol{\sigma}^s) = 0 & \text{on } \Omega_1 \\ \boldsymbol{\sigma}^s = \dfrac{E\nu}{(1+\nu)(1-2\nu)} \operatorname{div}(\boldsymbol{\eta})\mathbf{I} + \dfrac{E}{2(1+\nu)}(\nabla\boldsymbol{\eta} + \nabla\boldsymbol{\eta}^T) & \\ \boldsymbol{\eta} = 0 & \text{on } \Gamma_B \\ \boldsymbol{\sigma}^s \boldsymbol{n}^s = -\boldsymbol{\sigma}^f \boldsymbol{n}^f & \text{on } \Gamma, \end{cases}$$

where Γ_B, the boundary of the basement, and Γ, the union of the surfaces of the two cylinders, are such that $\overline{\Gamma}_B \cup \overline{\Gamma} = \partial\Omega_1$. The two tensors $\boldsymbol{\sigma}^s$ and $\boldsymbol{\sigma}^f$ are the stress tensors of the structure and of the fluid, respectively. We also assume that the coupling conditions between the fluid and the structure are assigned only at the cylinders boundary Γ which, unlike the previous test cases, is not a connected set. The outward normal, with respect to Ω_1, is denoted by $\boldsymbol{n}^s$ while $\boldsymbol{n}^f = -\boldsymbol{n}^s$ is outward with respect to the fluid domain Ω_2. The physical parameters, ρ^s, E and ν represent the density of the solid, the young modulus and the poisson ratio, respectively. For this test we have used $\rho_s = 1, E = 1e4, \nu = 0.48$. The fluid is described by the steady Stokes equations:

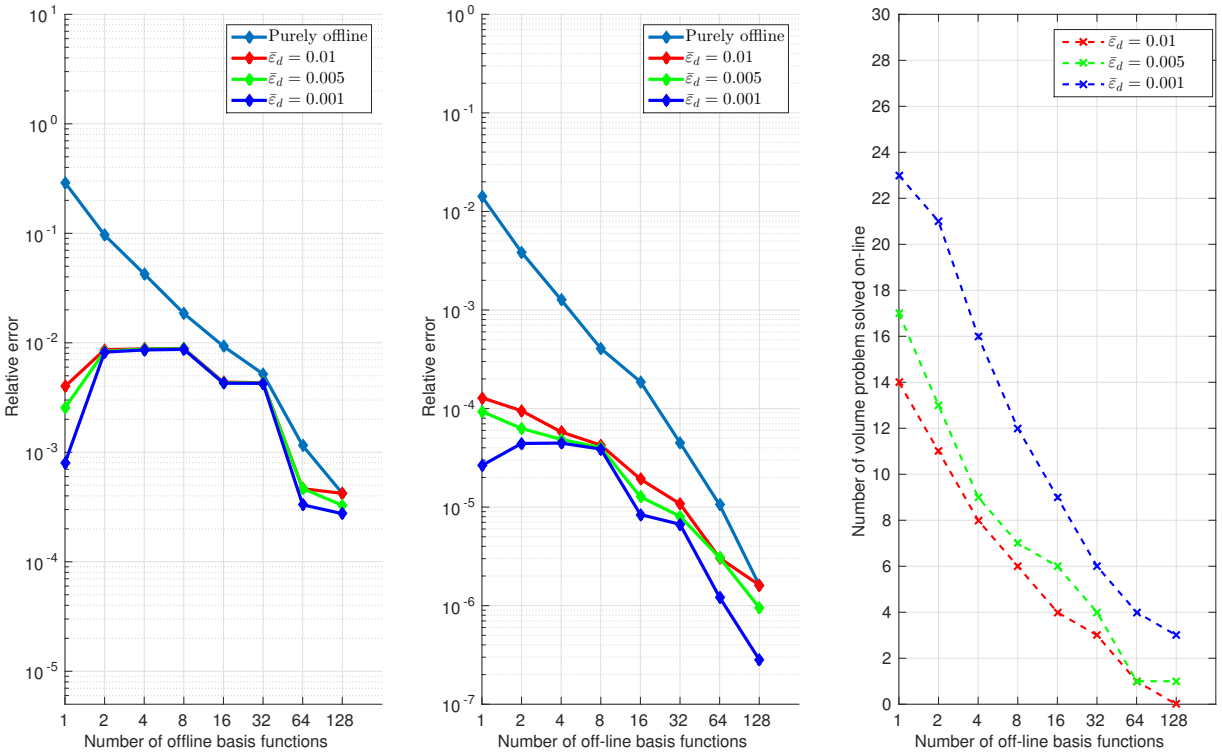

Figure 6.3: In the first two panels (left and center) the error of the reduced approach with respect to the corresponding finite element simulation is computed. In the left panel the relative error is computed with respect to $p_2|_\Gamma$ and it is measured with the $L^2((0,T);L^2(\Gamma))$-norm, while in the center panel the relative error on quantity p_1 is measured with an $L^2((0,T);L^2(\Omega_1))$-norm . The errors obtained with different approaches are compared for the offline method and for three different values of the tolerance parameter $\bar{\varepsilon}_d$: $\{0.01, 0.005, 0.001\}$. On the x-axis the number of offline basis function is reported, while on the third panel the number of basis functions that were added during the online phase is reported as a function of the offline basis dimension

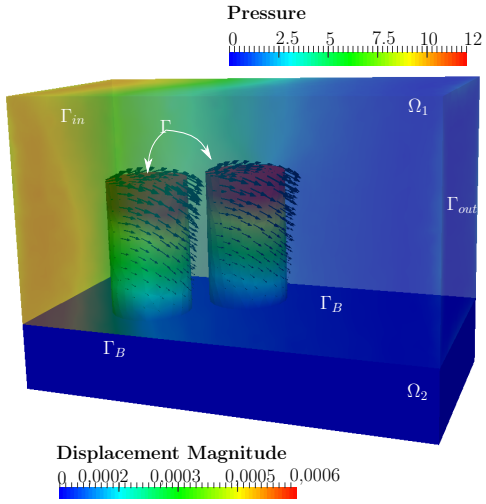

Figure 6.4: Solution of the complete problem at time $t = 0.00325102$. The color scale on the cylinders and on the basement represent the displacement, while the fluid domain is colored by the value of the pressure and transparent.

$$\mathcal{P}_2 \begin{cases} \operatorname{div}(\boldsymbol{\sigma}^f) = 0 & \Omega_2 \\ \operatorname{div} \boldsymbol{u} = 0 & \Omega_2 \\ \boldsymbol{\sigma}^f \boldsymbol{n}^f = 0 & \Gamma_{out} \\ \boldsymbol{\sigma}^f \boldsymbol{n}^f = -p_{in}(t)\boldsymbol{n}^f & \Gamma_{in} \\ \boldsymbol{\sigma}^f = \nu^f(\nabla \boldsymbol{u} + \nabla \boldsymbol{u}^T) - p\mathbf{I} & \\ \boldsymbol{u} = 0 & \Gamma_D \\ \boldsymbol{u} = \dot{\boldsymbol{\eta}} & \Gamma, \end{cases}$$

where $\boldsymbol{u}$ is the fluid velocity and p the pressure. The surface $\Gamma_{in} = \partial\Omega_2 \cap \{x = 0\}$ represents the inlet of the system. On the other side, $\Gamma_{out} = \partial\Omega_2 \cap \{x = 1\}$ is the outlet of the domain. On $\Gamma_D = \partial\Omega_2 \setminus (\Gamma_{in} \cup \Gamma_{out} \cup \Gamma)$ no slip boundary conditions are enforced. The parameter ν^f represents the kinematic viscosity and it was set to 0.035.

The inlet pressure is prescribed by

$$p_{in}(t) = \begin{cases} 10 & t < 0.05 \\ 10(1 - \frac{t-0.05}{0.075-0.05}) & 0.05 < t < 0.075 \\ 0 & t > 0.075 \end{cases}$$

An implicit Euler scheme has been used for the time discretization of the structural problem, with a time step $\delta t = 1.806125 \cdot 10^{-4}$ and P1 finite elements are used for space discretization. For the Stokes problem, we use P1-P1 stabilized finite

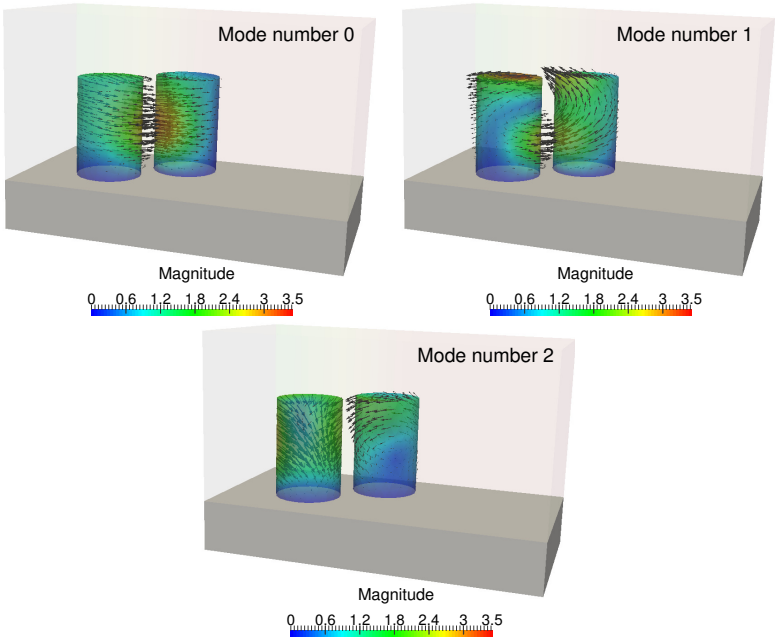

Figure 6.5: First three eigen-functions of the Poincaré-Steklov operator for the Stokes problem. The reconstruction is based on 50 Laplace-Beltrami eigenfunctions.

elements. A snapshot of the reference solution obtained through this discretization is reported in Fig. 6.4. For what concerns space discretization we have used 20920 tetrahedra for Ω_1 and 47735 for Ω_2. The number of nodes at the interface is 663, which means 1989 degrees of freedom for the displacement. The final time of the simulation was $T = 0.2$ for a total number of time steps equal to: 1108.

The coupling is imposed through a Dirichlet to Neumann map, that, as investigated in section 6.4, is featured by a slower convergence rate. The Laplace-Beltrami eigenfunctions used to sample the input space are, in this case, the solution of a vector eigenvalue problem on the cylinders surface. As a post-processing, following Section 6.3.3, we can approximate the Steklov eigenfunctions and the result is shown in Figure 6.5. In this case, the Poincaré-Steklov eigenfunctions are non-zero on the whole interface, even though it is the union of non-connected sets. The action of the Poincaré-Steklov operator couples the movement of the two cylinders. Moreover, for the present case, the physical dissipation of the elastic cylinders is purely induced by the coupling with the external Stokes flow and hence the dissipation is related to the Steklov eigenvalues.

In order to verify the quality of the reduced solution, we have reported the displacement of the center of the cylinders in Figure 6.6. We can see that few modal functions are enough to reproduce the correct displacement, even without online update. Observe that one basis function is, however, not sufficient to represent the system dissipation, and the oscillation of the cylinders tend to be largely underdamped.

In order to analyse in detail the computational costs of the method, different

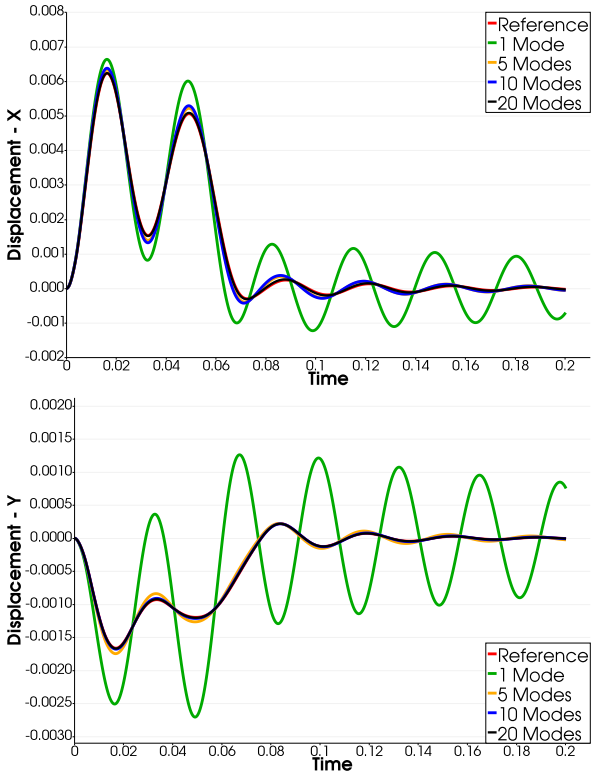

Figure 6.6: The displacement of the center point on the top of the first cylinder: x-component on the left and y-component on the right. The reduced approach is compared with the reference, finite-element solution by varying the number of modes in $\{1, 5, 10, 20\}$.

	$\tau_{\mathcal{P}_2}\,[s]$	$\tau^*_{\mathcal{P}_2}\,[s]$	ζ_S	$\tau_{\mathcal{P}_1}\,[s]$	$N_{dd}\,[-]$	ζ_{dd}	$\tau_{\text{it}}\,[s]$	ζ
Reference	1.06204	1.06425	1.0	0.640	6.06	1.00	10.309	1.00
$N_\ell = 1$	0.00105	0.01181	1011.5	0.609	2.96	2.05	1.805	5.71
$N_\ell = 10$	0.00136	0.01527	780.9	0.625	3.43	1.77	2.145	4.81
$N_\ell = 20$	0.00173	0.02764	613.9	0.617	3.52	1.72	2.176	4.74
$N_\ell = 40$	0.00233	0.03872	455.8	0.629	3.53	1.72	2.231	4.62

Table 6.2: Perfomance of the method for different number of basis functions.

parameters are measured:

- $\tau_{\mathcal{P}_2}$ is the averaged time needed for one fixed point iteration for the Stokes problem;
- $\tau^*_{\mathcal{P}_2}$ takes into account also the offline costs, *i.e.* $\tau^*_{\mathcal{P}_2} = \tau_{\mathcal{P}_2} + \delta$ where δ is the amortised cost of the offline phase computed as the ratio between the total cost of the offline phase and the number of online evaluations of the reduced representation of the operator;
- ζ_S is the ratio between $\tau_{\mathcal{P}_2}$ of the reference method and $\tau_{\mathcal{P}_2}$ of the reduced method;
- $\tau_{\mathcal{P}_1}$ is the averaged time needed for one fixed point iteration for the structure problem;
- N_{dd} is the averaged number of domain decomposition iterations per time step;
- ζ_{dd} is the ratio between the N_{dd} of the reference and the reduced method;
- τ_{it} is the average time needed for an entire time step;
- ζ is the average speed-up per time step, *i.e.* the ratio of the τ_{it} between reference and reduced methods.

The results for this test case have been obtained using GMRES preconditioned by a Restricted Additive Schwarz method, implemented in the PETSc library (PCASM), both for $\mathcal{P}_1$ and $\mathcal{P}_2$. The performances are summarized in Table 6.2. Observe that the reduction of the Stokes problem has been quite effective and it is between two and three orders of magnitude: the time required for the Stokes problem is negligible compared to the time needed for $\mathcal{P}_1$. By comparing the first two columns we also observe that, in this example, the offline costs are well amortised during the offline phase and that their impact is negligible compared to the reference cost. It is remarkable that, for this problem, the Reduced Order Model has also a regularising effect on the Domain Decomposition, so that the average number of iterations to achieve convergence is decreased with respect to the full-order method. This element contributed to the overall speed up, that, on one single simulation, results of about 4.5 (see the last two columns of the table), offline costs included.

6.6 Conclusions and perspectives

A Reduced-Order Modeling method has been presented to approximate the action of the Poincaré-Steklov operator for systems in which a non-linear complex model of interest ($\mathcal{P}_1$) is coupled to an external problem ($\mathcal{P}_2$). The approach aims at reducing the problem $\mathcal{P}_2$ whose solution is not necessarily of interest. It relies on an *offline* stage in which a sampling of possible inputs at the interface is done by means of the eigenfunctions of the Laplace-Beltrami operator. The main advantage of this choice is twofold: first, the eigenfunctions are obtained by a sparse eigenvalue problem defined at the interface only and enjoy desirable properties of approximation; second, this allows to make the offline phase independent of $\mathcal{P}_1$ and the coupling. The problem $\mathcal{P}_2$ is solved and the images of the Poincaré-Steklov operator are stored. An *online* update has been presented to make the method more robust to off-database cases. The numerical tests proposed, in 3D, confirmed that the method is simple and effective in a large variety of cases, being able to make the costs associated to the solution of $\mathcal{P}_2$ negligible compared to the costs associated to the solution of $\mathcal{P}_1$. Several perspectives arise, concerning the reduction of multiple external problems and networks of systems in interaction, the ability to deal with parametrized problems and the set-up of a more general approach to reduce non-linear external problems.

6.7 Appendix

In this part, a sufficient condition for the eigenfunctions of the Poincaré-Steklov operator to coincide with the eigenfunctions of the Laplace-Beltrami operator on the interface is given.

Proposition 2
Let $\Omega_2 = \mathcal{M}_1 \otimes \ldots \otimes \mathcal{M}_d \subseteq \mathbb{R}^d$ be the domain for $\mathcal{P}_2$. It is expressed as the cartesian product of 1D manifolds, and it admits a generalised orthonormal set of coordinates such that the Laplace equation is separable. Moreover Γ is a codimension-1 submanifold, which is defined by $x_1 = 0$. Let $\mathcal{P}_2$ be the Laplace equation defined on Ω_2. Then the eigenfunctions of the Poincaré-Steklov operator coincide with the eigenfunctions of the Laplace-Beltrami operator defined on Γ. ***Proof.*** *The Laplace equation written for a generic orthonormal curvilinear system reads:*

$$\Delta u_2 = \sum_{j=1}^{d} \frac{1}{h_j} \partial_{x_j} \left(g_j \partial_{x_j} u_2 \right) = 0,$$

where h_j, g_j contains the metric factors and are functions of the coordinates. The

Steklov eigenvalue problem reads:

$$\begin{aligned} -\Delta u_2 &= 0, \quad \text{on } \Omega_2 \\ \partial_n u_2 + \alpha u_2 &= \lambda u_2, \ \text{on } \Gamma \\ u_2 &= 0, \quad \text{on } \partial\Omega_2/\Gamma. \end{aligned}$$

By hypothesis u_2 admits a separable representation, i.e.

$$u_2 = \prod_{j=1}^{d} \hat{u}_j(x_j).$$

This expression is plugged into the eigenvalue equation leading to:

$$\begin{aligned} -\sum_{j=1}^{d} \left(\prod_{k\neq j}^{d} \hat{u}_k \right) \frac{1}{h_j} \partial_{x_j} \left(g_j \partial_{x_j} \hat{u}_j \right) &= 0, \quad \text{on } \Omega_2 \\ \frac{1}{h_1} \partial_{x_1} \hat{u}_1 \left(\prod_{k\neq 1}^{d} \hat{u}_k \right) + (\alpha - \lambda) \left(\prod_{k=1}^{d} \hat{u}_k \right) &= 0, \ \text{on } \Gamma \\ \left(\prod_{k=1}^{d} \hat{u}_k \right) &= 0, \quad \text{on } \partial\Omega_2/\Gamma. \end{aligned}$$

The system is equivalent to the following:

$$\begin{aligned} -\sum_{j=1}^{d} \frac{1}{\hat{u}_j} \frac{1}{h_j} \partial_{x_j} \left(g_j \partial_{x_j} \hat{u}_j \right) &= 0, \quad \text{on } \Omega_2 \\ \frac{1}{h_1} \partial_{x_1} \hat{u}_1 + (\alpha - \lambda) \hat{u}_1 &= 0, \ \text{on } \Gamma \\ \left(\prod_{k=1}^{d} \hat{u}_k \right) &= 0, \quad \text{on } \partial\Omega_2/\Gamma. \end{aligned}$$

The first equation can be decoupled into a system of d independent equations of the form:

$$\frac{1}{h_j} \partial_{x_j} \left(g_j \partial_{x_j} \hat{u}_j \right) = c_j \hat{u}_j.$$

with the closure condition:

$$-\sum_{j}^{d} c_j = 0.$$

On all the boundary except for Γ there are homogeneous boundary conditions. The solution of the $d-1$ equation for the coordinates $x_{2,\ldots,d}$ is thus obtained by using $c_j < 0$ and it is a set of harmonic oscillations in the direction x_j. As consequence

$c_1 > 0$ and it holds:

$$c_1 = -\sum_{j=2}^{d} c_j.$$

Moreover, when considering the conditions on Γ, the equation along x_1 reads:

$$\begin{aligned} \frac{1}{h_1}\partial_{x_1}\left(g_j \partial_{x_1}\hat{u}_1\right) &= c_1 \hat{u}_1, \\ \frac{1}{h_1}\partial_{x_1}\hat{u}_1 + (\alpha - \lambda)\hat{u}_1 &= 0, \text{ on } \Gamma \\ \hat{u_1} &= 0, x_1 = 1. \end{aligned}$$

When solved, this equation provides a relationship between λ and c_j. When restricted to Γ the solution of the problem reads:

$$u_2|_\Gamma = \hat{u}_1(0)\left(\prod_{j=2}^{d}\hat{u}_j(x_j)\right),$$

which is the set of the Laplace-Beltrami eigenfunctions on Γ up to normalisation. ■

Although the hypothesis for this condition to hold true are quite restrictive, they are common to a broad class of different problems and geometrical settings (think for instance to boxes, concentrical cylinders).

Chapter 7
Conclusions

This thesis dealt with the mathematical modelling of the eye with a particular focus on hemodynamics. The study of the interactions between different compartments characterized by different physics has been a common topic throughout the entire manuscript.

In Chapters 2 and 3 we proposed a simplified fluid-structure interaction model for the description of arterioles. The application we had in mind was the study of retinal autoregulation, but the model can be applied to arterioles in general. The use of a non-linear Koiter model combined with a layer of oriented fibers allowed us to model the arteriole vessel wall and to include a layer of smooth muscle cells. The use of a fixed mesh supported by a first-order transpiration made possible to keep the computational costs low enough to run simulations over a quite large image-based network of retinal arterioles. The approach leaded to numerical results in good agreement with published experimental data and it represents, to the best of our knowledge, the first attempt to model blood flow in a 3D network of retinal arteries, including autoregulation. However, some limitations remain and there is room for improvement in the model. First, despite working with small vessels we used a Newtonian model for the fluid ignoring the Fahraeus and the Fahraeus-Lindqvist effects. Second, the layer of smooth muscle cells contracts and dilates in response to an external stimulus, but the mechanisms behind the generation of such stimulus based on the physiological state of the tissue have not been included in this work. Third, the network of arterioles considered in the numerical experiments is completely isolated from the rest of the eye. The description of the downstream circulation, capillaries and venules, and of the surrounding tissues could be refined.

A step forward in this direction was done in the following chapters where we started working on a global model of the eye, where the retinal arterioles network could be included as well. In Chapter 4 we reviewed the medical and modelling literature on the fluid and structure mechanics of the eye. This review is not meant to be complete, but it was necessary for devising the models used in Chapter 5 and it represents a good introduction to the modelling of the eye. In Chapter 5 we worked on a global model of the eye. We explained our approach and the simplifying assumptions that were necessary for modelling such a complex organ. We presented a poro-elastic model for choroid hemodynamics and the Navier-Stokes-Boussinesq system for the flow in the anterior cavity. The model of the global is not complete yet, but we reported promising preliminary results on the flow in the anterior cavity, on the pore-pressure distribution in the choroid and on the coupling of the choroid

with the vitreous compartment. We are currently working on the extension of the model to a larger number of compartments to include the sclera, the cornea and the anterior cavity.

Finally, in Chapter 6 we presented a reduced order modelling technique to speed up multi-physics simulations. The technique has been tested on different applications where the nature of the coupled systems varied (two examples of fluid-fluid interaction and one of fluid-structure interaction). The results were good in terms of accuracy and speed-up. We also proved the convergence to the exact solution as the number of modal functions increases. However, the approach is now limited, for the secondary problem, to linear stationary equations and it would be worth to extend this approach to a wider class of problems and to consider its application as a preconditioner in domain decomposition loops.

Appendix A

A new tool to connect blood vessels in fundus retinal images

We annexed a proceeding of the conference EMBC 2015 (the 37th annual international conference of the IEEE Engineering in Medicine and Biology Society). In this work a semi-automic tool for the connection of vessels segments in retinal fundus images is presented.

A number of algorithms perform vessels segmentation in fundus images. Most of them provide a binary image to indicate whether a certain pixel is a vessel or it is the background. Others are able to recognise vessels segments and to provide useful features such as the shape and the width. However, these tools are not perfect and vessels networks result in a set of disconnected segments. In order to reconstruct the original network, we need to compute the connectivity. The approach we have followed is to use machine learning to join the segments. The tool presented in this work represents a step forward towards the automatization of the extraction of vessels network from retinal fundus images.

My role in this work was mostly in the implementation phase. I worked on the design and on the implementation of the data-structures for storing the segments and the networks. Moreover, I contributed to the extraction of the local features and to data visualization. The algorithm for the automatic detection of the connectivity was mainly developed by the other authors.

A New Tool to Connect Blood Vessels in Fundus Retinal Images*

Francesco Calivá[1], Matteo Aletti[2], Bashir Al-Diri[1], Andrew Hunter[1]

Abstract— **This paper presents a novel tool that allows a user to reconstruct the retinal vascular network from fundus images. The retinal vasculature consists of trees of arteries and veins. Common segmentation algorithms are not able to completely segment out the blood vessels in fundus images. This failure results in a set of disconnected or broken up vascular segments. Reconstructing the whole network has crucial importance because it can offer insight into global features not considered so far, including retinal fluid dynamics. This tool uses implicit neural cost functions to join vessel segments. Results have shown that the quality of the segmentation affects the outcome of connectivity algorithms and by enhancing the segmentation the connectivity can be improved.**

Keywords: vessels connectivity, junction resolution, connectivity tool, retinal trees.

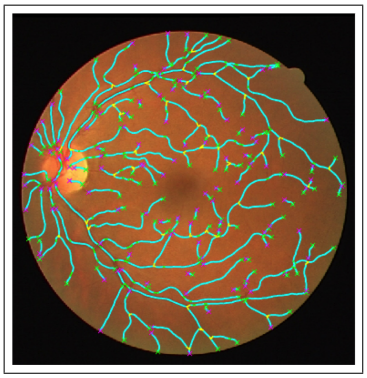

Fig. 1. Vascular graph obtained employing our tool on the first image of the DRIVE database [11].

I. INTRODUCTION

Several studies have proven that systemic diseases affect blood vessels' geometry [1]. The estimation of changes in the vascular geometry can help to diagnose or predict such diseases [2]. These include local pathologies that affect the heart, including stroke [3] or systemic diseases (e.g. diabetic retinopathy [4], hypertension [5]). The *retina* provides a noninvasive view of the vascular system. In this paper a new user-friendly tool that is able to recreate the retinal vascular network from segmented retinal vessels is presented. The segmentation of whole trees provides an opportunity to extract features that were not considered before, which can help studying the fluid dynamics within the retinal network. The platform is completely written in Matlab (The MathWorks Inc., Natick, MA, United States). It may be employed with the potential to detect changes which reflect the presence of disease. Despite the importance of this topic, few works are available in the literature [6] [7] [8] [9]. Usually the studies focus on the segmentation of blood vessel with few attempts to solve the connectivity problem. Many segmentation algorithms are accessible in the literature [2] [10] [11] [12]. They are often more accurate in detecting the vascular segments than the junctions. Some portions of blood vessels inside the junctions may be missed during the segmentation and the final result is an image partially segmented with a set of disconnected or broken up segments available; this makes difficult to carry out a full analysis of blood vessels' condition from standard imaging methodologies.

In the following section an overview of the literature is presented. In section III we describe the method used in our study. Finally, the results are presented in section IV and discussed in section V.

II. RELATED WORK

Can et al. [7] carried out the first study with an attempt to automatically extract features from vessels after segmentation. In [7] the blood vessels were represented using the centre line. The point where two or more segments intersect was considered the junction's centre. The intersection angles were calculated. This algorithm performed very well in solving small and easy junctions (e.g. bifurcations, crossings) with 3-4 segments, whereas it tended to fail in the presence of larger or more complex junctions. Later [6] presented a novel and sophisticated algorithm that was able to resolve complex junctions even in the presence of *broken-up* or *overlapping* vessels; segments were joined using a combination of a search area algorithm and neural cost functions, based on trained *self organizing feature maps* (SOFM). SOFMs belong to unsupervised artificial neural network models which can be employed for classification. During training, the SOFMs create *prototype vectors*. When applied, SOFMs produce a signal that expresses the Euclidean distance of the new data from the nearest prototype. In [6], segments were grouped in small local sets using *projective intersection* algorithm. Starting from both the end points, this algorithm projected centre lines and detected if any intersection

*This project has received funding from the European Union's Seventh Framework Programme for research, technological development and demonstration under grant agreement no 316990

[1]Francesco Calivá, Department of Computer Science, University of Lincoln, UK fcaliva@lincoln.ac.uk

[2]Matteo Aletti, Inria Paris-Rocquencourt & Sorbonne Universits UPMC Univ Paris 6, France matteo.aletti@inria.fr

[1]Bashir Al-Diri is a senior lecturer at the Department of Computer Science, University of Lincoln, UK baldiri@lincoln.ac.uk

[1]Andrew Hunter is Pro Vice Chancellor, University of Lincoln, UK ahunter@lincoln.ac.uk

978-1-4244-9270-1/15/$31.00 ©2015 EU

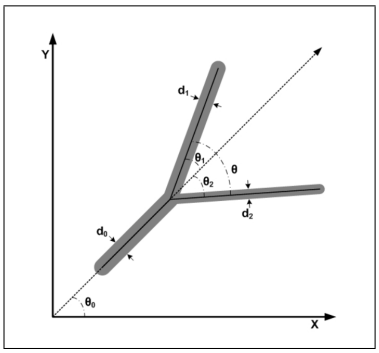

Fig. 2. The bifurcation features: diameters (d_i) and vessels direction described in terms of angles θ_i

occurred. Furthermore, [6] evaluated and quantified if the three lines, which respectively started from the centre point and the two edges of a segment end, intersected with the line that connected the two edges of another segment. The total number of collisions defined the *collision score*. To recognise the proper joining form, [6] created the datasets for the detection of bifurcations and bridges based on the extraction of features from observed instances (Fig. 2). This algorithm performed very well in the presence of large and complex junctions. Tsai et al. [9] developed a vessel tracing algorithm which solved the connectivity only for vessels branching or crossings. Recently [8] implemented a Bayesian framework to connect segments. This algorithm first separated the individual segments into a noncomplex network by grouping them into *junctions* and then joined them based on a Maximum a Posteriori (MAP) estimation. [8] showed poor results for large junctions.

We started our study by first evaluating which common artifacts led previous researches to a poor solution of the connectivity. In most of the cases, false and missing segments were the main cause. They both interfere with the generation of correct junctions. A direct consequence is the evaluation of possible connection between segments which shouldn't be considered together. Our tool, presented in this paper, addresses the connectivity problem, first by grouping subsets of segment ends into *cliques*, then an algorithm based on SOFM [6] allows to identify how likely the segments are to be connected. Our novel tool allows a user to identify the presence of false and missing segments, improving the final outcome of the connectivity.

III. METHOD

The *DRIVE Segment-Junction Set (DSJS)* [13] has been used to develop and test the tool. In this version of the *DRIVE database* (Digital Retinal Images for Vessel Extraction) [11] all the junction points, including bifurcations and crossings, have been removed thus all segments are isolated. Our task is to join the segments in order to reconstruct the whole retinal vascular network. The retinal vasculature consist of a forest of arterial and venous trees. Due to segmentation artifacts, the blood vessels appear broken in small segments. Each segment has two ends (e.g. for the i^{th}-segment they are s_i^1 and s_i^2). The tool includes an algorithm which first groups segments ends in small subsets forming cliques; then solves these local configurations. Within a clique, segments can be terminal, otherwise their ends can be connected in two ways:

- three ends can be joined to recreate a bifurcation;
- two ends can be connected to form a bridge;

Trifurcations have been treated as two consecutive bifurcations, where the second one's parent has length zero.

A. Calculating local segment profiles

The local segment profile gathers all the information used to study each segment within the network. Given the i^{th}-segment, first step is the *centre line extraction*. With this aim, using the vessel's edges coordinates, we applied the mathematical mean to obtain the centre line.

$$x_{i,c} = \frac{\sum_{j=1}^{2} x_{i,j}}{2}; y_{i,c} = \frac{\sum_{j=1}^{2} y_{i,j}}{2} \quad (1)$$

In (1), the index j refers to the i^{th}-vessel's edge. For each segment, we considered the information regarding the centre points located at the two extreme ends. To reduce errors (e.g. in case of segmentation artifacts), these particular centre points were calculated by averaging the x and y coordinates of the three last centre points at each of the two ends. We considered the following features: *local segment direction, local vessel diameter and local segment pixel intensity*.

- segment directions ($d_{i,j}, i = 1,2..N; j = 1,2$): edges and centre line were used to extract the features related to the segment's direction. First, we calculated for each segment, the edges' directions ($d_{i,e}$) along three points at each end. We considered the same number of points to calculate the centre line's direction ($d_{i,c}$). Also the vectors perpendicular to the cross section were taken into account ($d_{i,p}$). Finally we obtained the segment's direction as average of ($d_{i,e}$), ($d_{i,c}$) and ($d_{i,p}$);
- vessel diameter (D_i): at both the segment's ends, the distances between the two edges along three centre line points were averaged to calculate the vessel diameter;
- segment pixel intensity (SPI_i): we considered the green channel of the fundus image (I). Points inside the vessel were selected and we calculated the pixel intensity profiles using a bilinear interpolation tuning properly some weight parameters ($w_{k,p}, k = (1,2), p = 1,..P$ number of points considered) along x and y axis.

$$SPI_i = \sum_{p=1}^{P} \prod_{k=1}^{2} w_{k,p} * I \quad (2)$$

B. Generating cliques

A clique represents a group of segment ends which might be connected together. Each segment end belongs to only one clique. The clique generation started, growing a search area from each segments ends. The size of these regions directly affected the outcome of the connectivity algorithm, thus an optimal value was obtained empirically (Fig. 3). We found that the dimension of the search areas ($r_{searchArea}$) could be related to the image resolution or to the length

l_i of the i^{th}-segment under study. In particular, given w_I and h_I, respectively image's width and height:

$$r_{searchArea} = \begin{cases} \frac{max(w_I,h_I)}{20} & l_i \geq \frac{max(width,height)}{10} \\ \frac{l_i}{2} & otherwise \end{cases} \quad (3)$$

All the segments ends located within the search area, became members of the clique. Also, if two segments had both a third segment within their search area, the three search areas would be merged creating a big clique. At the end of this stage, the largest cliques could have nine segment ends.

C. Cost Function

The requirement to evaluate if two (or more) segments could be joined was the presence of intersections among them. First, the centre line of both the segments were grown. Three possible intersections could occur. The first was between the two centre lines. The others among each grown centre line and the line which connected the end points of the other segments' edges. The big challenge was to recognise the most appropriate way to join segments. Both bifurcation (Bif_{cost}) and bridge (Br_{cost}) costs were a combination of the intersection credit ($C_{i,j} = n_{i,j}/3$, where $n_{i,j} = [1,2,3]$ are the n collisions between the segments i and j) and the optimal cost given by the SOFMs' output described in section II. $Bif_{cost} = Bif_{SOFM}(1 - C_{1,2}C_{2,3}C_{3,1})$ $Br_{cost} = Br_{SOFM}(1 - C_{1,2})$. Once calculated all the possible joining combination for each segment end, the cost of being a terminal was defined as: $Term_{cost} = 1 - min(Bif_{cost}, Br_{cost})$.

D. Removing false segments

We observed that errors in solving the cliques occurred in the presence of false vessels, missing or overlapping segments. A false vessel consists of a set of pixels which during the segmentation was wrongly considered as belonging to a blood vessels. Typically, this error can be due to image blurry, sudden change of intensity within the background, or presence of lesions. Our tool allows the user to remove false segments from the segmentation results just with a mouse click at the location of one of the pixels which contain that particular segment (Fig. 4).

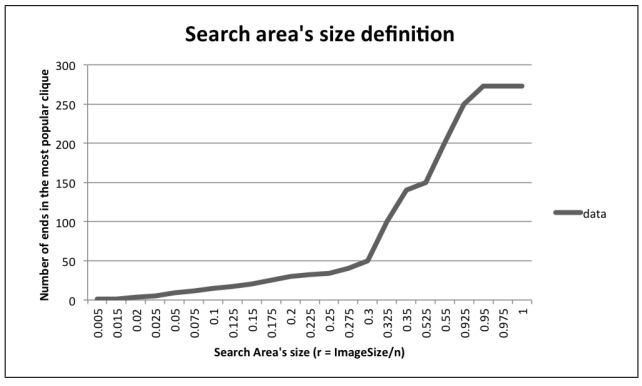

Fig. 3. A relation between the search area's size and the image resolution has been found. Large search areas reflect into cliques too popular ($n_{members} > 9$), which are difficult to solve. The optimal search area has been chosen so that the largest cliques discovered in our training sets have nine segment ends.

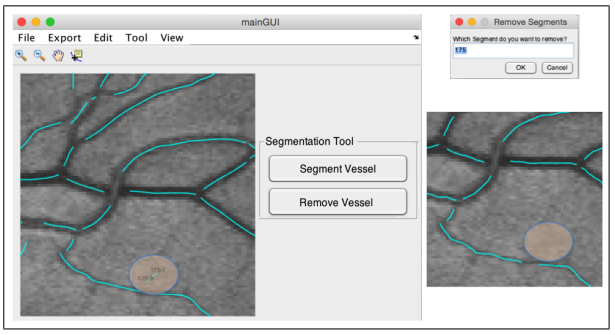

Fig. 4. False Segments Removal.

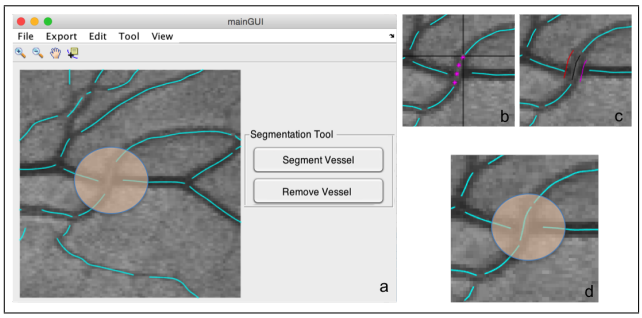

Fig. 5. Missing Segments Segmentation.

E. Segmenting missing segments

Missing segments are the result of the segmentation in areas where the blood vessels' edges are not clearly visible. Low contrast between background and the vessel lumen is the most common cause. Overlapping segments were found between two vessels running parallel to each other or at vessels' crossing. In both cases they were detected as a singular, wider vessel. With our tool these problems can be addressed (Fig. 5). We implemented a supervised segmentation algorithm for missing segments. This consists of the following steps:

- missing segment identification (Fig.5a);
- vessel centre lines definition;
- segmentation starting points seeding. The user should select these points, clicking with the mouse above the image's pixel which represent a non-segmented blood vessel (Fig.5b);
- smoothing centre lines using the *Lagrange polynomials*:

$$p(x) = \sum_{i=0}^{n} \left(\prod_{\substack{0 \leq j \leq n \\ j \neq i}} \frac{x - x_j}{x_i - x_j} \right) j_i \quad (4)$$

- automated blood vessels segmentation, defining the edges' location using the Gregson's algorithm [14] to estimate the segment's width (Fig.5c-d).

F. Repairing connectivity errors

In presence of errors, the user can act following a *Connectivity Error Repair* approach. Our interactive algorithm requires a mouse click above one of the segments which belong to the junction to be repaired. Then, the user is

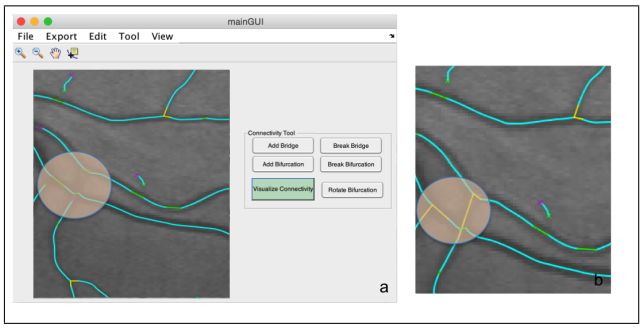

Fig. 6. Connectivity Error Repair. Two bridges have been broken (a) and replaced with two bifurcations (b).

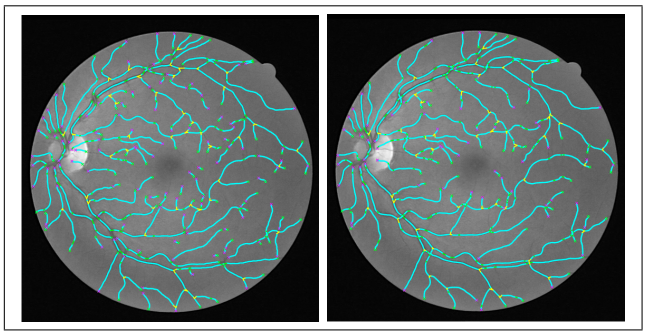

Fig. 7. The vascular network of the first retinal image in the DRIVE database [11]: (left) using the DSJS (left); (right) after the application of our Connectivity Error Repair tool.

guided along the process of adjusting the connectivity errors. This can be achieved by breaking bridges and bifurcations or creating new joints (Fig. 6).

Our tool gathers together all the functions previously described. The design of a *Graphic User Interface* (GUI) allows the user to easily access all functionality.

IV. RESULTS

In order to evaluate the performance of the proposed tool, we used the DRIVE database [11], which contains 8157 segment ends. Fig. 7-left shows the outcome of the connectivity algorithm applied to the first image of the aforementioned database. From the experiments, our tool was able to correctly connect 72.1% of the segments. 6.1% of the cliques were in part solved correctly whereas 21.8% were not solved at all. 8.4% of the failures were due to segmentation while 2.5% to the cliques' generation. Fig. 7-right shows how the results improve by increasing the segmentation accuracy. Our segmentation-repairing tool allowed us to isolate the errors attributable to segmentation and thereby to increase the performance of the connectivity algorithm to 77.3%. Additionally, we tested our tool on images of chicken chorioallantoic membrane vessel network, which evidenced the adaptability and robustness of our tool to research field not strictly related to the retinal imaging.

V. CONCLUSIONS

So far, the physiological principles behind the formation of vascular junctions have not been completely understood. In this work, we observed real bifurcations and bridges and we extracted their geometrical information in order to automatically recognise how vessel segments should be connected. The tool proposed in this work allows to solve the connectivity problem and repair possible errors. It was observed that false and missing segments directly affect the accuracy of the final result, and thus by using our segmentation enhancement tool the performance of the algorithm improved both the location and the solution of the cliques. Experiments using the DRIVE database were performed in order to test this tool. However, we intend to extend the experimental validation process to other public retinal image databases. To sum up, this work provides a friendly tool that can be extended to other research fields than the retinal imaging such as the analysis of the abnormalities in vessel branching in cerebral vascular patterns derived from MR Angiography, making this tool of further interest for clinical and research applications.

ACKNOWLEDGMENT

Weiwei Xiang, Institute for Physiology, Charité Universittsmedizin Berlin, thanks for testing our tool.

REFERENCES

[1] A. V. Stanton, B. Wasan, et al. Vascular network changes in the retina with age and hypertension. Journal of Hypertension, 13:17241728, 1995.
[2] Al-Diri, Bashir, Andrew Hunter, and David Steel. "An active contour model for segmenting and measuring retinal vessels." Medical Imaging, IEEE Transactions on 28.9 (2009): 1488-1497.
[3] Witt, Nicholas, et al. "Abnormalities of retinal microvascular structure and risk of mortality from ischemic heart disease and stroke." Hypertension 47.5 (2006): 975-981.
[4] Cheung, Ning, et al. "Quantitative assessment of early diabetic retinopathy using fractal analysis." Diabetes care 32.1 (2009): 106-110.
[5] Hughes, Alun D., et al. "Quantification of topological changes in retinal vascular architecture in essential and malignant hypertension." Journal of hypertension 24.5 (2006): 889-894.
[6] Al-Diri, Bashir, et al. "Joining retinal vessel segments." BioInformatics and BioEngineering, 2008. BIBE 2008. 8th IEEE International Conference on. IEEE, 2008.
[7] Can, Ali, et al. "Rapid automated tracing and feature extraction from retinal fundus images using direct exploratory algorithms." Information Technology in Biomedicine, IEEE Transactions on 3.2 (1999): 125-138.
[8] Qureshi, Touseef Ahmad, Andrew Hunter, and Bashir Al-Diri. "A Bayesian Framework for the Local Configuration of Retinal Junctions." Computer Vision and Pattern Recognition (CVPR), 2014 IEEE Conference on. IEEE, 2014.
[9] Tsai, Chia-Ling, et al. "Model-based method for improving the accuracy and repeatability of estimating vascular bifurcations and crossovers from retinal fundus images." Information Technology in Biomedicine, IEEE Transactions on 8.2 (2004): 122-130.
[10] Frangi, Alejandro F., et al. "Multiscale vessel enhancement filtering." Medical Image Computing and Computer-Assisted InterventationMICCAI98. Springer Berlin Heidelberg, 1998. 130-137.
[11] J.J. Staal, M.D. Abramoff, M. Niemeijer, M.A. Viergever, B. van Ginneken, "Ridge based vessel segmentation in color images of the retina", IEEE Transactions on Medical Imaging, 2004, vol. 23, pp. 501-509.
[12] Chaudhuri, Subhasis, et al. "Detection of blood vessels in retinal images using two-dimensional matched filters." IEEE Transactions on medical imaging 8.3 (1989): 263-269.
[13] DSJS, available at *http://reviewdb.lincoln.ac.uk*,
[14] P. Gregson, Z. Shen, R. Scott, and V. Kozousek, Automated grading of venous beading, Comput. Biomed. Res., vol. 28, no. 4, pp. 291-304, 1995.

Bibliography

[ACS08] Julia C. Arciero, Brian E. Carlson, and Timothy W. Secomb. Theoretical model of metabolic blood flow regulation: roles of ATP release by red blood cells and conducted responses. *American Journal of Physiology - Heart and Circulatory Physiology*, 295(4):H1562–H1571, 2008.

[ADHS09] Bashir Al-Diri, Andrew Hunter, and David Steel. An active contour model for segmenting and measuring retinal vessels. *IEEE Transactions on Medical Imaging*, 28(9):1488–1497, 2009.

[AGL16a] Matteo Aletti, Jean-Frédéric Gerbeau, and Damiano Lombardi. Modeling autoregulation in three-dimensional simulations of retinal hemodynamics. *Journal for Modeling in Ophthalmology*, 1(1):88–115, 2016.

[AGL16b] Matteo Aletti, Jean-Frédéric Gerbeau, and Damiano Lombardi. A simplified fluid–structure model for arterial flow. application to retinal hemodynamics. *Computer Methods in Applied Mechanics and Engineering*, 306:77–94, 2016.

[AGPT09] M. Astorino, J-F. Gerbeau, O. Pantz, and K. Traoré. Fluid-structure interaction and multi-body contact. Application to aortic valves. *Comp. Meth. Appl. Mech. Engng.*, 198:3603–3612, 2009.

[AHS+13] Julia Arciero, Alon Harris, Brent Siesky, Annahita Amireskandari, Victoria Gershuny, Aaron Pickrell, and Giovanna Guidoboni. Theoretical analysis of vascular regulatory mechanisms contributing to retinal blood flow autoregulation. *Investigative Ophthalmology & Visual Science*, 54(8):5584–5593, 2013.

[AL85] V.I. Agoshkov and V.I. Lebedev. Poincaré-Steklov's operators and the methods of partition of the domain in variational problems. *Computational Processes and Systems*, 2:173–227, 1985.

[AL17] Matteo Aletti and Damiano Lombardi. A reduced order representation of the Poincaré-Steklov operator: an application to coupled multi-physics problems. *International Journal for Numerical Methods in Engineering*, 2017.

[AN09] Albert Alm and Siv FE Nilsson. Uveoscleral outflow–a review. *Experimental eye research*, 88(4):760–768, 2009.

[APV15] Matteo Aletti, Simona Perotto, and Alessandro Veneziani. Educated bases for the HiMod reduction of advection-diffusion-reaction problems with general boundary conditions. Technical report, MOX Report, 2015.

[AS06] Ram Avtar and Rashmi Srivastava. Modelling the flow of aqueous humor in anterior chamber of the eye. *Applied mathematics and computation*, 181(2):1336–1348, 2006.

[AZW15] David Amsallem, Matthew J Zahr, and Kyle Washabaugh. Fast local reduced basis updates for the efficient reduction of nonlinear systems with hyper-reduction. *Advances in Computational Mathematics*, 41(5):1187–1230, 2015.

[BBG+14] C. Bertoglio, D. Barber, N. Gaddum, I. Valverde, M. Rutten, P. Beerbaum, P. Moireau, R. Hose, and J-F. Gerbeau. Identification of artery wall stiffness: in vitro validation and in vivo results of a data assimilation procedure applied to a 3D fluid-structure interaction model. *Journal of Biomechanics*, 47(5):1027–1034, March 2014.

[BBW+99] M Blum, Klaus Bachmann, Dominik Wintzer, Thomas Riemer, Walthart Vilser, and Jürgen Strobel. Noninvasive measurement of the bayliss effect in retinal autoregulation. *Graefe's archive for clinical and experimental ophthalmology*, 237(4):296–300, 1999.

[BČG+14] M Bukač, S Čanić, Roland Glowinski, Boris Muha, and Annalisa Quaini. A modular, operator-splitting scheme for fluid–structure interaction problems with thick structures. *International journal for numerical methods in fluids*, 74(8):577–604, 2014.

[BCZH06] Y Bazilevs, VM Calo, Y Zhang, and Thomas JR Hughes. Isogeometric fluid–structure interaction analysis with applications to arterial blood flow. *Computational Mechanics*, 38(4-5):310–322, 2006.

[Bek13] Toke Bek. Regional morphology and pathophysiology of retinal vascular disease. *Progress in retinal and eye research*, 36:247–259, 2013.

[BF14] Erik Burman and Miguel A Fernández. Explicit strategies for incompressible fluid-structure interaction problems: Nitsche type mortaring versus robin–robin coupling. *International Journal for Numerical Methods in Engineering*, 97(10):739–758, 2014.

[Bis00] Paul N Bishop. Structural macromolecules and supramolecular organisation of the vitreous gel. *Progress in retinal and eye research*, 19(3):323–344, 2000.

[BL12] Jöran Bergh and Jorgen Lofstrom. *Interpolation spaces: an introduction*, volume 223. Springer Science & Business Media, 2012.

[BM56] JA Beswick and Clement McCulloch. Effect of hyaluronidase on the viscosity of the aqueous humour. *The British journal of ophthalmology*, 40(9):545, 1956.

[BRD15] Rosalie Bélanger-Rioux and Laurent Demanet. Compressed absorbing boundary conditions via matrix probing. *SIAM Journal on Numerical Analysis*, 53(5):2441–2471, 2015.

[CAADH15] Francesco Calivà, Matteo Aletti, Bashir Al-Diri, and Andrew Hunter. A new tool to connect blood vessels in fundus retinal images. In *Engineering in Medicine and Biology Society (EMBC), 2015 37th Annual International Conference of the IEEE*, pages 4343–4346. IEEE, 2015.

[CDQ14] Claudia Maria Colciago, Simone Deparis, and Alfio Quarteroni. Comparisons between reduced order models and full 3D models for fluid–structure interaction problems in haemodynamics. *Journal of Computational and Applied Mathematics*, 265:120–138, 2014.

[CE13] TR Crowder and Vincent J Ervin. Numerical simulations of fluid pressure in the human eye. *Applied Mathematics and Computation*, 219(24):11119–11133, 2013.

[CGDF02] CR Canning, MJ Greaney, JN Dewynne, and AD Fitt. Fluid flow in the anterior chamber of a human eye. *Mathematical Medicine and Biology*, 19(1):31–60, 2002.

[CGH+14] Paola Causin, Giovanna Guidoboni, Alon Harris, Daniele Prada, Riccardo Sacco, and Samuele Terragni. A poroelastic model for the perfusion of the lamina cribrosa in the optic nerve head. *Mathematical biosciences*, 257:33–41, 2014.

[CGN05] P. Causin, J-F. Gerbeau, and F. Nobile. Added-mass effect in the design of partitioned algorithms for fluid-structure problems. *Comput. Methods Appl. Mech. Engrg.*, 194(42-44):4506–4527, 2005.

[CGSMVC10] Dominique Chapelle, J-F Gerbeau, J Sainte-Marie, and IE Vignon-Clementel. A poroelastic model valid in large strains with applications to perfusion in cardiac modeling. *Computational Mechanics*, 46(1):91–101, 2010.

[CHE14] ALEXANDER H-D CHENG. Fundamentals of poroelasticity. *Analysis and Design Methods: Comprehensive Rock Engineering: Principles, Practice and Projects*, 113, 2014.

[CHQZ07] C. Canuto, M.Y. Hussaini, A. Quarteroni, and T.A. Zang. *Spectral Methods: Fundamentals in Single Domains*. Scientific Computation. Springer Berlin Heidelberg, 2007.

[Cia00] Philippe G. Ciarlet. *Mathematical elasticity. Vol. III*, volume 29 of *Studies in Mathematics and its Applications*. North-Holland Publishing Co., Amsterdam, 2000. Theory of shells.

[CLC+17] Francesco Calivà, Georgios Leontidis, Piotr Chudzik, Andrew Hunter, Luca Antiga, and Bashir Al-Diri. Hemodynamics in the retinal vasculature during the progression of diabetic retinopathy. *Journal for modeling in Ophthalmology*, 2017.

[CM15] Paola Causin and Francesca Malgaroli. A mathematical and computational model of blood flow regulation in microvessels: Application to the eye retina circulation. *Journal of Mechanics in Medicine and Biology*, 15(02):1540027, 2015.

[CM16] Paola Causin and Francesca Malgaroli. Blood flow repartition in distensible microvascular networks: Implication of interstitial and outflow pressure conditions. *Journal of Coupled Systems and Multiscale Dynamics*, 4(1):14–24, 2016.

[Cou04] Olivier Coussy. *Poromechanics*. John Wiley & Sons, 2004.

[CPW14] Paul G Constantine, Eric T Phipps, and Timothy M Wildey. Efficient uncertainty propagation for network multiphysics systems. *International Journal for Numerical Methods in Engineering*, 99(3):183–202, 2014.

[CRD+11] Paolo Crosetto, Philippe Reymond, Simone Deparis, Dimitrios Kontaxakis, Nikolaos Stergiopulos, and Alfio Quarteroni. Fluid–structure interaction simulation of aortic blood flow. *Computers & Fluids*, 43(1):46–57, 2011.

[CRGMP14] Tomas Chacon-Rebollo, Vivette Girault, François Murat, and Olivier Pironneau. Analysis of a Simplified Coupled Fluid-Structure Model for Computational Hemodynamics. http://hal.upmc.fr/hal-01003208, April 2014.

[CZAL13] Liqun Cao, Lei Zhang, Walter Allegretto, and Yanping Lin. Multiscale asymptotic method for Steklov eigenvalue equations in composite media. *SIAM Journal on Numerical Analysis*, 51(1):273–296, 2013.

[DDFQ06] Simone Deparis, Marco Discacciati, Gilles Fourestey, and Alfio Quarteroni. Fluid–structure algorithms based on Steklov–Poincaré operators. *Computer Methods in Applied Mechanics and Engineering*, 195(41):5797–5812, 2006.

[DEDK96] Martin J Dumskyj, Jesper E Eriksen, Caroline J Doré, and Eva M Kohner. Autoregulation in the human retinal circulation: assessment

using isometric exercise, laser doppler velocimetry, and computer-assisted image analysis. *Microvascular research*, 51(3):378–392, 1996.

[DFGQ16] Simone Deparis, Davide Forti, Paola Gervasio, and Alfio Quarteroni. Internodes: an accurate interpolation-based method for coupling the galerkin solutions of pdes on subdomains featuring non-conforming interfaces. *Computers & Fluids*, 2016.

[DGDB+09] Anna I Dastiridou, Harilaos S Ginis, Dirk De Brouwere, Miltiadis K Tsilimbaris, and Ioannis G Pallikaris. Ocular rigidity, ocular pulse amplitude, and pulsatile ocular blood flow: the effect of intraocular pressure. *Investigative ophthalmology & visual science*, 50(12):5718–5722, 2009.

[DH97] J Douglas and C-S Huang. An accelerated domain decomposition procedure based on Robin transmission conditions. *BIT Numerical Mathematics*, 37(3):678–686, 1997.

[DQ03] M. Discacciati and A. Quarteroni. *Numerical Mathematics and Advanced Applications: Proceedings of ENUMATH 2001 the 4th European Conference on Numerical Mathematics and Advanced Applications Ischia, July 2001*, chapter Analysis of a domain decomposition method for the coupling of Stokes and Darcy equations, pages 3–20. Springer Milan, Milano, 2003.

[DSDJ98] Tim David, Steve Smye, Tim Dabbs, and Teifi James. A model for the fluid motion of vitreous humour of the human eye during saccadic movement. *Physics in medicine and biology*, 43(6):1385, 1998.

[EP14] Jens L Eftang and Anthony T Patera. A port-reduced static condensation reduced basis element method for large component-synthesized structures: approximation and a posteriori error estimation. *Advanced Modeling and Simulation in Engineering Sciences*, 1(1):1, 2014.

[ES+05] Moustafa El-Shahed et al. On the fluid flow in the anterior chamber of a human eye with slip velocity. *International communications in heat and mass transfer*, 32(8):1104–1110, 2005.

[FdOdSM14] José Augusto Ferreira, Paula de Oliveira, Pascoal M da Silva, and JN Murta. Numerical simulation of aqueous humor flow: From healthy to pathologic situations. *Applied Mathematics and Computation*, 226:777–792, 2014.

[FG06] AD Fitt and G Gonzalez. Fluid mechanics of the human eye: aqueous humour flow in the anterior chamber. *Bulletin of mathematical biology*, 68(1):53–71, 2006.

[FG09] M.A. Fernández and J-F. Gerbeau. Algorithms for fluid-structure interaction problems. In L. Formaggia, A. Quarteroni, and A. Veneziani, editors, *Cardiovascular Mathematics. Modeling and simulation of the circulatory system*, chapter 9, pages 307–346. Springer Verlag, 2009.

[FGS14] Miguel A Fernández, Jean-Frédéric Gerbeau, and Saverio Smaldone. Explicit coupling schemes for a fluid-fluid interaction problem arising in hemodynamics. *SIAM Journal on Scientific Computing*, 36(6):A2557–A2583, 2014.

[FLLT98] Charbel Farhat, Michael Lesoinne, and P Le Tallec. Load and motion transfer algorithms for fluid/structure interaction problems with non-matching discrete interfaces: Momentum and energy conservation, optimal discretization and application to aeroelasticity. *Computer methods in applied mechanics and engineering*, 157(1-2):95–114, 1998.

[FLV15] Miguel A Fernández, Mikel Landajuela, and Marina Vidrascu. Fully decoupled time-marching schemes for incompressible fluid/thin-walled structure interaction. *Journal of Computational Physics*, 297:156–181, 2015.

[FN14] Zheng Fang and David P Nicholls. An operator expansions method for computing Dirichlet–Neumann operators in linear elastodynamics. *Journal of Computational Physics*, 272:266–278, 2014.

[FVCJ+06] C Alberto Figueroa, Irene E Vignon-Clementel, Kenneth E Jansen, Thomas JR Hughes, and Charles A Taylor. A coupled momentum method for modeling blood flow in three-dimensional deformable arteries. *Computer methods in applied mechanics and engineering*, 195(41):5685–5706, 2006.

[GAG11] Lionel Gendre, Olivier Allix, and Pierre Gosselet. A two-scale approximation of the Schur complement and its use for non-intrusive coupling. *International Journal for Numerical Methods in Engineering*, 87(9):889–905, 2011.

[GHC+14a] Giovanna Guidoboni, Alon Harris, Lucia Carichino, Yoel Arieli, and Brent A Siesky. Effect of intraocular pressure on the hemodynamics of the central retinal artery: a mathematical model. *Mathematical biosciences and engineering: MBE*, 11(3):523–546, 2014.

[GHC+14b] Giovanna Guidoboni, Alon Harris, Simone Cassani, Julia Arciero, Brent Siesky, Annahita Amireskandari, Leslie Tobe, Patrick Egan, Ingrida Januleviciene, and Joshua Park. Intraocular pressure, blood pressure, and retinal blood flow autoregulation: A mathematical

model to clarify their relationship and clinical relevance. *Investigative ophthalmology & visual science*, 55(7):4105, 2014.

[GM09] Rafael Grytz and Günther Meschke. Constitutive modeling of crimped collagen fibrils in soft tissues. *Journal of the Mechanical Behavior of Biomedical Materials*, 2(5):522–533, 2009.

[GM10] Rafael Grytz and Günther Meschke. A computational remodeling approach to predict the physiological architecture of the collagen fibril network in corneo-scleral shells. *Biomechanics and modeling in mechanobiology*, 9(2):225–235, 2010.

[GMJ11] Rafael Grytz, Günther Meschke, and Jost B Jonas. The collagen fibril architecture in the lamina cribrosa and peripapillary sclera predicted by a computational remodeling approach. *Biomechanics and modeling in mechanobiology*, 10(3):371–382, 2011.

[GMSB16] Amir Gholami, Dhairya Malhotra, Hari Sundar, and George Biros. FFT, FMM, or Multigrid? a comparative study of state-of-the-art Poisson solvers in the unit cube. *SIAM Journal on Scientific Computing*, 38, 2016.

[GP13] Kirill Gostaf and Olivier Pironneau. Pressure Boundary Conditions for Blood Flows. http://hal.upmc.fr/hal-00865671, September 2013.

[GPLB10] Manik Goel, Renata G Picciani, Richard K Lee, and Sanjoy K Bhattacharya. Aqueous humor dynamics: a review. *The open ophthalmology journal*, 4(1), 2010.

[GR09] Christophe Geuzaine and Jean-François Remacle. Gmsh: A 3-D finite element mesh generator with built-in pre-and post-processing facilities. *International Journal for Numerical Methods in Engineering*, 79(11):1309–1331, 2009.

[GRS+84] JE Grunwald, CE Riva, RA Stone, EU Keates, and BL Petrig. Retinal autoregulation in open-angle glaucoma. *Ophthalmology*, 91(12):1690–1694, 1984.

[HAB+96] Alon Harris, Oliver Arend, Kathleen Bohnke, Elizabeth Kroepfl, Ronald Danis, and Bruce Martin. Retinal blood flow during dynamic exercise. *Graefe's archive for clinical and experimental ophthalmology*, 234(7):440–444, 1996.

[HB02] Jeffrey J Heys and Victor H Barocas. A boussinesq model of natural convection in the human eye and the formation of krukenberg's spindle. *Annals of biomedical engineering*, 30(3):392–401, 2002.

[HBT01] Jeffrey J Heys, Victor H Barocas, and Michael J Taravella. Modeling passive mechanical interaction between aqueous humor and iris. *Journal of biomechanical engineering*, 123(6):540–547, 2001.

[HGA+13] Alon Harris, Giovanna Guidoboni, Julia C Arciero, Annahita Amireskandari, Leslie A Tobe, and Brent A Siesky. Ocular hemodynamics and glaucoma: the role of mathematical modeling. *European journal of ophthalmology*, 23(2):139, 2013.

[HH02] Robert L Hester and Leah W Hammer. Venular-arteriolar communication in the regulation of blood flow. *American Journal of Physiology-Regulatory, Integrative and Comparative Physiology*, 282(5):R1280–R1285, 2002.

[HKP13] Dinh Bao Phuong Huynh, David J Knezevic, and Anthony T Patera. A static condensation reduced basis element method: approximation and a posteriori error estimation. *ESAIM: Mathematical Modelling and Numerical Analysis*, 47(1):213–251, 2013.

[HM88] Chi-Ming Hai and Richard A Murphy. Cross-bridge phosphorylation and regulation of latch state in smooth muscle. *Am J Physiol*, 254(1 Pt 1):C99–106, 1988.

[IQR16] Laura Iapichino, Alfio Quarteroni, and Gianluigi Rozza. Reduced basis method and domain decomposition for elliptic problems in networks and complex parametrized geometries. *Computers & Mathematics with Applications*, 71(1):408–430, 2016.

[JAB03] Peter Jeppesen, Christian Aalkjær, and Toke Bek. Myogenic response in isolated porcine retinal arterioles. *Current eye research*, 27(4):217–222, 2003.

[JAB13] Sara Jouzdani, Rouzbeh Amini, and Victor H Barocas. Contribution of different anatomical and physiologic factors to iris contour and anterior chamber angle changes during pupil dilation: Theoretical analysisfactors affecting iris profile during dilation. *Investigative ophthalmology & visual science*, 54(4):2977–2984, 2013.

[JSHB07] Peter Jeppesen, Javad Sanye-Hajari, and Toke Bek. Increased blood pressure induces a diameter response of retinal arterioles that increases with decreasing arteriolar diameter. *Investigative ophthalmology & visual science*, 48(1):328–331, 2007.

[KABP06] Satish Kumar, Sumanta Acharya, Roger Beuerman, and Arto Palkama. Numerical solution of ocular fluid dynamics in a rabbit eye: parametric effects. *Annals of biomedical engineering*, 34(3):530–544, 2006.

[KHR+11] JW Kiel, M Hollingsworth, R Rao, M Chen, and HA Reitsamer. Ciliary blood flow and aqueous humor production. *Progress in retinal and eye research*, 30(1):1–17, 2011.

[Kie98] Jeffrey W. Kiel. Physiology of the intraocular pressure. In J.Fehér, editor, *Pathophysiology of the eye: Glaucoma*, chapter 3, pages 79–107. Akadémiai Kiadó, 1998.

[KM14] Sreevani Kotha and Lasse Murtomäki. Virtual pharmacokinetic model of human eye. *Mathematical biosciences*, 253:11–18, 2014.

[KPR95] Eva M Kohner, Vinod Patel, and Salwan MB Rassam. Role of blood flow and impaired autoregulation in the pathogenesis of diabetic retinopathy. *Diabetes*, 44(6):603–607, 1995.

[Kra92] CE Krakau. Calculation of the pulsatile ocular blood flow. *Investigative ophthalmology & visual science*, 33(9):2754–2756, 1992.

[KS92] JW Kiel and AP Shepherd. Autoregulation of choroidal blood flow in the rabbit. *Investigative ophthalmology & visual science*, 33(8):2399–2410, 1992.

[KW12] Boris N Khoromskij and Gabriel Wittum. *Numerical solution of elliptic differential equations by reduction to the interface*, volume 36. Springer Science & Business Media, 2012.

[Lat67] Alan M Laties. Central retinal artery innervation: absence of adrenergic innervation to the intraocular branches. *Archives of Ophthalmology*, 77(3):405–409, 1967.

[LFO+89] Maurice E Langham, Richard A Farrell, Vivian O'Brien, David M Silver, and Peter Schilder. Blood flow in the human eye. *Acta Ophthalmologica*, 67(S191):9–13, 1989.

[LHS+04] James Lowell, Andrew Hunter, David Steel, Ansu Basu, Robert Ryder, and Richard Lee Kennedy. Measurement of retinal vessel widths from fundus images based on 2-d modeling. *IEEE transactions on medical imaging*, 23(10):1196–1204, 2004.

[LLB91] B Lee, M Litt, and G Buchsbaum. Rheology of the vitreous body. part i: Viscoelasticity of human vitreous. *Biorheology*, 29(5-6):521–533, 1991.

[LP10] Haw-Ling Liew and Peter M Pinsky. Matrix-Padé via Lanczos solutions for vibrations of fluid–structure interaction. *International Journal for Numerical Methods in Engineering*, 84(10):1183–1204, 2010.

[LS13] Trung Bao Le and Fotis Sotiropoulos. Fluid–structure interaction of an aortic heart valve prosthesis driven by an animated anatomic left ventricle. *Journal of Computational Physics*, 244(0):41 – 62, 2013. Multi-scale Modeling and Simulation of Biological Systems.

[MA14] Amirreza Modarreszadeh and Omid Abouali. Numerical simulation for unsteady motions of the human vitreous humor as a viscoelastic substance in linear and non-linear regimes. *Journal of Non-Newtonian Fluid Mechanics*, 204:22–31, 2014.

[MBX+12] P. Moireau, C. Bertoglio, N. Xiao, C. A. Figueroa, C. Taylor, D. Chapelle, and J-F. Gerbeau. Sequential identification of boundary support parameters in a fluid-structure vascular model using patient image data. *Biomechanics and Modeling in Mechanobiology*, 12(3):475–496, July 2012.

[McL09] Jay W McLaren. Measurement of aqueous humor flow. *Experimental eye research*, 88(4):641–647, 2009.

[Mil90] William R Milnor. *Cardiovascular physiology*. Oxford University Press, 1990.

[MKH10] Sae-Il Murtada, Martin Kroon, and Gerhard A Holzapfel. A calcium-driven mechanochemical model for prediction of force generation in smooth muscle. *Biomechanics and modeling in mechanobiology*, 9(6):749–762, 2010.

[Mos87] Robert A Moses. Intraocular pressure. *Adler2̆019s Physiology of the Eye: clinical application. CV Mosby Co*, pages 223–245, 1987.

[MQ89] Luisa D Marini and Alfio Quarteroni. A relaxation procedure for domain decomposition methods using finite elements. *Numerische Mathematik*, 55(5):575–598, 1989.

[MRH15] Immanuel Martini, Gianluigi Rozza, and Bernard Haasdonk. Reduced basis approximation and a-posteriori error estimation for the coupled Stokes-Darcy system. *Advances in Computational Mathematics*, 41(5):1131–1157, 2015.

[MSA+16] Aurelio Giancarlo Mauri, Lorenzo Sala, Paolo Airoldi, Giovanni Novielli, Riccardo Sacco, Simone Cassani, Giovanna Guidoboni, Brent Siesky, and alon Harris. Electro-fluid dynamics of aqueous humor production: simulations and new directions. *Journal for Modeling in Ophthalmology*, 1(2):48–58, 2016.

[MXA+12] P. Moireau, N. Xiao, M. Astorino, C. A. Figueroa, D. Chapelle, C. A. Taylor, and J-F. Gerbeau. External tissue support and fluid-structure

simulation in blood flows. *Biomechanics and Modeling in Mechanobiology*, 11(1):1–18, 2012.

[Nat95] Ramesh Natarajan. Domain decomposition using spectral expansions of Steklov–Poincaré operators. *SIAM Journal on Scientific Computing*, 16(2):470–495, 1995.

[Nat97] Ramesh Natarajan. Domain decomposition using spectral expansions of Steklov–Poincaré operators ii: A matrix formulation. *SIAM Journal on Scientific Computing*, 18(4):1187–1199, 1997.

[NMA15] Federico Negri, Andrea Manzoni, and David Amsallem. Efficient model reduction of parametrized systems by matrix discrete empirical interpolation. *Journal of Computational Physics*, 303:431–454, 2015.

[NMY02] Taiji Nagaoka, Fumihiko Mori, and Akitoshi Yoshida. Retinal artery response to acute systemic blood pressure increase during cold pressor test in humans. *Investigative ophthalmology & visual science*, 43(6):1941–1945, 2002.

[NV08] F. Nobile and C. Vergara. An effective fluid-structure interaction formulation for vascular dynamics by generalized robin conditions. *SIAM Journal on Scientific Computing*, 30(2):731–763, 2008.

[OEHB16] Giovanni Ometto, Mogens Erlandsen, Andrew Hunter, and Toke Bek. The role of retinopathy distribution and other lesion types for the definition of examination intervals during screening for diabetic retinopathy. *Acta Ophthalmologica*, 2016.

[ON08] Ean-Hin Ooi and Eddie Yin-Kwee Ng. Simulation of aqueous humor hydrodynamics in human eye heat transfer. *Computers in biology and medicine*, 38(2):252–262, 2008.

[PH08] Anna Pandolfi and Gerhard A Holzapfel. Three-dimensional modeling and computational analysis of the human cornea considering distributed collagen fibril orientations. *Journal of biomechanical engineering*, 130(6):061006, 2008.

[Pir14] Olivier Pironneau. Simplified Fluid-Structure Interactions for Hemodynamics. In Sergio R. Idelsohn, editor, *Numerical Simulations of Coupled Problems in Engineering*, volume 33 of *Computational Methods in Applied Sciences*, pages 57–70. Springer International Publishing, 2014.

[PLCG89] AR Pries, K Ley, M Claassen, and P Gaehtgens. Red cell distribution at microvascular bifurcations. *Microvascular research*, 38(1):81–101, 1989.

[PNG92] AR Pries, D Neuhaus, and P Gaehtgens. Blood viscosity in tube flow: dependence on diameter and hematocrit. *American Journal of Physiology*, 263:H1770–H1770, 1992.

[PRBR+08] Constantin J Pournaras, Elisabeth Rungger-Brändle, Charles E Riva, Sveinn H Hardarson, and Einar Stefansson. Regulation of retinal blood flow in health and disease. *Progress in retinal and eye research*, 27(3):284–330, 2008.

[PRMT+11] A Perez-Rovira, T MacGillivray, E Trucco, KS Chin, K Zutis, C Lupascu, D Tegolo, A Giachetti, PJ Wilson, A Doney, et al. Vampire: vessel assessment and measurement platform for images of the retina. In *Engineering in medicine and biology society, EMBC, 2011 annual international conference of the IEEE*, pages 3391–3394. IEEE, 2011.

[PS05] Rodrigo R Paz and Mario A Storti. An interface strip preconditioner for domain decomposition methods: application to hydrology. *International journal for numerical methods in engineering*, 62(13):1873–1894, 2005.

[PV12] Anna Pandolfi and Marcello Vasta. Fiber distributed hyperelastic modeling of biological tissues. *Mechanics of Materials*, 44:151–162, 2012.

[PW15] Benjamin Peherstorfer and Karen Willcox. Online adaptive model reduction for nonlinear systems via low-rank updates. *SIAM Journal on Scientific Computing*, 37(4):A2123–A2150, 2015.

[QR14] Alfio Quarteroni and Gianluigi Rozza. *Reduced Order Methods for Modeling and Computational Reduction*, volume 9. Springer, 2014.

[QV99] A. Quarteroni and A. Valli. *Domain Decomposition methods for partial differential equations*. Oxford University Press, 1999.

[Rep06] Rodolfo Repetto. An analytical model of the dynamics of the liquefied vitreous induced by saccadic eye movements. *Meccanica*, 41(1):101–117, 2006.

[RGSP85] Charles E Riva, Juan E Grunwald, Stephen H Sinclair, and BL Petrig. Blood velocity and volumetric flow rate in human retinal vessels. *Investigative ophthalmology & visual science*, 26(8):1124–1132, 1985.

[RPK95] SM Rassam, V Patel, and EM Kohner. The effect of experimental hypertension on retinal vascular autoregulation in humans: a mechanism for the progression of diabetic retinopathy. *Experimental physiology*, 80(1):53–68, 1995.

[RRG+86] Fane Robinson, Charles E Riva, Juan E Grunwald, Benno L Petrig, and Stephen H Sinclair. Retinal blood flow autoregulation in response to an acute increase in blood pressure. *Investigative ophthalmology & visual science*, 27(5):722–726, 1986.

[RSC05] Rodolfo Repetto, Alessandro Stocchino, and Chiara Cafferata. Experimental investigation of vitreous humour motion within a human eye model. *Physics in medicine and biology*, 50(19):4729, 2005.

[RSS10] R Repetto, JH Siggers, and A Stocchino. Mathematical model of flow in the vitreous humor induced by saccadic eye rotations: effect of geometry. *Biomechanics and modeling in mechanobiology*, 9(1):65–76, 2010.

[Sal15] Sandro Salsa. *Partial differential equations in action: from modelling to theory*, volume 86. Springer, 2015.

[SAN+04] J.J. Staal, M.D. Abramoff, M. Niemeijer, M.A. Viergever, and B. van Ginneken. Ridge based vessel segmentation in color images of the retina. *IEEE Transactions on Medical Imaging*, 23(4):501–509, 2004.

[SBG04] Barry Smith, Petter Bjorstad, and William Gropp. *Domain decomposition: parallel multilevel methods for elliptic partial differential equations*. Cambridge university press, 2004.

[SBW+02] Chanjira Sinthanayothin, JF Boyce, TH Williamson, HL Cook, E Mensah, S Lal, and D Usher. Automated detection of diabetic retinopathy on digital fundus images. *Diabetic medicine*, 19(2):105–112, 2002.

[SE12] Jennifer H Siggers and C Ross Ethier. Fluid mechanics of the eye. *Annual Review of Fluid Mechanics*, 44:347–372, 2012.

[SFL+89] David M Silver, Richard A Farrell, Maurice E Langham, Vivian O'Brien, and Peter Schilder. Estimation of pulsatile ocular blood flow from intraocular pressure. *Acta Ophthalmologica*, 67(S191):25–29, 1989.

[SKH08] Jonas Stålhand, Anders Klarbring, and Gerhard A Holzapfel. Smooth muscle contraction: mechanochemical formulation for homogeneous finite strains. *Progress in biophysics and molecular biology*, 96(1):465–481, 2008.

[SKHSK11] Pooria Sharif-Kashani, Jean-Pierre Hubschman, Daniel Sassoon, and H Pirouz Kavehpour. Rheology of the vitreous gel: effects of macromolecule organization on the viscoelastic properties. *Journal of biomechanics*, 44(3):419–423, 2011.

[SM99] Rudolf Schubert and Michael J Mulvany. The myogenic response: established facts and attractive hypotheses. *Clinical Science*, 96:313–326, 1999.

[SMP14] Paolo Sánchez, Kyros Moutsouris, and Anna Pandolfi. Biomechanical and optical behavior of human corneas before and after photorefractive keratectomy. *Journal of Cataract & Refractive Surgery*, 40(6):905–917, 2014.

[SP15] Irene Simonini and Anna Pandolfi. Customized finite element modelling of the human cornea. *PloS one*, 10(6):e0130426, 2015.

[SRC07] Alessandro Stocchino, Rodolfo Repetto, and Chiara Cafferata. Eye rotation induced dynamics of a newtonian fluid within the vitreous cavity: the effect of the chamber shape. *Physics in medicine and biology*, 52(7):2021, 2007.

[SS14] Babak Sharifimajd and Jonas Stålhand. A continuum model for excitation–contraction of smooth muscle under finite deformations. *Journal of theoretical biology*, 355:1–9, 2014.

[TW05] Andrea Toselli and Olof Widlund. *Domain decomposition methods: algorithms and theory*, volume 34. Springer, 2005.

[UOK+99] Eiichi Uchio, Shigeaki Ohno, Joju Kudoh, Koki Aoki, and Lech Tomasz Kisielewicz. Simulation model of an eyeball based on finite element analysis on a supercomputer. *British Journal of Ophthalmology*, 83(10):1106–1111, 1999.

[vAdB04] R. van Loon, P.D. Anderson, J. de Hart, and F. Baaijens. A combined fictitious domain/adaptative meshing method for fluid-structure interaction in heart valves. *Int. J. Num. Meth. Fluids*, 46:533–544, 2004.

[vAv06] R. van Loon, P.D. Anderson, and F.N. van de Vosse. A fluid-structure interaction method with solid-rigid contact for heart valve dynamics. *J. Comp. Phys.*, 217:806–823, 2006.

[VB89] E Michael Van Buskirk. The anatomy of the limbus. *Eye*, 3(2):101–108, 1989.

[VRH+12] Adan Villamarin, Sylvain Roy, Reda Hasballa, Orestis Vardoulis, Philippe Reymond, and Nikolaos Stergiopulos. 3D simulation of the aqueous flow in the human eye. *Medical engineering & physics*, 34(10):1462–1470, 2012.

[WKK+03] Tien Yin Wong, Ronald Klein, Barbara EK Klein, Stacy M Meuer, and Larry D Hubbard. Retinal vessel diameters and their associations

with age and blood pressure. *Investigative ophthalmology & visual science*, 44(11):4644–4650, 2003.

[WKSL72] SL-Y Woo, AS Kobayashi, WA Schlegel, and C Lawrence. Nonlinear material properties of intact cornea and sclera. *Experimental Eye Research*, 14(1):29–39, 1972.

[YCJBR03a] Jin Yang, John W Clark Jr, Robert M Bryan, and Claudia Robertson. The myogenic response in isolated rat cerebrovascular arteries: smooth muscle cell model. *Medical engineering & physics*, 25(8):691–709, 2003.

[YCJBR03b] Jin Yang, John W Clark Jr, Robert M Bryan, and Claudia S Robertson. The myogenic response in isolated rat cerebrovascular arteries: vessel model. *Medical engineering & physics*, 25(8):711–717, 2003.

[Zim80] Robert Lee Zimmerman. In vivo measurements of the viscoelasticity of the human vitreous humor. *Biophysical Journal*, 29(3):539, 1980.